(NASA-CR-174756) THE TRANSIENT OXIDATION OF SINGLE CRYSTAL NiAl+Zr M.S. Thesis. Final Report (Case Western Reserve Univ.) 243 p HC A11/MF A01 CSCL 11F

N85-11221

Unclas
G3/26 24372

NASA Contractor Report 174756

The Transient Oxidation of Single Crystal NiAl+Zr

Joseph K. Doychak

Case Western Reserve University
Cleveland, Ohio

September 1984

Prepared for

NATIONAL AERONAUTICS AND SPACE ADMINISTRATION
Lewis Research Center
Under Grant NAG 3-58

The Transient Oxidation of Single Crystal NiAl+Zr

J. K. Doychak

The 800°C oxidation of oriented single crystals of Zr doped β-NiAl was studied using transmission electron microscopy. The oxide phases and metal-oxide orientation relationships were determined to characterize the transient stages of oxidation prior to the transformation to or formation of α-Al_2O_3.

On (001) and (012) metal orientations, $NiAl_2O_4$ was the first oxide to form followed by δ-Al_2O_3 which becomes the predominant oxide phase. All oxides were highly epitaxially related to the metal; the orientation relationships being a function of parallel cation close-packed directions in the metal and oxide. On (011) and (111) metal orientations, γ-Al_2O_3 became the predominant oxide phase rather than δ-Al_2O_3 indicating a structural stability resulting from the highly expitaxial oxides. The relative concentration of aluminum in the oxide scales increased with time indicating preferential γ-or δ-Al_2O_3 growth.

Orientation relationships between the metal and oxide existed for all metal orientations studied. On (001) metal, the Bain relationship was always present and is given as:

$$\begin{array}{ccc} (001)_m & || & (001)_{ox} \\ [100]_m & || & [110]_{ox} \end{array}$$

The orientation relationship on (012) metal was:

$$\begin{array}{ccc} (012)_m & || & (112)_{ox} \\ [100]_m & || & [110]_{ox} \end{array}$$

Three orientation relationships existed on (011) metal at short oxidizing times, but only the Nishyama-Wassermann relationship persisted when γ-Al_2O_3 became the predominant oxide phase. The three orientation relationships are the Nishyama-Wassermann,

$$\begin{array}{ccc} (011)_m & || & (\bar{1}11)_{ox} \\ [100]_m & || & [110]_{ox} \end{array}$$

The Kurdjumov-Sachs,

$$(011)_m \;||\; (\bar{1}11)_{ox}$$
$$[11\bar{1}]_m \;||\; [01\bar{1}]_{ox}$$

and a third relationship,

$$(011)_m \;||\; (\bar{1}11)_{ox}$$
$$[21\bar{1}]_m \;||\; [01\bar{1}]_{ox}$$

On (111) metal, the orientation relationship contained three variants, 120° apart, and is given as:

$$(111)_m \;||\; \text{near } (021)_{ox}$$
$$[1\bar{1}0]_m \;||\; [100]_{ox}$$

Simplified computer modeling of the orientation relationships confirmed geometrical interface theories but did not provide sufficient information to predict energetically favorable orientation relationships.

Table of Contents

Introduction

A) Background

Continuing advancements in high-temperature technology have placed an increasing demand on the materials used for such applications. The development of high temperature alloys over recent decades has facilitated the operation of gas turbine engines, power generating plants and other high-temperature equipment. The title of "superalloys" has been given to metallic alloys designed to have superior strength and creep resistance at elevated temperatures in the range 800°C - 1100°C.

The improvements in alloy design characteristics of superalloys are based on optimum use of phase composition and morphology. The basic alloys consist of an iron, cobalt or nickel matrix with chromium added to improve strength and corrosion resistance. As operating temperatures are increased, corrosion resistance is maintained but strength falls off rapidly.[1] Additional alloying elements, each with a specific purpose, are added to increase the mechanical properties at higher temperatures. As many as a dozen elements comprise some modern superalloys.

As can be expected when taking into consideration the number of elements in superalloys, the corrosion characteristics are quite complex since they are related to oxide formation on the alloy surface. The alloying elements allow better mechanical properties at higher temperatures at the expense of good corrosion resistance. Two factors are involved in poorer corrosion resistance: 1) numerous oxide phases not considered to be protective and 2) degradation of protective oxides. Corrosion resistance has in the past been, and still is, obtained by coating superalloy components with a material that oxidizes to form a protective oxide scale. Oxidation resistance, though not completely synonymous with corrosion resistance, is the property that is under consideration.

The basis for using coatings is their ability to form a protective oxide scale. The requirements for a protective oxide are thermodynamic stability, and a slow growth rate of a complete, uniform, adherent scale. The oxides that conform best to these specifications are Cr_2O_3, SiO_2 and Al_2O_3. Of the three, Al_2O_3 has superior properties of a slow growth rate and high thermodynamic stability at operating conditions. Being an oxide of a very common and important alloying element, aluminum, Al_2O_3 is quite convenient to incorporate into the scheme of oxidation resistance.

Coating alloys must then have a sufficient aluminum content to provide a continuous alumina scale. An intermetallic compound such as NiAl would fulfill this requirement. Problems arise, however, when the entire oxide-coating-substrate system is taken into consideration. Interdiffusion between the coating and substrate alloys can result in depletion of the aluminum content of the coating to an extent where the coating can no longer supply enough aluminum for a continuous oxide scale. Chromium can be added to NiAl to increase the compatibility between the coating and substrate by decreasing the relative amount of Al in the coating alloy which decreases the compositional gradient. Optimum levels of Cr and Al are near 15 at % and 25 at % respectively.[2]

The ability to maintain a protective oxide scale also depends upon the ability to resist damage of the initial layer and reformation of the oxide once it has been damaged. Most operations involve cyclic conditions where the oxide-metal system undergoes differential thermal expansions and contractions. Upon cooling of a gas turbine engine for example, the oxide would be in compression because its thermal expansion coefficient is less than that of the underlying metal. Cracks can form in the oxide where local stress states warrant their formation, the theoretical stresses being much higher than the limits for the system as shown by Ebert[3] and by Garlick and

Lowell[4]. The oxide scales can also be damaged by debris from the atmosphere. Therefore, it is critical that the oxide layer be adherent, free from defects and easily reformed if bare metal is exposed.

The adherence of an oxide to a metal substrate has been found to be improved by additions of small amounts of reactive elements or oxide dispersions to the alloy. A number of different theories have been proposed to explain the mechanism by which this phenomenon occurs.

The growth stress mechanism, proposed by Golightly, Stott & Wood, suggests that dopant additions are incorporated into the inward growing oxide preventing counterdiffusion of aluminum cations via grain boundaries or dislocations.[5] Elemental additions or oxide dispersions added to the alloy were found to reduce voids at the metal-oxide interface.[6,7] This effect is known as the vacancy sink mechanism and has been observed in many studies of oxide adherence. The pegging mechanism involves intrusions of oxide into the alloy resulting from dopant additions.[8,9] A final mechanism is that of the possibility of enhanced chemical bonding between the oxide and metal resulting from dopant additions.[10] Of the four mentioned, no single mechanism has been found to be the dominant factor in adherence, but all may contribute. Oxide adherence is only one of

the factors involved in the oxidation resistance of alloys. Fundamentally, the formation and growth of the oxide layer are also important. Affecting the parameters involved in the oxide formation process can have an effect on the subsequent growth of the oxide and thus on the oxidation resistance of a material.

Improvements in the oxidation resistance of alumina forming alloys have been a major topic of high-temperature research. With the need for improvement in mind, the present oxidation study was proposed to expand on methods to obtain this goal. These methods involve controlling the scale growth rate by control of the scale microstructure. To eliminate other variables, a single phase, NiAl + Zr alloy will serve as the substrate. Therefore, it is convenient to review the literature on the formation and growth of Al_2O_3, on these and other Ni-base alloys. Special emphasis is placed on the transient stages of Al_2O_3 formation and growth.

B) The Formation and Growth of Al_2O_3 Scales

1) Thermodynamics

When a Ni-base alloy containing aluminum is exposed to an air atmosphere at an oxidizing temperature, a number of different oxidation reactions can take place. These are;

$$2Al\ (alloy) + 3/2\ O_2 = Al_2O_3 \qquad [1]$$

$$Ni\ (alloy) + 1/2\ O_2 = NiO \qquad [2]$$

when only Ni and Al are considered. According to Wagner [11] and Wallwork[12], these oxide phases can form as external scales having distinct phase boundaries, or as a mixed compound of the two oxide phases according to the reaction:

$$Ni\ (alloy) + 2Al\ (alloy) + 2O_2 = NiAl_2O_4 \qquad [3]$$

Kear et al[13] have described the initial oxidation stages of a Ni-15Cr-6Al alloy. The addition of chromium does not change the overall oxidation process but alters the kinetics of obtaining an uniform Al_2O_3 scale. Upon exposure to an oxidizing atmosphere where the partial pressure of oxygen exceeds the

dissociation pressure of all possible oxide phases of the metallic system, oxide nuclei form on the surface of the metal (Figure 1a). For a Ni-Al alloy, NiO, $NiAl_2O_4$ and Al_2O_3 form, whereas Cr in the metal would also induce formation of $Ni(Cr, Al)_2O_4$ and Cr_2O_3. The growth rates of NiO and the spinels are greater than those of the sesquioxides. Therefore, NiO and $Ni(Cr, Al)_2O_4$ would grow and completely cover the metal surface (Figure 1b). Further nucleation and lateral growth of the sesquioxides occurs at the metal-oxide interface until a complete layer of Al_2O_3 forms (Figure 1c). Further growth of the entire oxide layer at this stage is controlled by inward oxygen diffusion through the Al_2O_3 layer.

Pettit has developed the concept related to the maximum amount of Al in a Ni-Al alloy needed to form a complete healing layer of Al_2O_3.[14] The possible reactions that can take place on the alloy surface upon exposure to oxygen have been mentioned above. These reactions take place rapidly at the metal surface and are not an indication of overall equilibrium. Further growth of the oxides can be described by the combination of the above equations to give:

$$3\ NiAl_2O_4 + 2\ Al\ (alloy) = 4\ Al_2O_3 + 3\ Ni\ (alloy) \qquad [4]$$

$$4\ NiO + 2\ Al\ (alloy) = NiAl_2O_4 + 3\ Ni\ (alloy) \qquad [5]$$

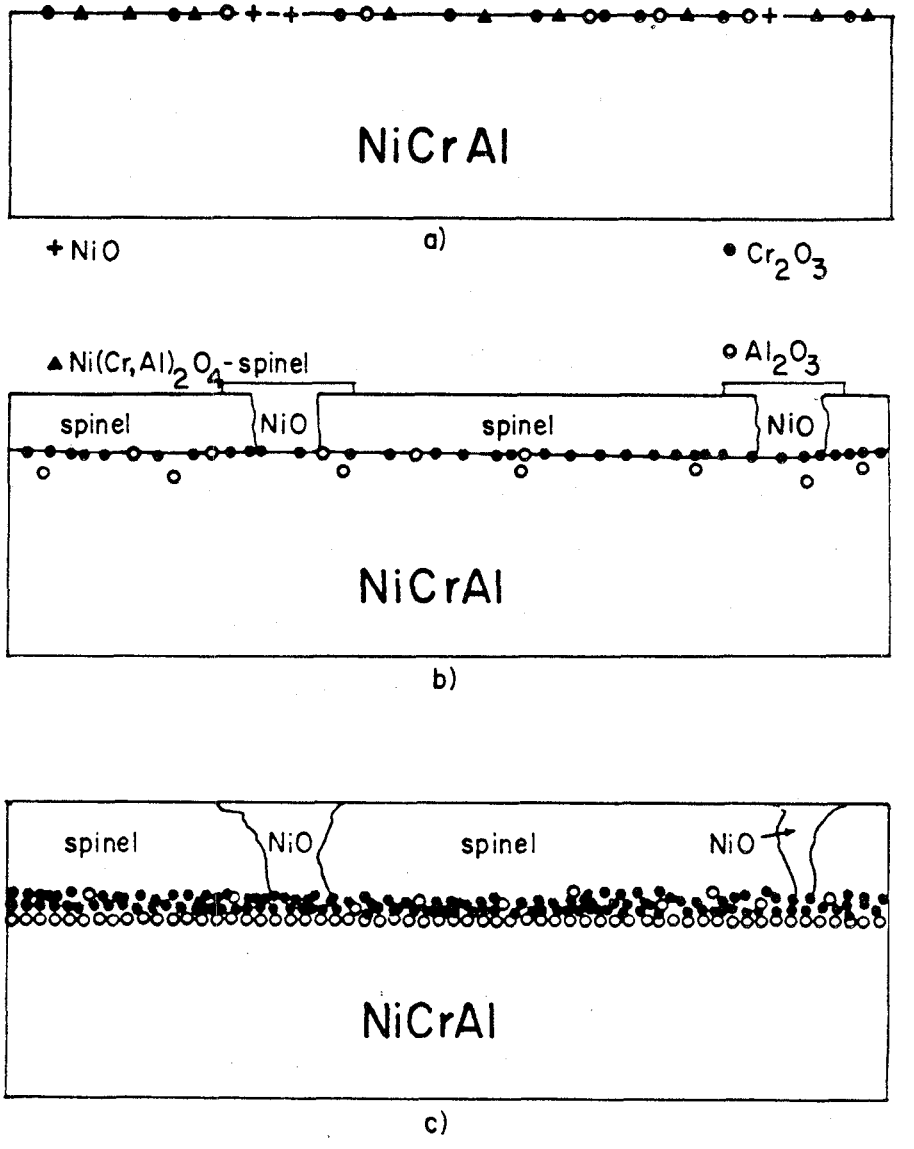

Figure 1

Schematic representation of the initial stages of oxidation on an Al_2O_3 forming alloy upon a) nucleation of all oxide phases b) formation of a complete oxide layer and c) formation of a healing layer of Al_2O_3. (Ref. 13)

The standard free energies of formation of the oxide phases are known and can be used to determine activity ratios of the elements, for both NiO and $NiAl_2O_4$ in equilibrium with the alloy, by applying the mass-action law to equations [4] and [5].

$$\Delta G_{[4]} = 4\Delta G^\circ_{Al_2O_3} - 3\Delta G^\circ_{NiAl_2O_4} = RT \ln(a^2_{Al}/a^3_{Ni}) \qquad [6]$$

where ΔG° is the standard free energy of formation and a_{Al}, a_{Ni} are the activities of Al and Ni respectively at the metal-oxide interface. For equation [4],

$$a^2_{Al}/a^3_{Ni} = \exp[(4\Delta G^\circ_{Al_2O_3} - 3\Delta G^\circ_{NiAl_2O_4})/RT] \qquad [7]$$

and likewise for equation [5],

$$a^2_{Al}/a^3_{Ni} = \exp[(\Delta G^\circ_{NiAl_2O_4} - 4\Delta G^\circ_{NiO})/RT] \qquad [8]$$

the activity ratios being proportional to concentration ratios. Calculations of activity ratios at various temperatures are tabulated in Table I. Since

$$(a^2_{Al}/a^3_{Ni})_{[5]} < (a^2_{Al}/a^3_{Ni})_{[4]} << 1 \qquad [9]$$

the aluminum activity can be approximated to be the square root of the aluminum activity squared over the nickel activity cubed, i.e., the activity of nickel is approximately unity. The thermodynamically stable oxide phases of equations [4] and [5] depend upon the activity ratio given above. The activities are also dependent upon the oxygen partial pressure, as can be surmised from equations [1], [2], and [3]. Figure 2 shows this for the formation reactions of the oxide phases. At 1000°C, an aluminum activity of approximately 10^{-17} corresponds to an equilibrium concentration of 1 ppm Al at an oxygen partial pressure of 10^{-6} atmospheres. According to Figure 2, Al_2O_3 is the most stable oxide phase at higher oxygen partial pressures and high Al concentrations. The relative stability of Al_2O_3 increases with decreasing temperatures. It is also evident that at atmospheric pressures, all oxide phases can form.

TABLE I

Equilibrium constants for the three-phase equilibria; Alloy-Al_2O_3-$NiAl_2O_4$ and Alloy-$NiAl_2O_4$-NiO.(Ref. 13)

Temperature(^{o}C)	Alloy-Al_2O_3-$NiAl_2O_4$	Alloy-$NiAl_2O_4$-NiO
900	$10^{-36.9}$	$10^{-41.4}$
1000	$10^{-34.3}$	$10^{-37.3}$
1100	$10^{-32.0}$	$10^{-34.1}$
1200	$10^{-29.7}$	$10^{-31.5}$
1300	$10^{-27.7}$	$10^{-29.2}$

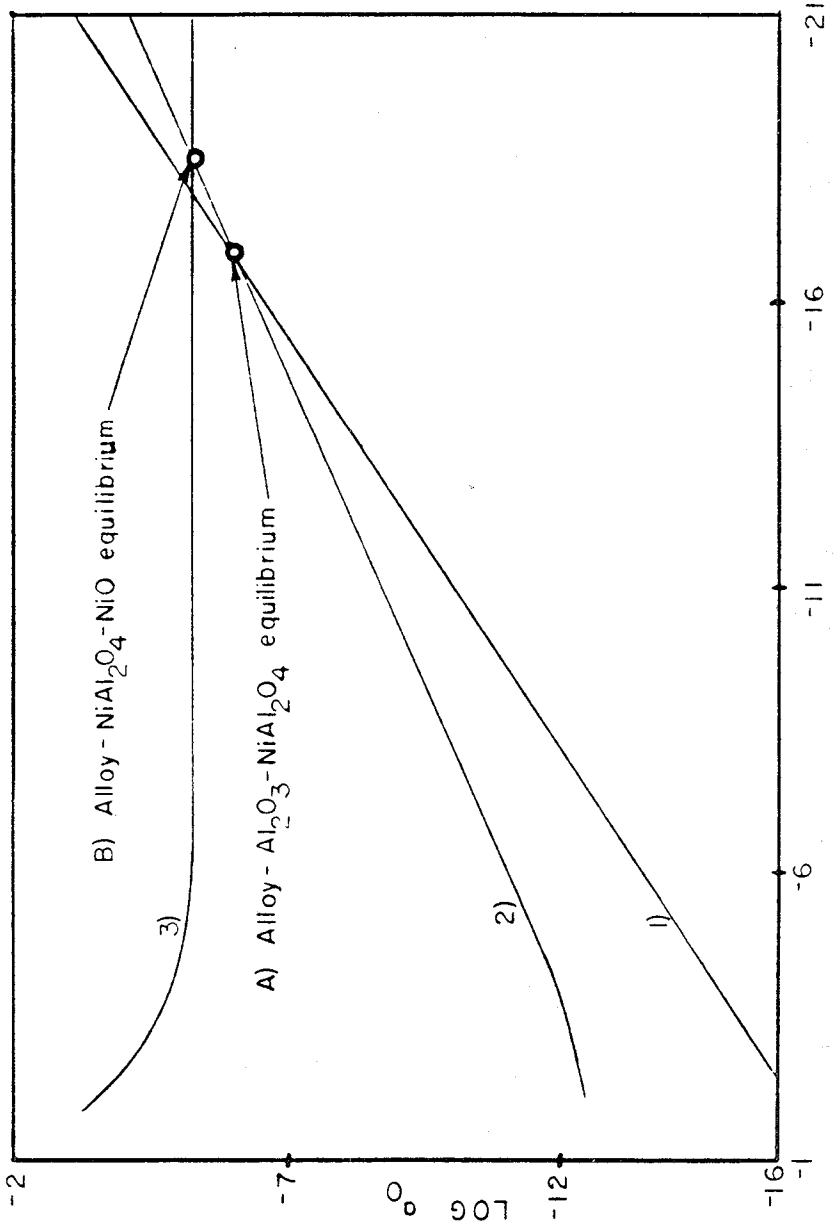

Figure 2

Stability diagram for oxide phases that can be formed on Ni-Al alloys at 1000°C. Curves 1, 2 and 3 are the alloy-Al_2O_3, alloy-$NiAl_2O_4$ and alloy-NiO equilibria, respectively. The aluminum concentration at point A is about 1 ppm. (Ref. 14)

2) Diffusion

A last consideration in the formation of a healing layer of Al_2O_3 involves diffusional processes, and in particular, Al diffusion away from the reaction layer at the metal-oxide interface, both inward into the metallic bulk alloy and outward through the oxide scale. A critical mole fraction of Al_2O_3 must be exceeded in the alloy, to permit the formation of an external scale. If it is not present, internal oxidation will occur. The critical mole fraction, N^*, is given by:

$$N^* = \left(\frac{\pi\Theta_c}{2\nu} N_0^S \frac{D_0}{D_{AB}}\right)^{\frac{1}{2}} \qquad [10]$$

Θ_c = critical volume fraction (0.1-1.0)

ν = stoichiometry factor in MO_ν oxide

N_0^S = mole fraction of oxygen at the surface

D_0 = diffusion coefficient of cations in the oxide

D_{AB} = alloy interdiffusion coefficient

In alumina forming alloys, the concentration of Al is sufficiently high to achieve a rapidly formed, uniform Al_2O_3 scale. Only after the supply of Al has been consumed by steady state oxidation or by repeated scale reformation will the alloy not be able to provide a sufficient Al concentration to maintain a uniform scale.

The oxidation and growth process is actually a diffusion process since mobile species, ionic or electronic in nature, diffuse through the oxide scale to react at the phase boundaries and form oxide. This applies in the growth of an Al_2O_3 scale in that the overall oxidation rate of an alumina forming alloy is dependent on the growth rate of the Al_2O_3 healing layer, once it has formed.

Oxygen diffusion in Al_2O_3 has been found to occur primarily along grain boundaries. Studies of grain boundary diffusion in bulk Al_2O_3 by Oishi and Kingery[15] and also by Reddy[16] have indicated this. ^{18}O tracer studies were used to determine the diffusion coefficient in the bulk and in grain boundaries as well as the activation energies. Studies of ^{18}O tracer diffusion in Al_2O_3 scales were performed by Reddy, Smialek and Cooper[17] indicating that 1) growth of the oxide did occur via inward oxygen grain boundary diffusion and 2) dopant additions had an effect on outward Al grain boundary diffusion related to oxide growth within the scale. Their ^{18}O tracer study was supported by SEM micrographs of the oxide scales. Their finding that Al_2O_3 scales grow by inward oxygen grain boundary diffusion agrees with Pt marker experiments[6].

3) Oriented Transient Oxides

Smialek studied Al_2O_3 scales on Y-doped and undoped NiCrAl alloys using transmission electron microscopy.[18] In his work, the morphological characteristics of the scales were related to processes such as grain growth, void growth and overall oxidation rate. Not only were mature, stable α-Al_2O_3 scales studied, but also the transient scales involving metastable forms of Al_2O_3 and other metal oxides were given consideration. The transient oxide scales had a preferred orientation whereas the mature α-Al_2O_3 scale had a random orientation.

These findings were used to speculate on the possibility of maintaining an oriented mature oxide scale to decrease the overall growth rate. Changing the misorientation between grains in metals is enough to cause drastic differences in the grain boundary diffusion coefficients.[19] This same idea, when applied to Al_2O_3 scales, would involve a decrease in the inward oxygen grain boundary diffusion through an oriented scale with low angle grain boundaries as opposed to the randomly oriented scale with high angle grain boundaries.

The misorientation principle was tested experimentally previous to Smialek's work. Khoi, Smeltzer and Embury performed an

oxidation study on single crystal nickel substrates.[20] Different crystal faces of nickel were oxidized and the growth rates measured. The slowest growth rates were found to be associated with the oxide having the highest degree of preferred orientation as found by X-ray diffraction and transmission electron microscopy (TEM). The preferential oxide orientations involved alignment of the closest-packed-direction in the oxide and metal, the system thus having specific orientation relationships. Excellent correlation between theory and experiment occurred when both lattice and grain boundary diffusion and grain growth rates of the oxide scales were taken into account.

The growth rates of protective oxide scales are compared using the parabolic rate constant, k_p, given as:

$$k_p = \frac{dX^2}{dt} \qquad [11]$$

where X is the oxide thickness and t the time. This equation states that the thickness of the oxide is proportional to the square root of time.

The growth rates of oxide scales on Ni-Al alloys vary with composition and temperature as shown in Figure 3. Pettit[14] found changes in mechanisms of oxidation for some Ni-rich

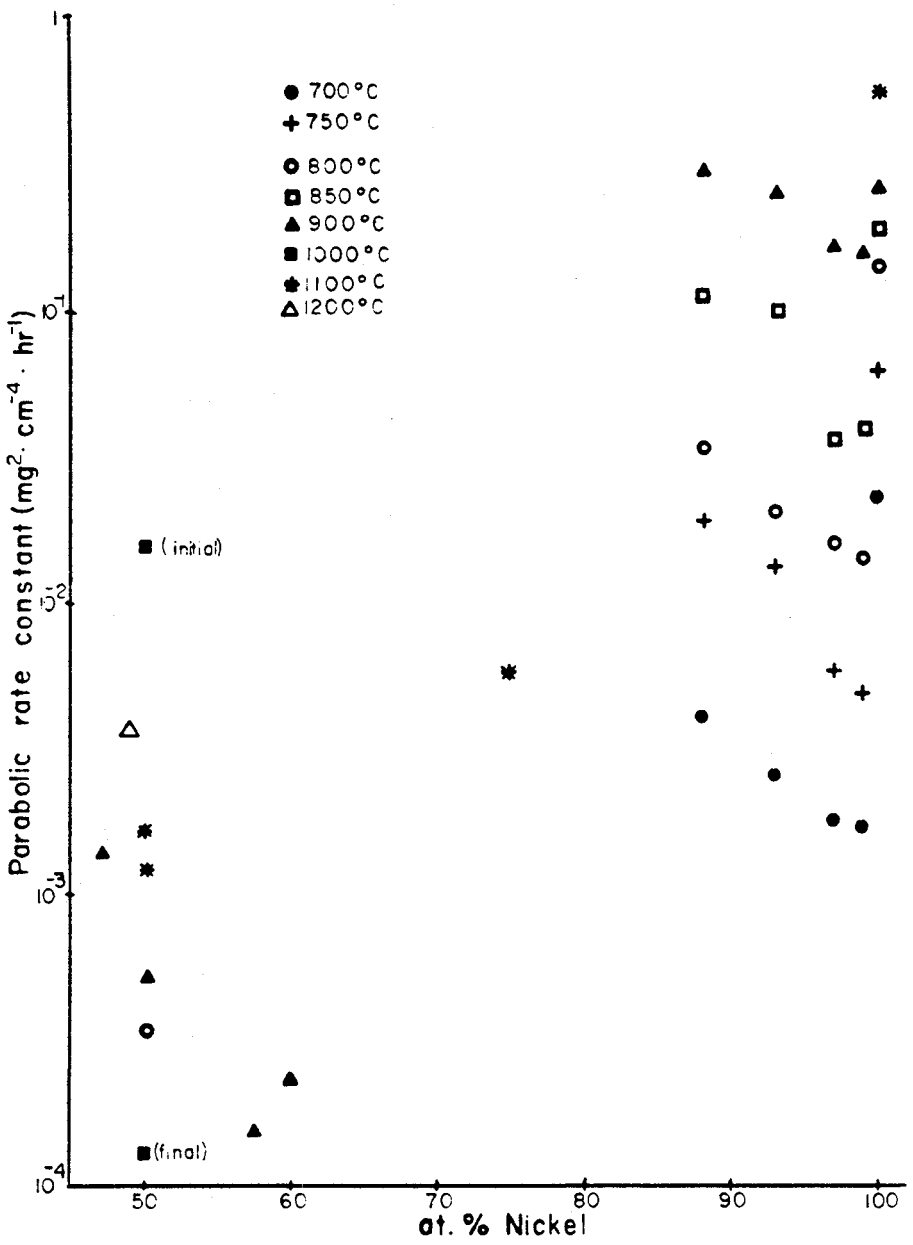

Figure 3

Measured parabolic rate constants for the growth of oxide on Ni-Al alloys at various temperatures.

alloys, especially at higher temperatures near 1200°C. Rybicki[21] found changes in oxidation mechanisms of a stoichiometric NiAl alloy at 1000°C. These mechanistic changes indicate a trend from transient stages of oxidation to final oxidation states. At higher temperatures and longer times, changes from NiO, $NiAl_2O_4$ and Al_2O_3 to exclusively Al_2O_3 occur. These changes involve the attainment of a complete external layer of Al_2O_3 as described previously. However, when Al_2O_3 is the only scale present, changes in growth rates can result from transformations of the alumina scale from metastable to more stable Al_2O_3 phases. The metastable forms of Al_2O_3 are spinel-like in structure whereas α-Al_2O_3 is rhombohedral and resembles a hexagonal structure. When found during transient stages of oxidation, the metastable Al_2O_3 phases usually have some specific orientation . Smialek[22] found the oxide phases to exhibit specific orientation relationships with each other while Koch and Romeo found indications of preferred orientation[23]. Felton and Pettit found that the metastable phases consisted of very fine, highly oriented oxide crystallites.[24]

There is evidence of oriented α-Al_2O_3 scales, but as yet no detailed study of preferred orientation. Hindam and Smeltzer found large oriented α-Al_2O_3 grains on β-NiAl separated by boundaries of small polycrystalline α-Al_2O_3.[25] Rybicki also

found a similar structure on NiAl + Zr indicating some tendency for oriented α-Al_2O_3[21]. Control of the transformation from the metastable forms of Al_2O_3 to α-Al_2O_3 is, therefore, critical to obtaining a preferred oxide orientation. The transformation to α-Al_2O_3 involves a 14% decrease in volume [26], generating tensile stresses in the oxide. This transformation involves a rearrangement of atomic positions in the crystal lattice.

The structure of α-Al_2O_3 is rhombohedral with space group $R\bar{3}c$. The oxygen atoms are in a nearly hexagonal closed-packed array. The metastable phases of Al_2O_3 have various other crystal structures, most of which are not known unequivocally. Al_2O_3 is well known to have many metastable phases and a thermodynamically stable α-Al_2O_3 phase. The metastable phases, or transition aluminas as they are called, are products of the thermal decomposition of various forms of aluminum hydroxides such as gibbsite, boehmite, bayerite, and alliayerite.[27] The final product at high temperature is always α-Al_2O_3. Figure 4 is an illustration of the decomposition sequence of alumina hydroxides. The most common form of metastable Al_2O_3 is the gamma phase (γ-Al_2O_3). It has a defect spinel structure as described by Verwey[28] with the oxygen atoms in a cubic array.

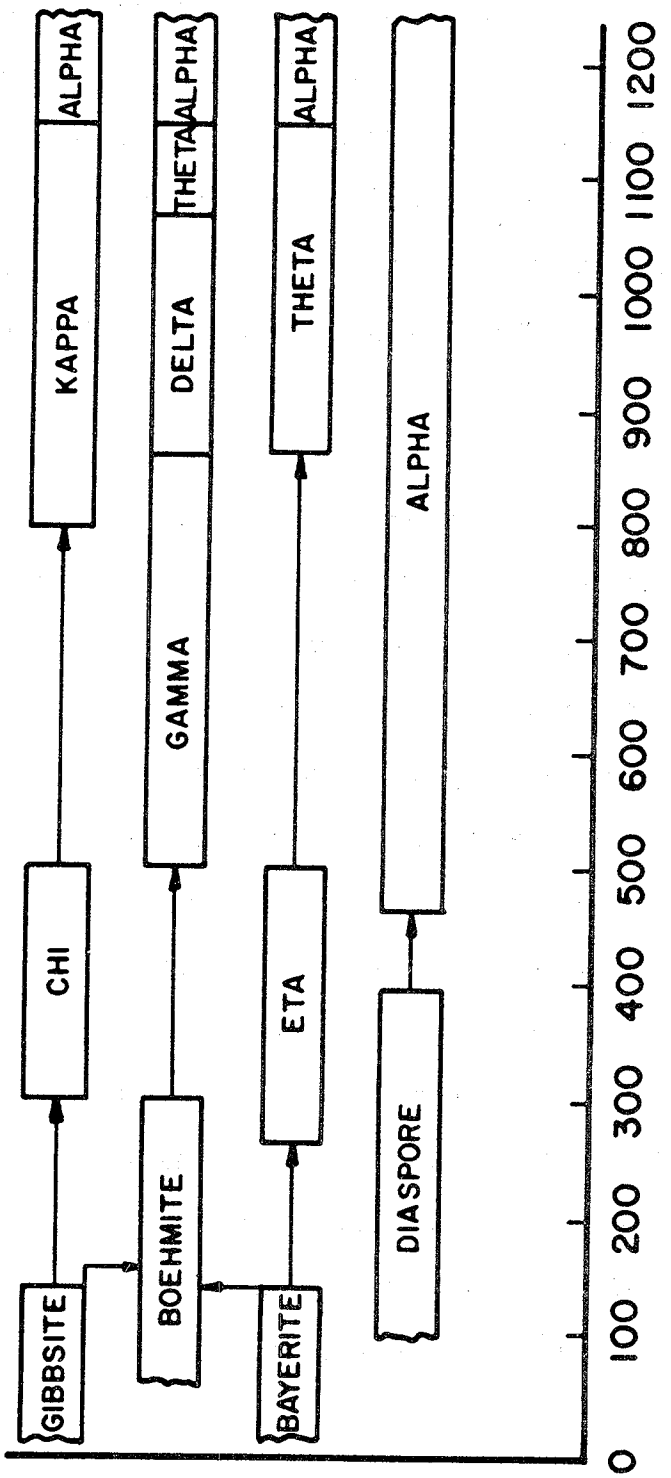

Figure 4

Decomposition sequence of aluminum hydroxides. (Ref. 26)

The transition aluminas can be obtained by a number of different processes, thermal oxidation being the one of interest. The oxidation of aluminum involves formation of an amorphous aluminum oxide, then nucleation of crystalline γ-Al_2O_3 [29-33]. Dilute aluminum alloys also form γ-Al_2O_3, initially.[34-36] NiAl alloys and NiCrAl alloys are no exception in that early stages of oxidation involve formation of γ-Al_2O_3.[22,37] δ-Al_2O_3 has been found in the oxidation study of Ramanarayanan[38] when moist air was used as an oxidizing atmosphere. Felton and Pettit found oriented δ-Al_2O_3 on Pt_5Al_3.[24] Two other oxide phases, possibly transition aluminas, have been found in another study[13].

The present and future reliance upon Al_2O_3 as a protective scale for high temperature materials has generated much research as can be attested by the literature. However, the complete understanding of mechanisms of oxidation involving diffusional growth, oxide adherence and the transformation to α-Al_2O_3 are far from being accomplished. This study is intended to serve as a basis for future work involving the lowering of growth rates of α-Al_2O_3 scales. It is believed that slower growth rates will occur from a decrease in oxygen grain boundary diffusion through low angle grain boundaries versus diffusion along high angle grain boundaries. The low angle grain

boundaries, or lack of grain boundaries, would result from a highly epitaxially oriented oxide scale. To obtain an epitaxial α-Al_2O_3 scale, the transformation to the alpha alumina phase must not be associated with the orientation randomization of the new oxide grains, a phenomenon possibly dependent on metal and transient oxide orientations.

The oxide phases, as well as the metal-oxide orientation relationships, are thus critical when predicting resultant α-Al_2O_3 morphologies. The goals of this study are the determination of the transient oxide phases formed on a NiAl + Zr alloy, along with the metal-oxide orientation relationships. This information is fundamental to the overall understanding of the oxidation of alumina forming alloys.

II. Materials and Procedure

A master ingot of nickel aluminide plus zirconium was purchased from TRW, Inc. Single crystals were to be cast using the selective grain growth process. In this process, the metal is poured at the selected temperature into a mold onto a copper chill plate. The chill plate is slowly lowered out of the hot zone at a controlled rate. Theoretically, a helix in the mold at the copper chill plate should prevent all grains from growing, except for that grain having the preferred growth orientation. This grain will survive the helical portion of the mold to form single-crystal bars. Unfortunately, in most of the cast bars, 2-3 grains survived the helix, solidifying only as a large-grained structure and not as single crystals. Chemical analysis of the bars is provided in Table II.

Oxidized specimens suitable for transmission electron microscopy (TEM) observation were prepared by first orienting large grains of the as-received metal to the required directions using Laue X-ray diffraction. The metal was sliced into 1 mm thick sections, from which 3 mm discs were spark machined. The discs were mechanically ground to a 600 grit finish and polished with 3 micron diamond paste. Specimens were then electropolished in a 2:1 methanol to nitric acid solution at 12V and 0°C.

TABLE II

Average concentration of NiAl + Zr*

Aluminum ---	29.35 wt%
Nickel ---	balance
Zirconium---	0.11 wt%
Oxygen ---	0.01 wt%
Carbon ---	16 ppm

*Results supplied by National Spectrographic Laboratories, Schiller Industries, Inc., Cleveland, Ohio

Oxidation of the specimens was performed at the NASA Lewis Research Center in preoxidized FeCrAl cups in air in a laboratory furnace. Specimens were oxidized for 0.1, 1.0, or 10.0 hours at a temperature of 800°C. Final preparation involved removing the oxide from one side of the specimen with SiC paper and back-thinning to the metal-oxide interface. The oxidized surface was protected by a piece of polyurethane, while the metal was electrochemically thinned away with a 2:1 methanol to nitric acid solution at 30V and -20°C. In most cases, a complete oxide layer remained after the metal had been thinned away to form a hole as depicted in Figure 5. Specimens were observed at 125 keV in a Phillips EM 400T transmission electron microscope.

To properly determine the orientation relationships between two phases using electron diffraction, diffracted intensities should be observed from both phases, simultaneously. In some instances in this study, there were insufficient thin areas in the metal and oxide diffracted intensities were absorbed by thicker metal regions. When thin metal areas were obtained, they were often deformed in relation to the bulk specimen since stresses induced by the oxidation process were sufficient to cause gross deformation of the thin metal area. In these cases, the metal and oxide orientations were determined sepa-

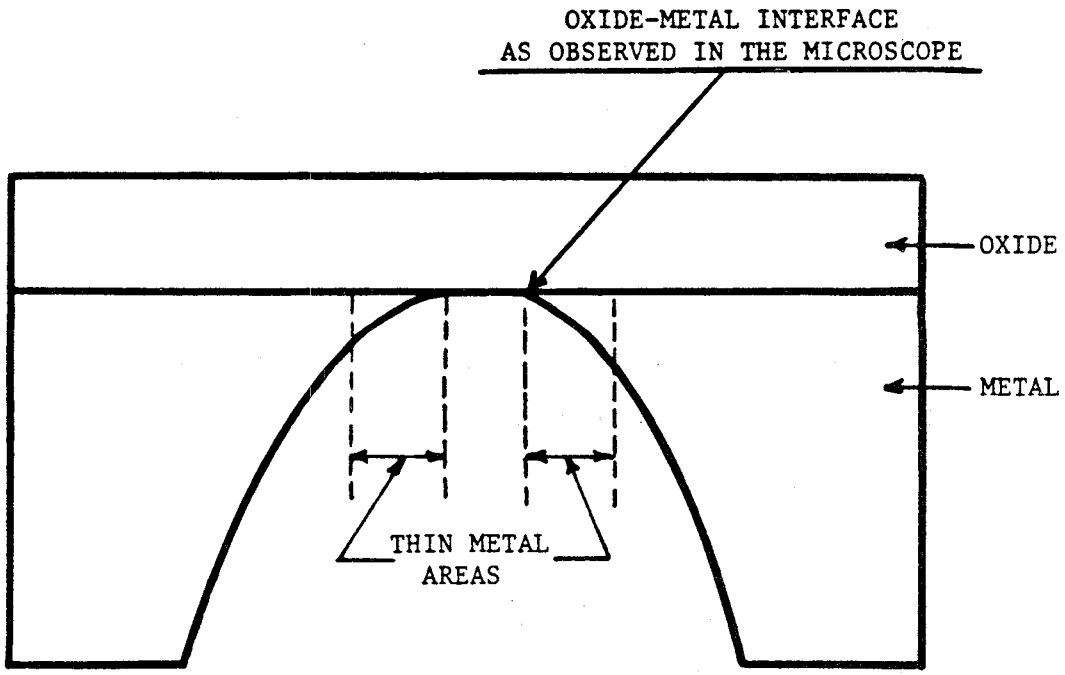

Figure 5

Schematic of a thin foil TEM specimen after backthinning to reveal oxide plus thin metal area.

rately. Metal orientations were determined using the Kikuchi map of the metal specimen obtained by removing the selector aperture, focusing the condenser lens and moving to a thick region where the map no longer moves when translating the specimen. Oxide orientations were determined using a large selector aperture and tilting to various zone axes. For both metal and oxide, this procedure was performed on as many stereographic triangles as possible near the center of the stereographic projection. The projections for both metal and oxide were plotted then superimposed to determine the orientation relationships.

III. Results

The data in its entirety were obtained on a Philips EM 400T electron microscope with X-ray analytical capabilities. The results, therefore, include mainly electron diffraction patterns and their analyses, bright and dark field images of the metal-oxide specimens and images from other microscopy techniques such as high resolution electron microscopy and $2\frac{1}{2}$ D imaging. Various camera constants were used to simplify the presentation of the electron diffraction patterns. The chemical composition data from Energy Dispersive Spectroscopy (EDS) will only be presented in semiquantitative terms.

The data will be presented in a metal orientation-time-temperature sequence. The metal orientations used were (001), (012), (011), and (111). The specimens were oxidized in air for 0.1 hr., 1.0 hr., and 10.0 hr. at 800°C. An (001) foil was also oxidized at 1100°C for 0.1 hr. with an electropolished oxidation surface to observe the effects of specimen surface preparation and temperature.

A) Metal Structure - Unoxidized

β-NiAl is an ordered B2 structure consisting of interpenetrating simple-cubic lattices of Ni and Al, the basis being 0,0,0

and $\frac{1}{2},\frac{1}{2},\frac{1}{2}$. All reflections of the simple cubic lattice can occur because of structure factor considerations. The primary reason for observing an unoxidized metal specimen was to characterize the metal substrate prior to oxidation. One surface was electropolished so that it was representative of the pre-oxidized surface condition. The specimen was then back-thinned from the opposite side so that the electropolished surface and the region directly beneath it could be observed in the electron microscope.

The micrographs in Figure 6 are typical metal structures imaged under two different diffracting conditions. No grain boundaries are present since the specimens are single crystals. The main features are dislocations and stacking faults extending approximately 0.2 μm from the electropolished surface into the bulk. The dislocations, in general, are inclined to the specimen surface as evidenced by thickness fringes along the dislocation lines. Some dislocations are dissociated as can be clearly seen by the weak beam dark field image of Figure 7. These are actually superdislocations with the region in between the dislocation lines being faulted.[39] These superdislocations are common to metals having the B2 structure.

Figure 6

Bright field images of β-NiAl (β) near an unoxidized metal surface. The images show dislocations(D) and stacking faults(SF) for diffraction vectors of a) $(\bar{2}00)_\beta$ and b) $(\bar{1}10)_\beta$.

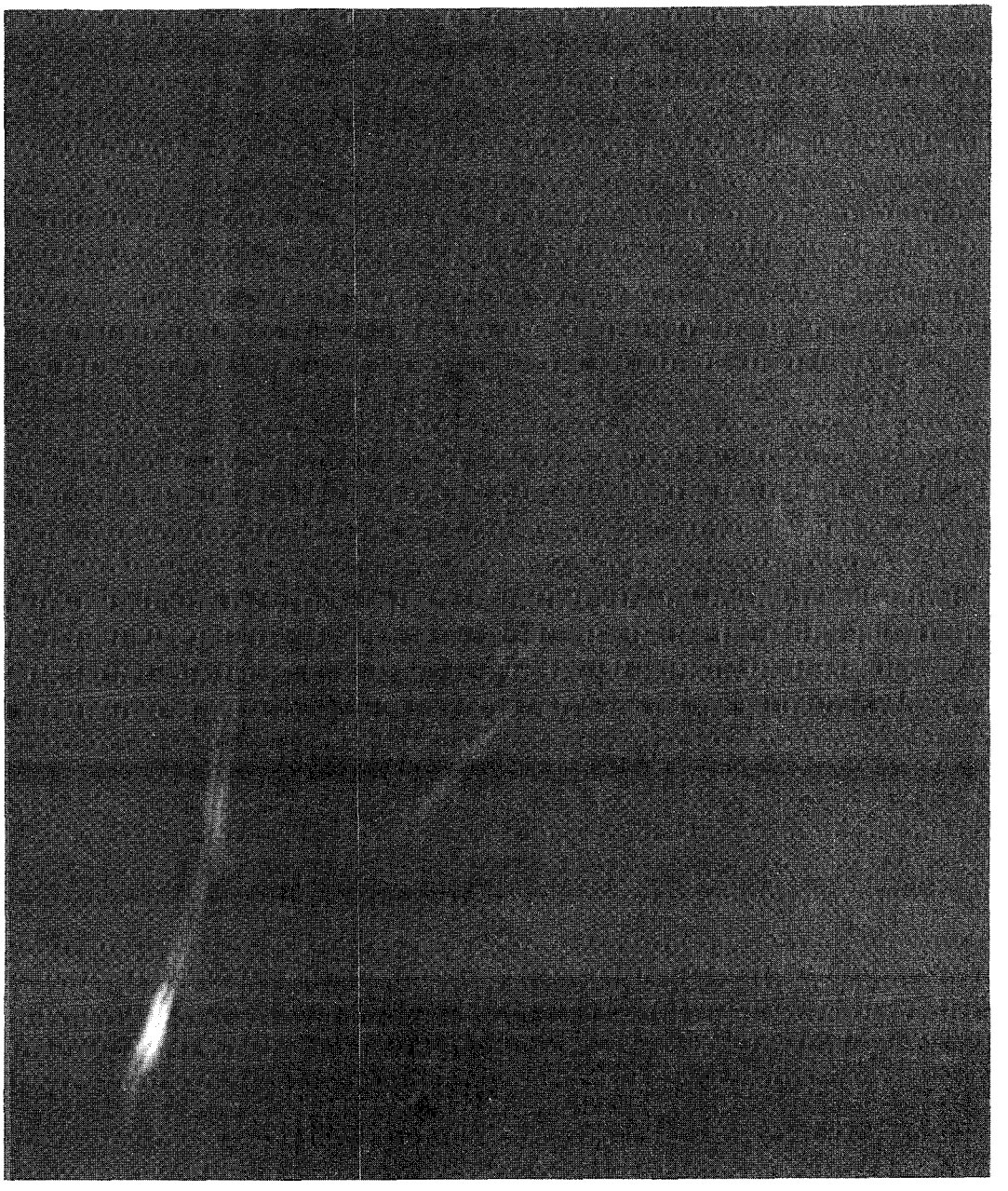

Figure 7

Weak-beam dark field image showing superdislocations in an unoxidized specimen.

The electron diffraction pattern in Figure 8 was taken at 0° tilt. The [012] metal direction is thus parallel with the beam direction as indicated by the accompanying analysis. The streaking occurs along ⟨110⟩ directions and is possibly due to the premartensitic transformation related to this material as described by Liu.[40] The extra spots at $\frac{1}{2}(100)$, $\frac{1}{2}(02\bar{1})$ and $\frac{1}{2}(12\bar{1})$ are the result of defect ordering in the β-NiAl. At the stoichiometric composition, all lattice sites are occupied by Ni and Al atoms on their respective sublattices. In Ni-rich β-NiAl, the extra Ni atoms are accommodated by vacancies on the Al lattice positions. When the composition of the alloy is Al-rich, aluminum atoms are substitutional solutes and will be incorporated into the nickel sublattice. Some long-range ordering associated with non-stoichiometric defects must then be occurring. Similar extra reflections are evident in the diffraction patterns of Figure 9, where extra spots are noticed at $\frac{1}{2}(100)$, $\frac{1}{2}(110)$, $\frac{1}{2}(021)$, $\frac{1}{2}(121)$ and $\frac{1}{4}(111)$.

As can be seen from the images and diffraction patterns, no evidence of any oxide phases could be found. However, an oxide film might be too thin to detect. The possibility of an air formed oxide or an anodic film formed by electropolishing existing on the surface prior to oxidation treatments was another reason for studying unoxidized metal.

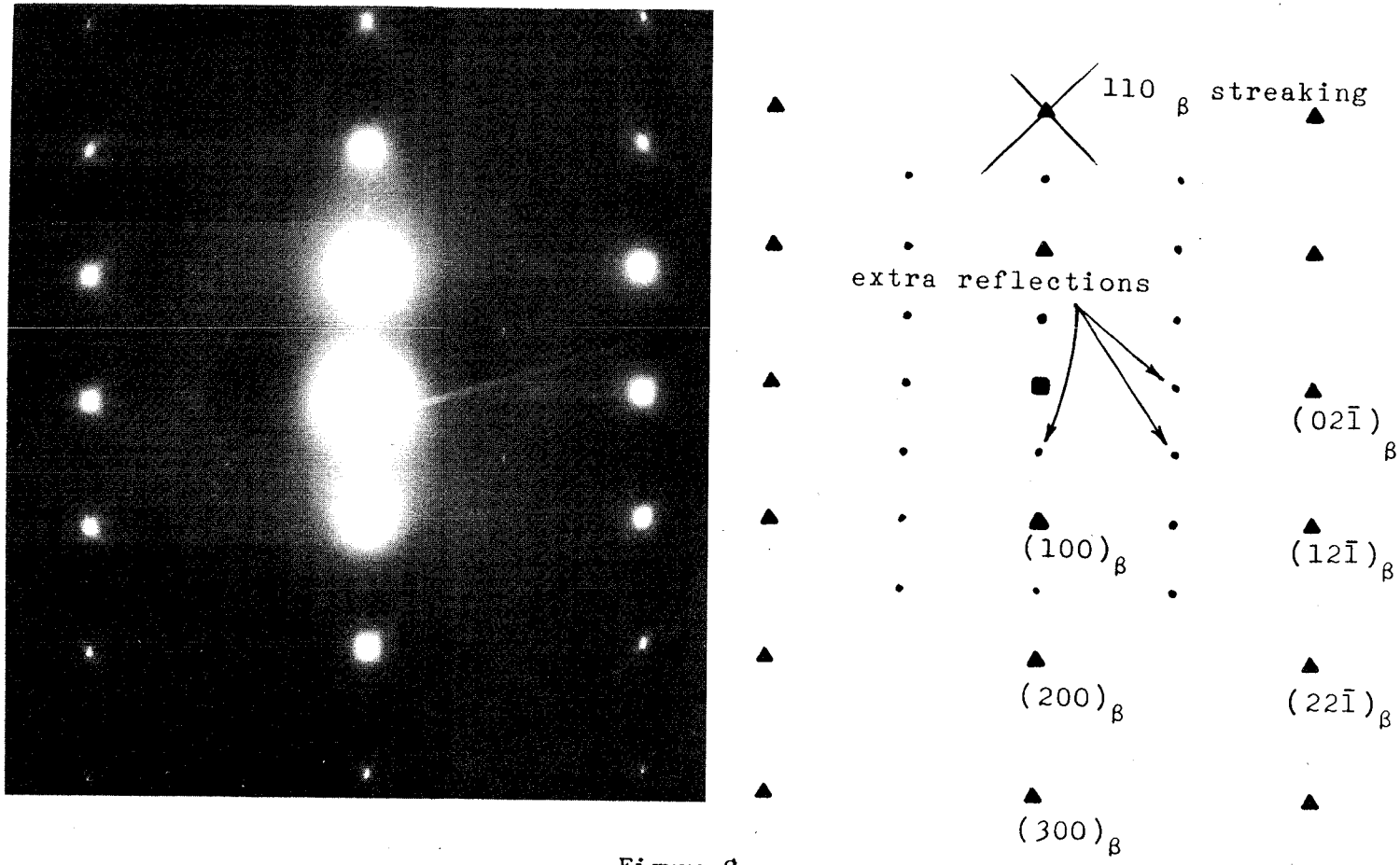

Figure 8

$[012]_\beta$ zone taken at 0° tilt showing extra reflections at $\frac{1}{2}(100)$, $\frac{1}{2}(02\bar{1})$ and $\frac{1}{2}(12\bar{1})$.

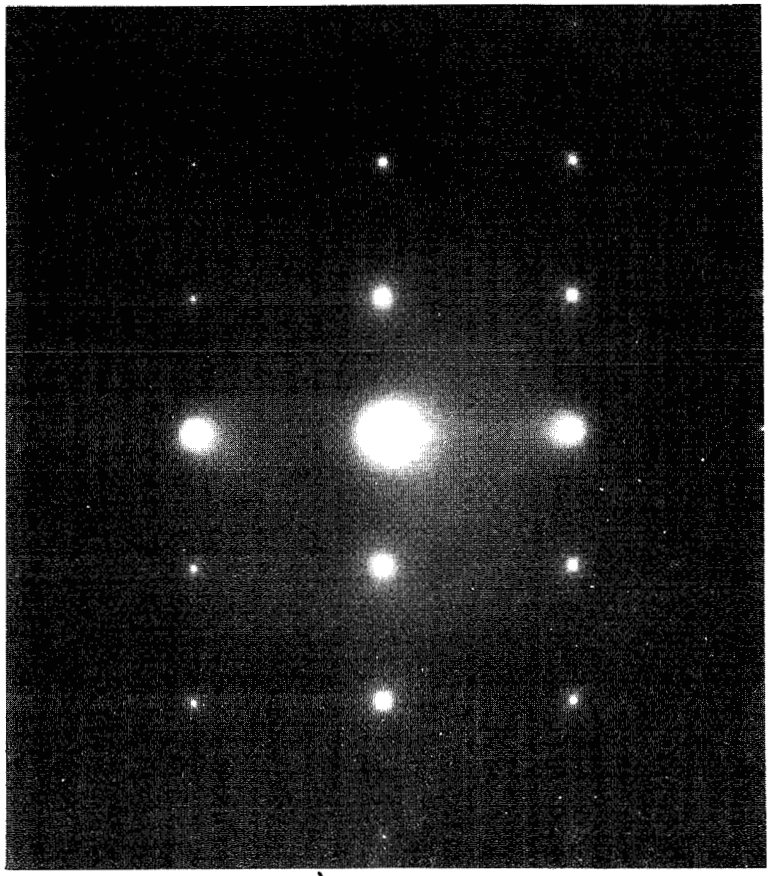

a)

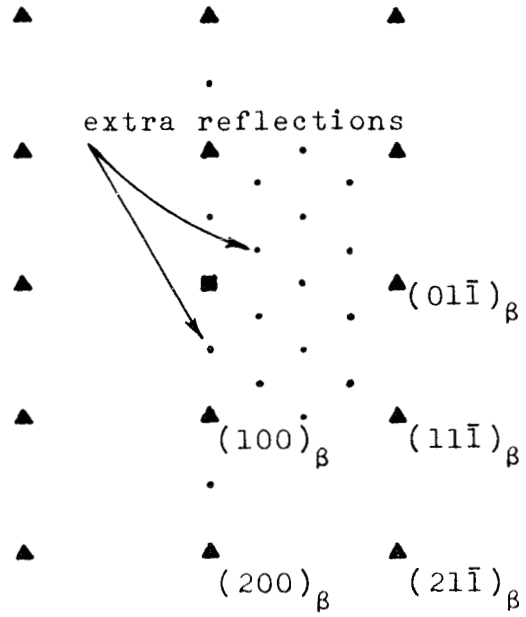

Figure 9

Diffraction patterns of β-NiAl showing extra reflections due to long-range ordering. The pattern in a) is an $[011]_\beta$ zone while the patterns in b) and c) are two-beam conditions from an $[\bar{1}12]_\beta$ zone and a $[001]_\beta$ zone, respectively.

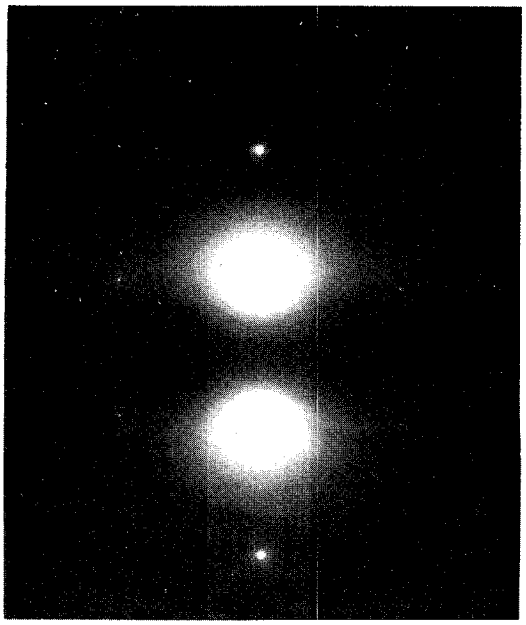

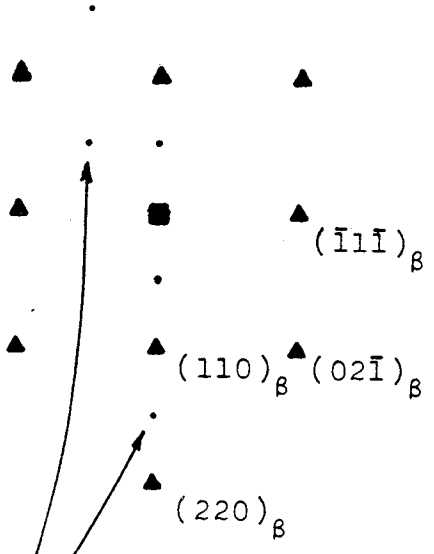

Figure 9b)

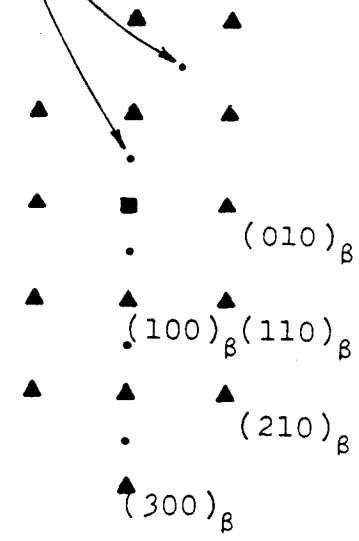

Figure 9c)

B) (001) Metal Orientation - Oxidized

1) 0.1 hours, 800°C

Emphasis will be placed on the description of the results from (001) oxidized metal specimens since many of the features found for this metal orientation are characteristic of all metal orientations. References to the (001) metal orientation will frequently be used.

The oxide that formed under the above conditions was thin enough to be transparent to 120 keV electrons. The metal, however, was electron transparent only to a finite distance in from the hole formed by back-thinning. When observing the metal, it must be realized that oxide was always present on one surface. The higher electron absorption of the metal prevented the oxide layer from being observed when in thick metal regions. Near the specimen hole where both oxide and thin metal are located, both the metal and oxide layer could be studied simultaneously. Figure 10 is a BF image of the oxide and metal + oxide areas of a specimen. The oxide is relatively uniform in thickness whereas the metal becomes progressively thicker towards the bulk. Figure 11 is the corresponding selected area diffraction pattern (SAD) taken from a thin metal

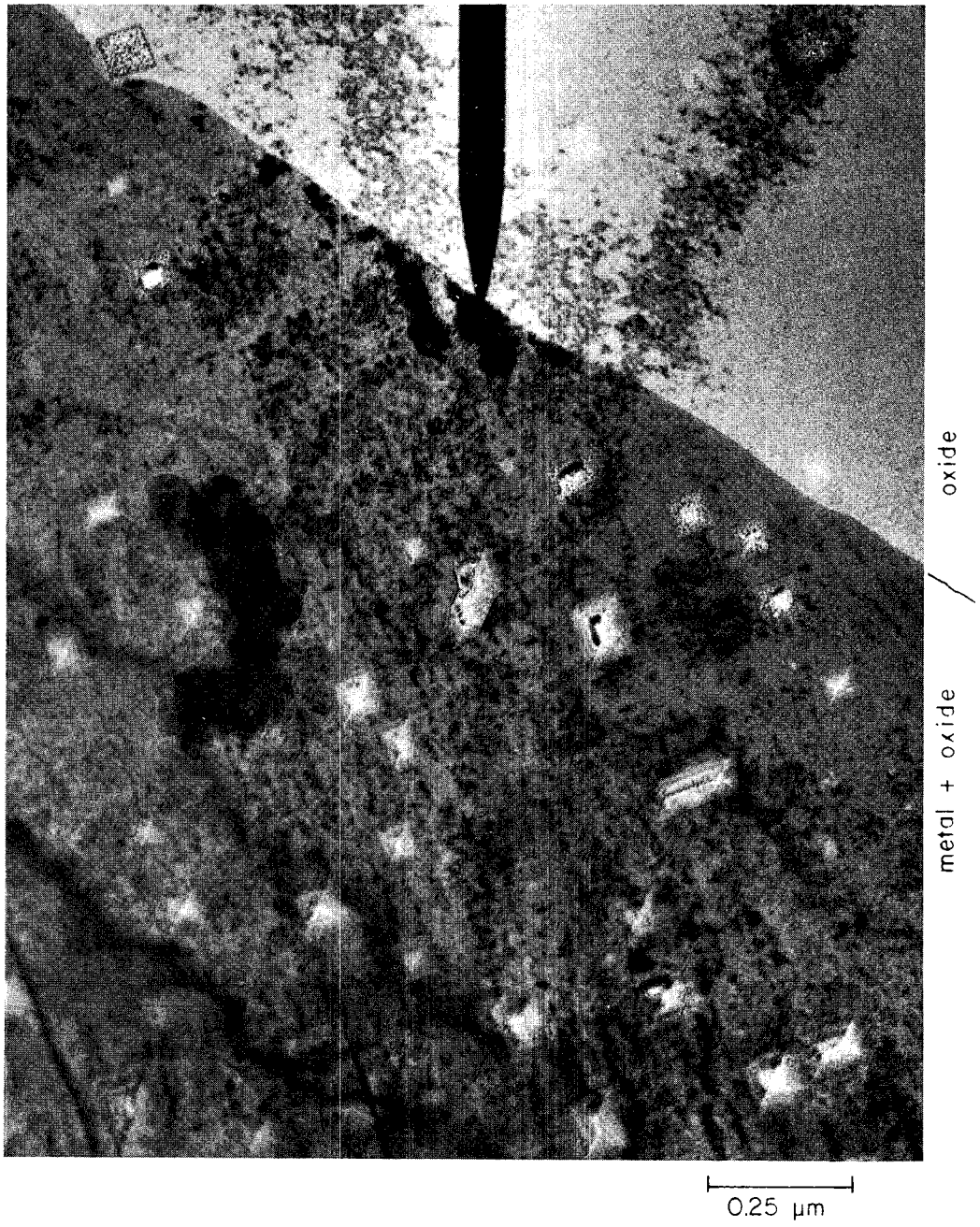

Figure 10

Bright field image of an oxide and oxide plus metal interface for an (001), 0.1 hour, 800°C specimen.

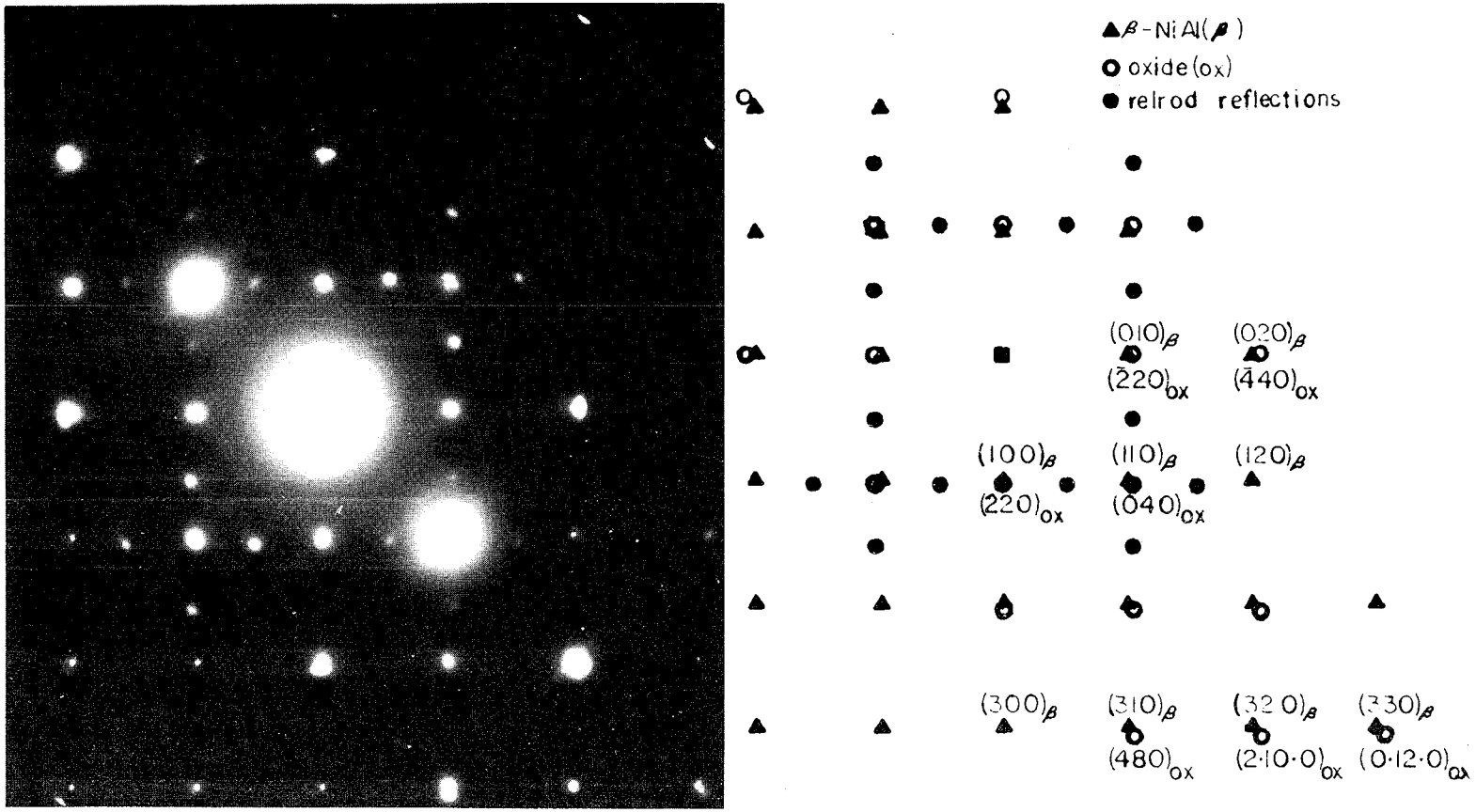

Figure 11

Selected area diffraction pattern of metal plus oxide from a region near the interface in Figure 10. Zone axis: near $[001]_{\beta}$, near $[001]_{ox}$.

region where both metal and oxide diffracted intensities are transmitted.

The proper analysis of electron diffraction patterns allows the phases and orientations of the phases to be identified. Both metal and oxide reflections are present in Figure 11 and indexed as shown in the accompanying schematic. This SAD was taken at 0° tilt of the specimen stage. Both metal and oxide are within 1° of having their [001] direction lying perpendicular to the oxidation plane and parallel to the electron beam direction. This would indicate that the metal specimen, oriented by the Laue X-ray diffraction technique, was oriented so that its surface was not exactly the (001) plane but slightly angled from the exact orientation. The Kikuchi center for an [001] metal zone (Figure 12) taken in a thicker metal region was found to be 1.25° away from the 0° tilt condition.

Exact metal-oxide orientations could not be determined simply by taking separate SAD's of thin areas of both phases because these areas frequently contained bend contours. A biaxial tensile stress is developed at the metal interface upon oxidation because the Pilling-Bedworth ratio of the oxide is greater than unity. Upon backthinning the metal away, the stress at the interface becomes large enough to cause gross deformation in both the metal and the oxide. Figure 13 is a BF image of

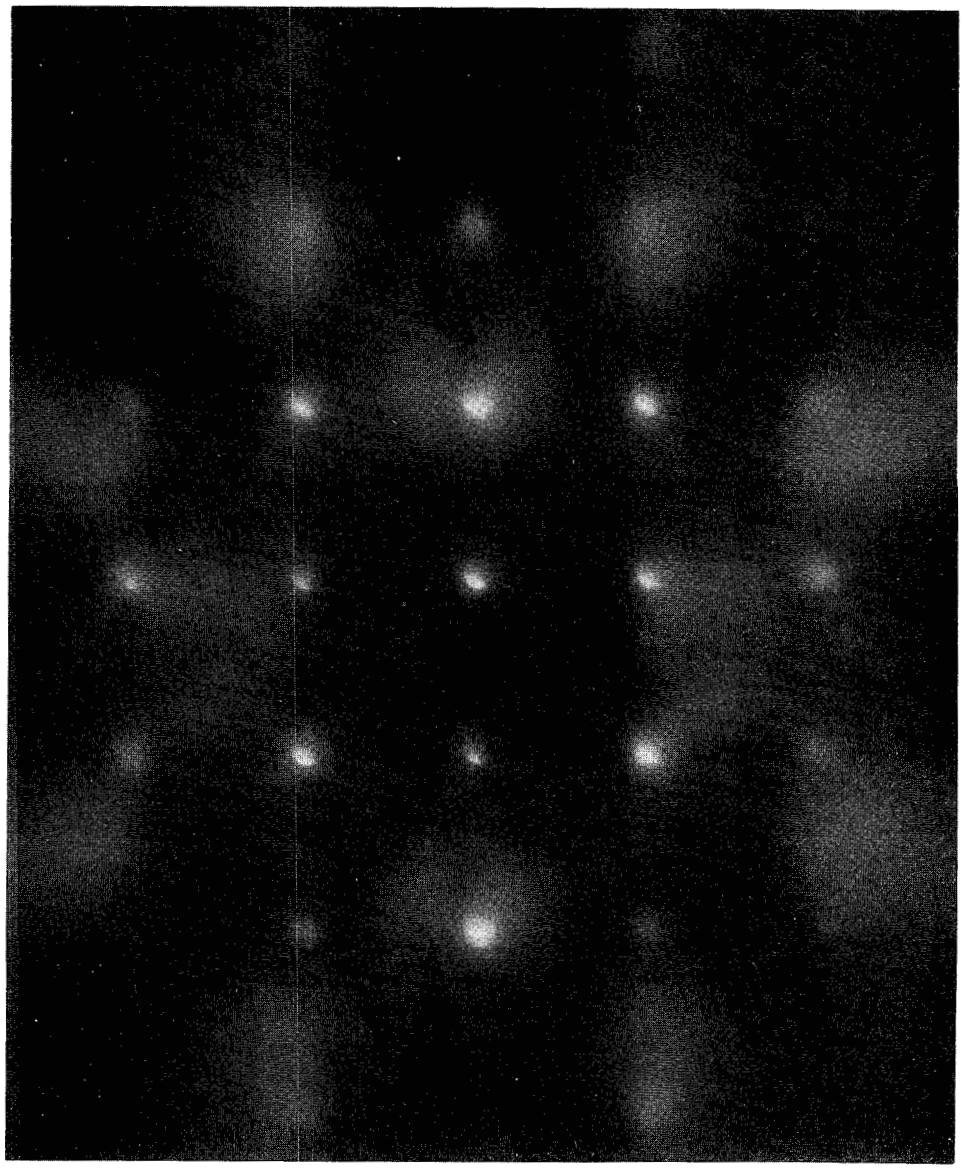

Figure 12

Exact [001] Kikuchi center of β-NiAl; 1.25° tilt from the as-oxidized plane.

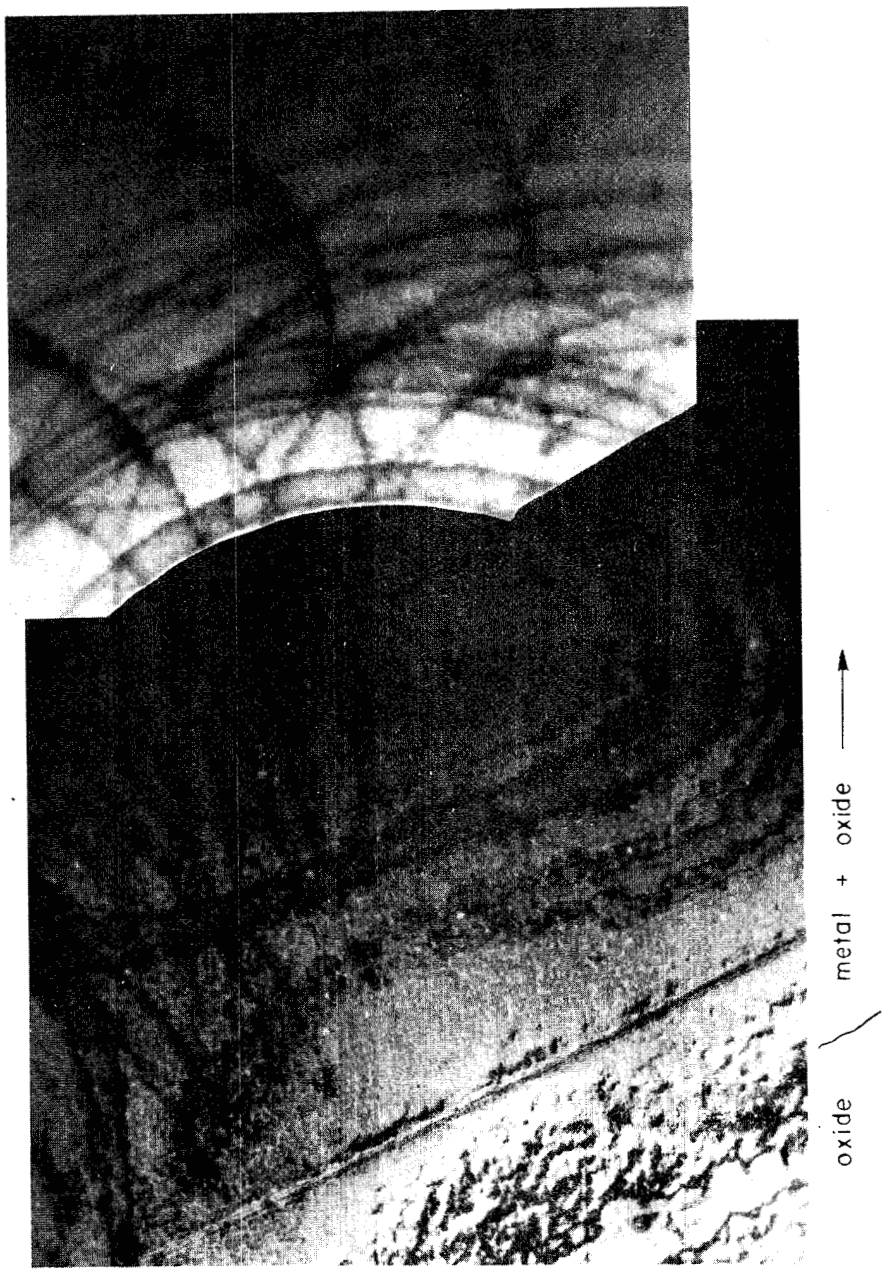

Figure 13

High voltage electron micrograph of thicker metal regions showing bend contours in an (001) specimen oxidized for 10.0 hours at 800°C.

the thicker regions of metal from a specimen oxidized for 10.0 hours. This micrograph was taken on a high voltage electron microscope* which enabled the thicker metal regions to be observed. The bend contours are seen to extend far into the bulk metal. Specimens oxidized for shorter times should not have as much deformation, but in thin regions the effect is enough to prevent exact determination of oxide and metal orientations. Kikuchi maps of thicker, less deformed metal regions were then used to determine the precise metal orientations. Oxide orientations had to be determined separately because diffracted intensities from the oxide were absorbed by the thicker metal.

The same difficulties occurred when determining the exact orientation of thin oxide layers. Figure 14 is a BF-DF pair with the corresponding SAD of the area marked with the dark arrow. All light regions of the DF image have the same [001] orientation while the orientation of darker regions varies up to 18°. A selected area diffraction pattern from one of the misoriented regions is given in Figure 15 and shows that the orientation is near an [013] zone. Figure 15 also contains the

---

*Argonne National Laboratories, Kratos/AEI - EM7

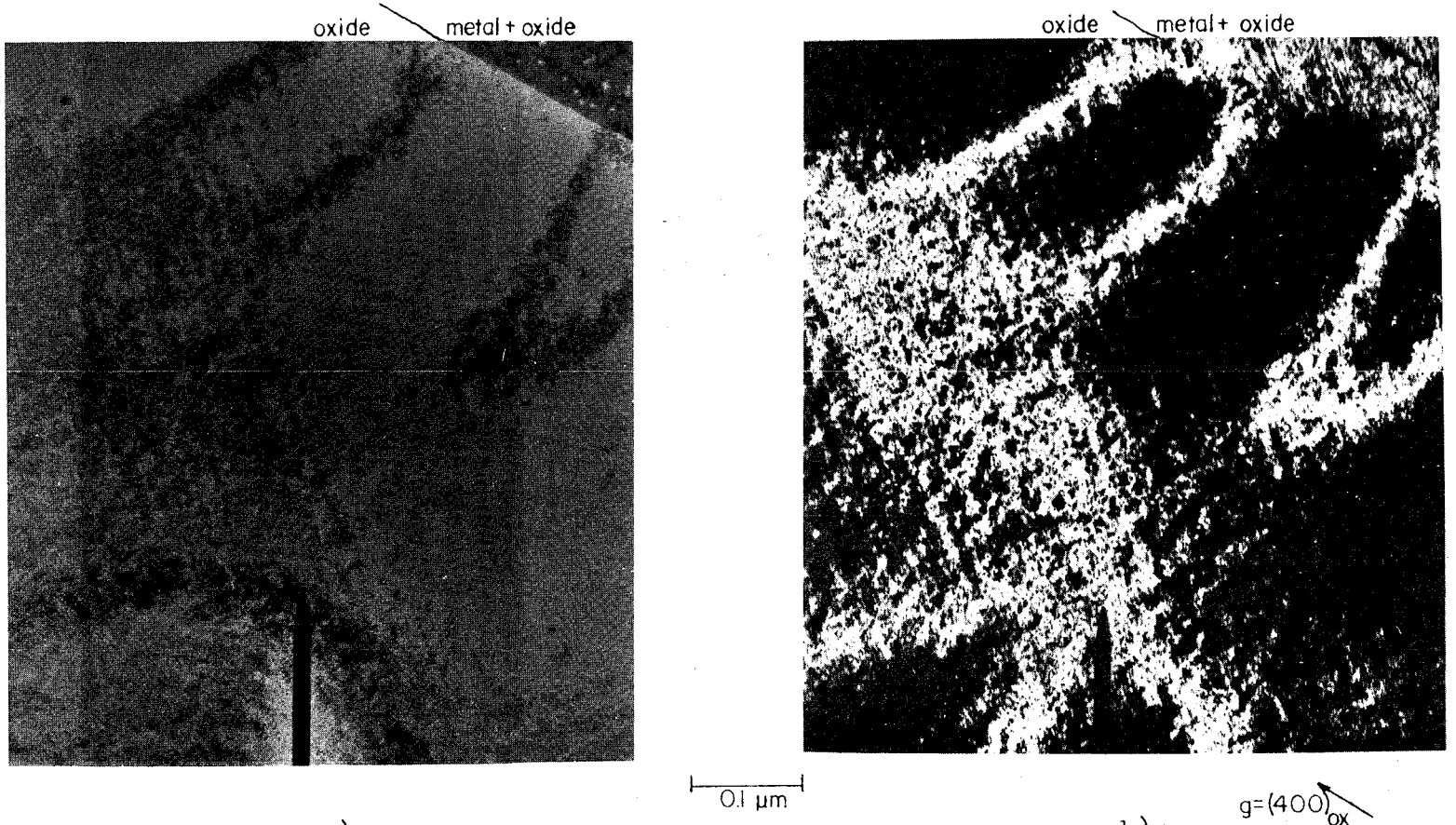

Figure 14

Bright field-dark field pair of an oxide layer with bend contours from an (001), 0.1 hour, 800°C specimen. The arrow in the bright field image of a) points to a region having an [001] orientation shown in the accompanying selected area diffraction pattern. The same region is indicated in the dark field image of b).

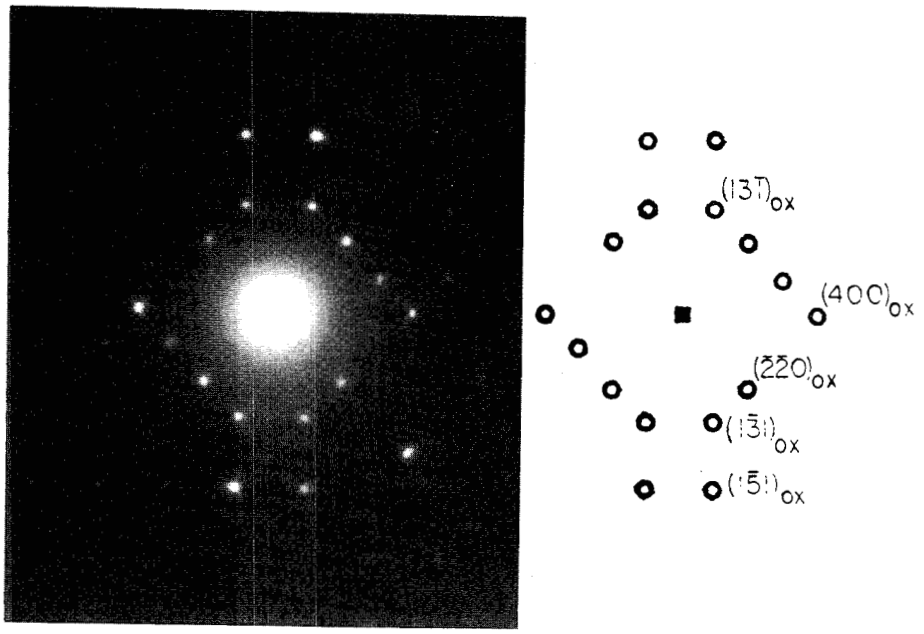

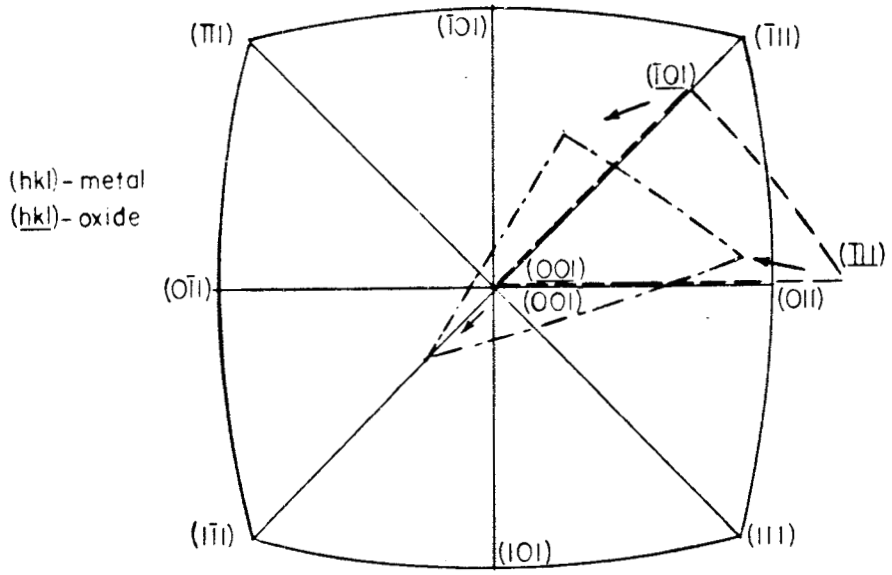

Figure 15

Selected area diffraction pattern of a bent region in Figure 14 showing a near [013] oxide zone. The stereographic projection shows the orientations of the metal, the unbent oxide regions and the bent oxide regions. The translation from the unbent to bent oxide stereographic triangles is indicated with arrows.

stereographic projections of extreme regions along an oxide bend contour showing the orientation change.

Exact oxide orientations, indicative of the true oxide orientation prior to back thinning, were obtained by finding a reasonably uniform region of oxide, devoid of bend contours, that was consistent with the results found on other (001) specimens. The realization that deviations in oxide orientations on an (001) metal orientation for short oxidation times are just bend contours greatly facilitated the metal-oxide orientation determination.

If certain crystallographic planes and directions of the oxide tend to align with particular planes and directions in the metal upon nucleation and growth, the oxide is said to have an orientation relationship with the metal. The preferred orientation between the metal and oxide is a result of epitaxial growth. The orientation relationships are described by parallel planes and parallel directions or sets of parallel directions in the parallel planes. In this study, the parallel planes are always the plane of oxidation. The orientation relationship found for the metal and oxide on an (001) oriented metal is:

$$(001)_m \,||\, (001)_{ox}$$
$$[100]_m \,||\, [110]_{ox}$$
$$[110]_m \,||\, [010]_{ox}$$

This orientation relationship is depicted in Figure 16 with stereographic projections of the metal and oxide. As can be seen, the (001) oxide and metal planes are aligned at the center of the projection but the oxide projection is rotated 45° about the [001] direction. This same orientation relationship need only be described with one of the stereographic triangles from each of the metal and oxide phases. The orientation relationship mentioned above is commonly known as the Bain relationship, a classical orientation relationship found between face-centered cubic and body-centered cubic materials.

The electron diffraction pattern of Figure 11 is again presented in Figure 17 but with a more detailed and complete analysis. Electron diffraction is a convenient technique for determining orientation relationships and phases present, as will be discussed with reference to this figure. The actual metal and oxide phases present are determined by calculating d-spacings of the reflections from the equation:

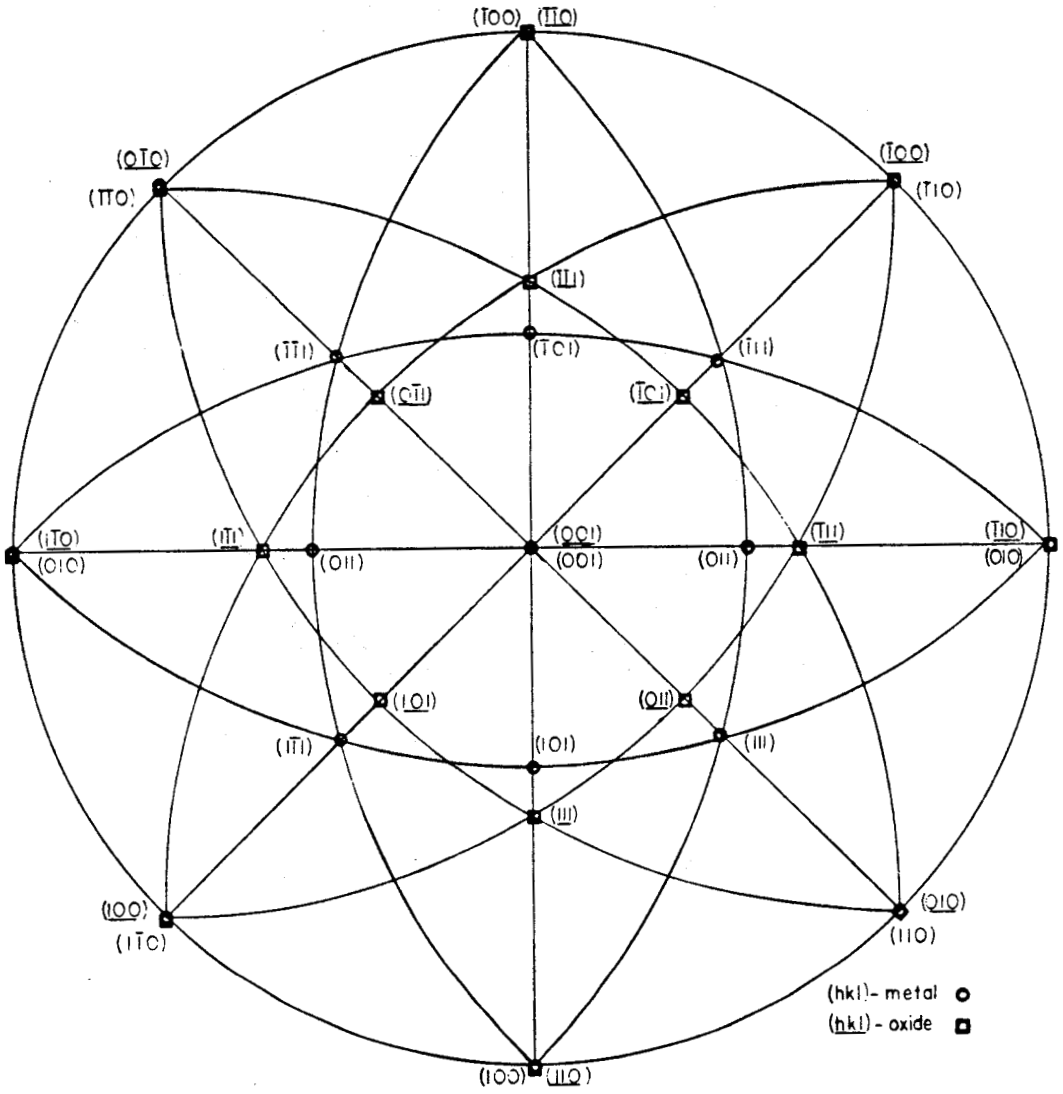

Figure 16

The Bain orientation relationship represented by stereographic projections of the metal and oxide phases.

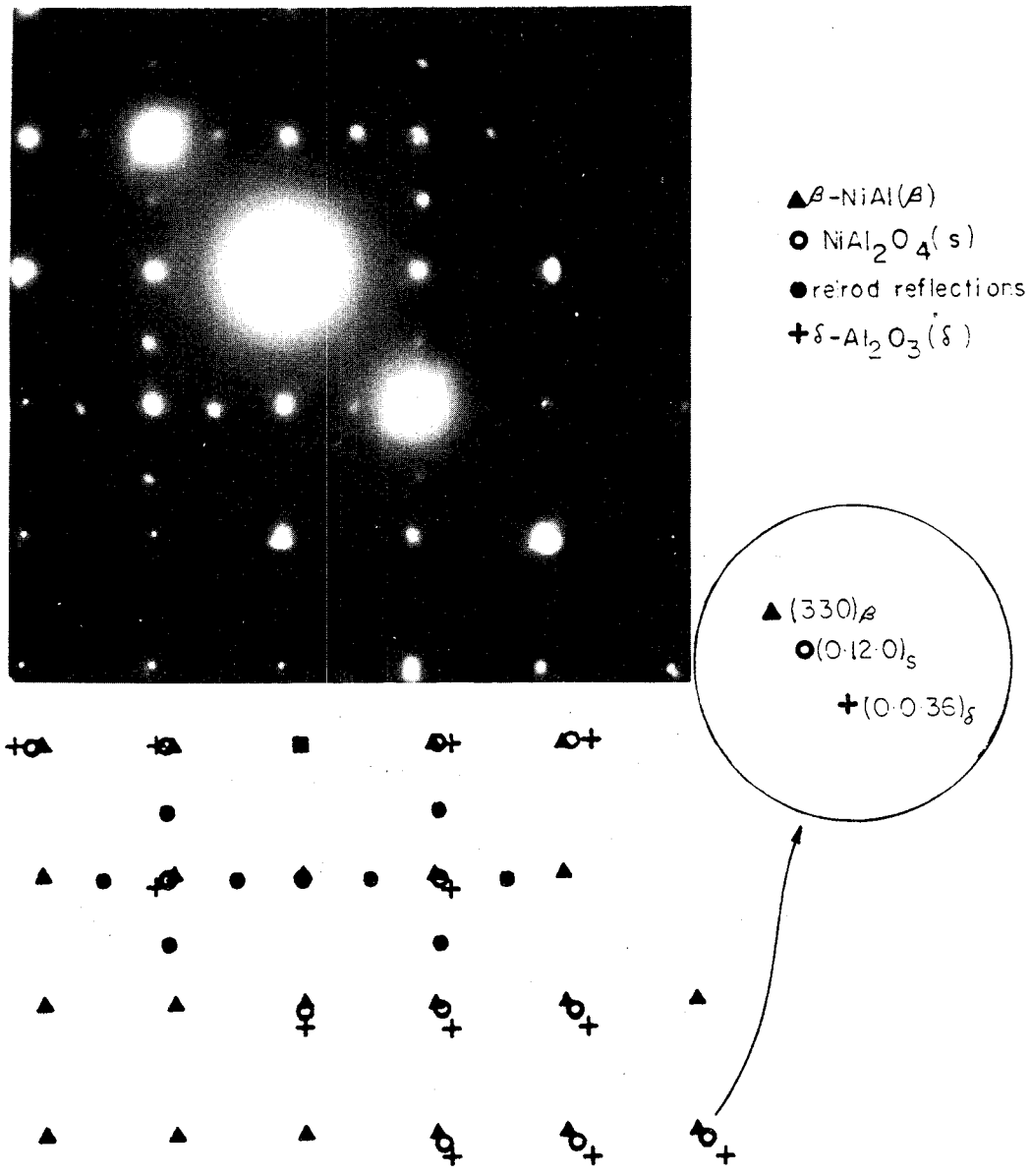

Figure 17

Diffraction pattern of Figure 11 showing reflections from metal and two oxide phases. The enlarged inset shows reflections from β-NiAl, $NiAl_2O_4$ and δ-Al_2O_3. Zone axis: near $[001]_\beta$, near $[001]_{s,\delta}$.

$$L = Rd \qquad [12]$$

R = distance from the central spot

λ = wavelength

L = camera length

λL = camera constant

The definition of d-spacing for a cubic crystal is given by:

$$d = \frac{a_o}{(h^2 + k^2 + l^2)^{\frac{1}{2}}} \qquad [13]$$

where a_o is the lattice constant of the material and h,k,l are the Miller indices of that particular reflection. If the camera constant for a particular SAD is known, all reflections should in practice have a unique h,k,l assigned to them. Fortunately the metal phase, β-NiAl, acts as a reference from which the camera constant can be determined within 1%, usually. The lattice constant of this β-NiAl material was determined to be 2.882 Å using X-ray diffraction.

The oxide was found to be $NiAl_2O_4$, γ-Al_2O_3 or a mixture of these two. Both $NiAl_2O_4$ and γ-Al_2O_3 have spinel type structures with lattice constants of 8.048 Å and 7.908 Å, respectively[41]. The published d-spacings for these oxide phases are

tabulated in Appendix A. The lattice constants are only 1.8% apart thus making it difficult to distinguish between the two phases. A rare situation where the two phases are distinguishable is near the (330)β-NiAl reflection enlarged in the inset of Figure 17. Two distinct reflections outside the metal spot can be seen, the inner one corresponding to the $(0{\cdot}12{\cdot}0)NiAl_2O_4$ reflection and the outer one to the $(0{\cdot}12{\cdot}0)\gamma\text{-}Al_2O_3$ reflection. The measured spacings are within 1% of the published values.

The parallel planes of the metal-oxide orientation relationship are taken to be the planes corresponding to the zone axes at 0° tilt or actually, the chosen metal plane very near 0° tilt. In the present case, the metal and oxide [001] zone axes are parallel. The parallel directions in these planes can be identified by the alignment of the reflections for the phases of interest. These parallel directions are shown in the schematic of Figure 17 and correspond with the Bain relationship.

The spinel structure has a face-centered cubic arrangement of atoms in the sublattices resulting in the normal allowed reflections for FCC materials in the diffraction patterns of the oxide. Extra reflections are present in Figure 17 along

the ⟨100⟩ oxide directions. They are not associated with the [001] zone but are rather, higher order Laue zone reflections resulting from relrod intersections of the first Laue zone with the Ewald sphere. The relrods result from the thin oxide layer with the reflections being {311}, {511}, etc. A detailed explanation for the spacings and locations of the relrod reflections is given in Appendix B.

Additional relevant information from electron diffraction of the oxide is shown in the SAD's of Figure 18 and 19. Evidence of {200} reflections is seen in the SAD of an [001] oxide zone indicating the possibility that the $NiAl_2O_4$ spinel phase has the space group $F\bar{4}3m$ instead of Fd3m according to Heuer and Mitchell[42] and Smith.[43] The diffuse intensity as outlined in the accompanying schematics is indicative of the onset of δ-Al_2O_3 formation. The structure of δ-Al_2O_3 is similar to γ-Al_2O_3 in that both have defective spinel-type structures but δ-Al_2O_3 is tetragonal with a c/a ratio approximately equal to three.[27] Its a_o value of 7.943 Å is less than one-half percent larger than that of γ-Al_2O_3. A more detailed look into δ-Al_2O_3 will be given in the discussion. Figure 19 contains SAD's of a near [101] oxide zone and a $[1\bar{1}2]$ oxide zone. In the [101] zone, extra reflections are noticed alongside the

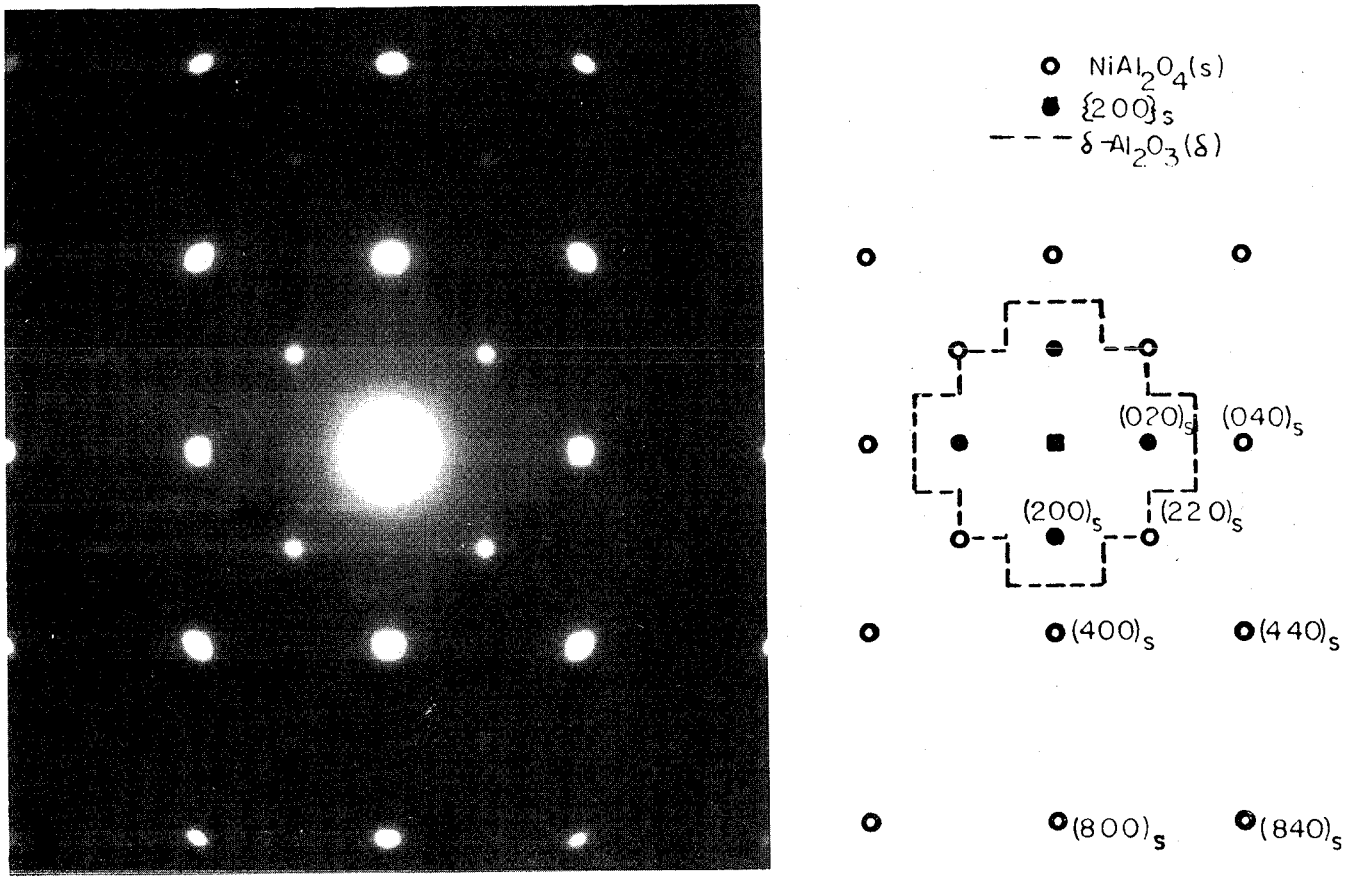

Figure 18

[001] oxide zone from an (001), 0.1 hour, 800°C specimen. {200} reflections and diffuse intensity from δ-Al_2O_3 are indicated.

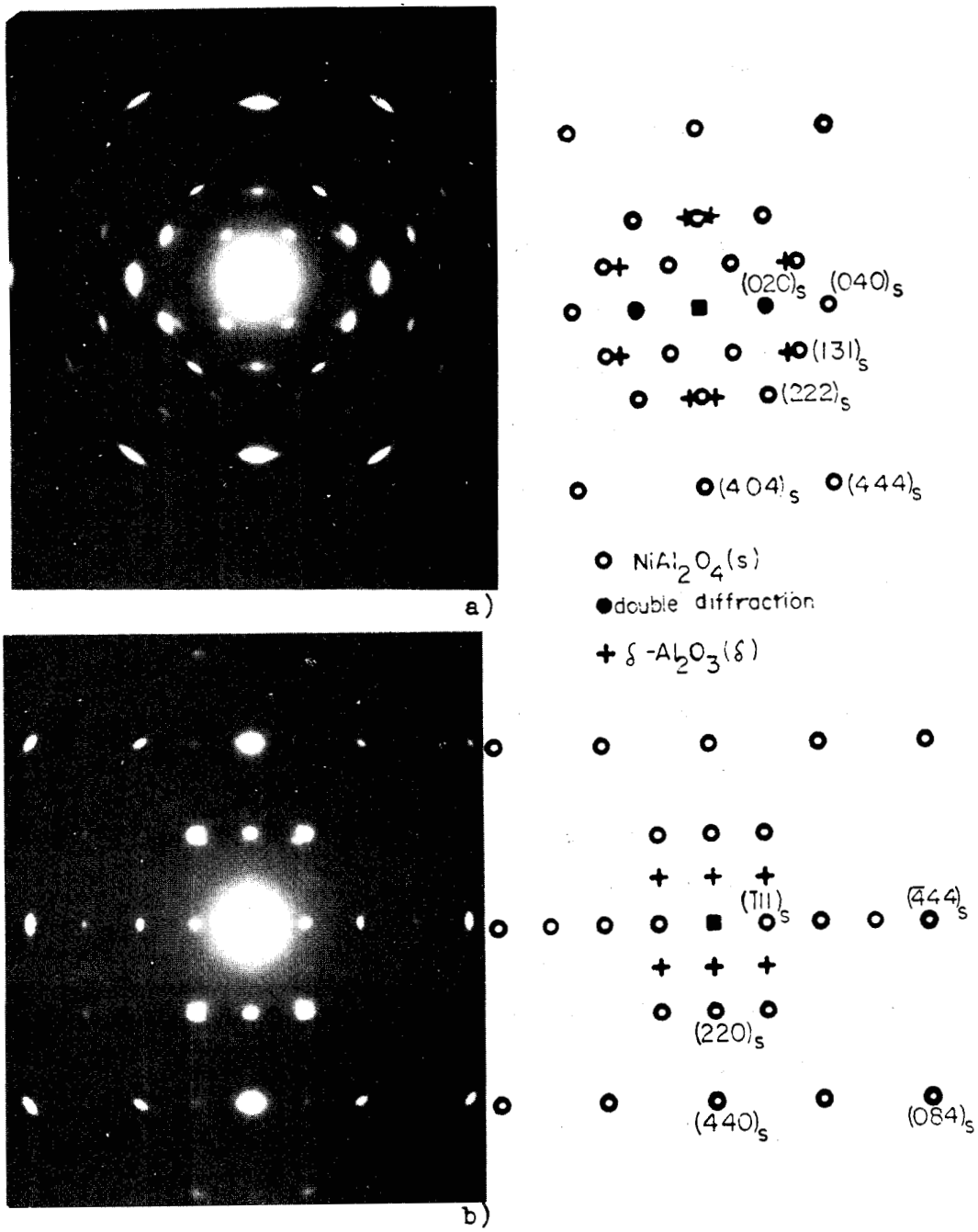

Figure 19

Diffraction patterns of 0.1 hour, 800°C oxide from an (001) specimen tilted to a) near an $[\bar{1}01]$ zone and b) a $[1\bar{1}2]$ zone. Reflections corresponding to δ-Al_2O_3 are indicated.

{220} reflections. These eventually become the {223} δ-Al_2O_3 reflections when only δ-Al_2O_3 is observed. The extra reflections are not properly spaced at the {223} δ-Al_2O_3 position indicating a possible transition between γ-Al_2O_3 and δ-Al_2O_3. Another possibility is that besides $NiAl_2O_4$, the other oxide phase is a less developed form of δ-Al_2O_3. The presence of δ-Al_2O_3 in the $[1\bar{1}2]$ oxide zone is evident with reflections at $\frac{1}{2}$ {220} spacings.

The chemical composition of just the oxide layer was determined using the X-ray energy dispersive apparatus of the electron microscope. Relative amounts of Al and Ni, as measured, do not correspond with any stoichiometric oxide, however. The Al/Ni ratio for this oxide was 1.34. This value does not correspond well with electron diffraction results. According to diffraction pattern analyses, only $NiAl_2O_4$ and Al_2O_3 (γ or δ) were present in the oxide layer. The expected minimum Al/Ni ratio would be 2.0 which would occur if only $NiAl_2O_4$ was present. Since Al_2O_3 is a component of the oxide layer, the Al/Ni ratio should be larger than 2.0. This discrepancy could arise from nickel fluorescence of aluminum x-rays.

The microstructure of the oxide layer is shown in Figure 20. The BF image shows a uniform layer with a change in contrast

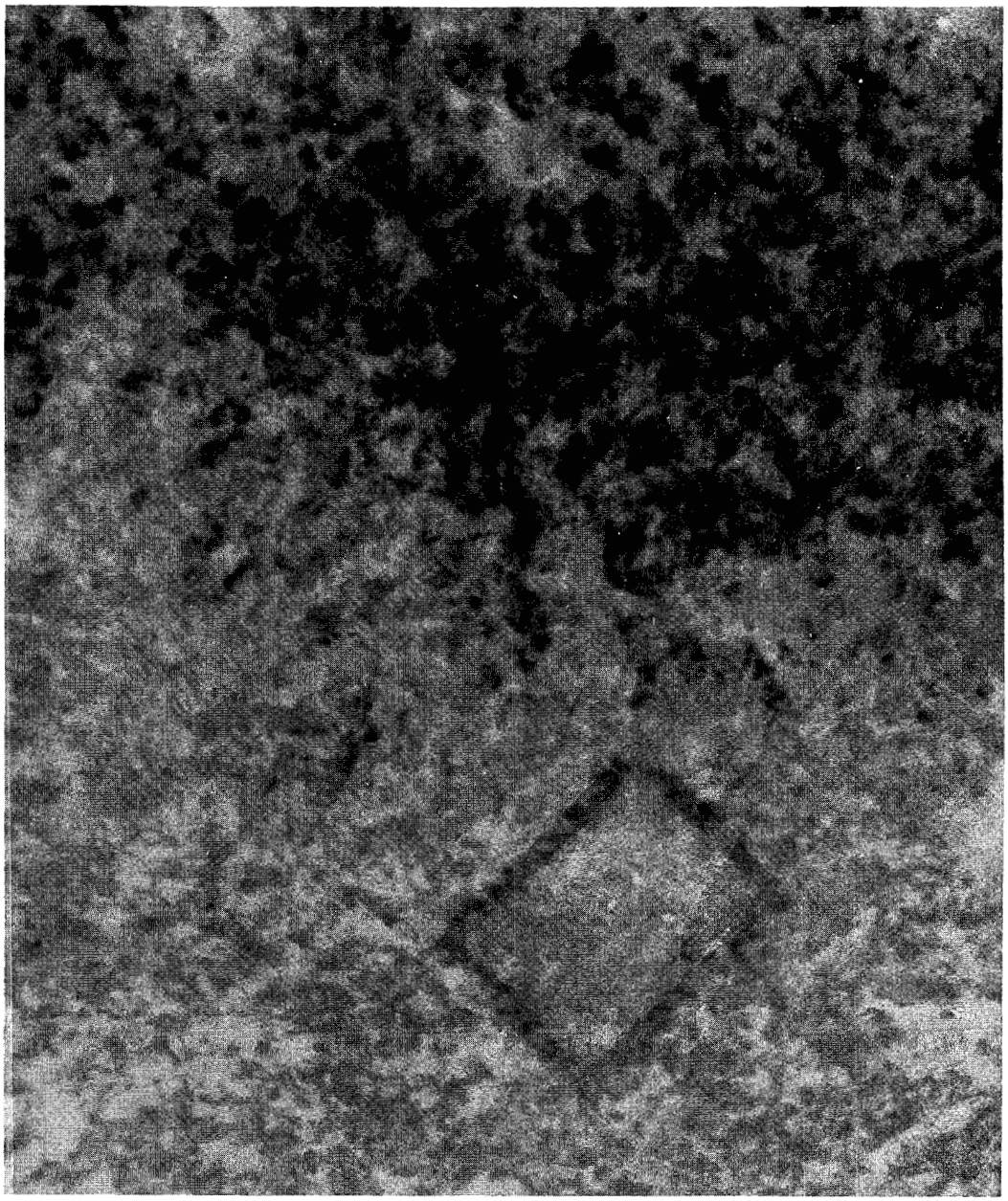

Figure 20a)

Microstructure of the oxide layer on an (001), 0.1 hour, 800°C specimen. a) Bright field image shows cubical voids, bend contours and some porosity.

Figure 20b)

Dark field image of a) helps to delineate individual oxide crystallites. The inset is an SAD of the oxide indicating a uniform orientation of the area not included in the bend contour.

resulting from a very mild bend contour. Imprints of cubical voids from the metal substrate are still evident. The single crystal electron diffraction pattern indicates the orientation of the oxide layer to be uniform. The width of the diffraction spots is a measure of the amount of misorientation of the small crystallites comprising the oxide layer. The DF image allows the individual crystallites of oxide to be distinguished. The crystallite sizes range form 5 to 20 nm.

The combined metal plus oxide microstructure is shown in the DF image of Figure 21. The interface between oxide alone and metal plus oxide is indicated. In this thin metal region where both oxide and metal are present, the interesting features are the cubical voids and the large number of fringes. The cubical voids result from oxidation induced vacancies coalescing along high energy surfaces.[45] The edges of the voids are along the ⟨100⟩ metal directions. The voids can be seen to be pyramidal in nature; therefore, their faces would be {110} planes. This agrees with results by Smialek in an SEM study of oxidized β-NiAl.[45]

The fringes result from a phase difference between the electron wave functions of the metal and oxide, and are called Moire fringes. A geometrical analogue for Moire fringe formation is

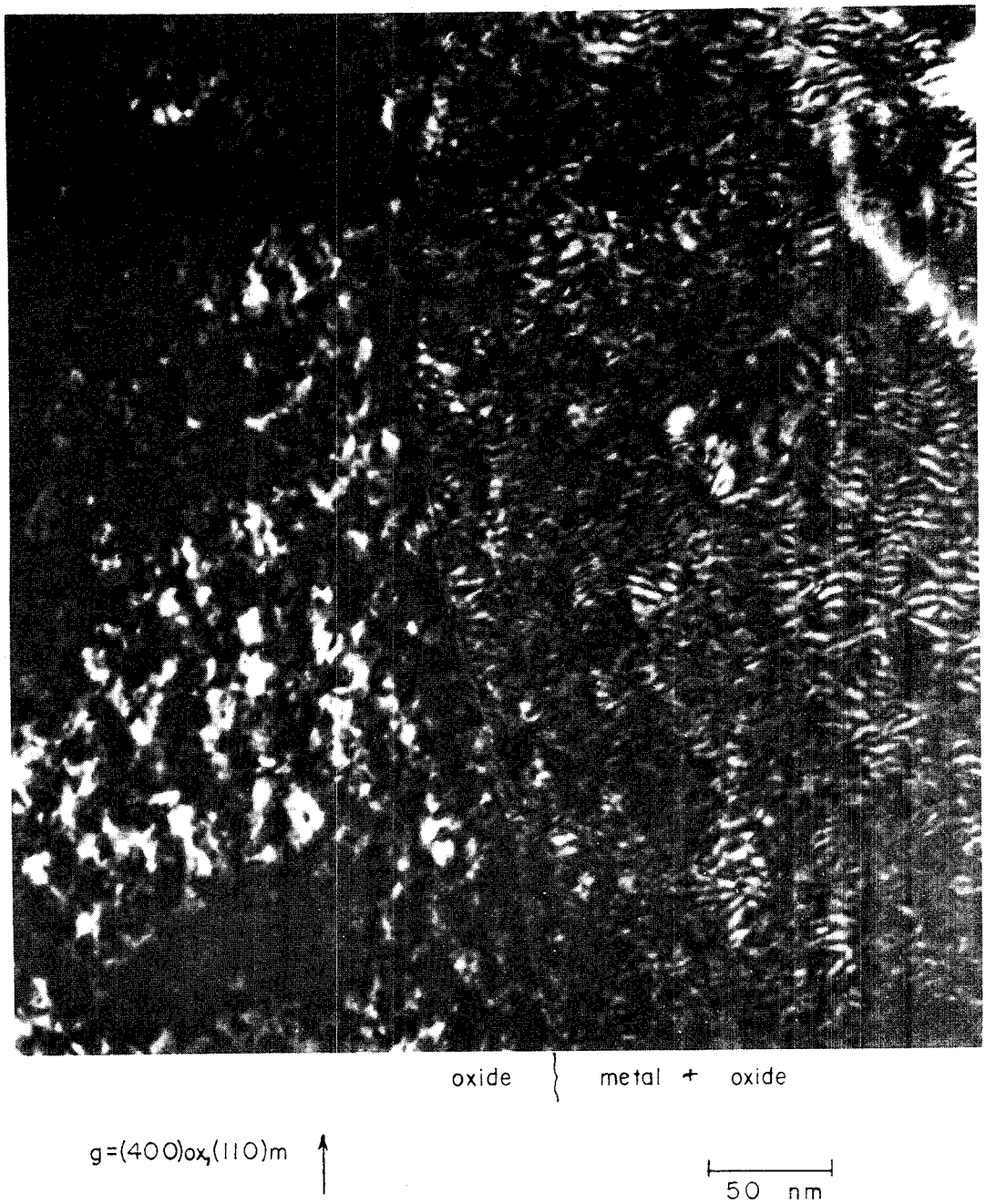

Figure 21

Dark field image of the oxide and metal plus oxide regions. Cubical voids and Moire fringes are the main features.

presented in Figure 22. There are two ways Moire fringes can form which result in parallel Moire fringes, rotational Moire fringes or combinations of the two. Rotational Moire fringes are caused when two crystals, having the same lattice spacing and structure, overlap and are rotated relative to each other. The fringe spacing, D_r, is given by:

$$D_r = \frac{1}{|g \sin\alpha|} \qquad [14]$$

where g = 1/d = the reciprocal lattice vector with dimensions of $(\text{length})^{-1}$; α = the rotation angle in radians. The fringes are parallel to the change in g-vectors of the two lattices.

Parallel Moire fringes are formed when two crystals having different lattice spacings overlap, the g-vectors being of different length but the same direction. Figure 21 shows that the Moire fringes in this case run perpendicular to the g-vector difference. The spacing of parallel Moire fringes, D_p, is given by:

$$D_p = \frac{1}{|g_1 - g_2|} \qquad [15]$$

The Moire fringes in Figure 23 result from the difference in spacing of the (110) β-NiAl reflection and the (400) reflection

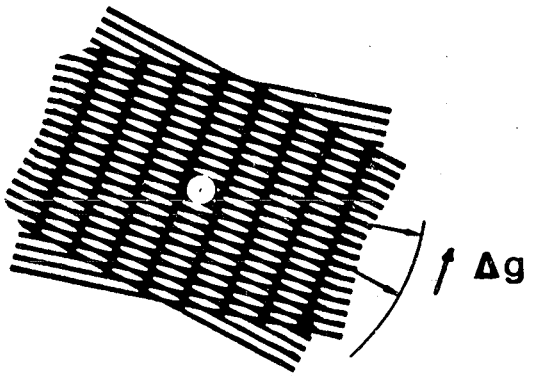

$$D_r = \frac{1}{g \sin \alpha}$$

a)

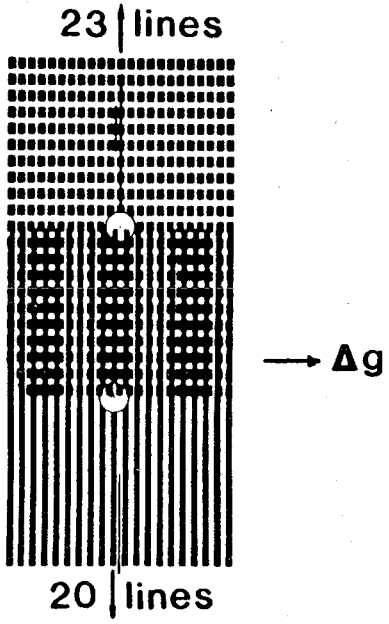

$$D_p = \frac{1}{|g_1 - g_2|}$$

b)

Figure 22

Geometrical analogue of Moire fringe formation for a) rotational and b) parallel Moire fringes.

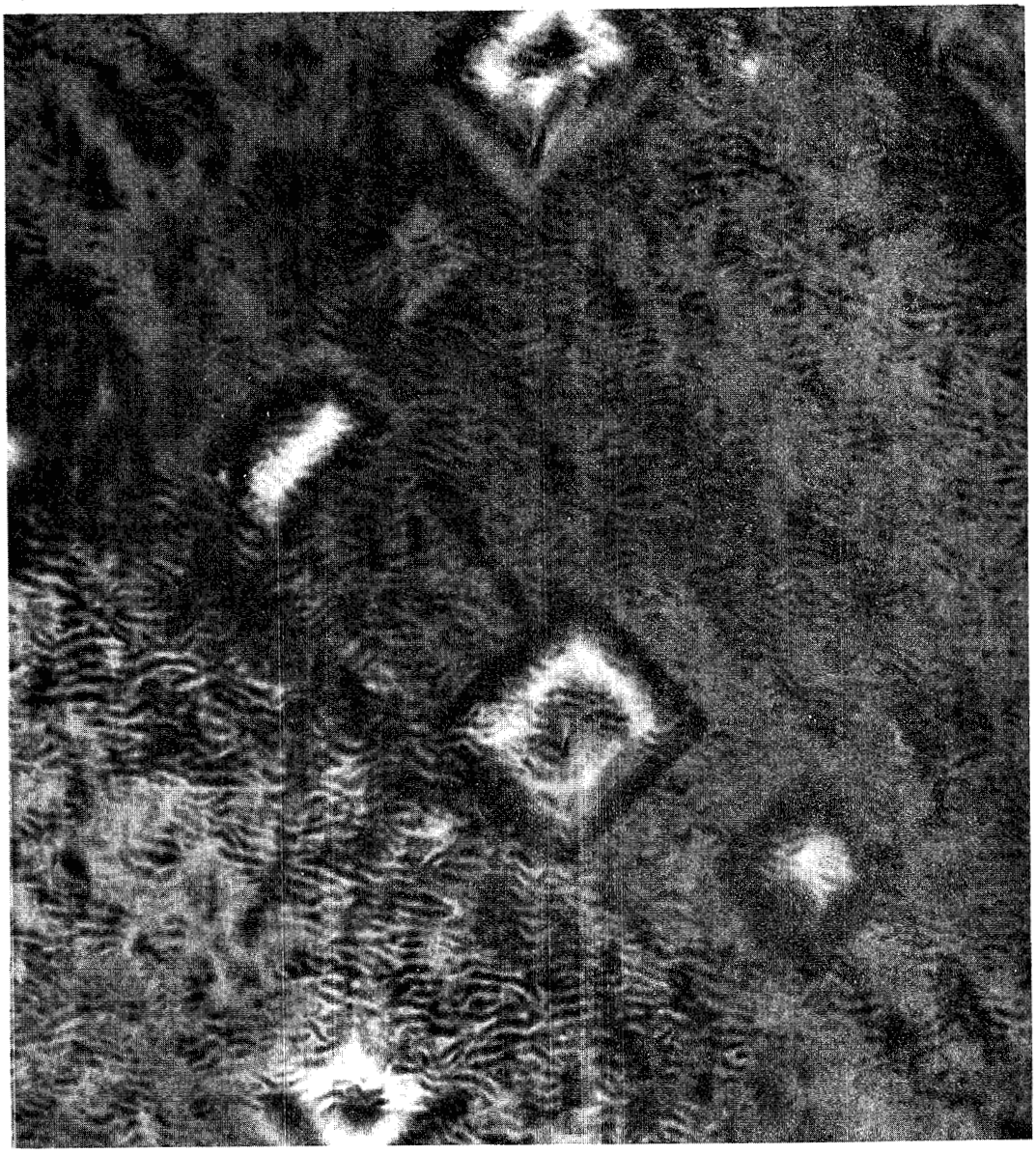

Figure 23

Another region of metal plus oxide showing Moire fringes in a bright field image. The fringes result from interference of the $(110)_{metal}$ and $(400)_{oxide}$ reflections of Figure 11.

from $NiAl_2O_4$, δ-Al_2O_3, and/or γ-Al_2O_3. There is also some slight rotation of the fringes which is caused by thickness variations of the oxide crystallites and by the rotational Moire effect from the definite width of the oxide reflection. The Moire fringe spacing for combined parallel and rotational fringes, D_{p-r}, is given as: [46]

$$D_{p-r} = \frac{d_1 d_2}{((d_1 d_2)^2 + d_1 d_2 \alpha^2)^{1/2}} \qquad [16]$$

The Moire fringe spacings of Figure 23 range between 3 nm and 8 nm wide. This corresponds well with the calculated parallel Moire fringe spacing from the (110) β-NiAl and (400) γ-Al_2O_3 reflections of 6.6 nm. The general direction of the fringes lies perpendicular to the g-vectors of the more intense reflections in Figure 17, giving another indication for parallel Moire fringes.

Moire fringes are still observed over thicker metal regions as shown in Figure 24, indicating the presence of an oxide layer. However, a high density of dislocations, arrayed in a network fashion, is also observed. The dislocations lie along $\langle 100 \rangle$ directions primarily, a common slip direction in alloys with the B2 structure.[39] These dislocations clearly result from the effects of an oxide layer as evidenced by comparing the unox-

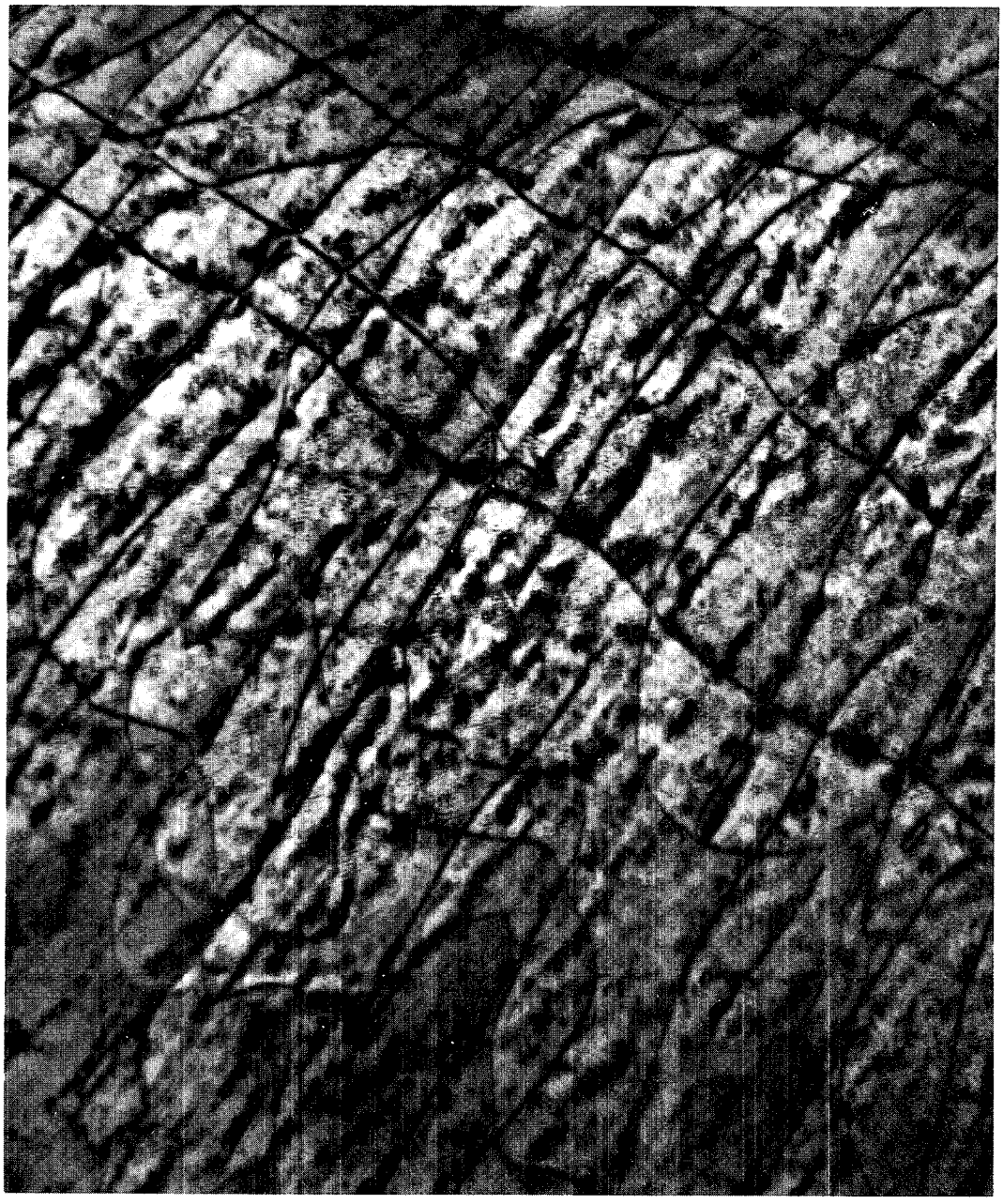

0.25 μm

Figure 24

Bright field image of thicker metal from an (001), 0.1 hour, 800°C specimen. Interface dislocation networks and Moire fringes are evident.

idized metal of Figure 6 with Figure 24. The extreme length of the dislocation lines indicate that they lie in a plane parallel to the surface. This same type of dislocation network has been found for NiCrAl alloys and was believed to be a network of edge dislocations resulting from a biaxial stress in the metal at the metal-oxide interface.[18]

2) 1.0 hours, 800°C

A BF image of the oxide and metal plus oxide interface is shown in Figure 25. Similar features as in the 0.1 hour condition can be recognized. Moire fringes, approximately 2.5 nm wide, occur where both oxide and metal overlap. The oxide has thickened relative to the 0.1 hour condition and can now be delineated from the metal where they overlap. Individual oxide crystallites approximately 10-30 nm in diameter can be resolved.

The corresponding SAD in Figure 26 shows a Bain type orientation relationship similar to that found in the 0.1 hour case. However, a definite change in oxide structure has occurred. The extra reflections at 1/3 (400) spacings are an indication of δ-Al_2O_3. These superlattice reflections occur because the c/a ratio of tetragonal δ-Al_2O_3 is approximately equal to

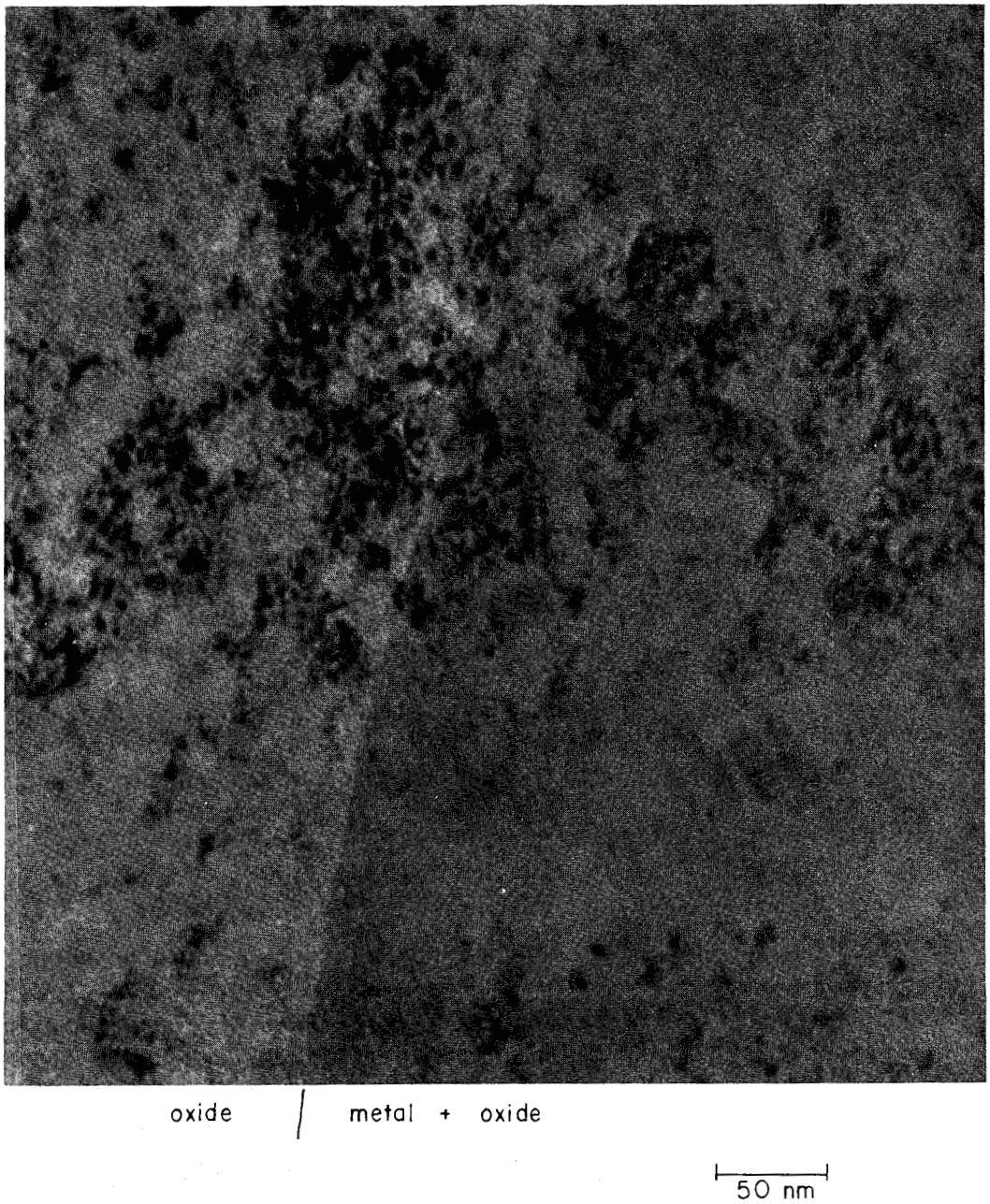

Figure 25

Bright field image of an oxide and metal plus oxide region from an (001) specimen oxidized for 1.0 hours at 800°C. Moire fringes can be observed where both oxide and metal are present.

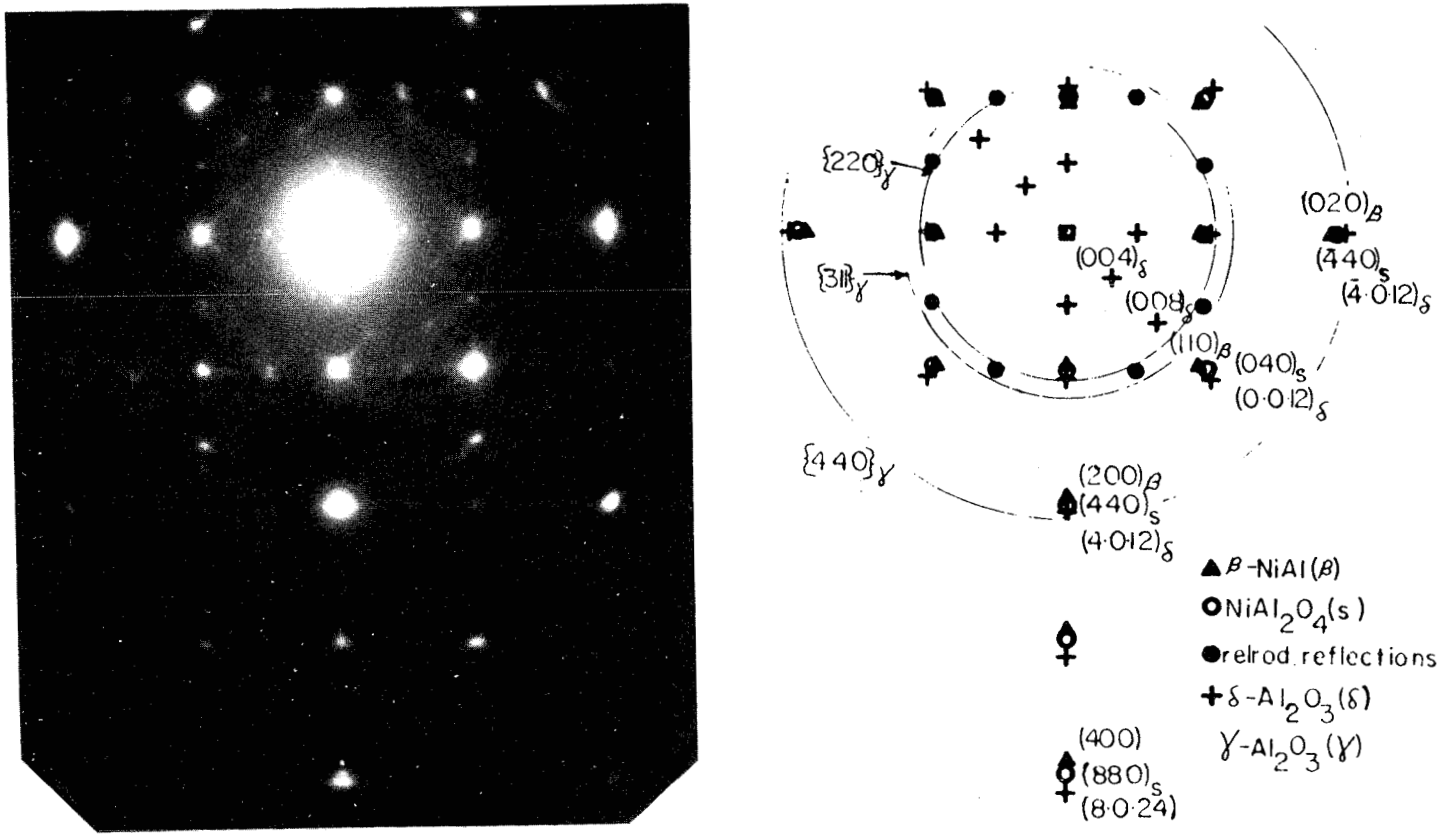

Figure 26

Selected area diffraction pattern from a metal plus oxide region on an (001), 1.0 hour, 800°C specimen. δ-Al_2O_3 is now evident from the 1/3(400) oxide reflections. Zone axis: near $[001]_{\beta}$, near $[001]_{s,\delta,\gamma}$.

three. Only one variant is obvious in the diffraction pattern but this can be due to being slightly off the zone axis. The occurrence of these reflections indicates that the [001] directions of δ-Al_2O_3 lie in the plane of oxidation. Therefore, the orientation relationship might now be written to include δ-Al_2O_3 as:

$$(001)_{\beta\text{-NiAl}} \parallel (001)_{NiAl_2O_4,\ \gamma\text{-}Al_2O_3} \parallel (010)_{\delta\text{-}Al_2O_3}$$
$$[100]_{\beta\text{-NiAl}} \parallel [110]_{NiAl_2O_4,\ \gamma\text{-}Al_2O_3} \parallel [103]_{\delta\text{-}Al_2O_3}$$
$$[110]_{\beta\text{-NiAl}} \parallel [100]_{NiAl_2O_4,\ \gamma\text{-}Al_2O_3} \parallel [100]_{\delta\text{-}Al_2O_3}$$

The distinct rings in the diffraction pattern correspond to randomly oriented γ-Al_2O_3. X-ray analysis of the oxide indicated the presence of less than 1% of Cr, Si, Cu, and Fe as impurities. These impurity levels are greater than what was normally found in most oxide scales. The impurities might be responsible for the formation of the randomly oriented oxide.

A very good indication that $NiAl_2O_4$ is still present is shown by the multiple reflections near the (400) β-NiAl spot. The middle reflection is from $NiAl_2O_4$ and the outer reflection is from δ-Al_2O_3 and possibly γ-Al_2O_3. Another variant of δ-Al_2O_3 with the [001] direction perpendicular to the oxidation plane

could result in {110} δ-Al_2O_3 reflections just inside of the {103}δ-Al_2O_3 reflections. The d-spacings for these two reflections are only about 0.7% different.

The Al/Ni ratio for this oxide was measured to be 3.08. This corresponds to an increase in Al_2O_3 formation over the 0.1 hour condition. The electron diffraction data also represents an increased Al_2O_3 formation over $NiAl_2O_4$ in regards to intensities and the presence of both the gamma and delta forms of Al_2O_3. (Summaries of oxide phases and Al/Ni ratios for all metal orientations and oxidizing conditions are presented in Table VI and Table VII, respectively).

3) 10.0 hours, 800°C

With increasing oxidation time, δ-Al_2O_3 becomes the predominate oxide phase. A diffraction pattern of an [001] oxide zone is shown in Figure 27 and is indicative of the entire oxide layer. This SAD was taken at a tilt of less than 2°.

Figure 28 shows an area of both metal and oxide with the corresponding SAD. The oxide is so thick that an interface between metal plus oxide and oxide alone cannot clearly be defined.

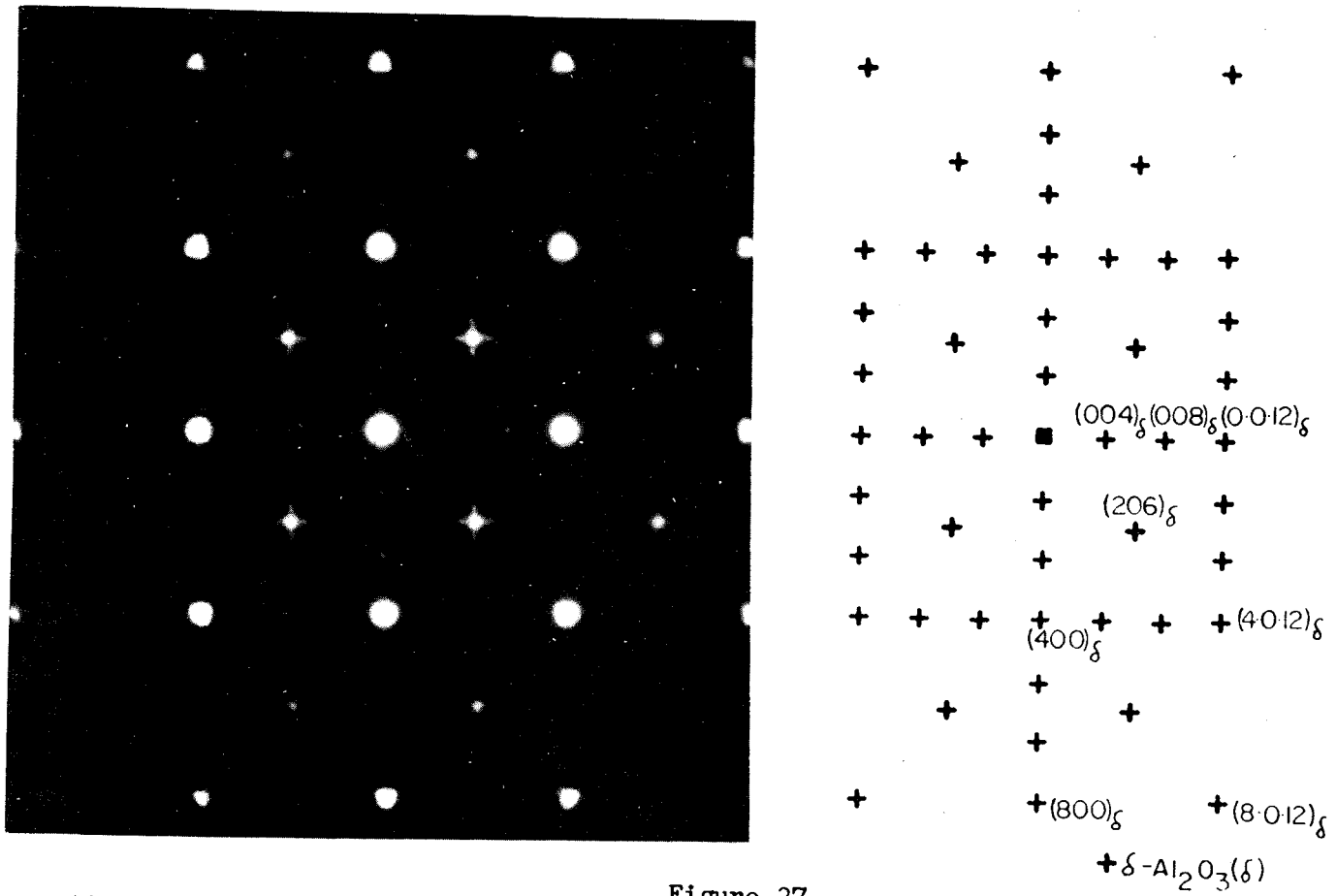

Figure 27

Selected area diffraction pattern of the oxide layer on an (001), 10.0 hour, 800°C specimen. This pattern was taken at a tilt of less than 2°. Only one variant of the δ-Al_2O_3 is indexed. Zone axis: $[001]_\delta$.

Figure 28a)

Bright field image of an oxide and metal plus oxide region from an (001), 10.0 hour, 800°C specimen. The oxide is too thick to determine the exact oxide and metal plus oxide interface.

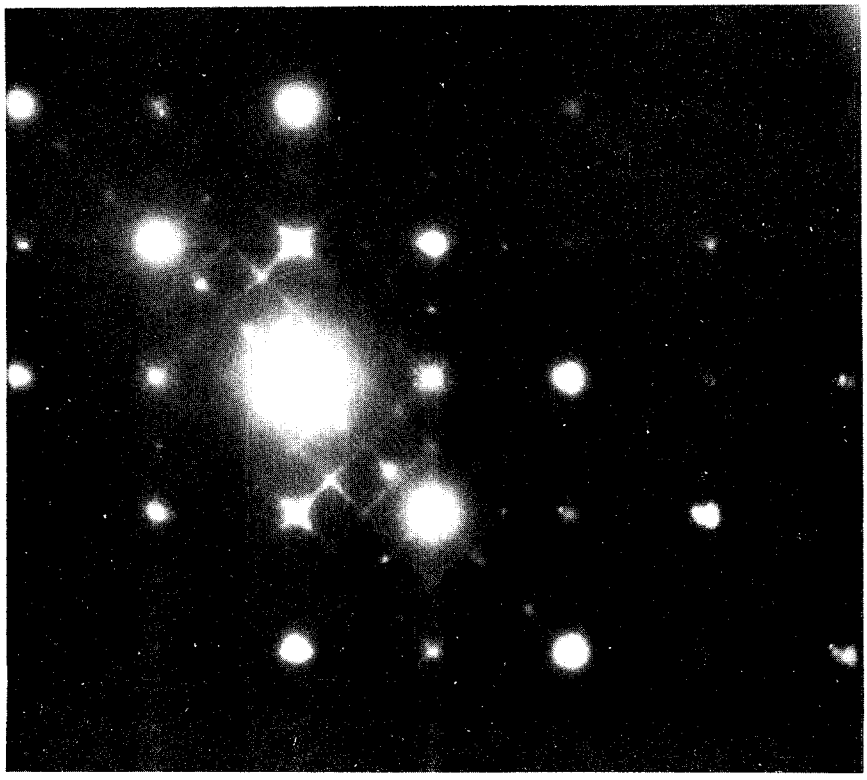

Figure 28b)

Selected area diffraction pattern from a metal plus oxide region of Figure 28a). The oxide consists of $NiAl_2O_4$ and δ-Al_2O_3 as shown by the double oxide reflections near $(400)_\beta$. Zone axis: near $[001]_\beta$, near $[001]_{s,\delta}$.

Remnants of cubical voids and Moire fringes are still evident where the metal is present. A higher magnification micrograph of the oxide in Figure 29 shows oxide subgrains, not clearly defined, approximately 100 to 200 nm in size. Possible Moire fringes are also evident.

The (400) β-NiAl reflection and adjacent oxide reflections again indicate the presence of $NiAl_2O_4$ along with δ-Al_2O_3. However, the Al/Ni ratio of 10.20 means that $NiAl_2O_4$ is no longer a major oxide phase when compared with oxide compositions from shorter oxidation times.

Another specimen oxidized under the same conditions showed quite a different oxide morphology. Figure 30 is a BF image of this oxide with a SAD from the lighter region indicated by the arrow. The oxide in this region corresponds to a randomly oriented spinel phase having a lattice constant approximately equal to $NiAl_2O_4$ and γ-Al_2O_3. X-ray analysis of the lighter regions indicated considerably higher levels of Ni and Cr as compared to the network around the patches. This would indicate that the randomly oriented oxide is most likely nickel-chromate spinel, $NiCr_2O_4$, having a lattice constant of 8.320 Å. The patches probably form during electropolishing where the electrolyte would preferentially erode the chromium rich areas

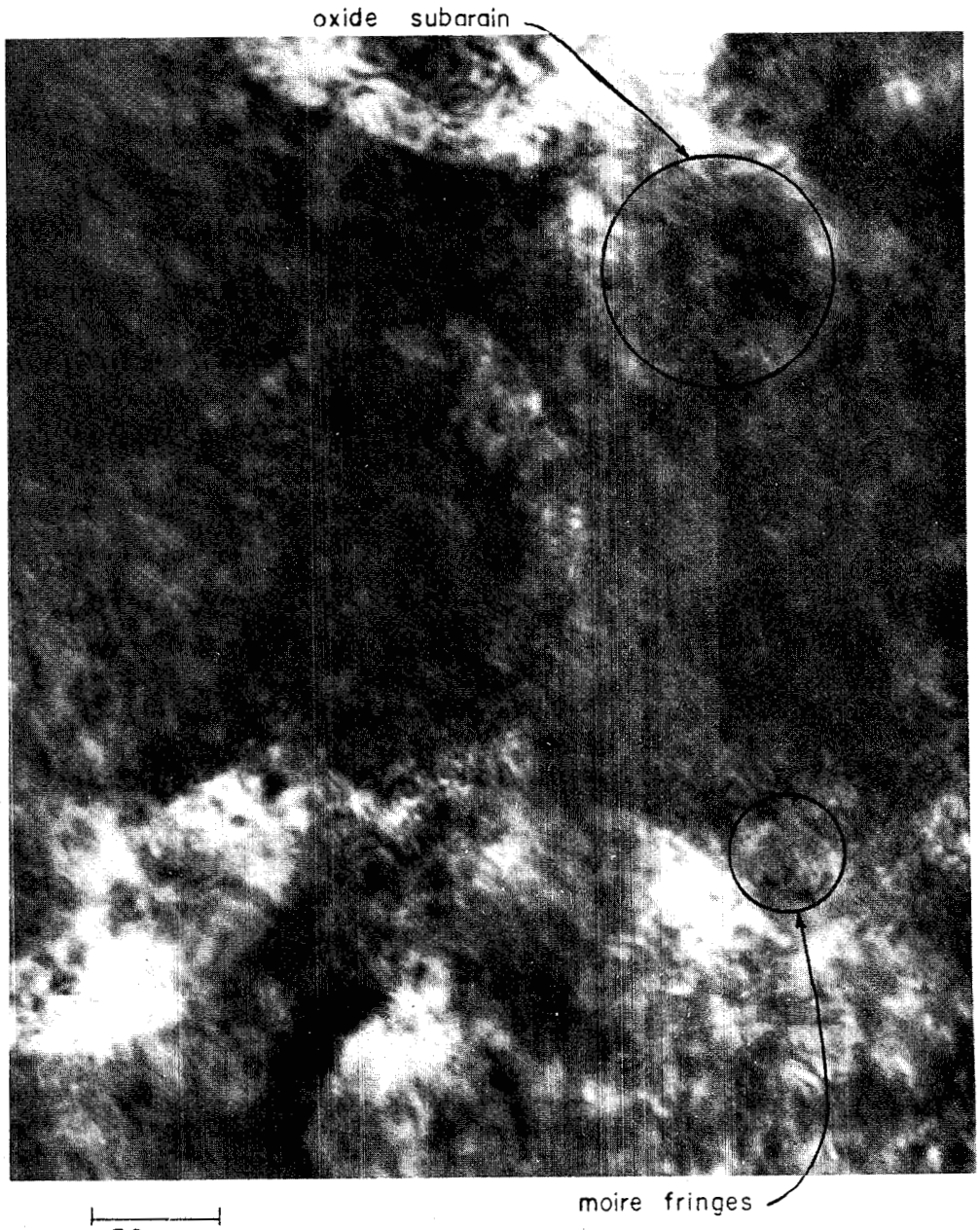

Figure 29

Higher magnification bright field image in just an oxide region of Figure 28a). Possible oxide subgrains and Moire fringes are indicated.

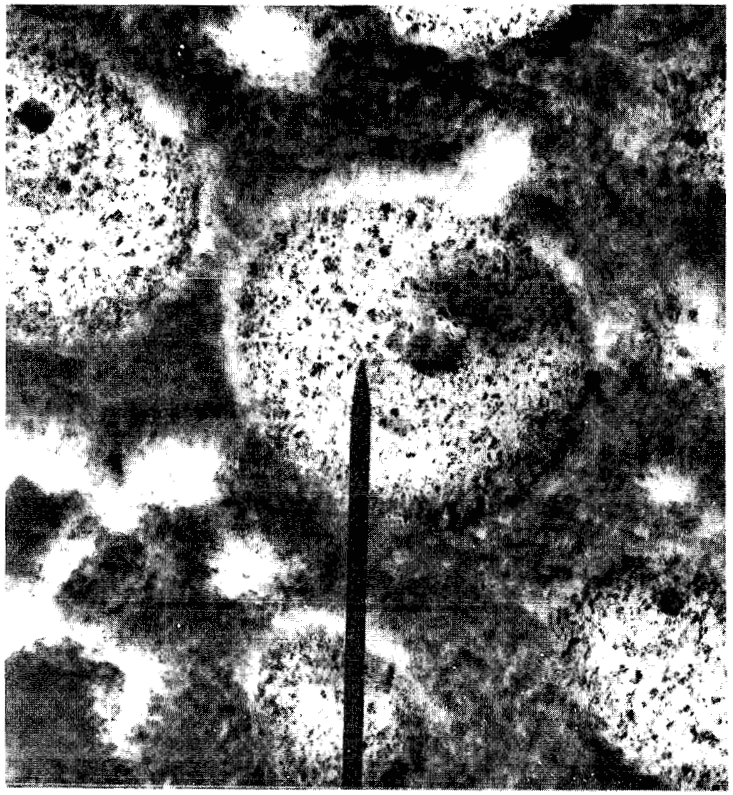

a)

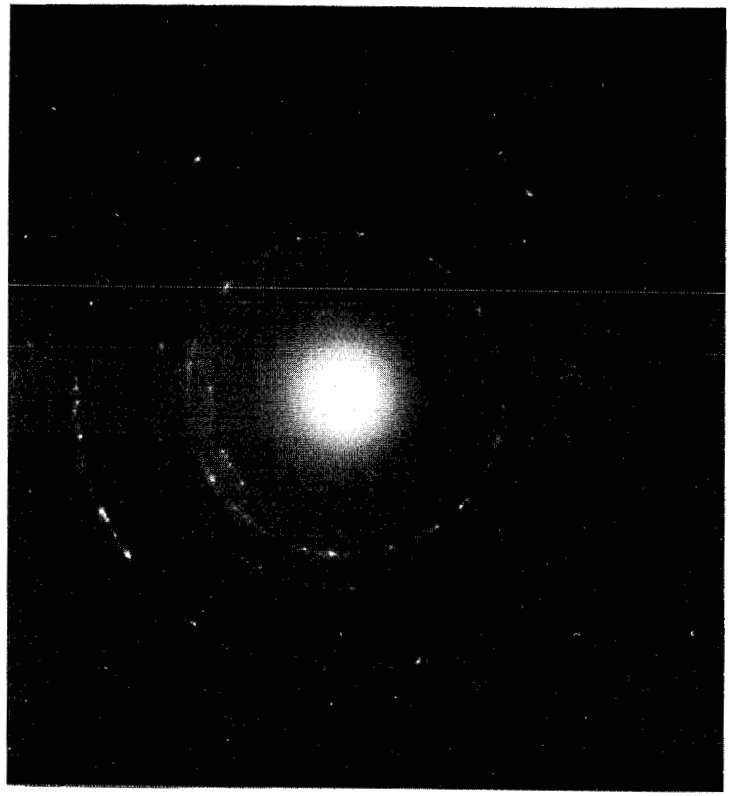

b)

Figure 30

Bright field image of an oxide and corresponding diffraction pattern from the region indicated by an arrow. The patches in a) are believed to occur from impurity oxides, probably $NiCr_2O_4$. The SAD of these regions in b) indicates rings from a spinel structure having a lattice constant near that of $NiCr_2O_4$.

of the oxide thereby reducing the thickness in those regions.

The orientation relationships are the same for 1.0 hour and 10.0 hour oxidation times. Clearly, at least two variants of δ-Al_2O_3 are present in the 10.0 hour case, the c-axes lying perpendicular to each other in the plane of oxidation. The possibility remains of a third variant with the c-axis in the direction perpendicular to the foil normal.

4) 0.1 hours, 1100°C

Some specimens were oxidized at 1100°C for 0.1 hours to determine if the scales consisted of oriented transient phases. Also, the specimens were not electropolished prior to oxidation to determine the effect of a rough surface on oxide orientation. Figure 31a is a BF image of the oxide scale under these conditions. Indications of scratch marks are noticed in the scale. However, this seemed to have little effect on oxide orientation since the same orientation relationship exists as that for all other (001) oriented specimens. The diffraction pattern in Figure 31b shows the Bain relationship between the metal and oxide with slight rotational variations up to 5°. The oxide consists of $NiAl_2O_4$ and δ-Al_2O_3.

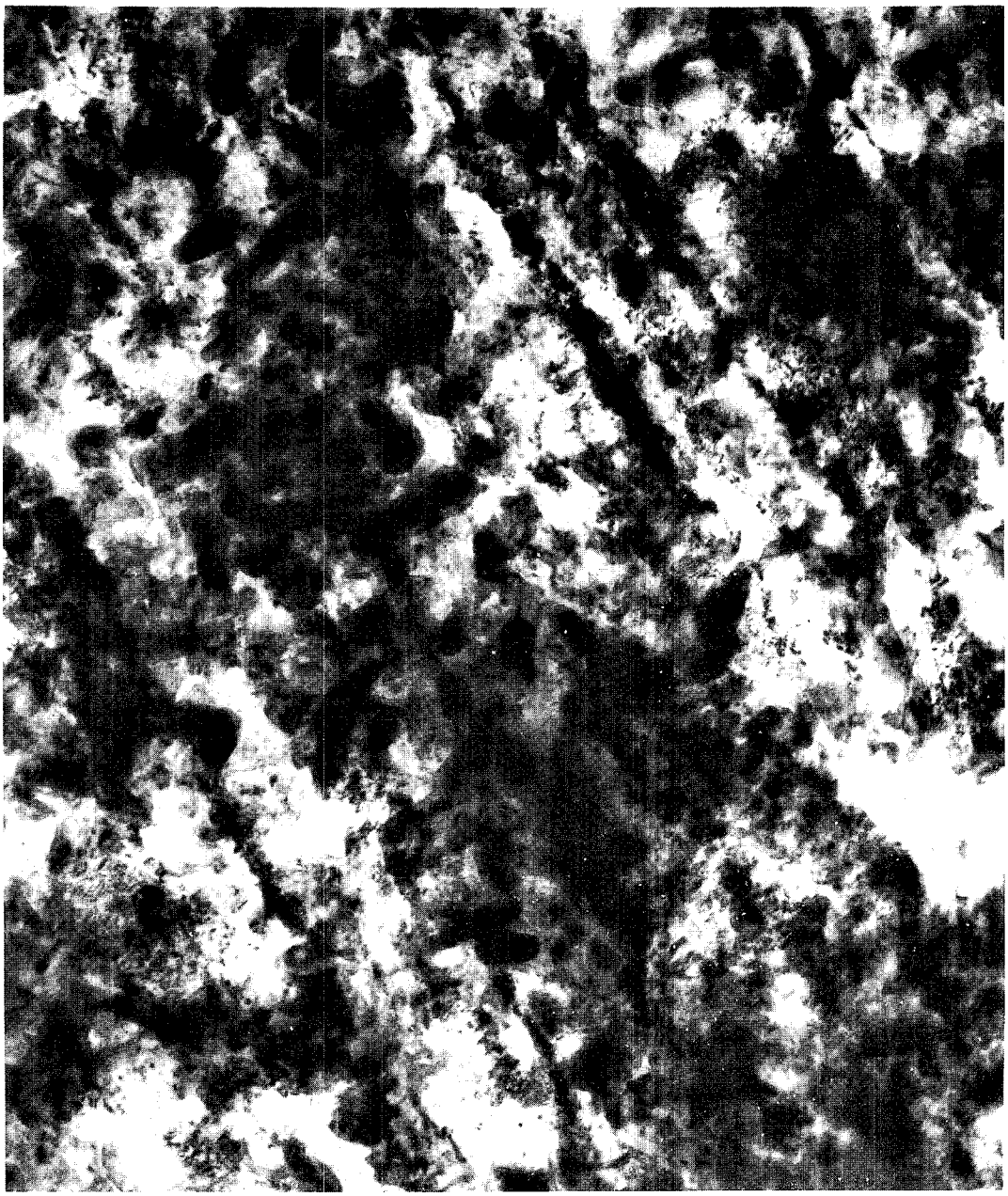

Figure 31a)

Bright field image of an oxide layer on an (001), 0.1 hour. 1100°C specimen. The linear texture highlights scratch marks on the non-electropolished metal surface.

Figure 31b)

Selected area diffraction pattern from a metal plus oxide region on an (001), 0.1 hour, 1100°C specimen. The oxide consists of δ-Al_2O_3 and $NiAl_2O_4$. Zone axis: near $[001]_{\beta}$, near $[001]_{s,\delta}$.

The high Al/Ni ratio of 14.1 for the oxide suggests that δ-Al_2O_3 is the predominate oxide phase. This agrees with Figure 31b, because only the more intense reflections of $NiAl_2O_4$, as determined by X-ray diffraction analysis, are evident in the diffraction pattern.[41] This same effect is seen in Figure 32 as the {400} $NiAl_2O_4$ reflections are strong but the {220} reflections are almost non-existent.

C) (012) Metal Orientation - Oxidized

1) 0.1 hours, 800°C

Although an (012) oriented metal does not represent an extreme orientation on the stereographic triangle as the other metal orientations do, it does represent a low index plane intermediate between two major orientations which can be used to qualify some of the results. Also, the [012] direction was a preferred growth direction in the cast alloy bars thus making this metal orientation a logical choice for an oxidation study.

The oxide that formed on the (012) metal orientation is highly epitaxially related to the metal. Figure 33 illustrates this with a) predominately metal and b) only oxide reflections in these diffraction patterns. The (012) Kikuchi center in Figure

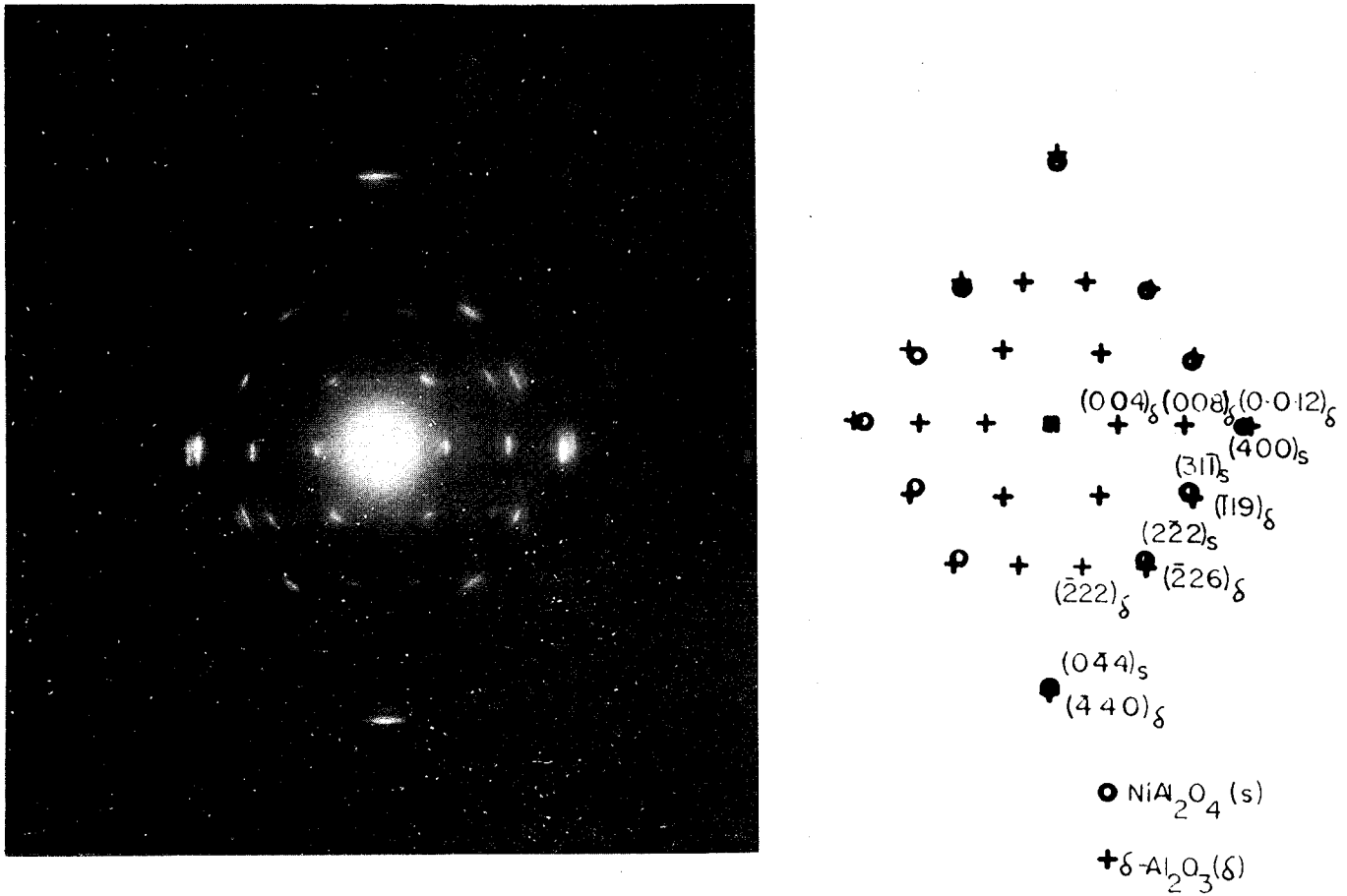

Figure 32

Selected area diffraction pattern of an [011] oxide zone. δ-Al_2O_3 is the major oxide phase for this (001), 0.1 hour, 1100°C condition.

33a demonstrates the precise metal orientation. The metal-oxide orientation relationship for this case was found to be:

$$(012)_m \;||\; (112)_{ox}$$
$$[100]_m \;||\; [110]_{ox}$$

The oxide consisted of both $NiAl_2O_4$ and γ or δ-Al_2O_3 as determined by the Al/Ni ratio equal to 1.60. Many of the extra reflections found in these diffraction patterns can be attributed to double diffraction between β-NiAl and $NiAl_2O_4$. However, by tilting to other oxide zone axes, evidence of γ or δ-Al_2O_3 can be observed which might be hidden by the central spot of Figure 33b. The extra "wing" reflections near the {311} relrod reflections in Figure 34a have a d-spacing similar to the $\{222\}_\gamma$-Al_2O_3 reflections but do not correspond with adjacent higher order Laue zones. (See Appendix B for higher order Laue reflections.) These reflections could be associated with δ-Al_2O_3, representing the formation of that oxide phase. This possible δ-Al_2O_3 formation is also shown in the [101] oxide zone in Figure 34b. These extra reflections are located in the same places as in the [101] oxide zone on an (001) oriented metal of Figure 19, previously mentioned.

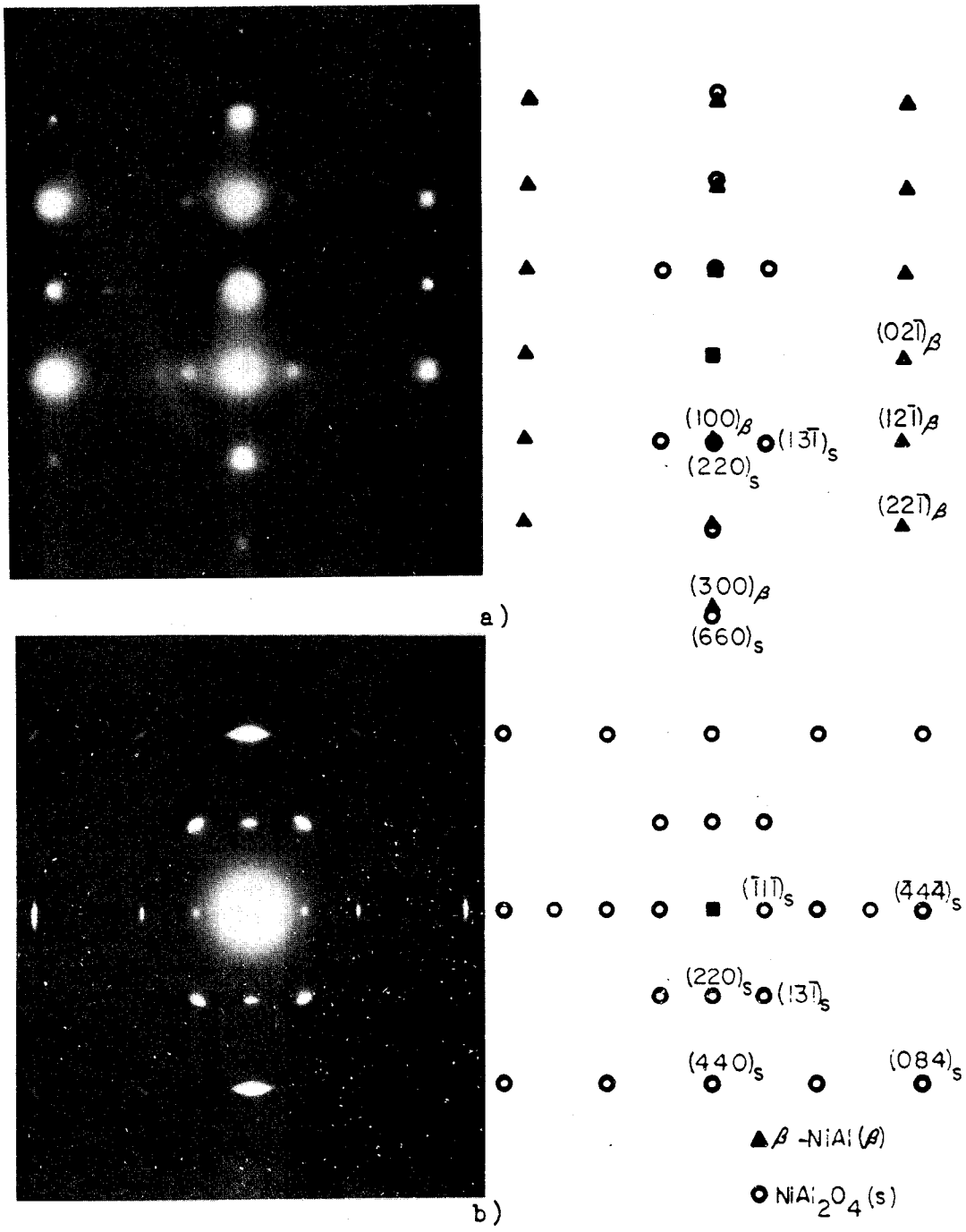

Figure 33

Selected area diffraction patterns from an (012) specimen oxidized for 0.1 hours at 800°C. The diffraction pattern in a) is from a metal plus oxide region whereas b) is a pattern of oxide only. Zone axis: a) $[012]_\beta$, $[112]_s$, b) $[112]_s$.

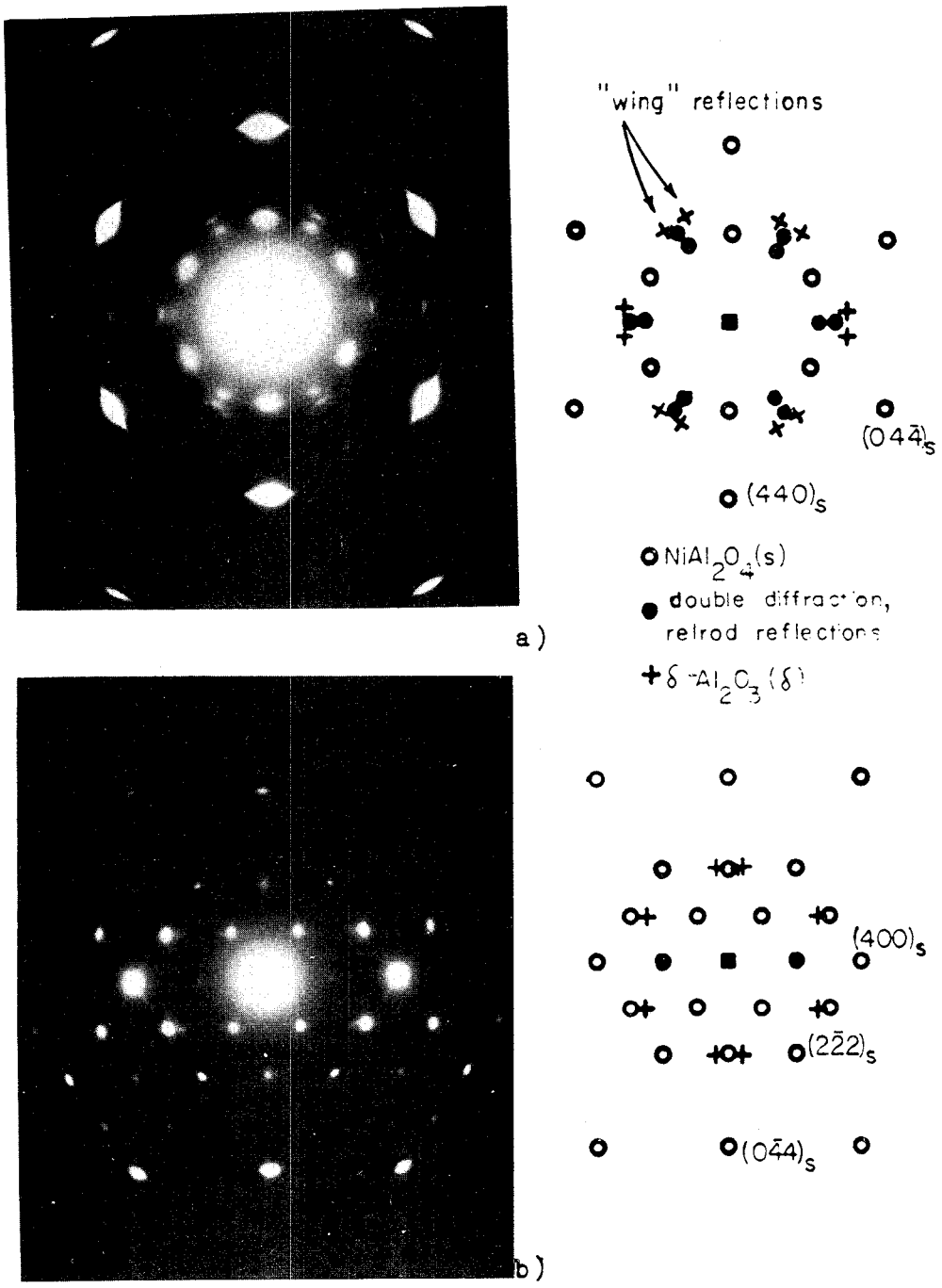

Figure 34

Oxide zones from an (012), 0.1 hour, 800°C specimen. The extra "wing" reflections in the [111] zone of a) are associated with the existence of δ-Al_2O_3. Evidence of δ-Al_2O_3 is also seen in b), in an [011] oxide zone.

The BF-DF pair in Figure 35 shows the oxide and metal plus oxide regions at the hole in the metal specimen. The SAD for this pair is shown in Figure 36. The specimen was tilted so that an $\langle 011 \rangle$ metal direction was nearly parallel to the beam direction. However, another set of metal reflections indicates an [012] zone axis. These two interpenetrating single crystal patterns result from the bulk metal specimen and possibly from a deformed metal area.

Upon increasing the magnification of a DF image, a large number of Moire fringe patterns are evident on the regions of both oxide and thin metal. These fringes are a result of interference between the (200) β-NiAl reflection and the (440) $NiAl_2O_4$ reflection shown in the previous SAD. Figure 37 shows that the fringes have a wide range of spacings and directions. This variation results from the combined rotational and parallel contributions to Moire fringe formation from the closeness of the two d-spacings of the reflections, and the large amount of rotational variance in the arc reflection of $NiAl_2O_4$. The schematic drawing of Figure 38 describes the terminology used when explaining the large rotational and spacing differences in the fringes. The angle, α , represents the rotational variance of the diffracted spots but the angle, γ , is the actual rotational variation that the Moire fringes can have. Table

Figure 35

Bright field-dark field pair of oxide and metal plus oxide regions from an (012), 0.1 hour 800°C specimen.

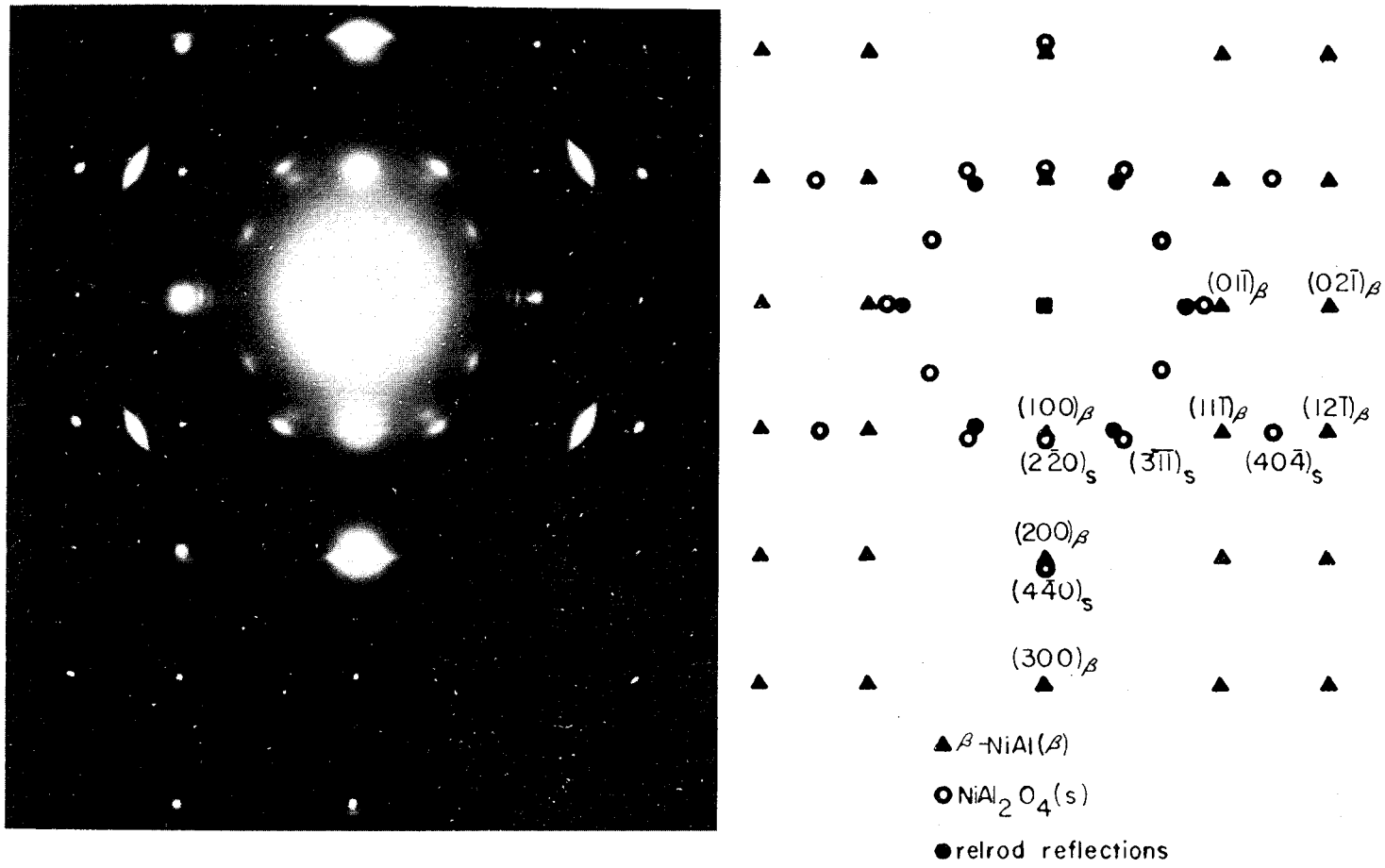

Figure 36

Selected area diffraction pattern from a metal plus oxide region of Figure 35. Two different orientations of metal are observed.

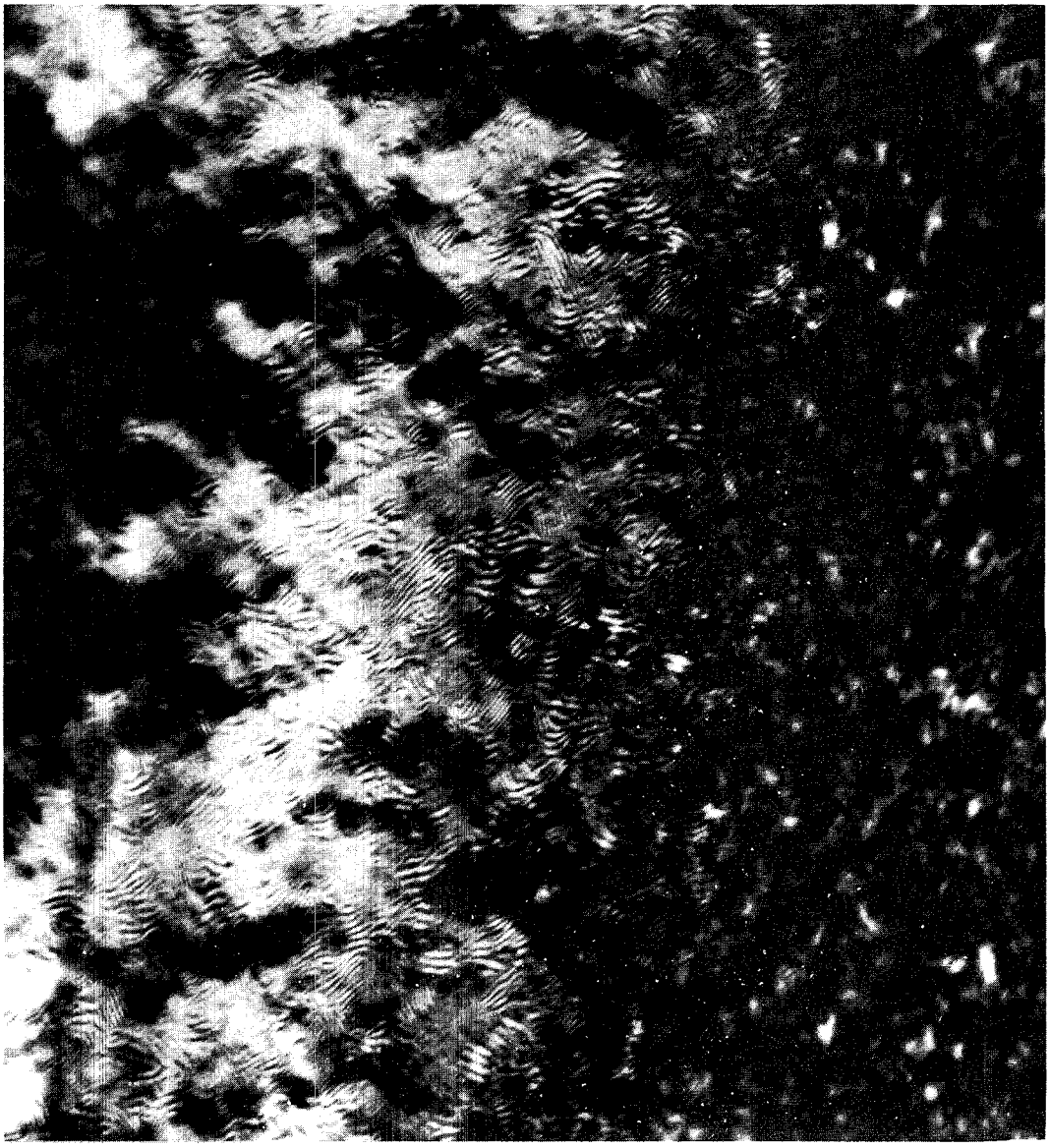

Figure 37a)

Dark field image of an (012), 0.1 hour, 800°C specimen. Moire fringes are observed where oxide and thin metal overlap.

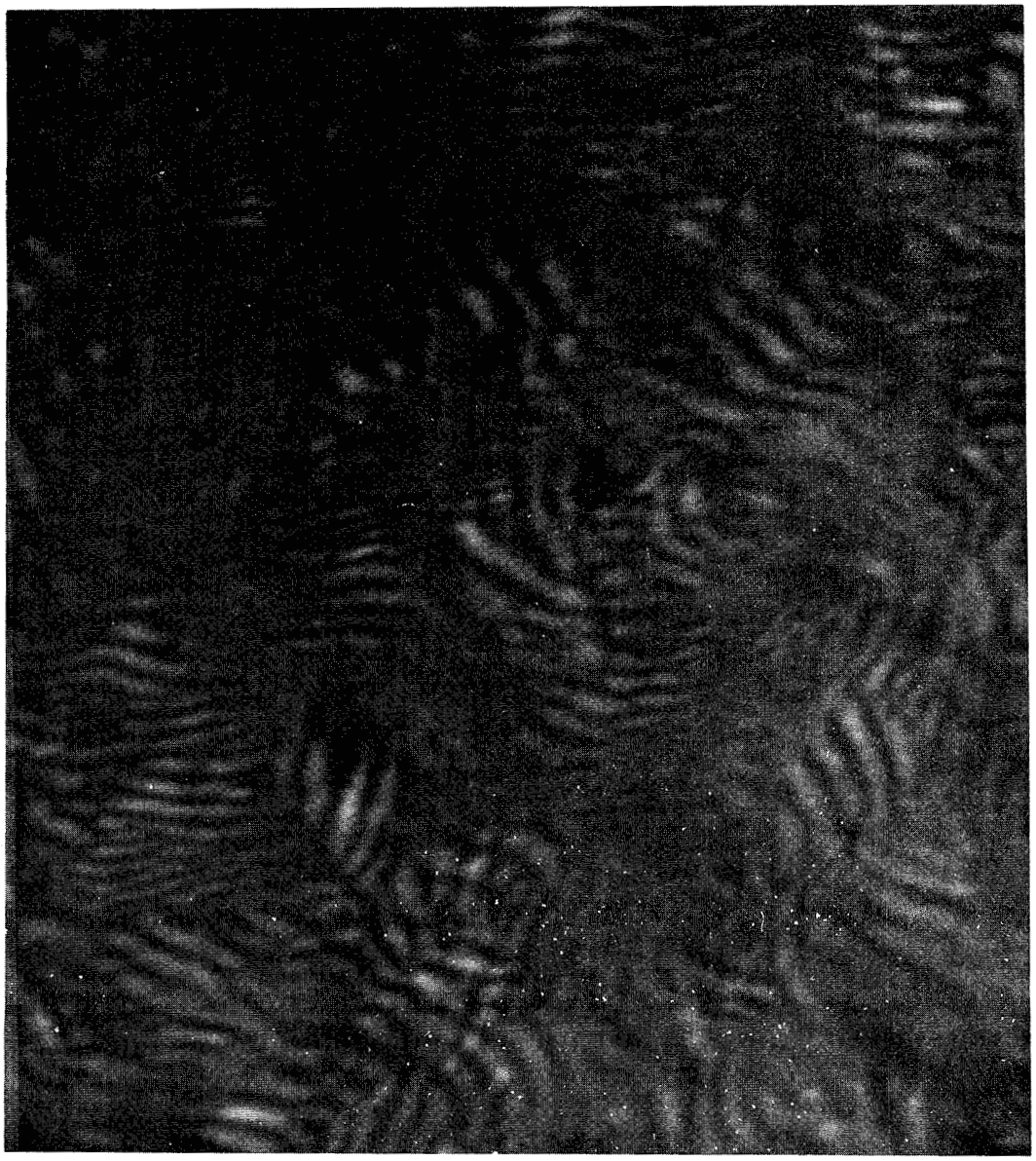

Figure 37b)

High magnification dark field image of a metal plus oxide region in Figure 37a). The spacings and directions of fringes are a function of the metal-oxide $\vec{g}$-vector difference.

Figure 38

Schematic of the geometrical terminology used to describe Moire fringe spacings and directions. The diffraction pattern of Figure 36 is used as an example.

III is a list of the calculated fringe spacings using the combined parallel and rotational formula. The angle, α , was measured from the diffraction pattern in Figure 36 and was found to be $\pm$ 10°. The angle, γ, was calculated by using the geometrical formula:

$$\sin \gamma = \frac{\sin \alpha}{[1 + (d_2/d_1)^2 - 2(d_2/d_1 \cos \alpha)]^{\frac{1}{2}}} \qquad [17]$$

For small α's, the fringe spacings should be the largest, corresponding to fringes lying nearly perpendicular to the metal g-vector. From Table III, $\gamma$is seen to reach 90° near an α of about 9.2°. The Moire fringes from reflections having this rotational difference are perpendicular to these at α equals 0° and are therefore parallel to the metal g-vector. The fringe spacing for these fringes should be the smallest. This proves to be the case as shown in the indicated g-vectors of Figure 37. From the actual micrograph, the largest fringe spacing, corresponding to α equal 0°, was measured to be approximately 23 nm, whereas the calculated fringe spacing from known d-spacings and α equals 0° is 11.4 nm. This difference is possible with less than a 0.5% change in the d-spacings of the metal or oxide. The predicted trend is evident, however, that the largest spacings occur when the fringes are primarily parallel Moire fringes and the smallest spacings occur when a maximum rotation effect is present.

TABLE III

Calculated fringe spacings and angles for Moire fringes on an (012), 0.1 hour specimen in Figure 37.

α°	D(nm)	γ°
0	11.39	0
0.5	9.36	35.0
1.0	6.66	54.7
1.5	4.93	65.1
2.0	3.86	71.2
3.0	2.66	78.0
4.0	2.02	81.8
5.0	1.62	84.3
6.0	1.36	86.2
7.0	1.17	87.6
8.0	1.02	88.9
9.0	0.91	89.9
10.0	0.82	90.9

Using these Moire fringes, an oxide crystallite size can be approximately determined by domains of unidirectional fringes corresponding to individual oxide crystallites. The domains of fringes were found to be between 5 and 25 nm in diameter. This apparent grain size agrees with that found for an (001) metal oxidized for 0.1 hours.

A similar crystallite size is obtained when Moire fringes are imaged using a {111} β-NiAl and {440} $NiAl_2O_4$ reflection. The difference in d-spacing is greater for these reflections; therefore the Moire fringe spacing will be much reduced.

That is indeed the result as shown in Figure 39. The Moire fringe spacing varies from approximately 0.6 to 0.9 nm depending upon the amount of rotation of the g-vectors as listed in Table IV. The large fringes can be purely rotational in nature and result from an overlapping of oxide crystallites.

The boundaries between each oxide crystallite are not always well defined, but can be noticed by slight changes in directions of the Moire fringe domains. The fringe directions between most domains (crystallites) generally varies only by a few degrees. This is evidence of low angle grain boundaries between oxide grains. A limited number of high angle boundaries are observed.

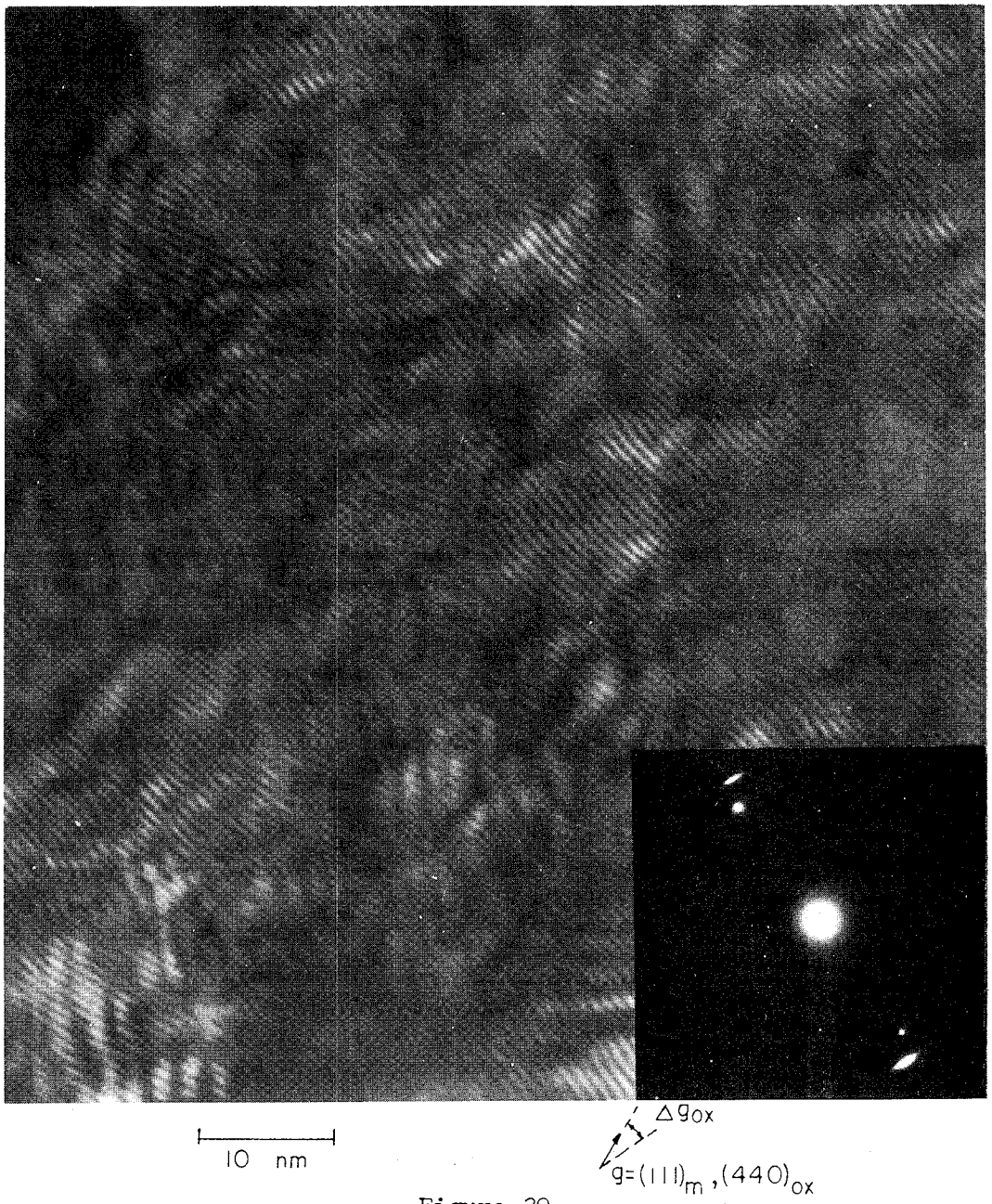

Figure 39

Moire fringes on an (012), 0.1 hour, 800°C specimen. The fringe spacing is reduced because the difference in d-spacings from the metal and oxide reflections used to create this image is large.

TABLE IV

Calculated fringe spacings and angles for Moire fringes on an (012), 0.1 hour specimen in Figure 39.

α°	D(nm)	γ°
0	0.87	0
1.0	0.87	6.2
2.0	0.86	12.4
3.0	0.84	18.3
4.0	0.81	23.9
5.0	0.78	29.2
6.0	0.75	34.1
7.0	0.72	38.7
8.0	0.68	42.9
9.0	0.65	46.7
10.0	0.60	51.9

C-2

2) 1.0 hours, 800°C

Figure 40 is a diffraction pattern from both a metal and oxide region of a specimen showing the same metal-oxide orientation relationship as found for the 0.1 hour condition. The oxide phases were determined to be $NiAl_2O_4$, γ-Al_2O_3, and δ-Al_2O_3 from this SAD. The presence of δ-Al_2O_3 is assured by the 1/2 {110} type reflections. The Al/Ni ratio was found to be only 1.59, less than that of the 0.1 hour (012) specimen. A higher ratio is expected since δ-Al_2O_3 is present as an oxide phase for 1.0 hour oxidation moreso than the 0.1 hour case. This anomaly is attributed to a possible error in x-ray data collection for the 1.0 hour specimen.

The bright field-dark field pair in Figure 41 shows similar oxide structures at other oxidizing times and metal orientations, Moire fringes again being evident. However, the BF images in Figure 42 show new structural features relating to voids, grain morphologies and sizes. Grain boundaries can be delineated with difficulty, but still show junctions between grains. Because the orientation difference could be so slight from grain to grain, a minimum contrast difference exists between individual grains. Some of the features can be voids which may not be grain boundary porosity.

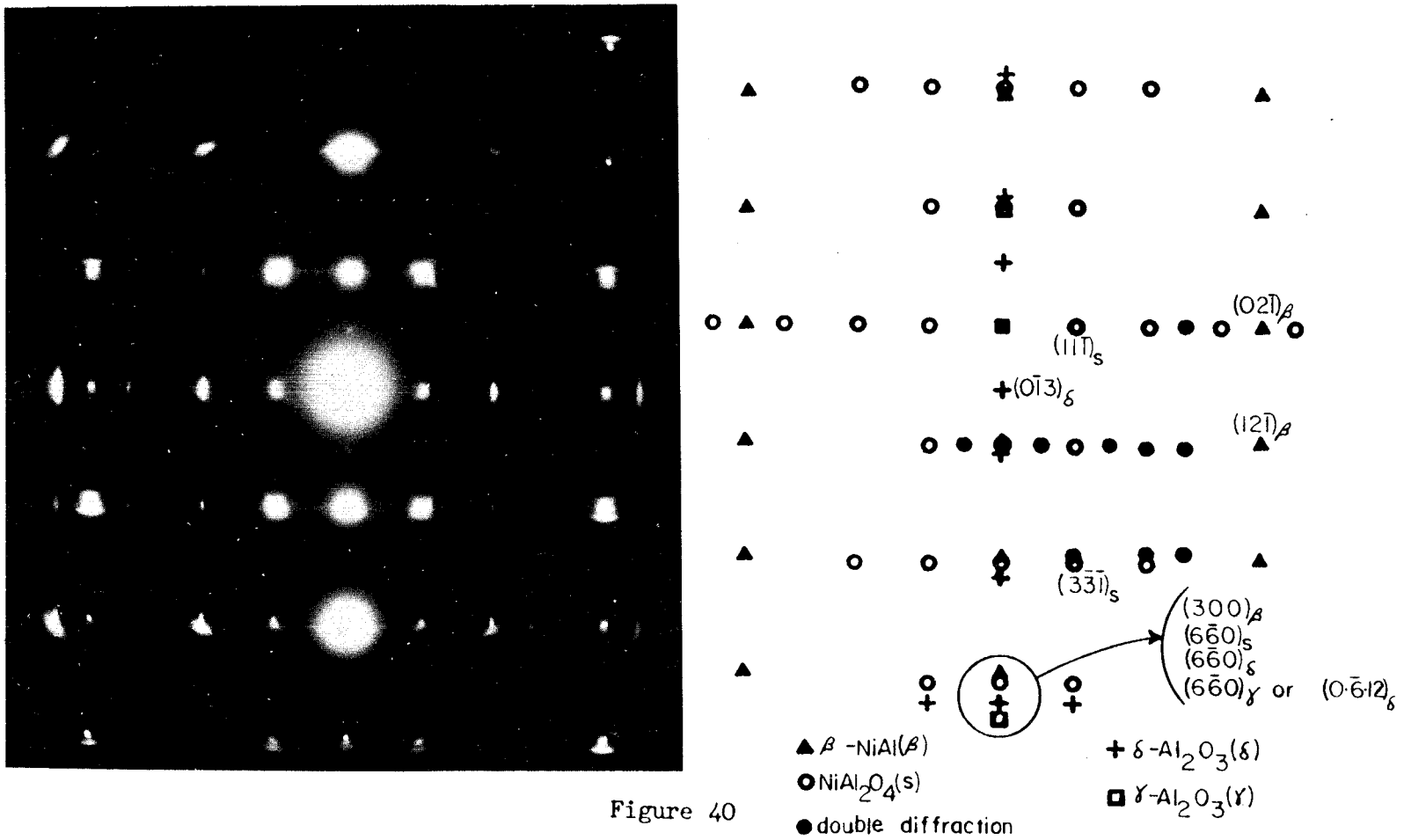

Figure 40

Electron diffraction pattern from a metal plus oxide region on an (012), 1.0 hour, 800°C specimen. Many extra reflections result from δ-Al_2O_3 or double diffraction. Zone axis: $[012]_\beta$, $[112]_{s,\delta,\gamma}$.

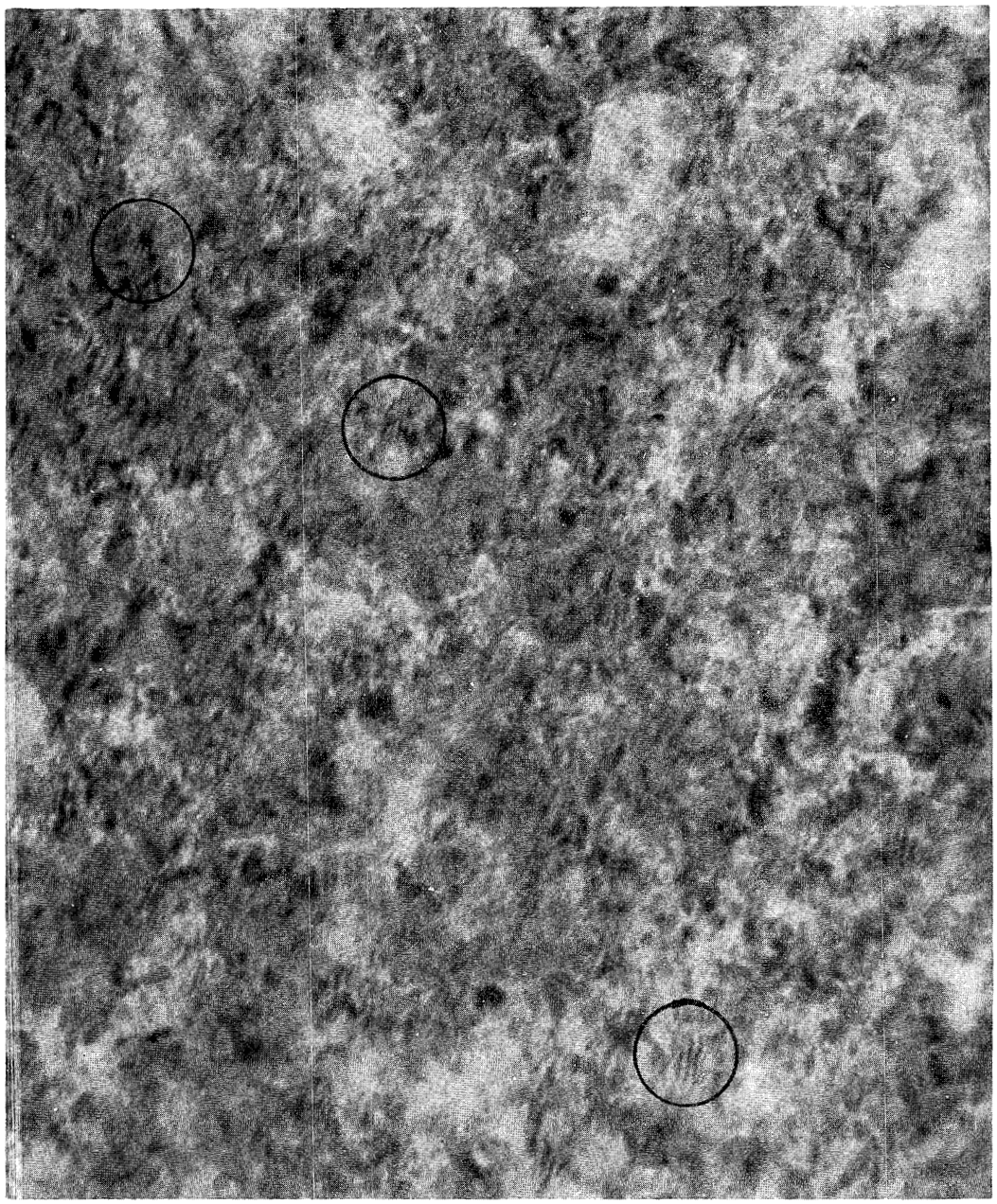

a) bright field

Figure 41

Bright field-dark field pair of oxide formed on an (012), 1.0 hour, 800°C specimen. Circled regions show Moire fringes.

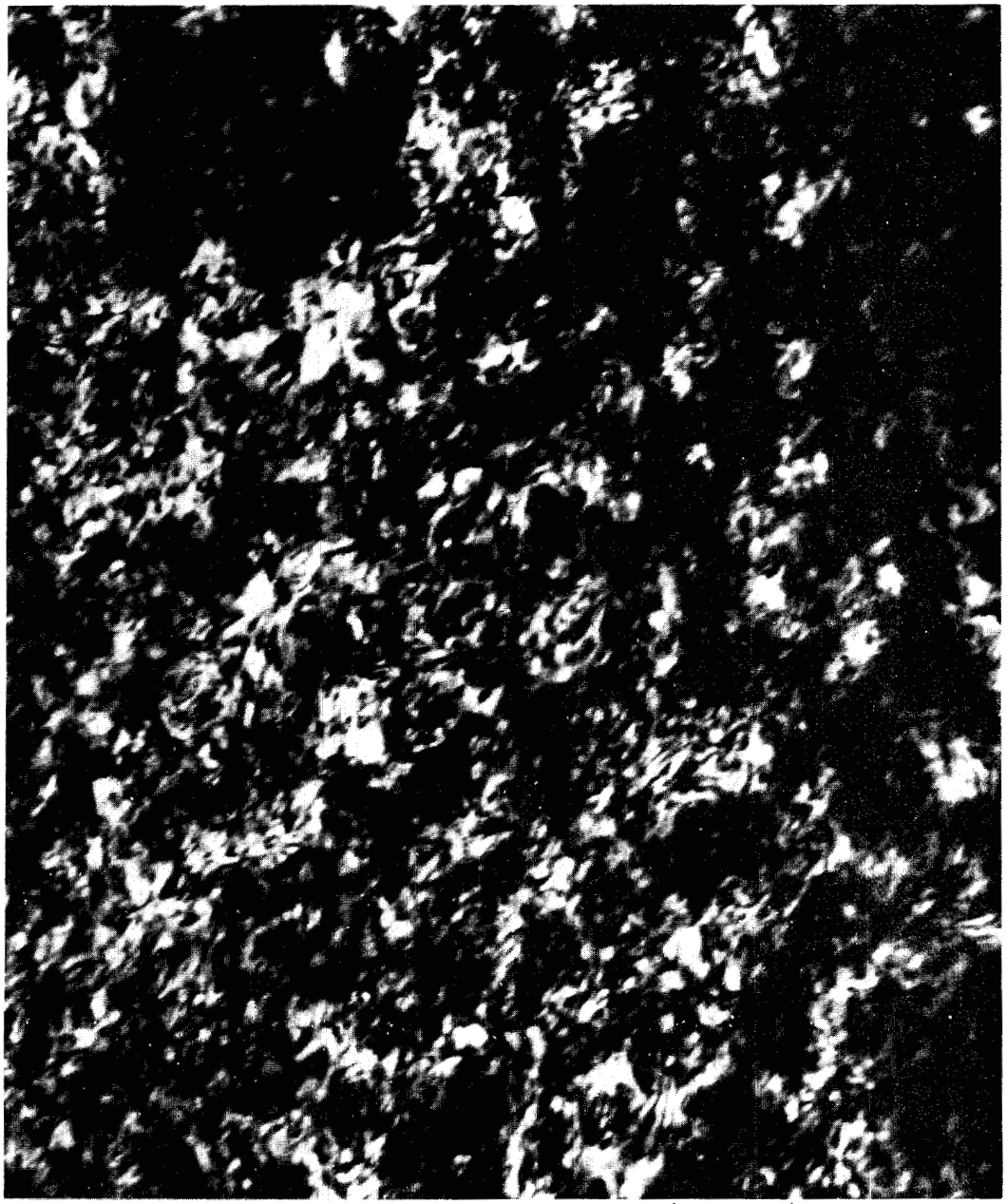

Figure 41b)

Dark field image of the oxide region shown in Figure 41a).

Figure 42

Bright field images from different areas of oxide on an (012), 1.0 hour, 800°C specimen. Moire fringes(M), grain boundaries(GB) and voids(V) are indicated.

The measured grain size ranges from 0.7 to 40 nm. Most grains appear to be approximately 20 nm in size. This does not indicate much grain growth, however, between 0.1 and 1.0 hours at the oxidation temperature.

3) 10.0 hours, 800°C

No images or X-ray data were obtained for this condition. The electron diffraction patterns of Figure 43 serve the purpose of oxide phase determination. There was no change in the orientation relationship from the shorter oxidation times.

The oxide in Figure 43b is indexed to be predominately δ-Al_2O_3. The same is true when tilting the oxide layer to near a $\langle 113 \rangle$ type cubic zone axis in a different region shown in Figure 43c. The same {222} "wing" reflections, first discovered in a [111] oxide zone on a 0.1 hour, (012) metal orientation (Figure 34) are evident in the well developed δ-Al_2O_3 zone shown in Figure 44.

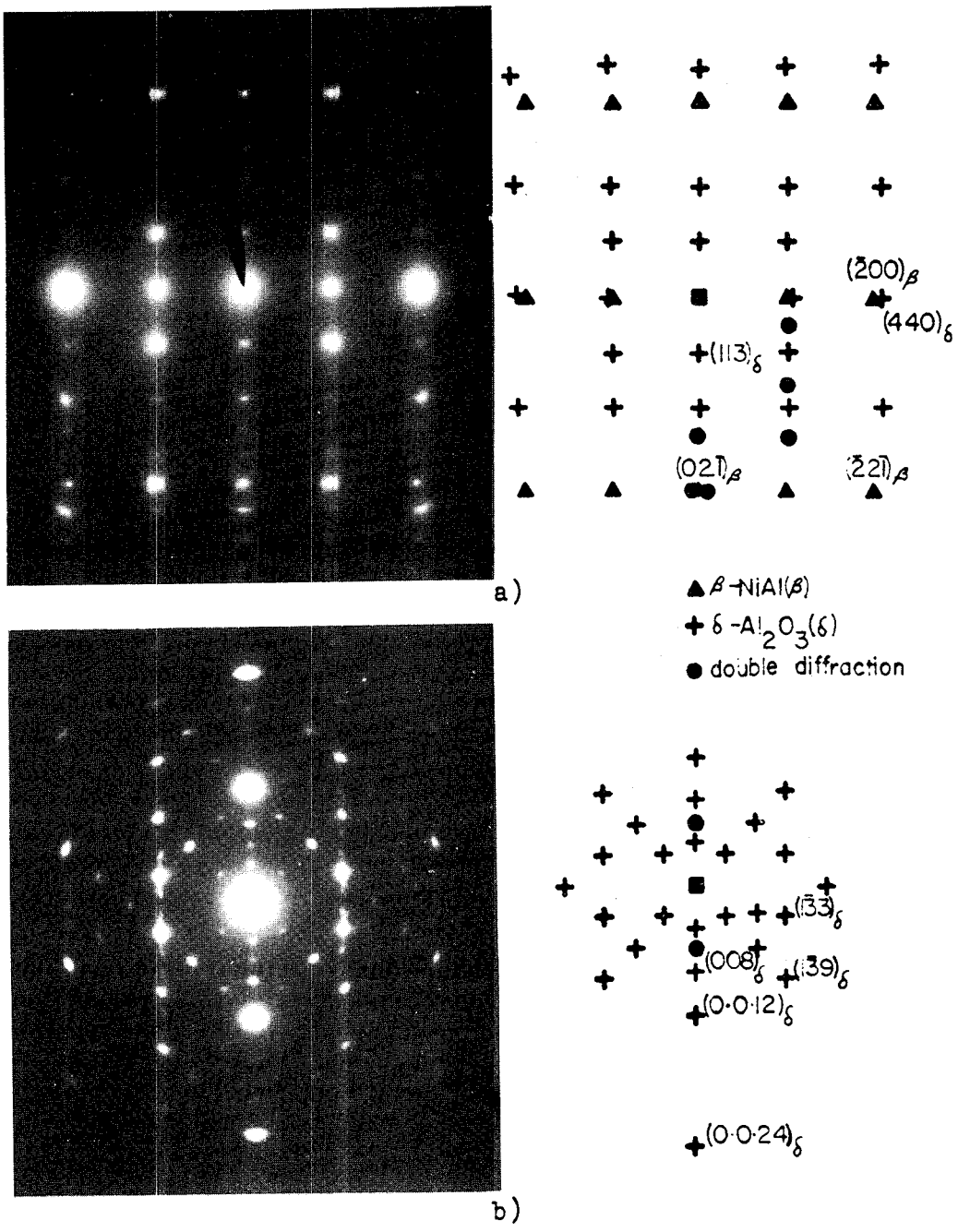

Figure 43

Diffraction patterns of an (012), 10.0 hour, 800°C specimen. a) Metal plus oxide SAD at 0° tilt shows the same orientation relationships as shorter oxidation times. b) [310] oxide zone shows δ-Al_2O_3 as the predominant oxide phase.

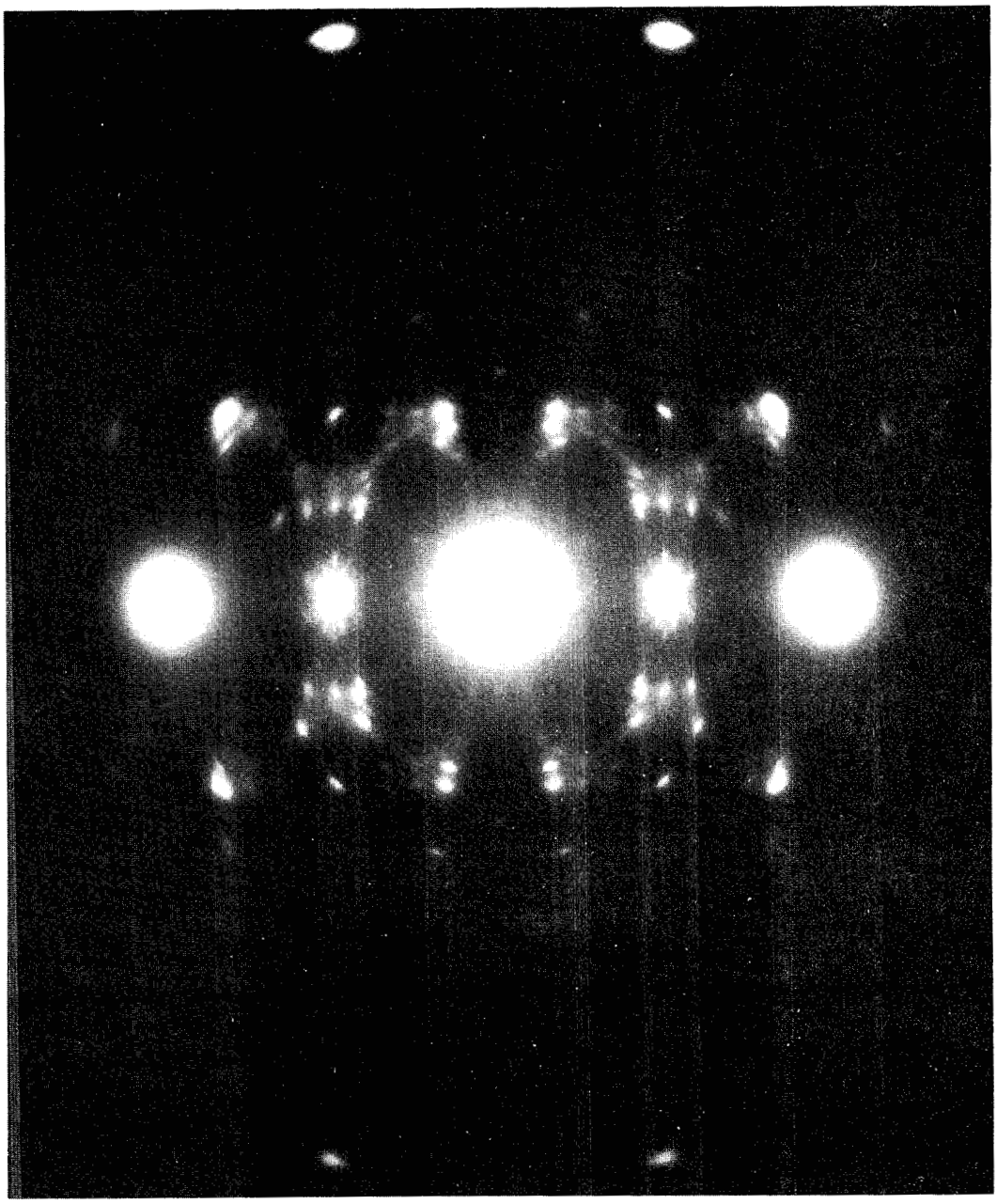

Figure 43c)

δ-Al_2O_3 zone on an (012), 10.0 hour, 800°C specimen. The zone corresponds most closely to a [113] cubic zone.

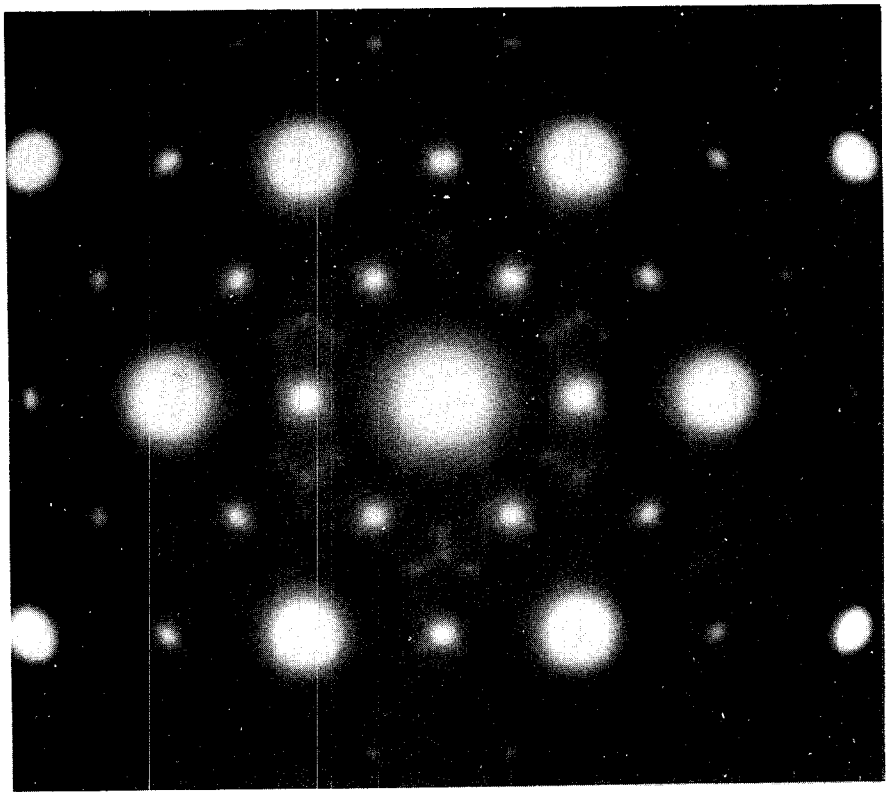

Figure 44

δ-Al_2O_3 zone from the same specimen as in Figure 43. The "wing" reflections from [111] oxide zones at shorter oxidation times are present as distinct reflections.

D) (011) Metal, Oxidized

1) 0.1 hours, 800°C

This condition for an (011) metal orientation produced three distinct metal-oxide orientation relationships. The oxide consisted only of $NiAl_2O_4$ according to electron diffraction with a Al/Ni ratio of 0.73. Figure 45a is an SAD of both a metal and oxide region to show the presence of both phases. The orientation relationship present in the diffraction pattern is given as;

$$(011)_m \quad || \quad (\bar{1}11)_{ox}$$

$$[100]_m \quad || \quad [110]_{ox}$$

and is known as the Nishyama-Wassermann (N-W) orientation relationship. The N-W orientation relationship is common to FCC-BCC systems.

Two extra {440} oxide reflections are also noticed lying nearly parallel with a metal $\langle 211 \rangle$ direction. The same region of the specimen was observed following a very brief ion-thinning procedure to "clean-up" the foil and is shown in Figure 45b with a diffraction pattern. The extra reflections found in the

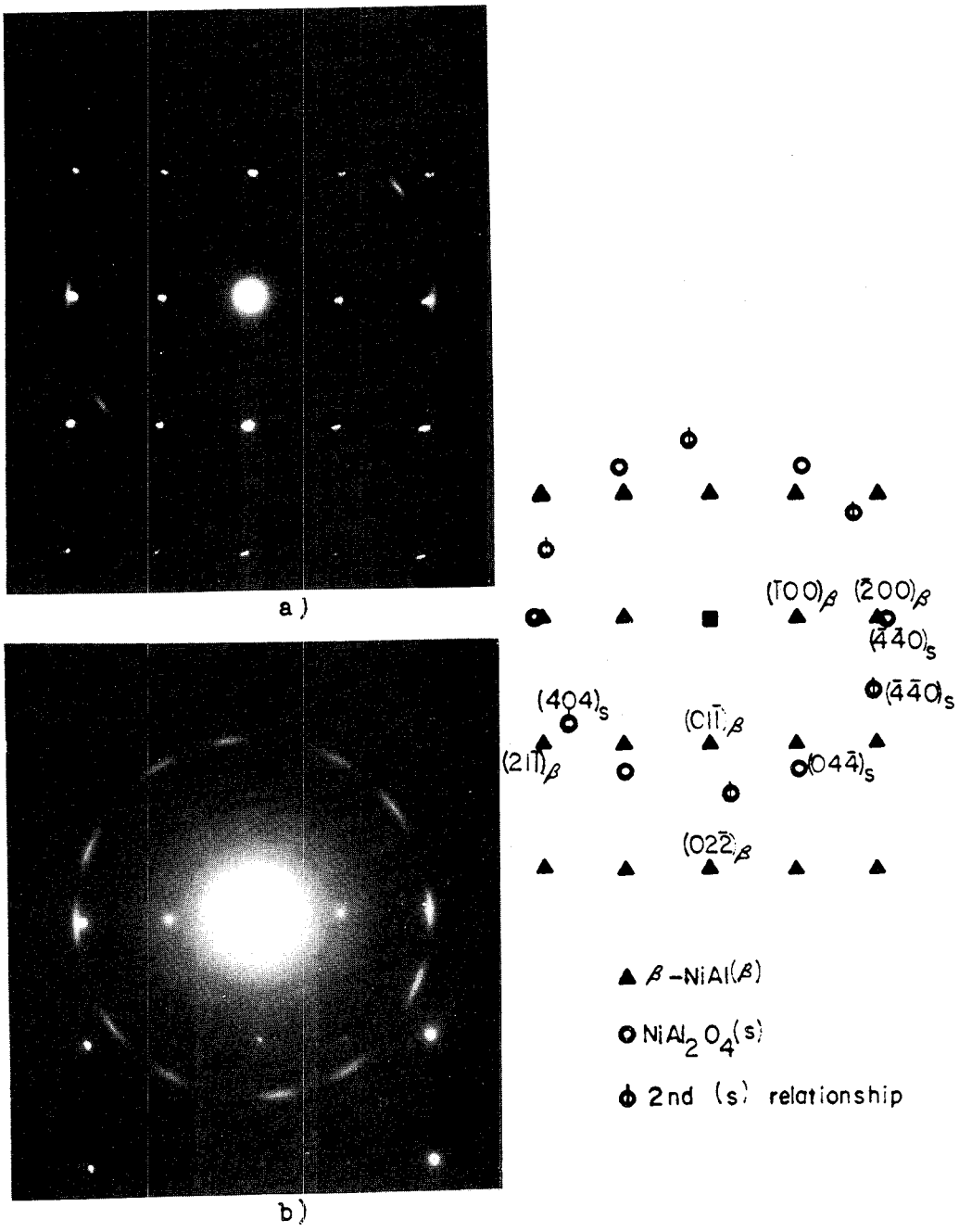

Figure 45

Selected area diffraction patterns of a metal plus oxide region on a (011), 0.1 hour, 800°C specimen. a) Extra reflections are from a secondary orientation of oxide. b) Same specimen as in a), after an ion thinning treatment from the oxide side. Two different orientation relationships are present. Zone axis: $[011]_\beta$, $[\bar{1}11]_s$.

previous figure are seen to belong to another complete oxide orientation. The same $(\bar{1}11)$ oxide plane lies parallel to the (011) metal plane as in the N-W orientation relationship, but a different set of directions in the metal and oxide are aligned parallel to each other resulting in a different orientation relationship given as:

$$(011)_m \quad || \quad (\bar{1}11)_{ox}$$

$$[21\bar{1}]_m \quad || \quad [01\bar{1}]_{ox}$$

This orientation relationship involves a rotation of the oxide by 24.7° in the plane of oxidation relative to the N-W relationship. Dark field images from each orientation relationship are shown in Figure 46. There seems to be no segregation or clustering of crystallites from one particular orientation relationship. Therefore, this effect appears to be random. A corresponding bright field image of this region in Figure 47 shows voids and possibly individual grains. The grain size is approximately 10-30 nm by these measurements.

A third orientation relationship is shown in Figure 48. This SAD was taken from a different region of the same specimen as in Figure 46 and 47. As in the previous orientation relationship, the same oxide plane lies parallel to the metal but is

Figure 46

Dark field images of oxide on an (011), 0.1 hour, 800°C specimen. The image in a) was obtained from a {440} oxide reflection of the N-W relationship while the image in b) was from the other orientation relationship.

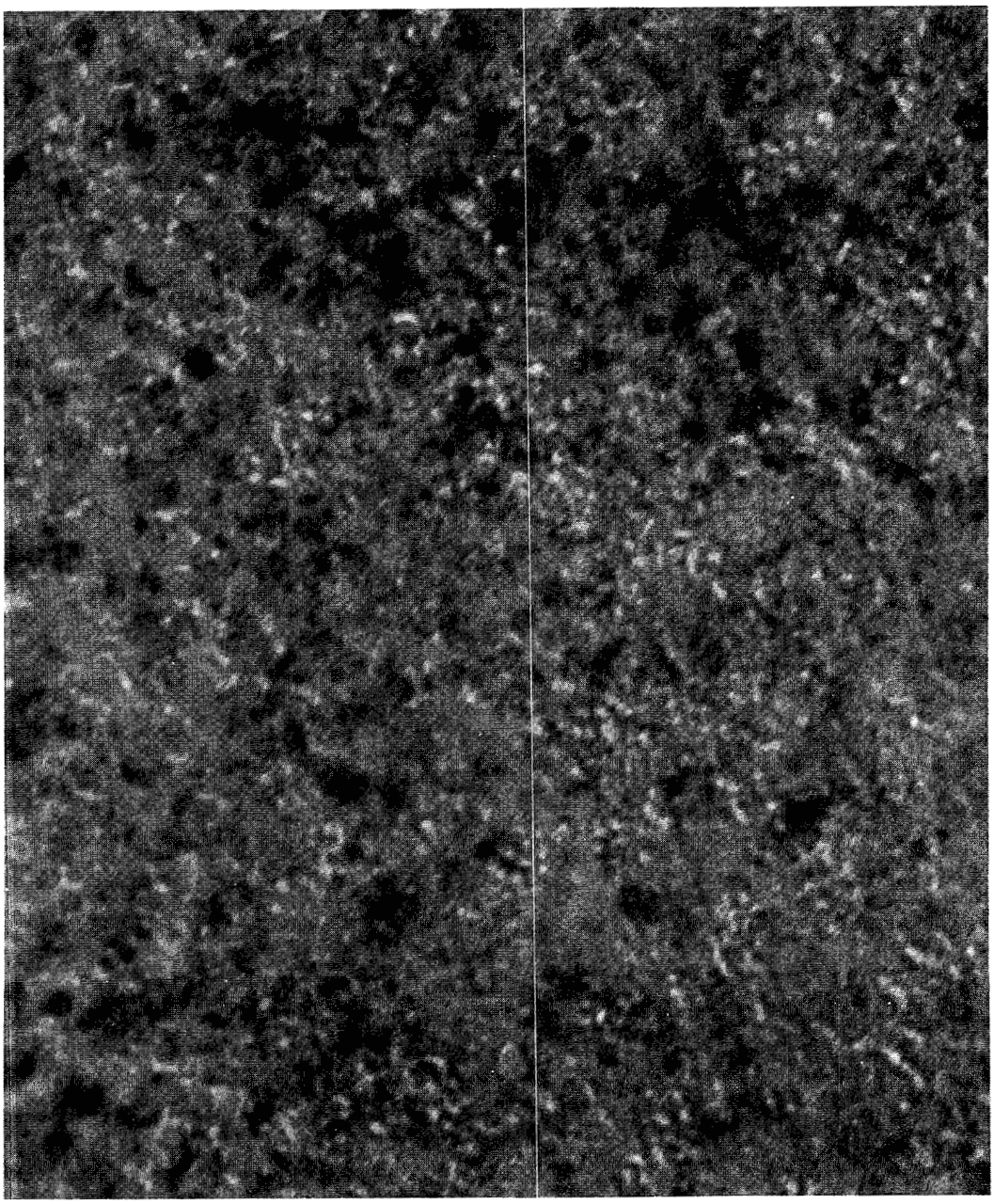

Figure 47

Bright field image of the same (011) specimen as in Figure 46 showing individual grains outlined by voids and some intragranular porosity.

Figure 48

Selected area diffraction pattern from a different region of the same (011) specimen. The primary orientation relationship is the Kurdjumov-Sachs relationship. Zone axis: $[011]_\beta$, $[\bar{1}11]_s$.

rotated relative to the N-W relationship. However, the oxide plane is only rotated by 5.3° resulting in the Kurdjumov-Sachs (K-S) orientation relationship given as:

$$(011)_m \quad || \quad (\bar{1}11)_{ox}$$

$$[11\bar{1}]_m \quad || \quad [01\bar{1}]_{ox}$$

The degree of oxide misorientation is large for this metal orientation as compared to other metal orientations. This effect is shown in the diffraction patterns of Figure 49 for a $\langle 111 \rangle$ and $\langle 110 \rangle$ $NiAl_2O_4$ zone axis respectively. The width of the oxide arcs approach 20° with an indication of a random orientation from the (440) ring in Figure 48a. Extra reflections are from higher order Laue zones as shown in Appendix B.

To study the possibility of clustering of one particular oxide orientation, $2\frac{1}{2}$D electron microscopy was used. This technique, described by Bell[47], is a dark-field imaging technique utilizing special properties of electron optics to obtain a mock stereo image. By altering the focus of a dark-field image, new image areas shift into the aperture positions, the directions of shifting being parallel with the diffraction vectors. The shifts create an artificial parallax which make images at two

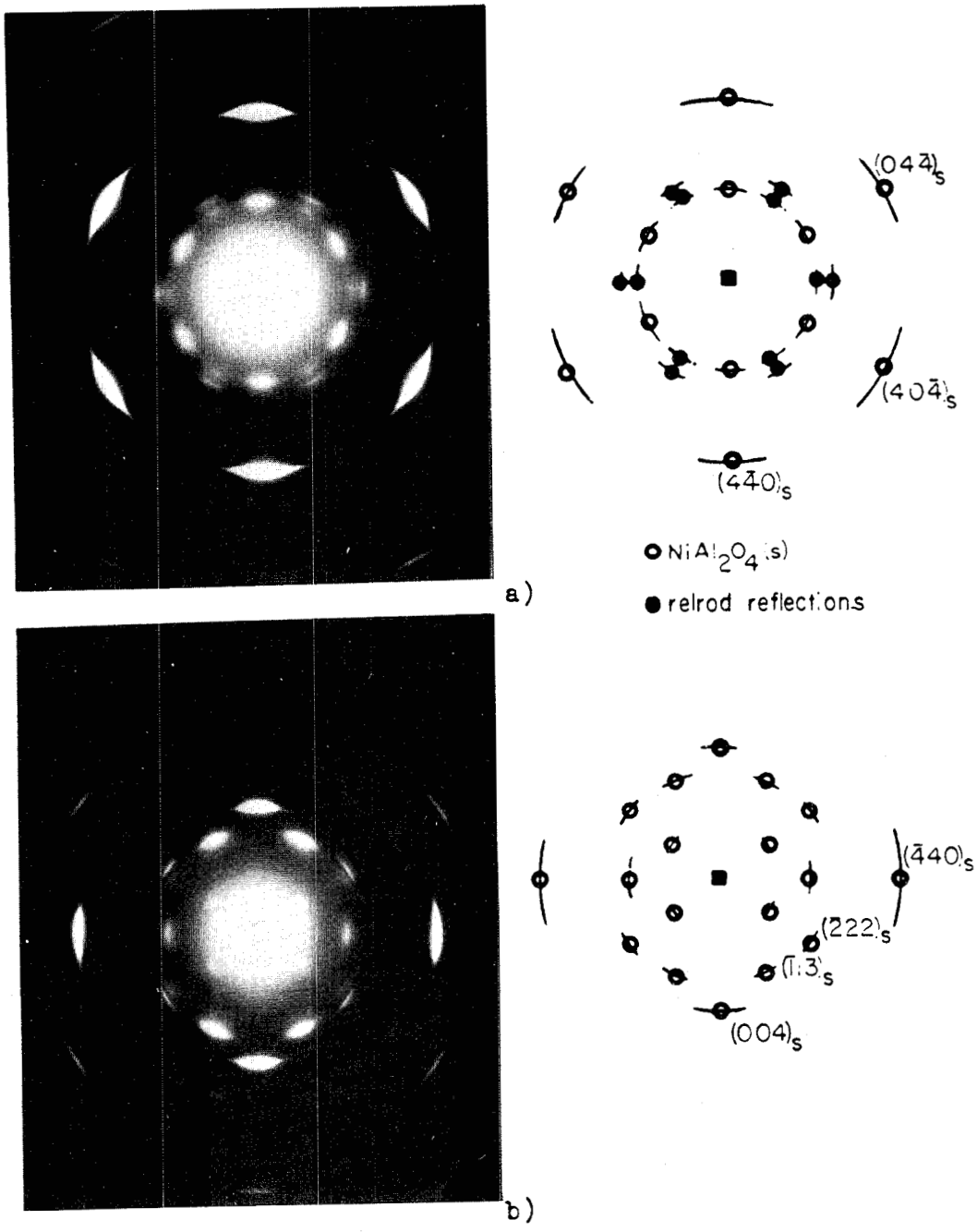

Figure 49

Diffraction patterns of oxide zone axes from an (011), 0.1 hour, 800°C specimen. The oxide is primarily $NiAl_2O_4$; a) a [111] zone and b) a [110] zone. The orientations of oxide crystallites are quite random as observed by the width of the arcs.

different focusing conditions suitable for stereo imaging. The actual depths observed do not correspond to any spatial difference but can be related to different positions in the objective aperture. Regions with different orientations will appear to be at different levels in the stereo image as shown in Figure 50. A 2½D pair is shown in Figure 51. When viewed through a stereoscope, adjacent oxide grains appear to be on different levels corresponding to different orientations. This indicates that there is no major tendency to form regions of oxide crystallites having the same orientation.

2) 1.0 hours, 800°C

The Al/Ni ratio for this condition has increased to 5.11 from 0.73 in the 0.1 hour condition, indicating an increased formation of Al_2O_3. The electron diffraction patterns of Figure 52 indicate that only one orientation relationship now exists which relates Al_2O_3 to the metal. Both γ-Al_2O_3 and δ-Al_2O_3 are evident, δ-Al_2O_3 being indicated by the extra spots in the (111) zone of Figure 52, but mainly from the 1/3 {400} reflections in Figure 52b. The orientation relationship is given as;

$$(011)_m \;||\; (\bar{1}11)_{ox}$$
$$[100]_m \;||\; [110]_{ox}$$

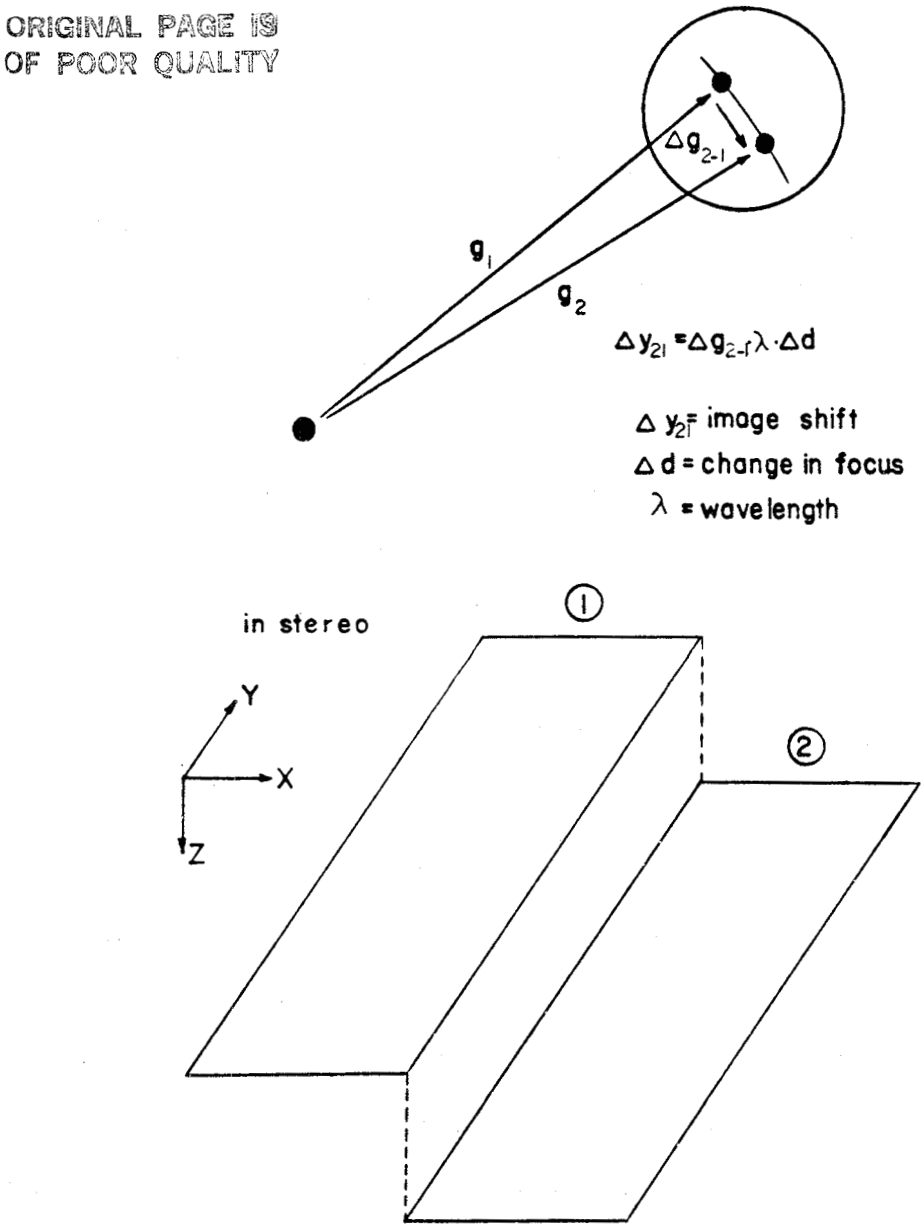

Figure 50

Schematic of the 2½D imaging technique. (Ref. 47)

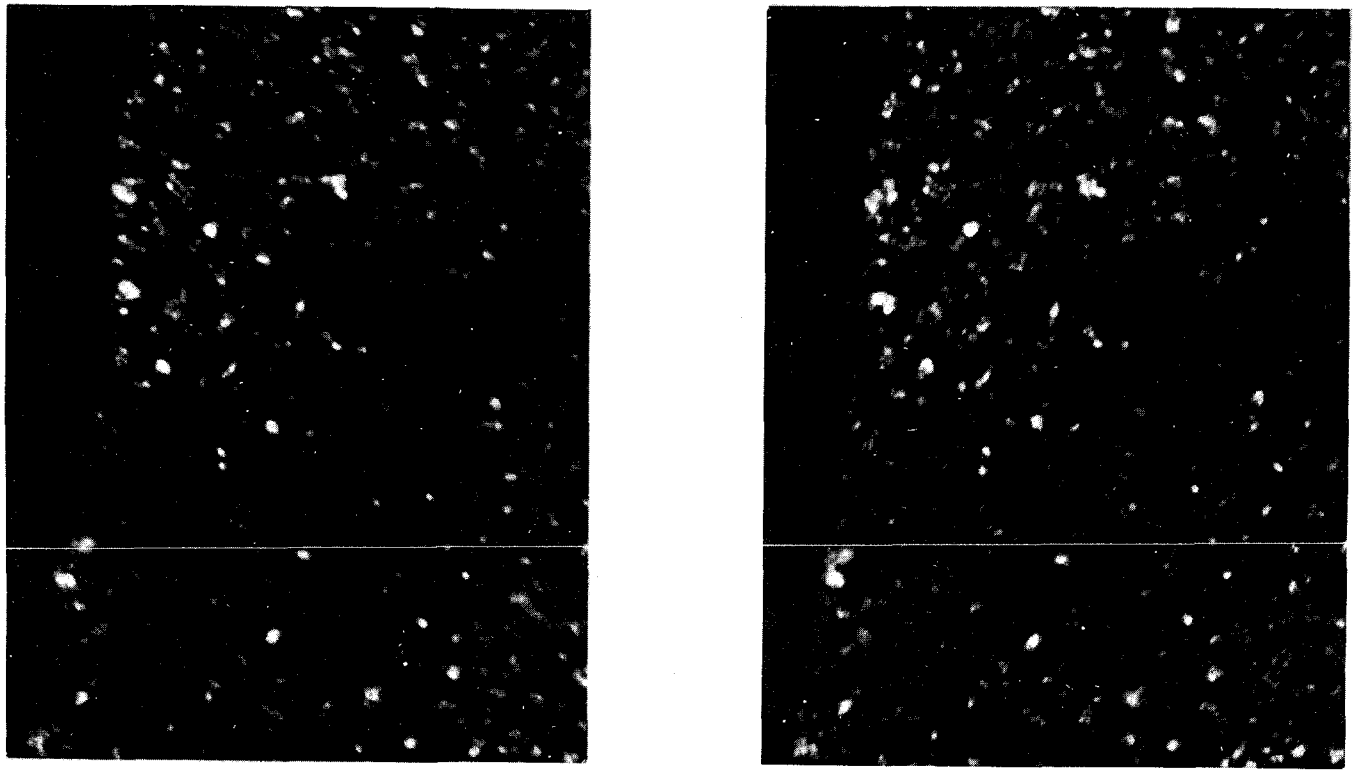

Figure 51

$2\frac{1}{2}$D dark field pair of oxide on an (011), 0.1 hour, 800°C specimen. When observed with a stereoscope, crystallites are seen not to be clustered in layers but rather are randomly distributed through the thickness.

which is the Nishyama-Wassermann orientation relationship. The difficulties in describing the structure of δ-Al_2O_3 prevent exact determination of an orientation relationship of this oxide phase to the metal, at the present time.

3) 10.0 hours, 800°C

The same N-W orientation relationship exists for the 10.0 hour oxide but only γ-Al_2O_3 is evident as shown in the diffraction patterns in Figure 53 for two different exposure times. δ-Al_2O_3 has either transformed to γ-Al_2O_3 or has become a minor oxide phase. The Al/Ni ratio for this condition has increased to 19.42.

A bright field image of the oxide is shown in Figure 54. The major features in this image are the dark precipitates lying primarily along $\langle 110 \rangle$ directions in the oxide. Similar Widmanstatten precipitates have been found by Smialek in oriented γ-Al_2O_3 scales formed on a doped NiCrAl alloy.[22] These $\{ 111 \}$, $\langle 110 \rangle$ precipitate blades are attributed to a transition phase between the spinel to corundum Al_2O_3 phases.

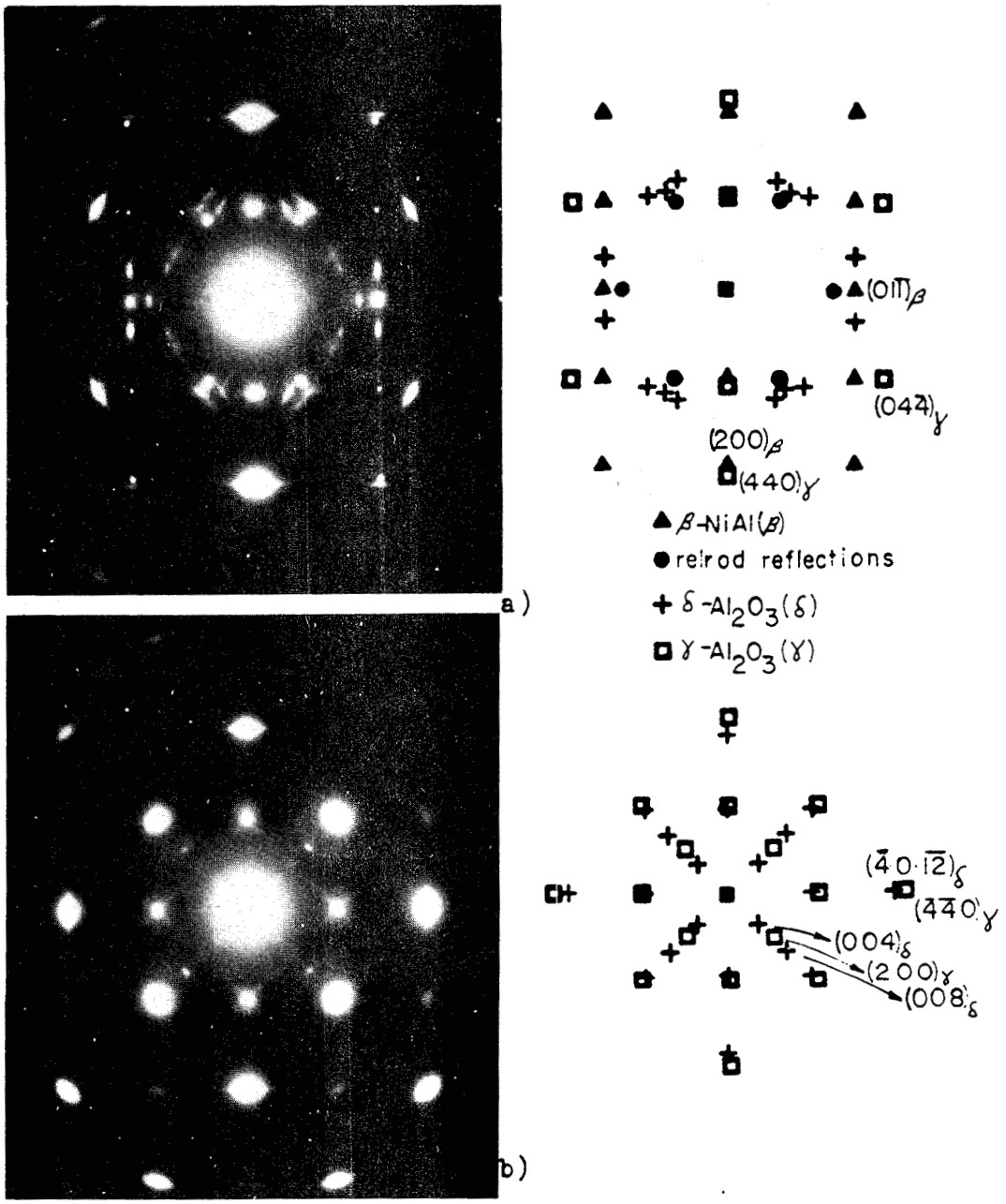

Figure 52

Selected area diffraction patterns from an (011) specimen oxidized at 800°C for 1.0 hours. a) [011] metal zone plus [111] oxide zone. Both γ-Al_2O_3 and δ-Al_2O_3 are evident; δ-Al_2O_3 by the "wing" reflections. b) [100] oxide zone showing γ-Al_2O_3 and δ-Al_2O_3 having the same orientation. Because the exact orientation of δ-Al_2O_3 in a) is unknown, indices were not assigned to the δ-Al_2O_3 reflections.

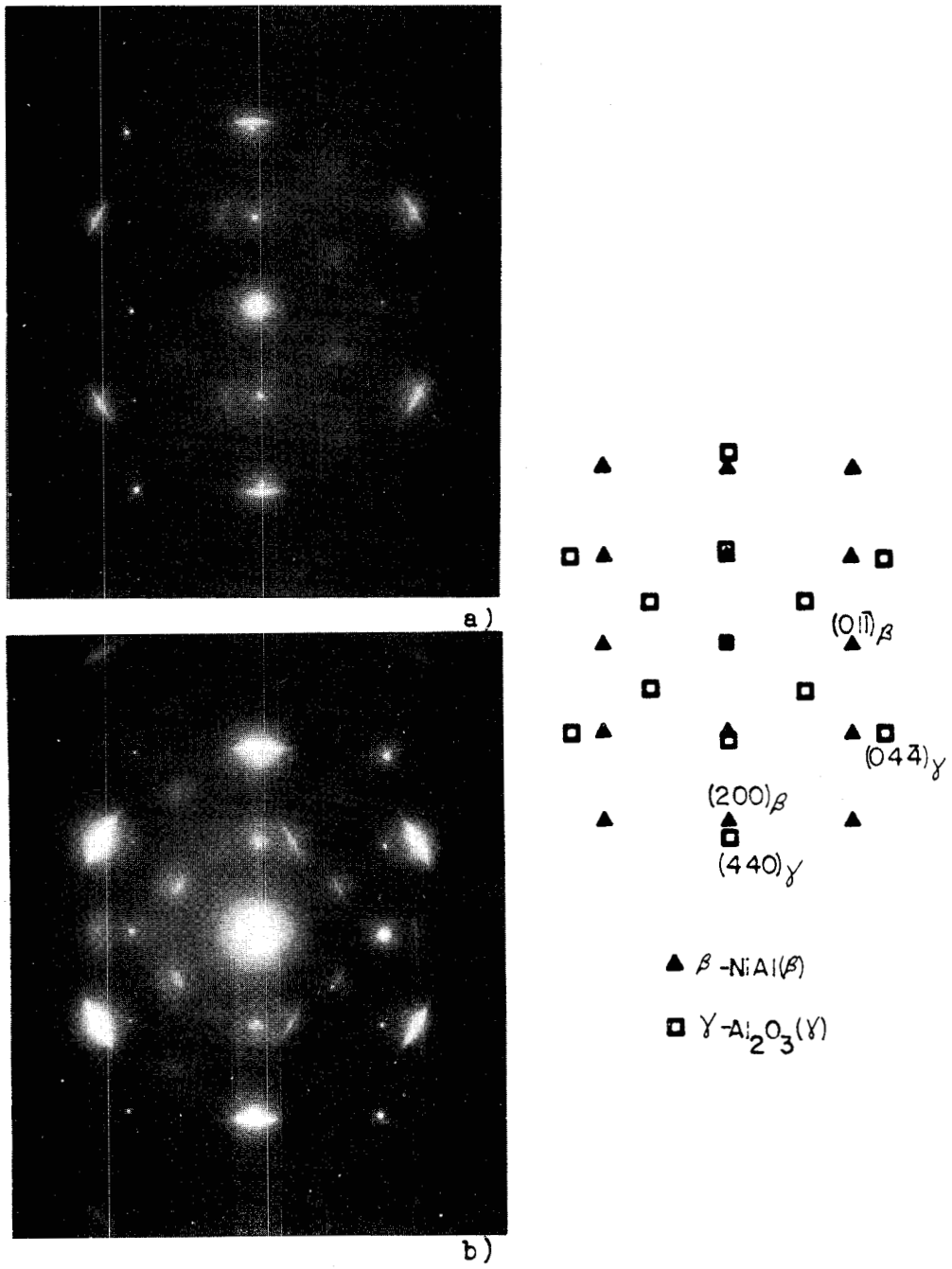

Figure 53

Selected area diffraction patterns of a metal plus oxide region from an (011), 10.0 hour, 800°C specimen. Two different exposure times indicate that the oxide layer consists of only γ-Al_2O_3 having the Nishyama-Wassermann relationship with the metal. Zone axis: $[011]_\beta$, $[\bar{1}11]_\gamma$.

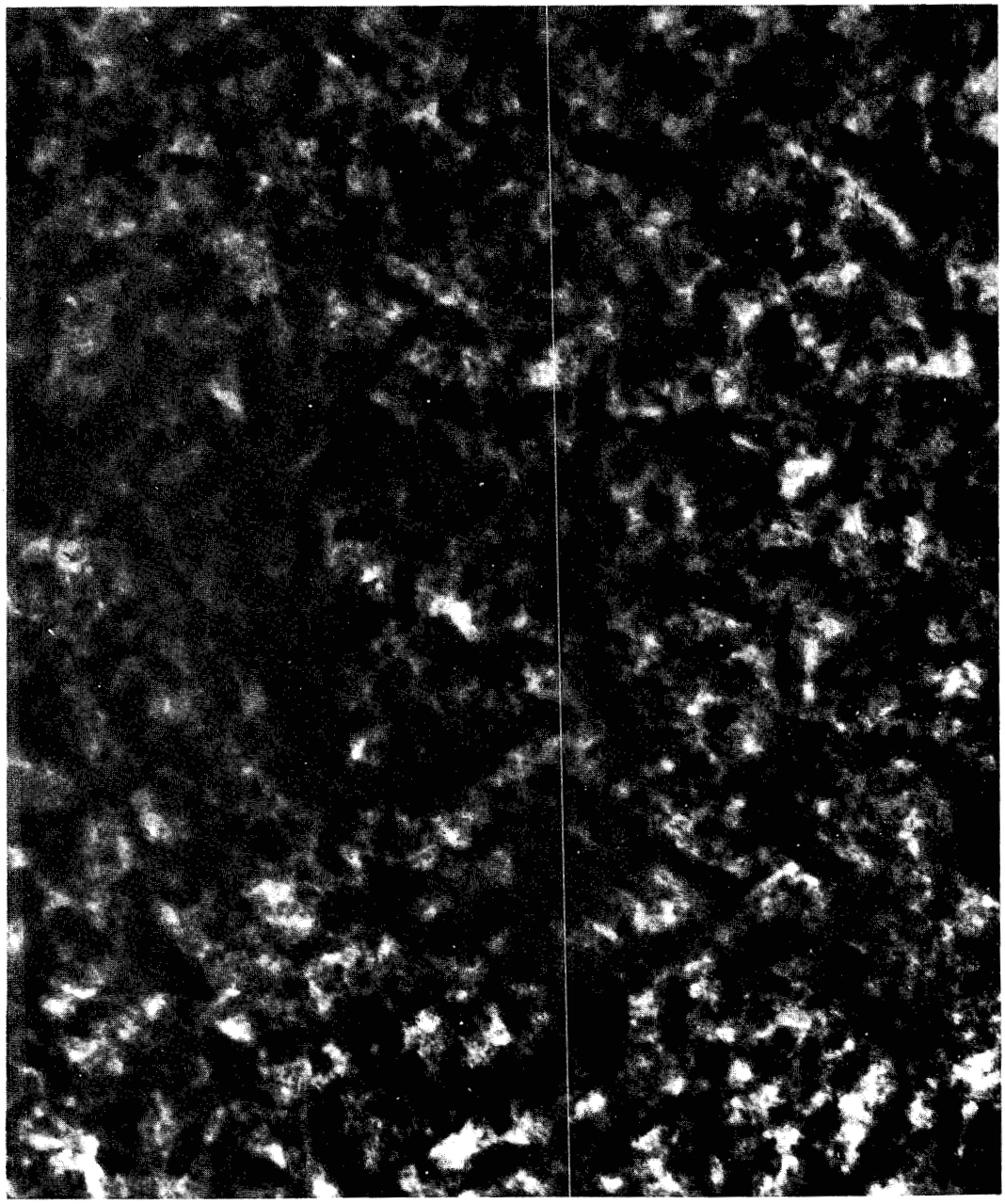

Figure 54

Bright field image of oriented γ-Al_2O_3 on an (011) metal specimen oxidized for 10.0 hours at 800°C. The Widmanstatten precipitates lie along ⟨110⟩ directions.

E) (111) Metal, Oxidized

1) 0.1 hours, 800°C

A selected area diffraction pattern of oxide is shown in Figure 55a. This SAD was taken at 0° tilt. A nearly symmetric arrangement of {400} oxide reflections is observed. Figure 55b shows both metal and oxide are slightly tilted from 0°. The array of oxide reflections with relationship to the metal is clearly shown. The oxide was indexed to be $NiAl_2O_4$ and had an Al/Ni ratio equal to 0.72, similar to the oxide for the same oxidizing conditions on (011) metal.

The metal-oxide orientation relationships for this metal orientation were not obtainable from specimens oxidized under these conditions due to limited thin area and difficulties in being able to tilt to required zone axes. However, a similar 0° tilt metal and oxide pattern was obtained for the 1.0 hour, (111) metal for which the orientation relationship was determinable. The relationship is simply stated now but will be explained in more detail under the 1.0 hour, (111) heading. The orientation relationship was found to be;

$$(111)_m \quad || \quad \text{near } (021)_{ox}$$
$$[1\bar{1}0]_m \quad || \quad [100]_{ox}$$

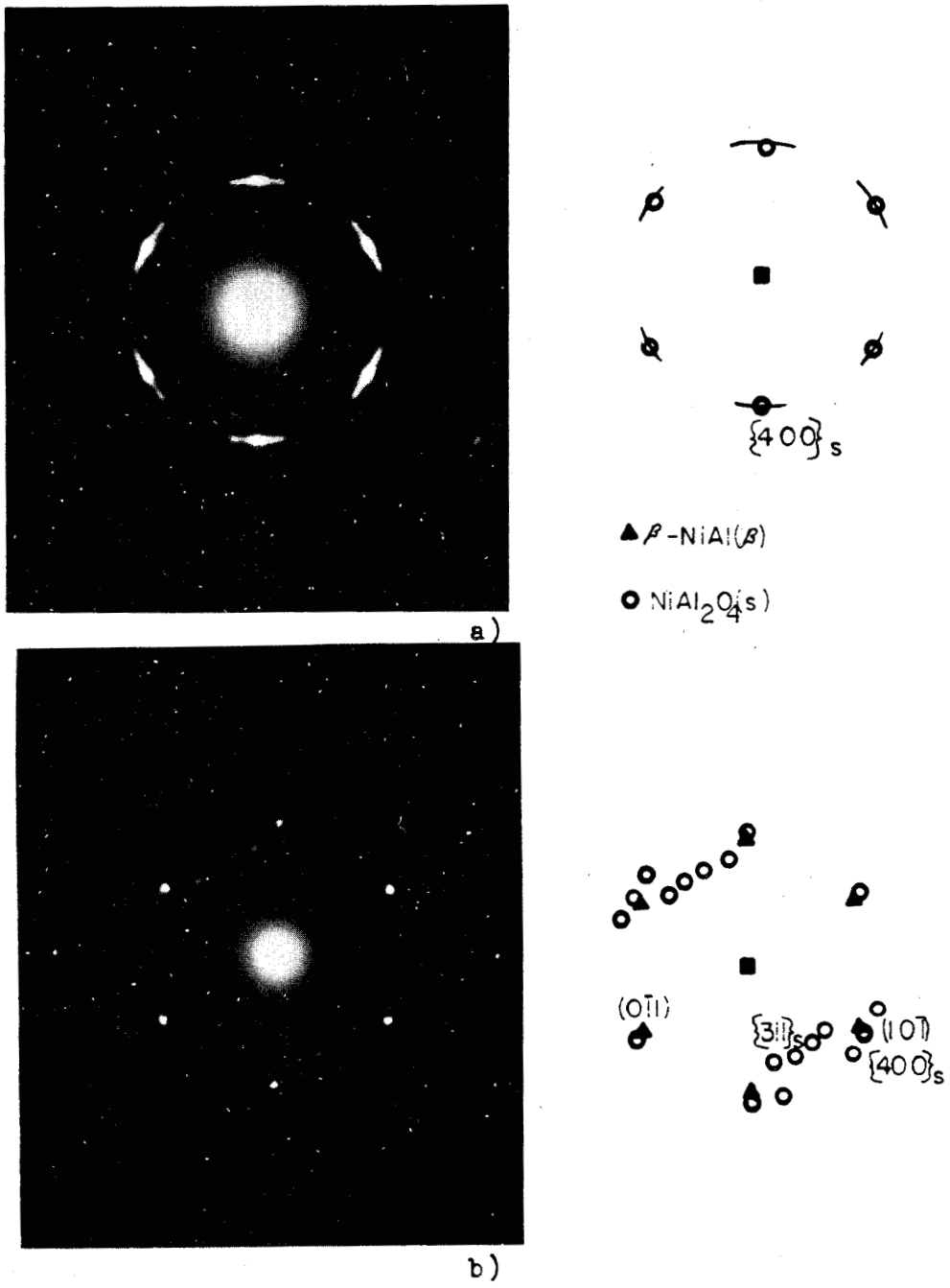

Figure 55

Selected area diffraction patterns from a (111), 0.1 hour, 800°C specimen; a) oxide at 0° tilt and b) oxide plus metal tilted slightly from 0°.

having three variants, 120° apart.

A justification for three variants being involved in this orientation relationship is shown in the high resolution dark field image of Figure 56 of Moire fringes on the 0.1 hr. specimen. The spacings and angles correspond well with the corresponding diffraction pattern for metal and $NiAl_2O_4$. Circled regions in the image show directions of Moire fringes lying at 120° from each other. This is a result of oxide crystallites from different variants of the orientation relationship lying next to each other. There does not appear to be any preference for crystallites from any one variant of the orientation relationship to be clustered.

2) 1.0 hours, 800°C

The orientation relationship for this condition mentioned earlier, is again given as;

$$(111)_{metal} \;||\; \text{near } (021)_{oxide}$$
$$[1\bar{1}0]_{metal} \;||\; [100]_{oxide}$$

having three variants, 120° apart. This orientation relationship was determined primarily by tilting the specimen to each of the three symmetric $\langle 112 \rangle$ metal zones, each being 19.5° away

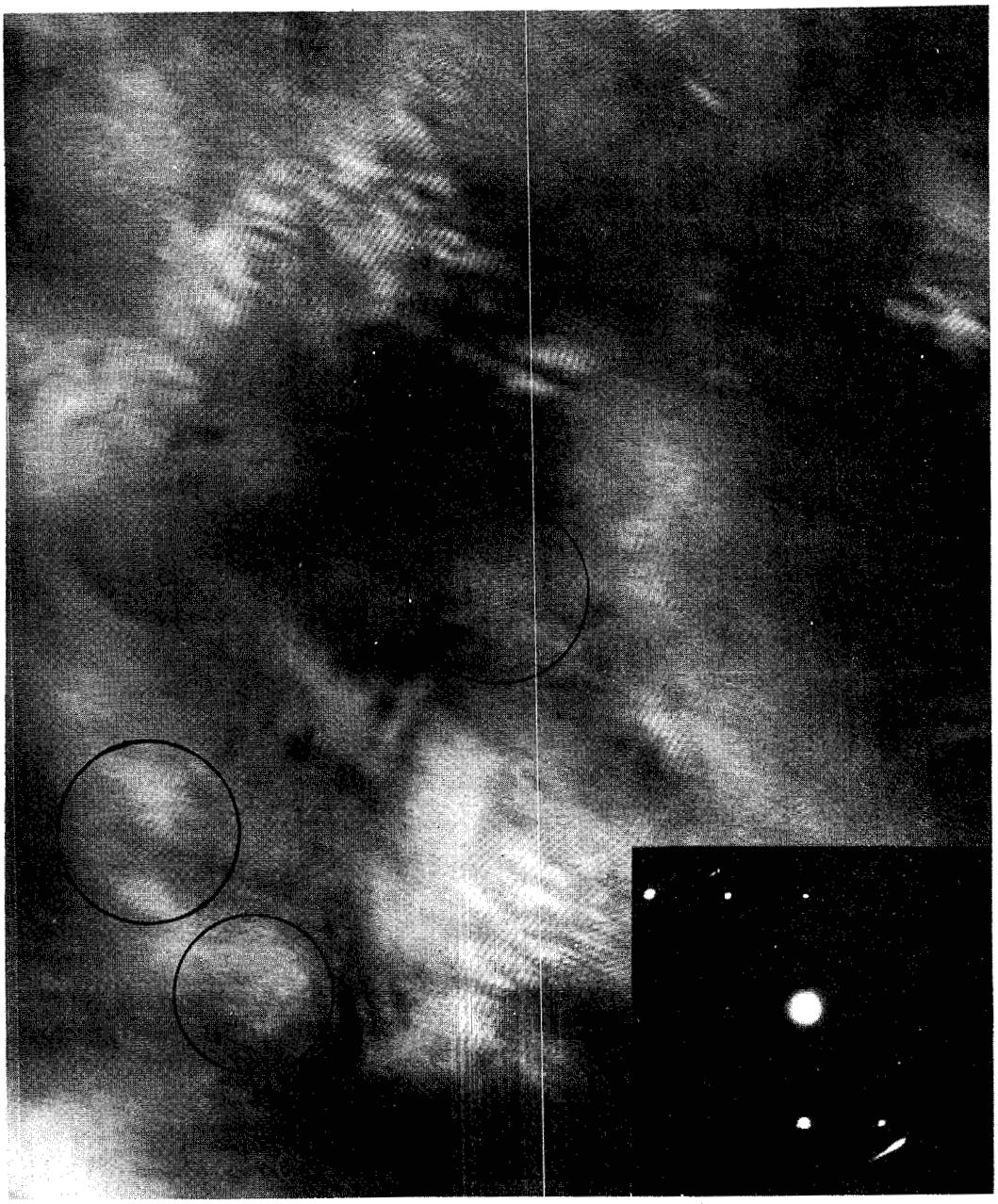

Figure 56

High resolution dark field image of Moire fringes on a (111), 0.1 hour, 800°C specimen. Three variants of the orientation relationship result in fringe directions 120° from each other (circled regions).

from the [111] zone axis and 61.9° away from each other. At each ⟨112⟩ metal zone a similar diffraction pattern was obtained, shown in Figure 57. Included in each pattern is an ⟨011⟩ oxide zone axis and extra reflections from two other variants. The reflections for each diffraction pattern were plotted on a stereographic projection. Most of the reflections corresponded to one of the three ⟨011⟩ variants. Threefold symmetry was established as well as the particular oxide orientations. When plotted on a [111] stereographic projection representing the metal orientation, the three oxide variants are easily distinguished as shown in Figure 58. Figure 59 is shown to portray the similarities between the 0° tilt diffraction patterns for a 0.1 hour and 1.0 hour specimen.

According to the diffraction pattern in Figure 60 of a region of oxide from a different specimen oxidized under the same conditions, the oxide is randomly oriented. X-ray analysis of this oxide showed impurity levels of Cr and Zr with a relatively higher concentration of Ni than the oriented scale. Double rings at the {400} and {440} positions help to identify the phases as $NiCr_2O_4$ and possibly γ-Al_2O_3 or $NiAl_2O_4$.

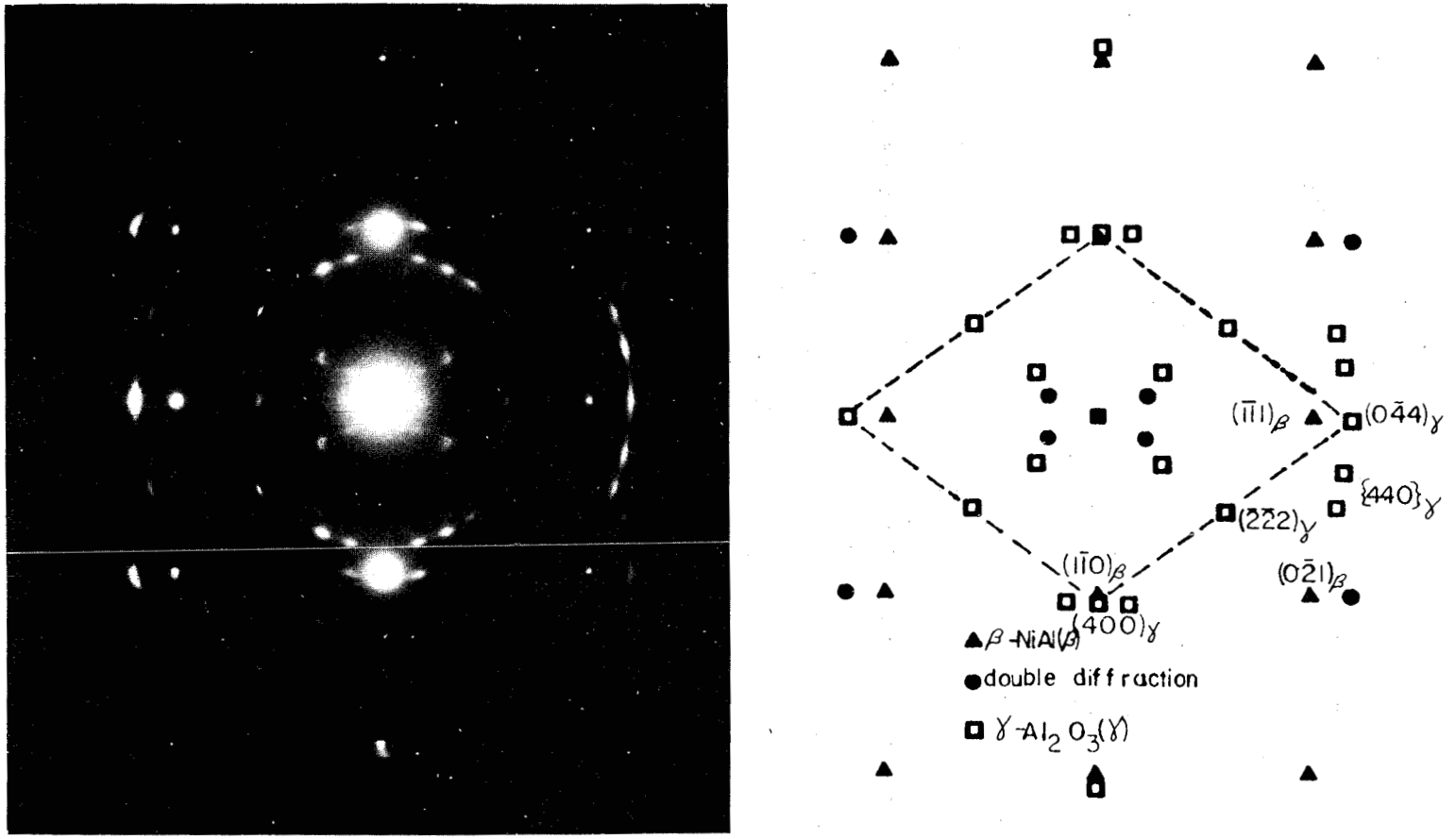

Figure 57

Selected area diffraction pattern from a (111), 1.0 hour, 800°C specimen tilted to a ⟨112⟩ metal zone axis. The oxide orientation is the same at each of the three ⟨112⟩ metal zones and includes a ⟨110⟩ oxide zone plus reflections from the two other orientation variants.

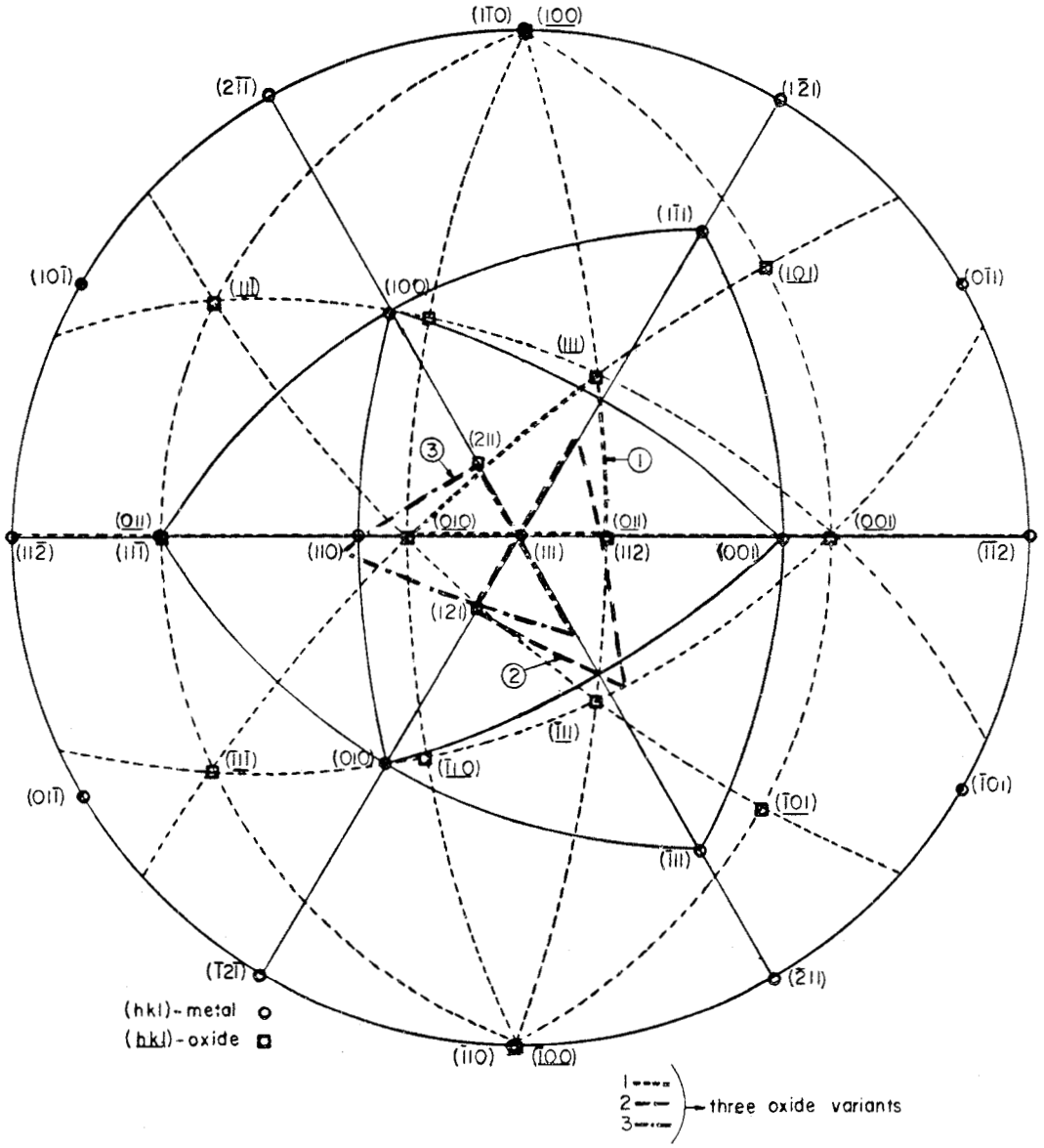

Figure 58

Stereographic projection of the orientation relationship on (111) metal. Three variants, 120° apart, account for the threefold symmetry of the metal (111) surface.

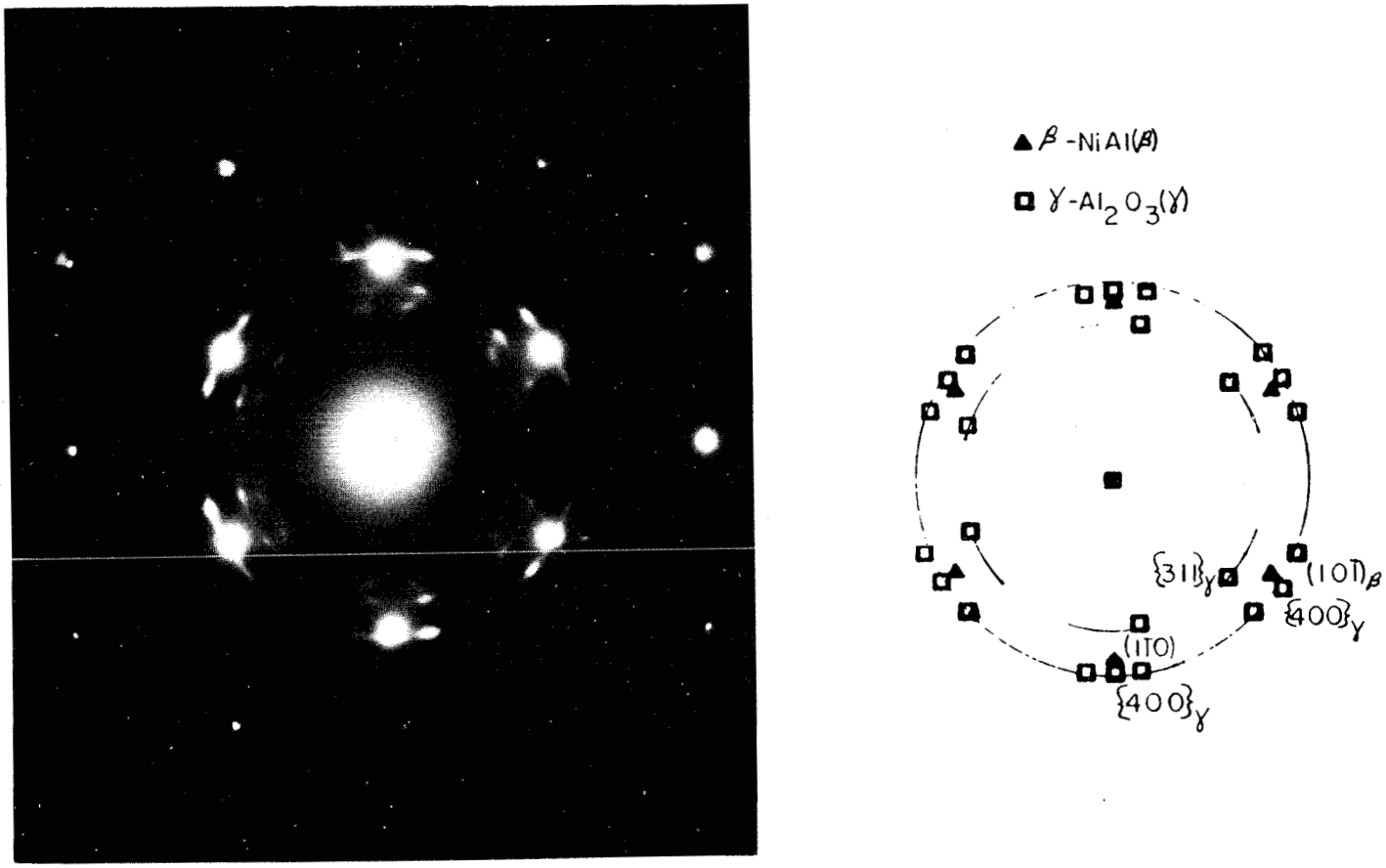

Figure 59

Selected area diffraction pattern of a metal plus oxide region near 0^{o} tilt on the same specimen as in Figure 57. The orientation relationship is the same as the (111), 0.1 hour, 800^{o}C condition.

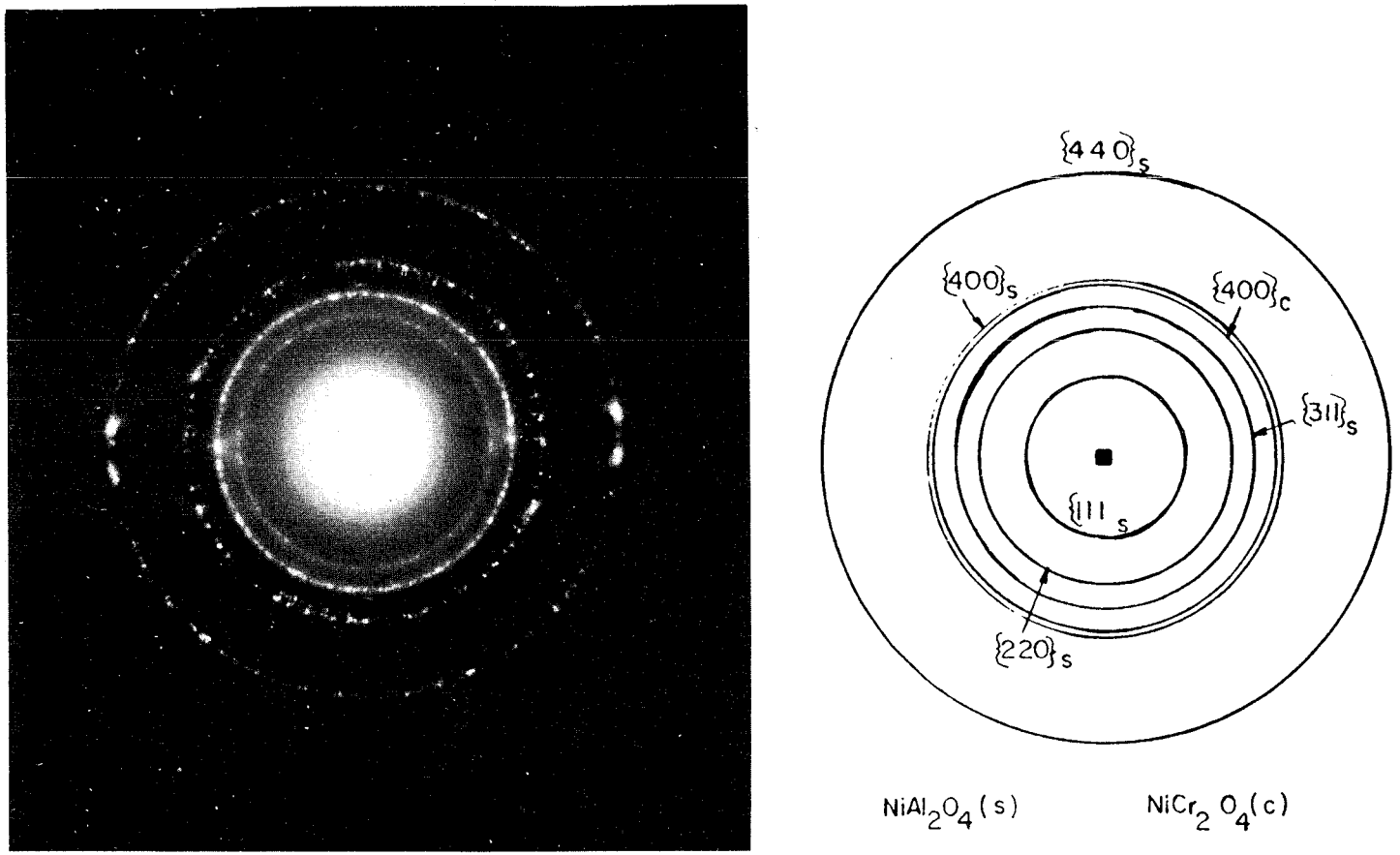

Figure 60

Diffraction pattern of randomly oriented oxide from a region on a (111), 1.0 hour, 800°C specimen where the impurity level was high. One of the components is indexed to be $NiCr_2O_4$.

3) 10.0 hours, 800°C

The increased thickness of the oxide layer for these specimens prevented detailed analysis. However, Figure 61 indicates the same orientation relationship as found for shorter oxidizing times on (111) metal. γ-Al_2O_3 is the only oxide phase. The corresponding Al/Ni ratio for this oxide was 20.86.

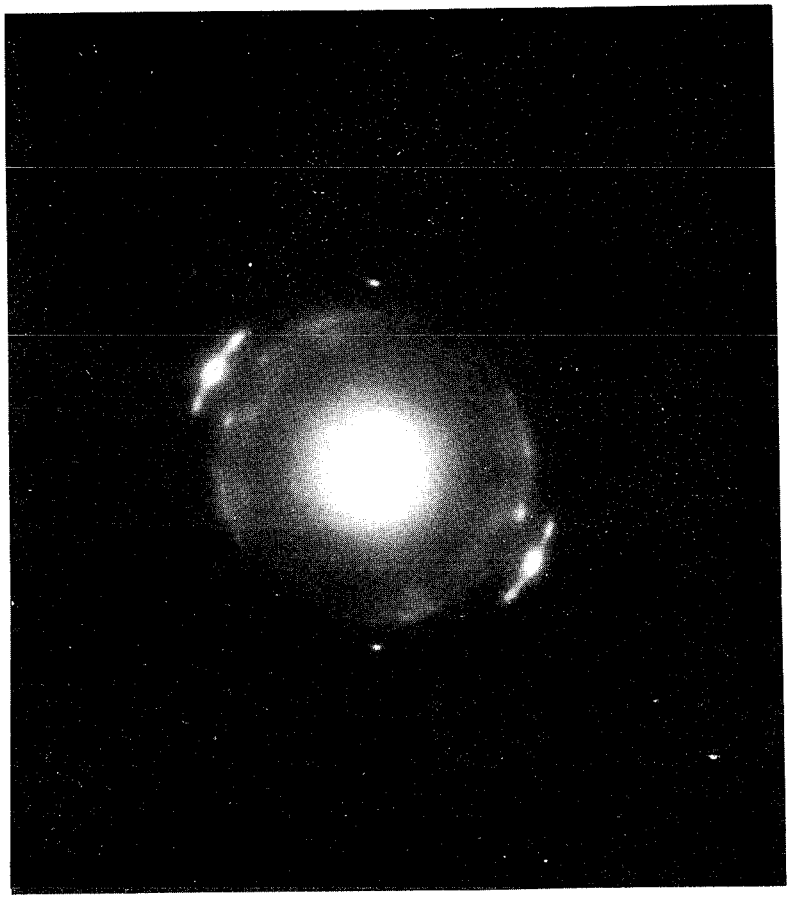

Figure 61

Selected area diffraction pattern from a (111), 10.0 hour, 800°C specimen. The same orientation relationship exists as in the shorter oxidation times.

IV. DISCUSSION

The emphasis of this work has been on the determination of oxide phases that grow on β-NiAl + Zr and the orientation relationships that exist between the oxide and the metal substrate. Therefore, one section of the discussion will be devoted to each of these two topics. A third section will relate this material to implications on nucleation and development of α-Al_2O_3 scales on β-NiAl alloys.

A) Transient Oxide Phases on Oriented β-NiAl + Zr

1) Crystal structure and identification of oxide phases

Many results of this study are based upon characteristics and changes in the crystal structures of the oxide phases that form. Therefore, the following discussion is developed so that comparisons between the oxide phases can be made.

Three oxide phases formed on β-NiAl + Zr at 800°C for oxidation times up to 10.0 hours. These oxides are $NiAl_2O_4$, γ-Al_2O_3 and δ-Al_2O_3. The structures of all three oxides are based on the spinel structure described by Bragg.[48] The chemical formula is based on an AB_2O_4 designation with A and B

representing divalent and trivalent cations respectively. The spinel structure contains a face-centered cubic array of oxygen anions of which there are 32 per unit cell. Eight A cations occupy one-eighth of the tetrahedral sites in a unit cell while one-half of the octahedral positions are filled with sixteen B cations.

The structure just described is termed a "normal" spinel and is the structure of aluminate and chromate spinels. Most ferrites have a "inverse" spinel structure in which the A cations and half the B cations are on the octahedral sites and the remaining B cations occupy the tetrahedral sites. No spinel phase is strictly normal or inverse, and the degree of randomness of the cation distribution increases with temperature, changing site preference energies for particular distributions of cations.[49]

Nickel-aluminate spinel, $NiAl_2O_4$, is a normal spinel[50], with a lattice parameter of 8.048 Å.[41] Measured values of a_o for $NiAl_2O_4$ agree well with this value. Its structure is shown in Figure 62. There is some disagreement as to the space group of spinel. Fd3m was the generally accepted space group but Grimes suggested that the space group is $F\bar{4}3m$, one of lower symmetry.[51] Hwang et al, and later Heuer and Mitchell[42] agreed that the space group of spinel is probably $F\bar{4}3m$ because of the

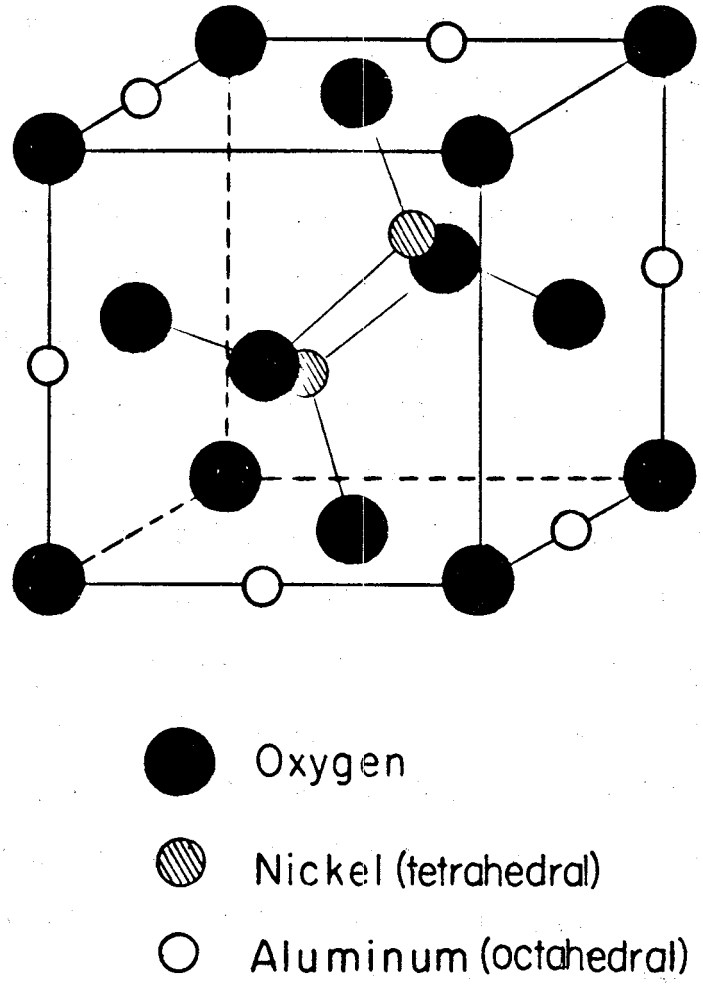

Figure 62

Structure of $NiAl_2O_4$, a normal spinel.

presence of {200} reflections in an [001] $MgAl_2O_4$ zone. However, Smith suggested the possibility of double diffraction in the first order Laue zone causes {200} relrod reflections to occur in the zeroth order Laue zone.[43]

In the present study, weak {200} oxide reflections were observed in [001] oxide zones only, when $NiAl_2O_4$ was present as a major oxide phase. For an (001) and (012) metal oxidation plane, the {200} reflections disappear after 0.1 hours oxidation time but persist through 1.0 hour on (011) oriented metal. The persistence of {200} oxide reflections for 1.0 hours, (011) specimens could indicate that the same reflections occur from γ-Al_2O_3, another spinel phase. However, γ-Al_2O_3 has been described to have the space group Fd3m for for which the {200} reflections are forbidden. No definite conclusions can be drawn on the possibility of a difference in space groups between $NiAl_2O_4$ and γ-Al_2O_3 because γ-Al_2O_3 was not present by itself on any of the specimens.

γ-Al_2O_3 belongs to a group of materials known as the transition aluminas.[27] There are at least seven different phases, all having the formula Al_2O_3, which form metastably as natural and synthetic forms of anhydrous aluminum oxide are heated. Near 1000°C, α-Al_2O_3 forms, which is the stable phase, and the

transformation sequence ends. The transformation sequence involves continuous ordering of cations in a cubic anion arrangement until further heating causes a rearrangement of the anion sublattice to an approximate hexagonal array of the rhombohedral α-Al_2O_3 structure.

Thermal oxidation of alumina forming alloys also involves the transformation of metastable phases to α-Al_2O_3. However, only γ-Al_2O_3 and δ-Al_2O_3 have been found prior to α-Al_2O_3 formation. The structure of γ-Al_2O_3 is a defect spinel structure as described by Verwey.[28,53] In one phase, designated γ'-Al_2O_3 by Verwey, aluminum cations occupy, on the average, 21 1/3 of all available cation positions, the oxygen ions being arranged in a face-centered cubic lattice. The cations are randomly distributed over all the octahedral and tetrahedral positions. In γ-Al_2O_3, the cations are in a more ordered arrangement resembling the spinel structure, but an average of 2 2/3 of the octahedral positions are vacant per unit cell.

The published value for the lattice constant of γ-Al_2O_3 is 7.908 Å.[41] The measured values for the lattice constant of γ-Al_2O_3 found on (011) and (111) metal specimens of 7.906 ± .002 Å agrees with this value.

Most of the literature refers to δ-Al_2O_3 as being tetragonal with a c/a ratio approximately equal to three. The tetragonal superstructure was first discovered by Braun when determining the structure of $LiFe_5O_8$, a spinel phase.[54] Van Oosterhout and Rooiymons defined the structure from a similar superstructure found in gamma-ferric oxide.[55] The space group of this new structure was $P4_1$, a derivative of the spinel space group.

The similarities between maghemite (γ-Fe_2O_3) and γ-Al_2O_3 were discussed by Smith.[56] The same superstructures exist between the gamma forms of iron and aluminum oxide during the transformation to the stable alpha phases, α-Fe_2O_3 being isotructural with α-Al_2O_3.

There is some ambiguity in the exact values for the lattice constants of δ-Al_2O_3. Rooymans reported the values:[57]

$$a_o = 7.96 \text{ Å}, \quad c_o = 23.40 \text{ Å}$$

The c/a ratio in this case would be 2.94. Tertian and Papée calculated the values to be:[58]

$$a_o = 7.943 \text{ Å}, \quad c_o = 23.50 \text{ Å}$$

and the c/a ratio is 2.959. When possible, the lattice constants and/or the c/a ratios were determined for δ-Al_2O_3 found in this study. Figure 63 presents portions of diffraction patterns enlarged to show all phases present with reference to a β-NiAl reflection. The diffraction patterns are taken from (012) metal specimens oxidized for 1.0 hour and 10.0 hours respectively. For the 1.0 hour oxide, three distinct oxide reflections occur near the metal spot. The reflection nearest the metal spot was indexed to be a $\{660\}NiAl_2O_4$ reflection having a d-spacing of 0.946 Å. The middle oxide reflection has a d-spacing equal to 0.936 Å corresponding to a $\{660\}$ δ-Al_2O_3 reflection. The a_o value is calculated to be 7.940 Å. The d-spacing of the outer reflection equals 0.925 Å. If this corresponds to a $(6\cdot0\cdot18)$ δ-Al_2O_3 reflection, the c_o value is calculated to be 23.303 Å. The calculated c/a ratio is 2.935 which is in good agreement with the published values. The results of the same calculations for the 10.0 hour oxide are:

$$a_o = 7.959 \text{ Å}, \; c_o = 23{,}376 \text{ Å}$$
$$c/_a = 2.937$$

Similar calculations were performed on (001) metal specimens oxidized for 1.0 and 10.0 hours. For a 1.0 hour oxide:

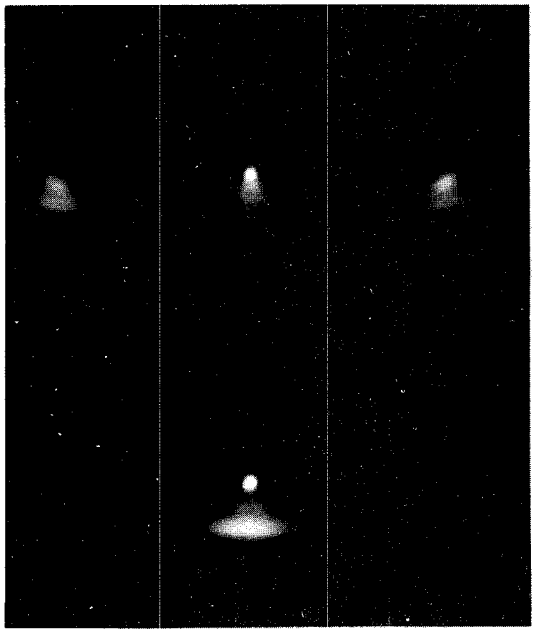

a)

▲$(300)_\beta$
○$(660)_s$
+$(660)_\delta$
□$(660)_\gamma$ or $(6{\cdot}0{\cdot}18)_\delta$

▲$(400)_\beta$
○$(880)_s$
(+$(880)_\delta$
□$(880)_\gamma$ or $(8{\cdot}0{\cdot}24)_\delta$

b)

▲$(300)_\beta$

▲$(400)_\beta$
○$(880)_s$
(+$(880)_\delta$
□$(880)_\gamma$ or $(8{\cdot}0{\cdot}24)_\delta$

▲ β-NiAl(β)
○ $NiAl_2O_4$(s)
+ δ-Al_2O_3(δ)
□ γ-Al_2O_3(γ)

Figure 63

Portions of diffraction patterns from metal plus oxide regions of a) an (012), 1.0 hour, 800°C specimen and b) an (012), 10.0 hour , 800°C specimen. The multiple reflections near β-NiAl reflections help in the determination of the lattice constants of δ-Al_2O_3.

$$a_o = 7.874\ \text{Å}, \quad c_o = 23.354\ \text{Å}$$
$$c/_a = 2.966$$

The diffraction pattern showed an {880} $NiAl_2O_4$ reflection with a d-spacing of 1.416 Å. Using $NiAl_2O_4$ as a reference instead of $^{\beta}$-NiAl, the newly calculated lattice constants of $^{\delta}$-Al_2O_3 are:

$$a_o = 7.913\ \text{Å}, \quad c_o = 23.470\ \text{Å}$$

The lattice constants of $^{\delta}$-Al_2O_3 after 10.0 hours oxidation time on an (001) metal specimen are:

$$a_o = 7.908\ \text{Å}, \quad c_o = 23.064\ \text{Å}$$
$$c/_a = 2.917$$

An average c/a ratio for $^{\delta}$-Al_2O_3 calculated from many diffraction patterns of an (001), 10.0 hour specimen was 2.960 ± .05 Å. This value is believed to be the most realistic estimate for δ -Al_2O_3 in this study.

The published and measured values for the lattice constants of δ-Al_2O_3 are summarized in Table V. There appears to be no trend in the change of lattice constants for metal orientation

TABLE V

Lattice constants of δ-Al_2O_3 from published data and from measured values in this study.

a_o (Å)	c_o (Å)	c/a	Remarks
7.960	23.40	2.94	Ref. 60
7.943	23.5	2.959	Ref. 61
7.940	23.303	2.935	(012), 1.0 hrs.
7.959	23.376	2.937	(012), 10.0 hrs.
7.874	23.354	2.966	(001), 1.0 hrs.
7.913	23.470	2.966	(001), 1.0 hrs, Ref. with $NiAl_2O_4$
7.908	23.064	2.917	(001), 10.0 hrs.

or oxidation time. This concern developed because of discrepancies found in the diffraction data for δ-Al_2O_3. First, the published d-spacings and indices in the X-ray Powder Diffraction File, card #16-394, are not accurate enough to be used as a reference. For example, the (102) and (004) reflections are assigned a d-spacing of 6.4 Å. Calculated values using the assigned lattice constants place these reflections 0.7 Å apart. Appendix C lists published d-spacings and assigned indices as well as calculated d-spacings for the same indices. Also included are the calculated values from the present study using the lattice constants:

$$a_o = 7.950 \text{ Å}, \quad c_o = 23.340 \text{ Å}$$

which are average values of the measured lattice constants on (012) specimens being the most consistent valves.

Next, assignment of indices to specific reflections in diffraction patterns involves relaxing some basic crystallographic principles. For instance, in the diffraction pattern of Figure 64, the δ-Al_2O_3 zone corresponds to a $\langle 112 \rangle$ cubic zone. Correct assignment of indices requires a stereographic projection of this particular tetragonal system to be used. Figure 65 is a tetragonal stereographic projection

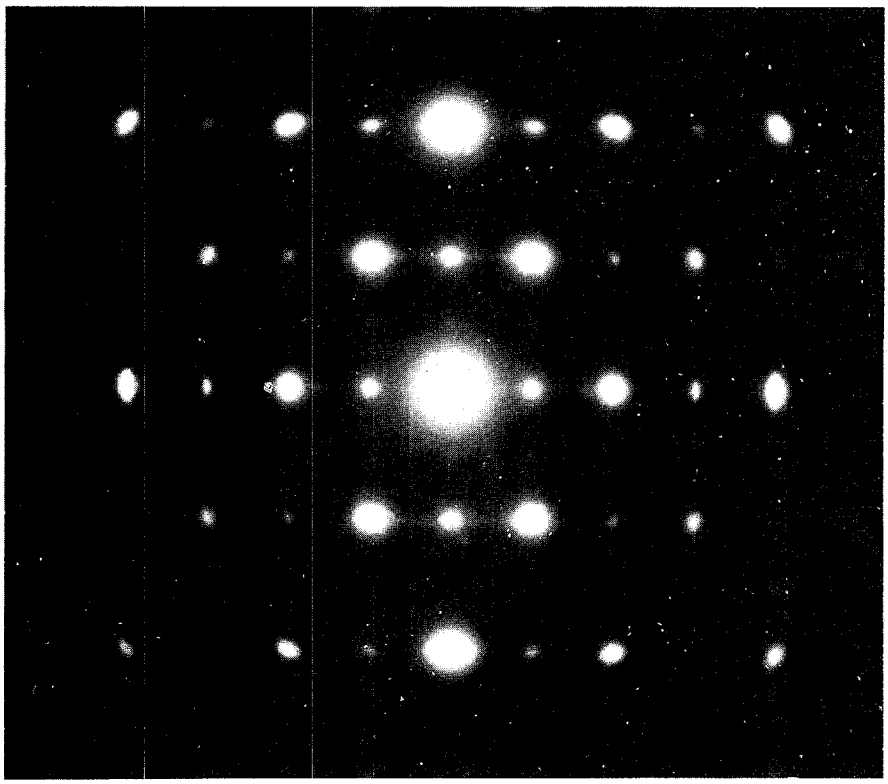

Figure 64

δ-Al_2O_3 zone axis corresponding to a $\langle 112 \rangle$ cubic zone axis. The indexing scheme suggests the possibility of 2 or more variants of δ-Al_2O_3.

using a c/a ratio equal to 2.936 taken from the averaged lattice constants. Formulae to determine projection angles are found in the reference by Andrews et al.[59] One projection is for a variant having the c-axis perpendicular to the projection plane, i.e. an (001) stereographic projection and the other projection has the c-axis in the plane of the projection ((0$\bar{1}$0) projection). The two poles corresponding to a $\langle 112 \rangle$ cubic pole are the [116] in the (001) projection and the [1$\bar{2}$3] pole in the (0$\bar{1}$0) projection. Neither pole superimposes exactly over the position of a cubic $\langle 112 \rangle$ pole on a cubic (001) projection, the difference being less than 1° in both cases. However, in the diffraction pattern of Figure 64, the angle between the two principal directions is exactly 90°. The traces of the zones at 90° from each of these tetragonal poles, do not intersect enough low indice poles to account for the diffraction pattern. There is no rational low-indices zone axis which satisfies exact diffraction conditions of Figure 64.

Therefore, all three orthogonal variants of δ-Al_2O_3 are assumed to be present to account for the symmetry of the diffraction patterns. This same conclusion allows for the similarities between diffraction patterns of δ-Al_2O_3 on (012) and (001) oriented metal oxidized for 10.0 hours. A variety of δ-Al_2O_3 zones along with indexing schemes are given

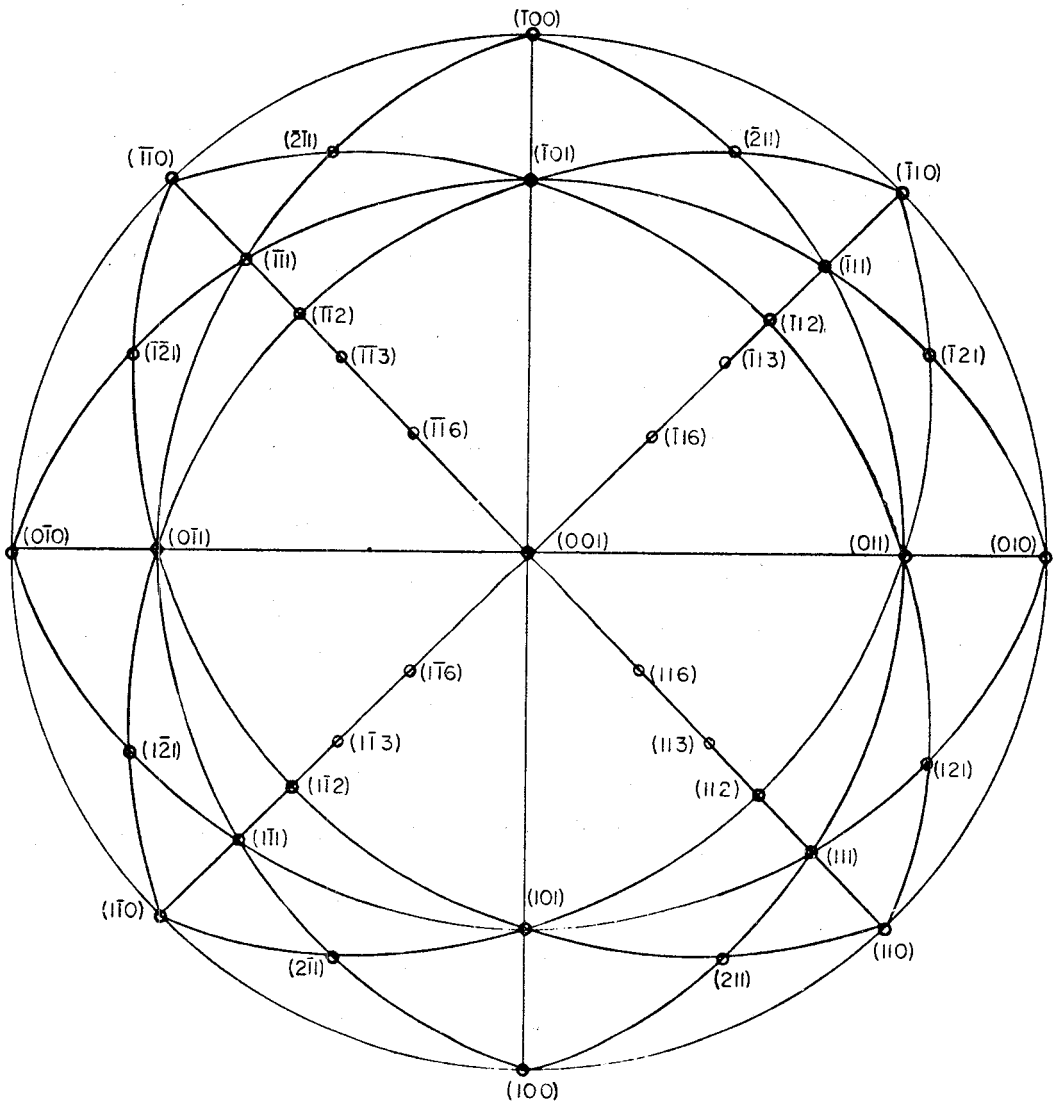

a)

Figure 65

Stereographic projections of tetragonal δ-Al_2O_3 using a c/a ratio equal to 2.936; a) an (001) projection[2] and b) an (0$\bar{1}$0) projection.

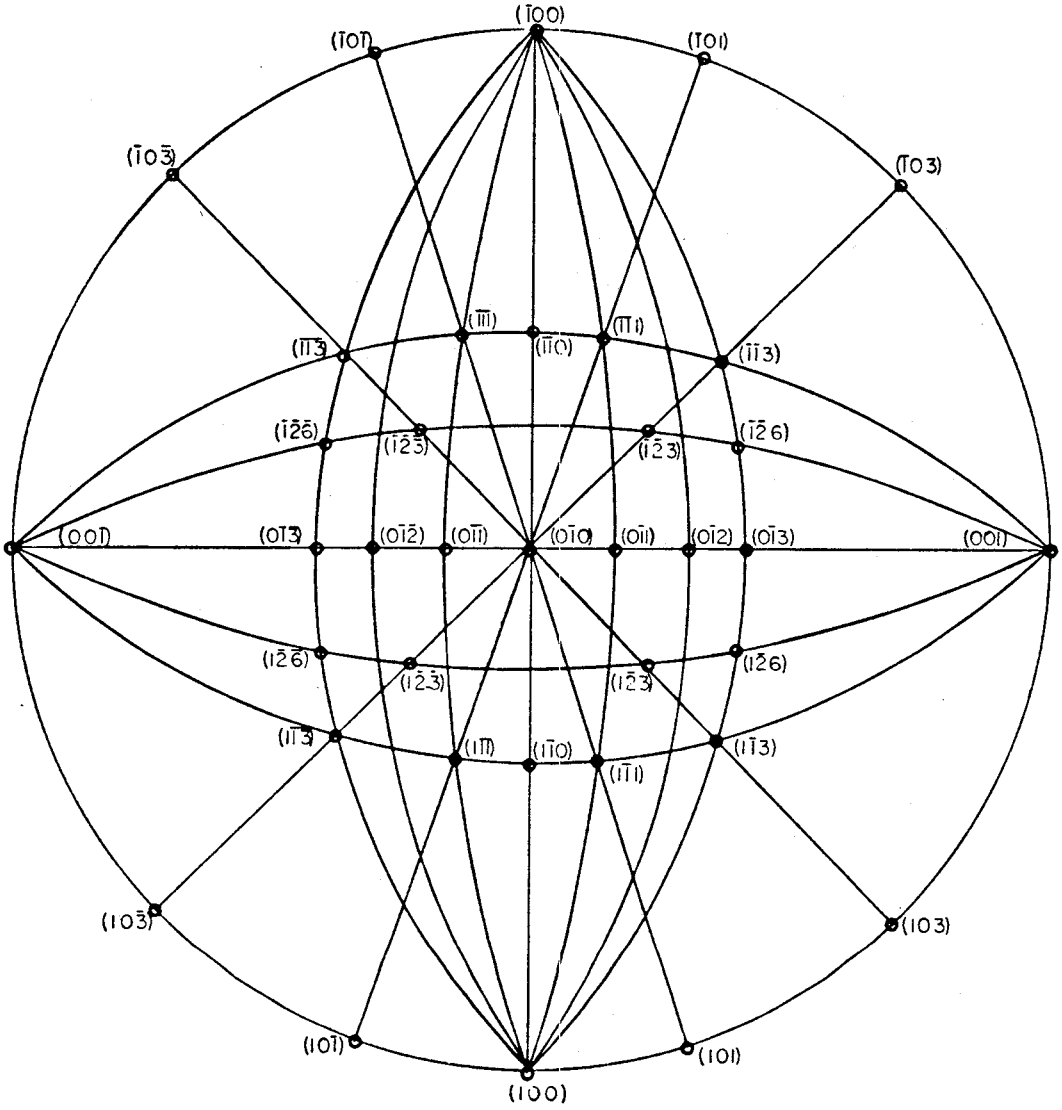

Figure 65b)

$(0\bar{1}0)$ projection of δ-Al_2O_3.

in Appendix D for different metal orientations. Brief explanations of the diffraction patterns describe the orientations at which the specimens were tilted to obtain the zones axis patterns and also similarities or differences between patterns.

δ-Al_2O_3 is considered to be a transition phase between γ-Al_2O_3 and α-Al_2O_3, the cations being more ordered than γ-Al_2O_3. However, lines of diffuse intensity along c-axis directions in the diffraction patterns of Figure 66 suggest that this ordering is still not complete. This same phenomena was found by Lippens and de Boer in their study of the transformations of aluminum hydroxides.[60] The transformation from δ-Al_2O_3 to α-Al_2O_3 usually involved formation of θ-Al_2O_3, a well-ordered monoclinic phase. However, Rooksby[61] discovered that a highly ordered δ-Al_2O_3 phase can transform immediately to α-Al_2O_3 without first converting to θ-Al_2O_3, the transition phase considered to have the highest degree of order.[63] The amount of cation ordering may be a function of the moisture content of the transition alumina phase. δ-Al_2O_3 is considered to be a hydrous phase of Al_2O_3 as all of the transition aluminas are. An important finding was made by Ramanarayaman[38] who found δ-Al_2O_3 on a Y_2O_3 doped NiCrAl alloy at 900°c when the moisture content of the oxidizing atmosphere was high. In dry air, only α-Al_2O_3 was found at 900°C. Yet

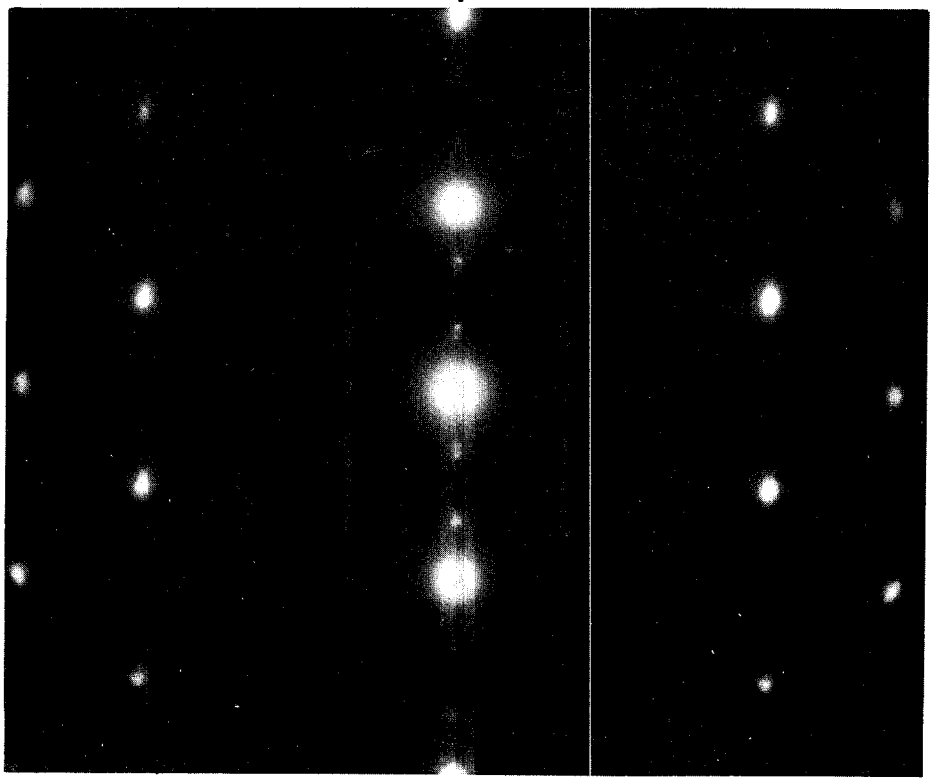

Figure 66

δ-Al_2O_3 zone axis showing diffuse intensity along the c-direction.

the opposite is true for the Fe-O system. The cubic transition phase, γ-Fe_2O_3 is stabilized by high moisture contents, whereas the tetragonal form of Fe_2O_3 is present under dry conditions.[56]

In the present study, the moisture content of the atmosphere was not determined and was assumed to vary between lots of oxidation runs. However, this seemed to be of minor importance when a new effect was discovered. Specimens having an (012) and (011) metal orientation were oxidized side-by-side in the same furnace yet the oxide phases were quite different. On the (012) specimen, oriented δ-Al_2O_3 was the only evident phase, the scale being uniform throughout. On an (011) specimen, oriented γ-Al_2O_3 was the predominant oxide phase after 10.0 hours oxidation time. This result is related to the different structures of γ-Al_2O_3 and δ-Al_2O_3 and their formation on different metal orientations. This point will be discussed in relation to the overall oxidation process occurring on oriented β-NiAl alloys.

2) Summary of oxide phases and compositions

A summary of the oxide phases that formed on each metal orientation and the oxidation times are shown in Table VI. Table VII lists the Al/Ni ratios of the oxides for the same vari-

TABLE VI

Summary of oxide phases found on oxidized single-crystal β-NiAl + Zr for oxidation times up to 10.0 hours at 800°C.

	(001)	(012)	(011)	(111)
0.1 hrs. --	S, γ-δ	S, γ-δ	S,(γ)	S,(γ)
1.0 hrs. --	δ, S,(γ)	δ, S,(γ)	γ, δ, S	γ, S
10.0 hrs. --	δ, S	δ, S	γ, S	γ, S

( ) denotes a possible phase

S - $NiAl_2O_4$
γ - γ-Al_2O_3
δ - δ-Al_2O_3

TABLE VII

Al/Ni ratios for oxide layers found on single-crystal β-NiAl + Zr for oxidation times up to 10.0 hours at 800°C. Values in parenthesis are the fractions of Al_2O_3 in the oxide scales.

	(001)	(012)	(011)	(111)
0.1 hrs. --	1.34(.46)	1.60(.55)	0.73(.01)	0.72(.01)
1.0 hrs. --	3.08(.77)	1.59(.55)	5.11(.86)	5.08(.86)
10.0 hrs. --	10.20(.93)	---------	19.42(.96)	20.86(.97)

ables. The trends occurring in both of these tables will now be discussed to develop a unified model for the transient oxidation of oriented β-NiAl.

The oxide phases in Table VI are listed in order of predominance. At 800°C and 0.1 hour oxidation times, $NiAl_2O_4$ forms on all metal orientations. On (001) and (012) specimens, δ-Al_2O_3 is also evident but does not appear to be well defined. This may occur because γ-Al_2O_3 forms initially and immediately begins to transform to δ-Al_2O_3. This phase or mixture of phases is designated as (γ-δ)-Al_2O_3. The presence of (γ-δ)-Al_2O_3 explains the difference in Al/Ni ratios of Table VII for (012), (001) and for (011), (111) specimens. For an (001) specimen at 0.1 hours, the oxide layer consists of approximately 46% Al_2O_3 whereas an (012) specimen has about 55% Al_2O_3. The larger atomic scattering factor for Ni might explain the reason for the low intensity of Al_2O_3 reflections in the electron diffraction patterns.

For 1.0 hours at the oxidation temperature of 800°C, the percent of Al_2O_3 in the oxide layer has increased for all metal orientation except (012). Most likely, the percentage of Al_2O_3 has increased along the same lines as (001) because of their

similar initial condition and current oxide phases. The percentages of Al_2O_3 have increased to 77%, 86% and 86% for (001), (011) and (111) specimens respectively. The scales on (001) and (012) orientations now include two oxide phases; $NiAl_2O_3$ and δ-Al_2O_3. On (011) orientations, all three oxide phases are found, whereas on (111) orientations, only $NiAl_2O_4$ and γ-Al_2O_3 are found. Oxides due to Cr and Fe impurities are also present in some cases. When the impurities are detected, the oxides attributed to them are randomly oriented spinels.

The results for 10.0 hour oxidation times complete the transient oxide developments for this study. The Al/Ni ratios are again similar for (011) and (111) specimens and have increased to 96% and 97% Al_2O_3 respectively. The (001) orientation involved an increase in percent Al_2O_3 to 93%. No data were available for the (012) metal orientation. No change in the predominant oxide phase occurs since the 1.0 hour oxidation time but some morphological developments have taken place. The crystallite sizes of the impurity oxide phases have now increased as evidenced by the distinguishable spots on the rings in the diffraction pattern of Figure 30. Also, δ-Al_2O_3 is no longer evident on (011) specimens.

Additional information will help in explaining the growth process of the oxide. A means of determining the relative thicknesses of the oxide layers can be approximated by observing the diffuseness of the diffraction patterns. Figure 67 is a series of selected area diffraction patterns of oxide layers on (001), (012), (011) and (111) specimens respectively at 0° tilt. All diffraction patterns were taken for similar exposure times. The sharpness of the diffraction spots decreases from (001) to (111) indicating more scattering and thus thicker oxide layers. This agrees with the Al/Ni ratios of Table VII in that (111) has the largest increase indicating more growth of Al_2O_3 relative to the other metal orientations.

Evidence of inhomogeneous oxide growth is provided in the images of Figures 68-70 from an (011), 10.0 hour specimen. Bright field images indicate regions where the selector aperture was placed. From the images, pits in the oxide layer are seen. The pits are covered with a layer of randomly oriented impurity oxide. X-ray analysis showed increased levels of Cr and Ni in these regions. As the thickness of the oxide increases away from the pits, the oxide becomes predominantly oriented γ-Al_2O_3. A stereo pair in Figure 71 indicates that the random oxide is near the gas-oxide interface and not at the metal-oxide interface. The same morphology was observed for

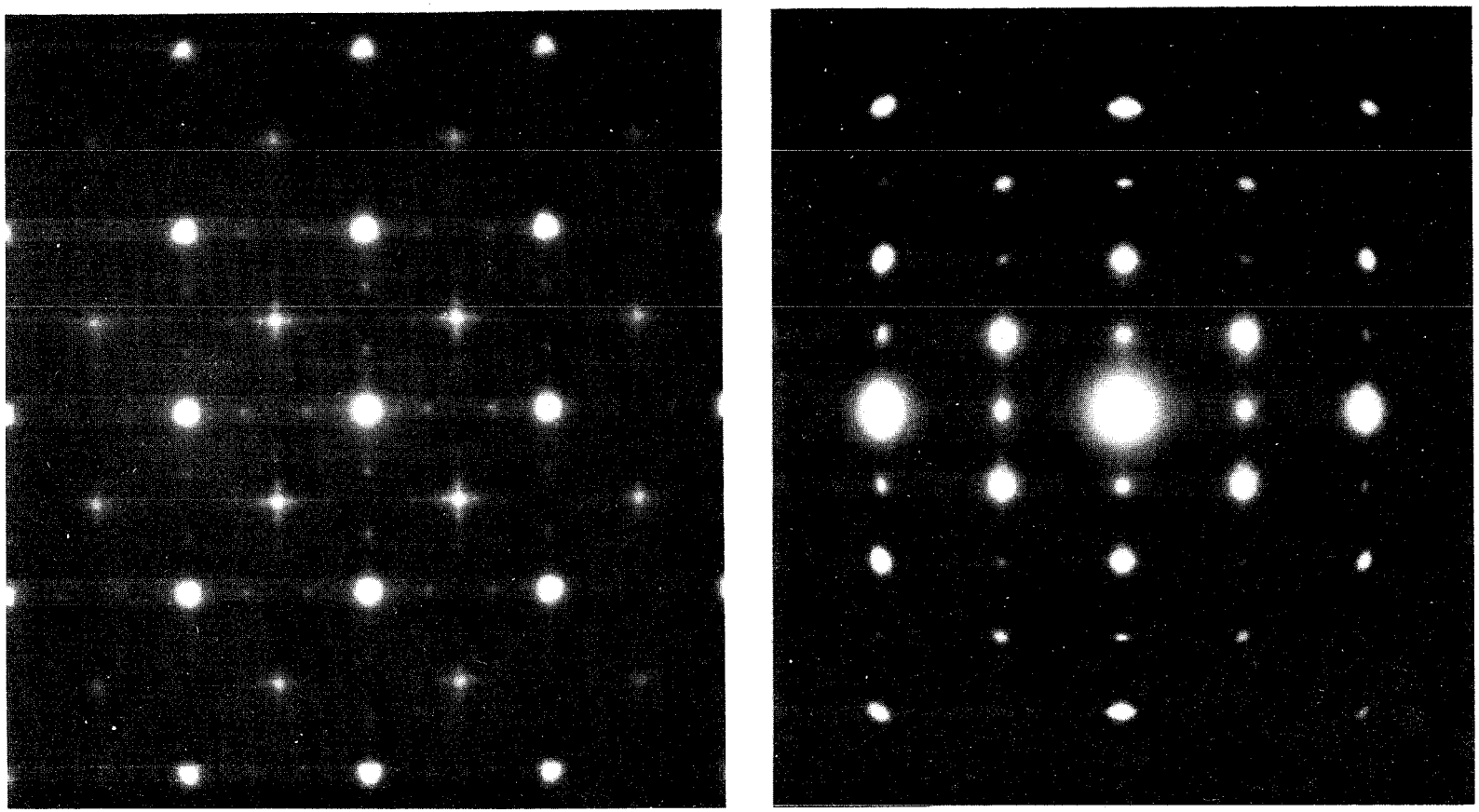

a) b)

Figure 67

Selected area diffraction patterns of 10.0 hour oxides on a) (001) metal, b) (012) metal, c) (011) metal and d) (111) metal. These patterns are shown to compare the diffuseness of diffraction spots as orientation changes. By this technique, the thickness of the oxide appears to increase from a) to d).

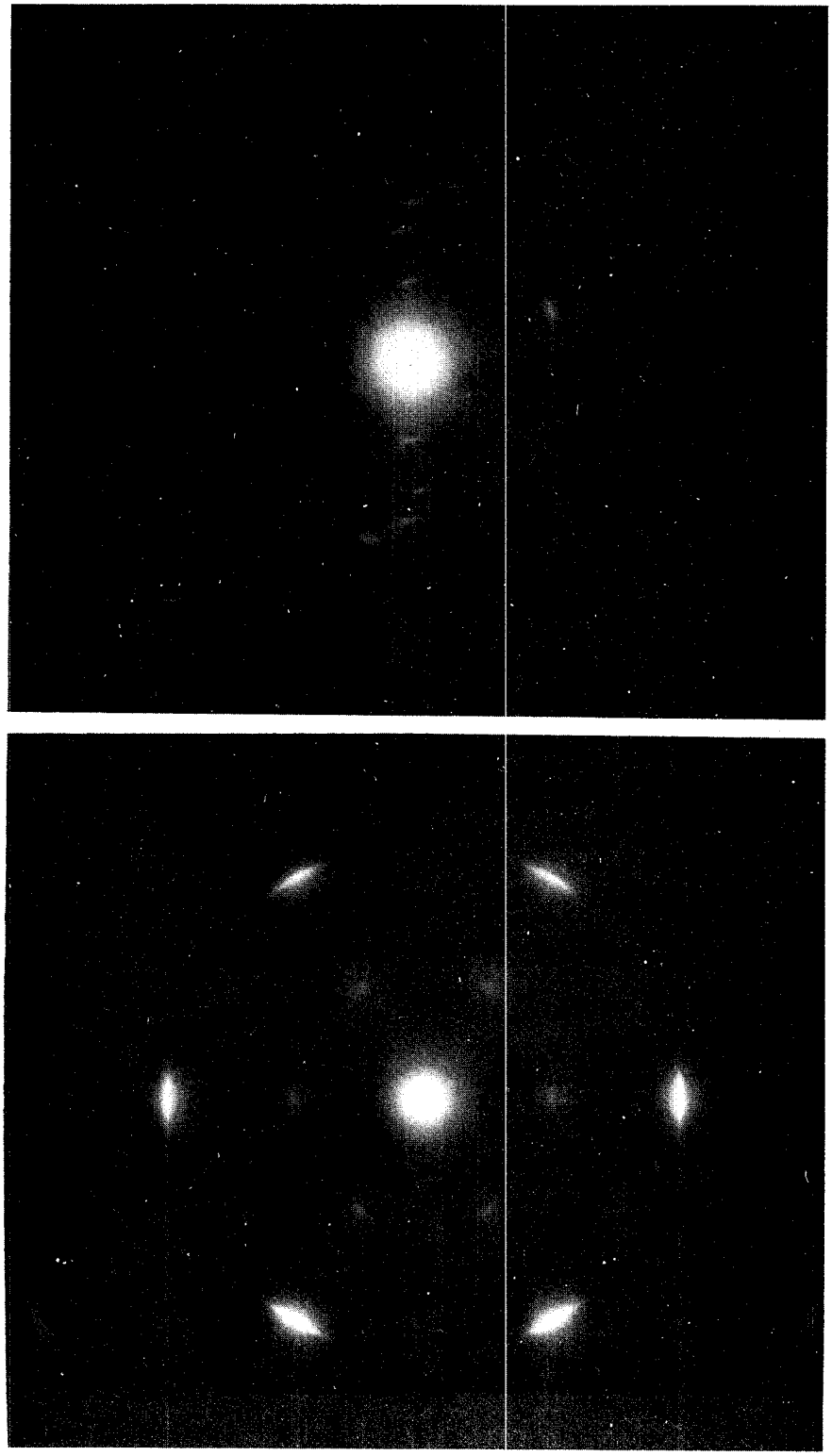

d)

c)

Figure 67

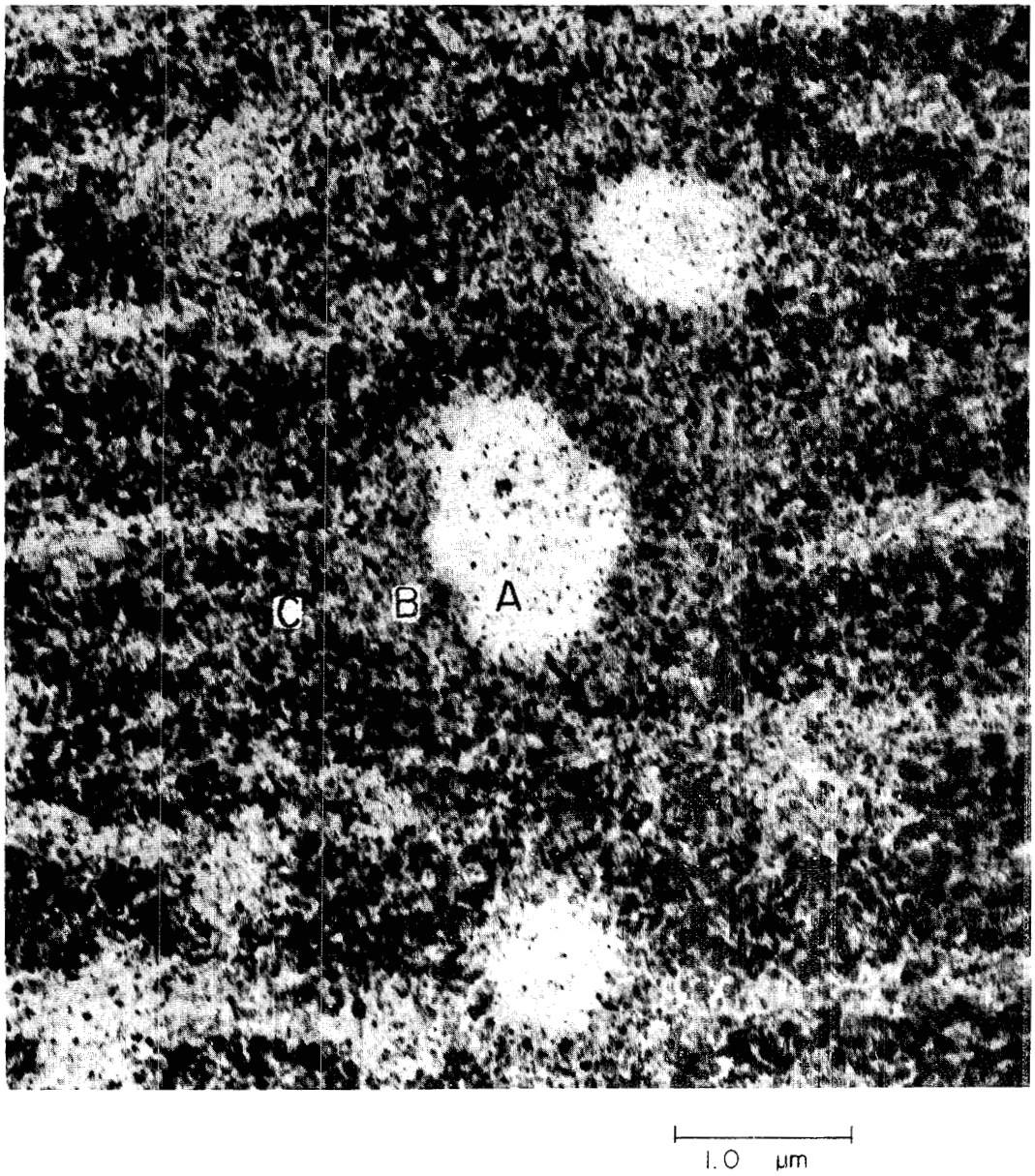

Figure 68

Bright field image of inhomogeneous oxide growth on an (011) metal specimen oxidized for 10.0 hours at 800°C. The non-uniform scale is related to the presence of impurities in the oxide scale.

Figure 69

Selected area diffraction patterns from regions in Figure 68. The thicker regions of the oxide are predominantly oriented γ-Al_2O_3 whereas the thin oxide over the pits in the scale are randomly oriented cubic oxides containing impurities.

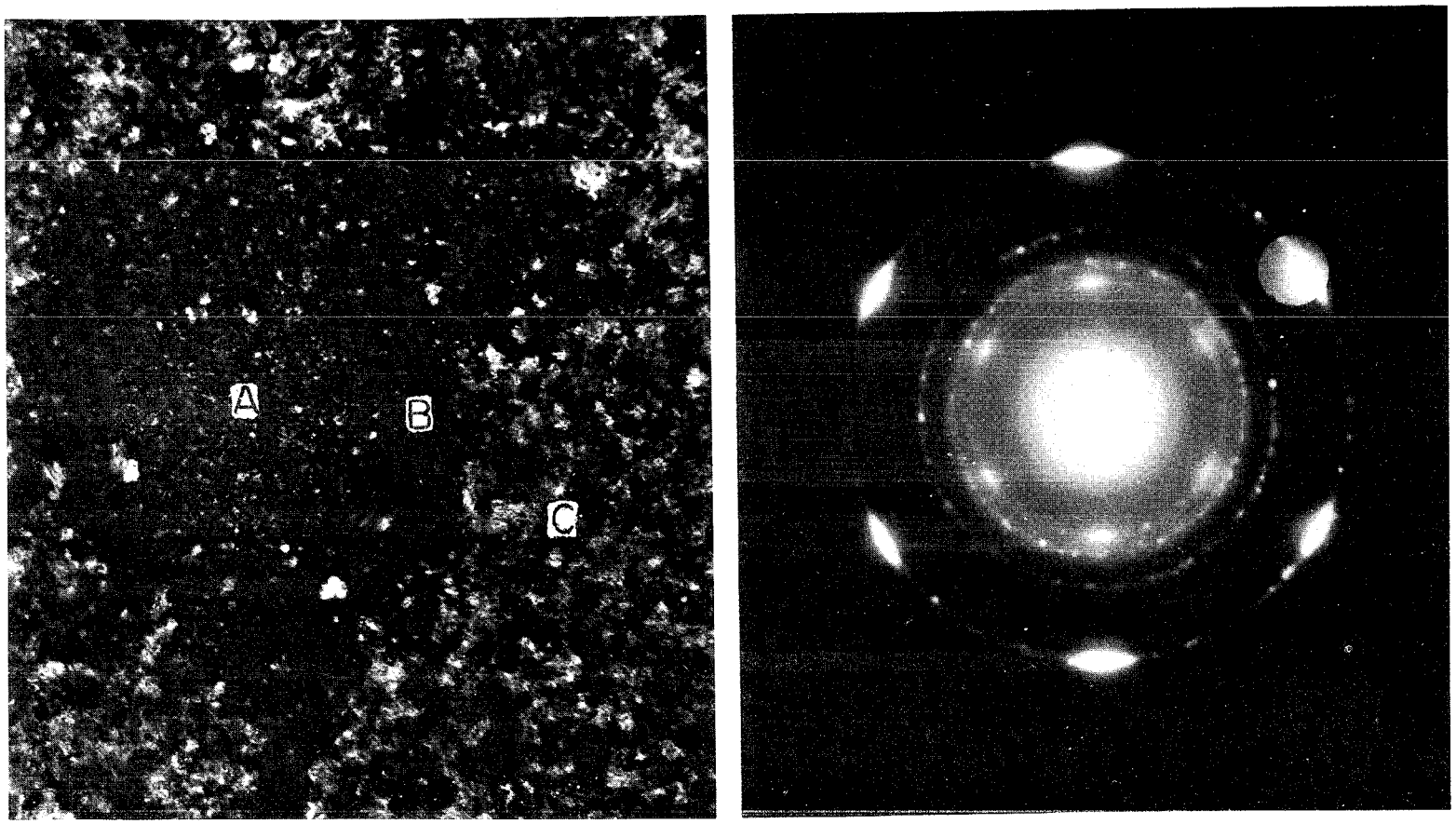

Figure 70

Dark field image with the corresponding SAD of a pitted region in Figure 68, the same areas being indicated. The reflection used is indicated by the image of the objective aperture in the SAD and shows that oriented γ-Al_2O_3 is in the thicker regions.

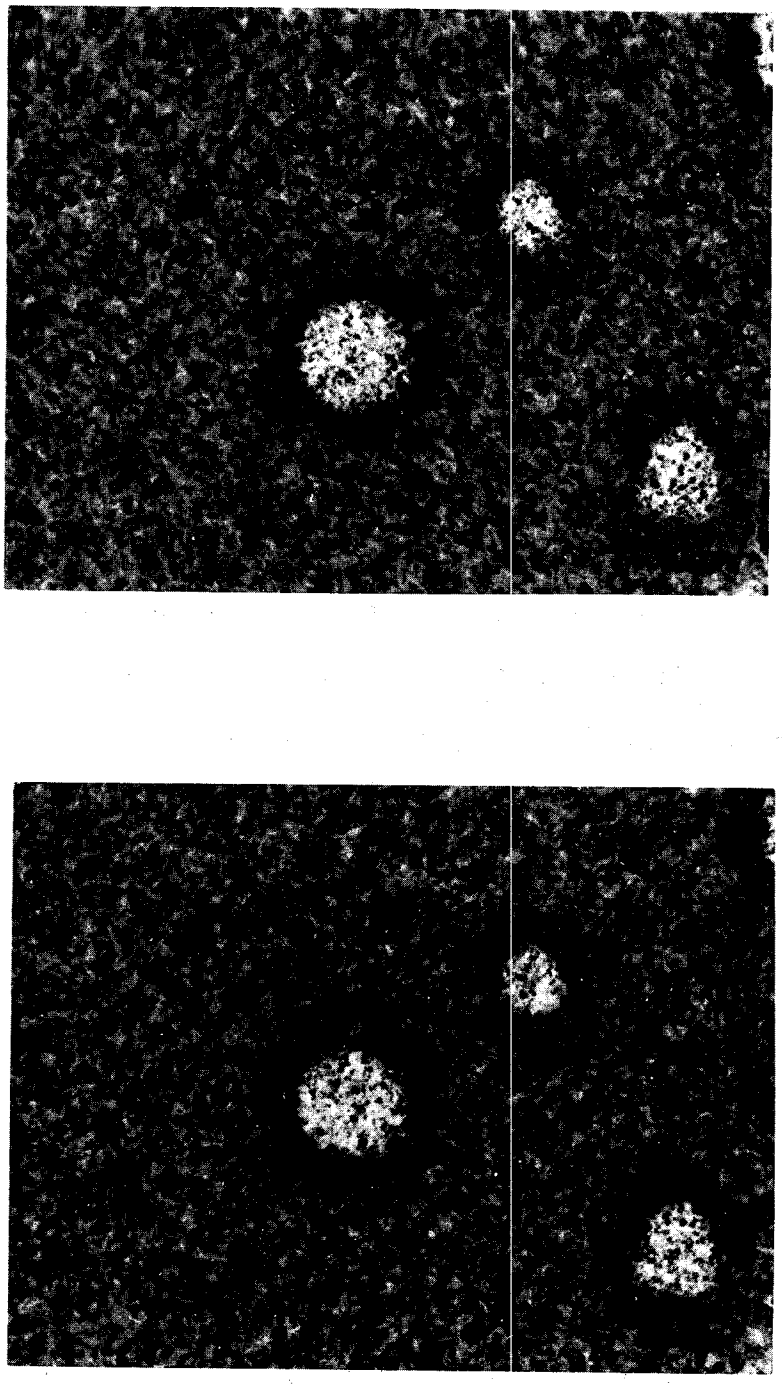

Figure 71 Stereo pair of pitted regions in Figure 68. The random oxide is determined to be near the gas-oxide interface.

the regions of randomly oriented oxide, for the 10.0 hour, (001) specimen of Figure 30.

3) Formation and growth sequence of the oxide phases

The first oxide to form on a metal surface at higher temperatures is usually expitaxially related to the metal substrate. Studies by Howes,[63] Lloyd et al,[64] and Cox et al[65] on iron-chromium alloys have shown the initial oxide layers consist of epitaxially oriented spinel phases. The metal orientation and composition are major factors in determining the degree of orientation. In their studies, $FeCr_2O_4$ and γ-Fe_2O_3 were the initial oxides to form. These phases correspond to $NiAl_2O_4$ and γ-Al_2O_3 of the Ni-Al system in the present work and other related studies.[22,37] For the major metal orientations chosen in the present study, all initial oxide phases were epitaxially oriented to the metal. The orientation relationship between the metal and oxide will be discussed later.

The growth of the oxide layer is a result of further oxidation of the metal which is a diffusion process. Therefore, diffusion must occur through the $NiAl_2O_4$, δ-Al_2O_3 and γ-Al_2O_3 phases. Questions arise as to what chemical species diffuse

and in what directions. Since $NiAl_2O_4$ is found only at the very early stages of oxidation, diffusion of Ni through the oxide does not contribute to the further growth of the oxide layer. This assumption is based on the finding that there is negligible solubility of NiO in $NiAl_2O_4$ as compared to Al_2O_3 in $NiAl_2O_4$.[66] The growth of the impurity oxides is not considered here. The diffusing species are then Al or O ions. These ions can diffuse through the oxide layer to form new oxide at the oxide-gas interface or at the metal-oxide interface. For simplicity, formation of new oxide within an existing phase is neglected. If aluminum cations diffuse faster than oxygen anions, the new oxide will form at the gas-oxide interface. If the reverse is true, oxidation will occur at the metal-oxide interface.

In spinels, cation diffusion is faster than the oxygen diffusion as determined by Oishi and Ando in $MgAl_2O_4$.[68] The species of cation as well as the defect concentration will determine to what extent the cation mobility is greater. For example, Fe has a very high mobility because of its ability to alternate valence states between the ferric and ferrous ions.

Its ability to transfer between octhedral and tetrahedral sites allows for fast diffusion.[69] The mobility of chromium in $NiCr_2O_4$ is faster than the mobility of Al in $NiAl_2O_4$ as determined by Hauffe and Pschera.[70] As the cation mobility increases, the relative anion to cation diffusion decreases. A highly defective structure of the cation sublattice, such as γ-Al_2O_3, should involve an increased cation diffusivity because of the increased number of vacancies. Halloran and Bowen discussed this in their study of ion diffusion in iron-aluminate spinels.[71] The diffusivity of Al in γ-Al_2O_3 would be expected to be higher than in $NiAl_2O_4$. The differences in structure between γ-Al_2O_3 and δ-Al_2O_3 indicate that Al diffusion in these materials could be different. δ -Al_2O_3 is considered to have more of an ordered cation distribution. A recent microscopy study suggests that the periodicity of defects in γ-Al_2O_3 is imperfect because antiphase boundaries are only quasi periodic.[72] In δ-Al_2O_3, the antiphase boundaries are periodic.

The difference in the oxidation characteristics between metal orientations found in this study suggests that the substrate orientation has a definite influence on the transient oxidation of alumina forming alloys. Results suggest that the (001) and (012) metal orientations are similar and the (011) and (111)

metal orientations are similar in their oxidation characteristics.

A schematic of the proposed sequence of oxidation for (001) and (012) metal is shown in Figure 72. Upon exposure to the atmosphere, nuclei of nickel and aluminum cubic oxides combine to form a layer of $NiAl_2O_4$ which is highly epitaxially related to the metal. Since aluminum diffusion is relatively fast, γ-Al_2O_3 forms at the oxide-gas interface as an extension of the $NiAl_2O_4$ spinel lattice. A solid solution of $NiAl_2O_4$ and γ-Al_2O_3 most probably occurs in the early stages. Since the oxide is still thin, some inward oxygen diffusion may occur through short circuit paths and form γ-Al_2O_3 at the metal-oxide interface. This is considered to be a minor contribution, however.

The transformation temperature from γ-Al_2O_3 to δ-Al_2O_3 is considered to be around 850°C (Figure 4). Yet on (001) and (012) metal orientations, δ-Al_2O_3 is stable at 800°C. γ-Al_2O_3 begins to transform to δ-Al_2O_3 with the transformation being incomplete at 0.1 hours oxidation time. The Al_2O_3 transition phase at this stage is called (γ-δ) Al_2O_3.

At 1.0 hour oxidation time, the transformation to δ-Al_2O_3 is complete. The oxide layer has thickened with $NiAl_2O_4$ still

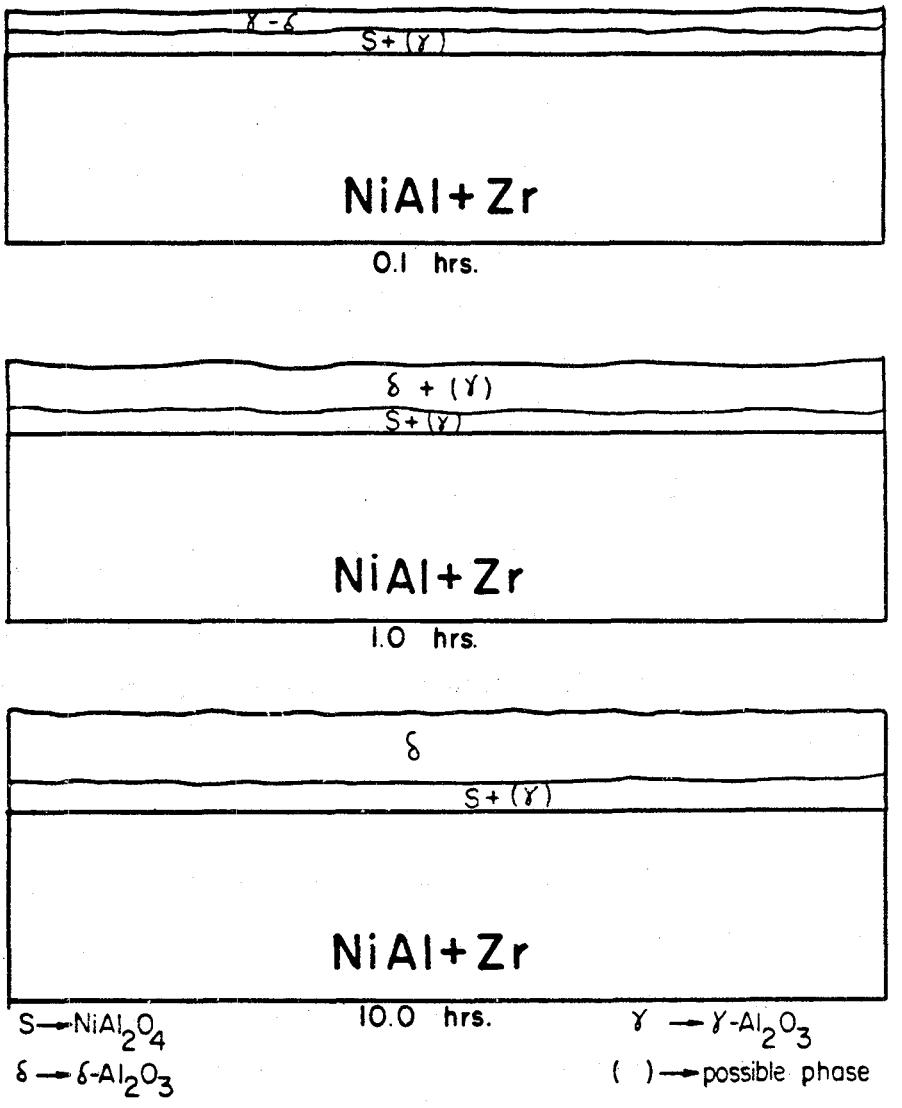

Figure 72

Schematic of the oxidation sequence with time at 800°C on (001) and (012) metal orientations.

incorporated as an inner layer of the scale. At 10.0 hours, the scale is too thick to observe diffraction from $NiAl_2O_4$.

The overall kinetics of stable oxide formation appear to be slower on (011) and (111) metal orientations during transient stages. Figure 73 indicates that $NiAl_2O_4$ forms and grows epitaxially through 0.1 hours of oxidation. Neither γ-Al_2O_3 nor δ-Al_2O_3 forms a complete layer of oxide. The only Al_2O_3 to form after 0.1 hours appears to be in solid solution with $NiAl_2O_4$, if it is present at all. Only one oxide phase, having a lattice constant near 7.92 Å, was evident. This value is intermediate between the lattice constants of γ-Al_2O_3 and $NiAl_2O_4$, but nearer to γ-Al_2O_3. The lower Al/Ni ratio of this scale suggests $NiAl_2O_4$ is the predominant phase of the solid solution. After 1.0 hours oxidation time, γ-Al_2O_3 has formed and is expitaxially related to the metal. On (011) specimens δ-Al_2O_3 also formed but its exact orientation relationship was indeterminate. However, δ-Al_2O_3 did show a preferred orientation. For (011) and (111) metal orientations, γ-Al_2O_3 is more stable than δ-Al_2O_3 at 800°C. This is believed to be a result of the crystallographic structural orientation relationships between the metal and oxide. These metal orientations either stabilize the cubic spinel structure of both $NiAl_2O_4$ and γ-Al_2O_3 or they inhibit the formation of a

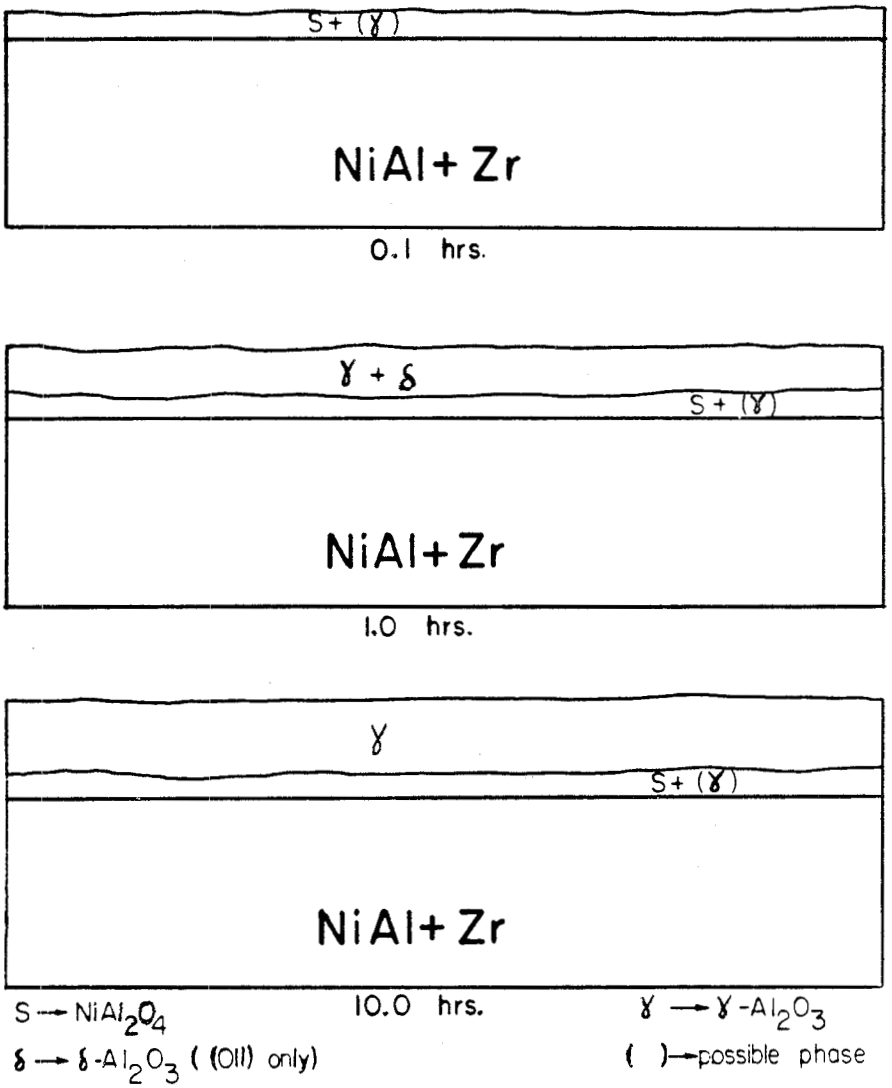

Figure 73

Schematic of the oxidation sequence with time at 800°C on (011) and (111) metal orientations.

tetragonal structure such as δ-Al_2O_3. This is evident because the δ-Al_2O_3 formed after 1.0 hours on (011) metal, but is not present after 10.0 hours. Since δ-Al_2O_3 did form after 1.0 hour on (011) metal, this phase is probably the more stable Al_2O_3 transition phase at 800°C. However, δ-Al_2O_3 is less stable on these metal orientations because the (111) cubic plane that forms on (011) metal has no simple corresponding plane in the tetragonal structure of δ-Al_2O_3. Thus, the near (012) spinel plane that forms on (111) metal would be more stable than a similar plane in δ-Al_2O_3.

The transient oxidation of β-NiAl alloys is therefore seen to be dependent on metal orientation as well as other variables. δ-Al_2O_3 is the stable phase at 800°C but does not persist on (011) and (111) metal orientations because these orientations tend to stabilize the cubic structure of the spinel phase, γ-Al_2O_3. The transient oxidation of alumina forming alloys must then be understood in terms of metal-oxide orientation relationships as well as thermodynamics.

B) Orientation Relationships

1) Rationale for epitaxial oxide formation

The first oxide to form on a metal surface is a result of the chemisorption of oxygen ions on the surface. Depending upon the surface construction of the metal surface, oxygen ions will fill lower energy sites and attempt to match the surface structure. This matching of the surface structure is only applicable when a monolayer or so of the oxide phase is present. Soon afterward, the crystallographic structure of the particular oxide phase predominates and no longer attempts to mimic the metal surface structure. Once monolayer oxide growth has occured, the original metal free surface is no longer stable. Therefore, the bulk metal structure influences subsequent growth of the oxide.

Further growth of the oxide involves a best fit, lowest energy matching between the metal and oxide structures. Initially, the cation sublattice of the oxide phase will just be an extension of the metal lattice. This requires crystallographic directions and planes of the oxide structure to align with appropriate planes and directions of the metal structure. The two main factors affecting the specific directions and planes

in the oxide are the difference in structure between the metal and oxide phase and the difference in spacings along cation close-packed directions. The first factor determines the plane in the oxide that forms parallel to the metal surface. The second determines the degree to which the oxide phase will tend to orient itself with the metal. The smaller the lattice parameter differences are along cation close-packed directions, the less strain energy is involved with oxide growth. Therefore, systems with small differences in the above mentioned lattice parameter will tend to be well oriented. This is a criterion for an epitaxial orientation relationship between a metal and the initial oxide phase that forms on it.

Many aspects of oriented oxide growth have been neglected to this point. These aspects involve such questions as to what occurs when interfacial strains become too large to continue homogeneous oriented growth and how individual oxide crystallites, from nucleation, combine and grow together. These have been the topics of many studies dealing with interfaces, to be described below.

2) Interface theories of interphase boundaries

Success in describing and predicting interface structures has been achieved in terms of models only. There are too many parameters involved to predict exactly what is occurring. Studies on both low angle grain boundaries and on interphase boundaries have been performed with interphase boundaries being of concern in this study. Interphase boundaries can occur through a number of transformations within an already existing matrix or can be obtained by nucleation and growth. Since oxidation is a nucleation and growth process, discussion on interphase boundaries will be limited to this mechanism.

All models are based on the assumption that the energy of the interphase boundary must be at a minimum. Two different approaches at an interface model have been considered. The more exact, but also more tedious methods have been proposed by Frank and van der Merwe[73] and by Fletcher[74]. These models attempt to determine the energy of a given surface based on atomic potentials.

Another group of models attempts to predict minimum energy of a surface based strictly on geometrical calculations. Bollman's O-lattice concept[75] and a model by Rigsbee and Aaronson[76] are examples of geometrical models.

Given two periodic, superimposed lattices, there will be regions of good fit between points on the two lattices separated by regions of poor registry. A dislocation placed along the region of worst fit will accommodate the difference between the two lattices. These dislocations are known as misfit dislocations. All models assume the presence of misfit dislocations. A review by Kinsman and Aaronson provides experimental evidence of misfit dislocations.[77]

The misfit dislocation model proposed by Frank and van der Merwe determines the energies of periodic networks of misfit dislocations. The minimum energy dislocation network corresponds to the most probable interface structure. Energies are calculated assuming the strain energy in the interface plan consists of two components: 1) elastic relaxation due to bonding and mismatch of the two different lattices and 2) homogeneous strain in each lattice. The model by Fletcher involves nearest neighbor interactions both across the interface and on either side of the interface. This is the most general interface model but can also be adopted to incorporate misfit dislocations as in the previous model. The large number of parameters involved, choice of the correct interatomic potentials to be used, and computer time put limits on the efficient use of this model even though its predictive capabil-

ities are high. One important result from this model indicates that the majority of strain energy is limited to the interfacial plane and one or two monolayers on either side of the interface. This is accomplished by misfit dislocations to form a semi-coherent interface. An incoherent interface, where no misfit dislocations are present, would have the strain energies resulting from contributions at large distances on either side of the interface. Therefore, the assumption of a two-dimensional system instead of a three dimensional system appears to be reasonable in most models.

The geometrical models are based on Bollman's O-lattice theory. The O-lattice is the coincident site lattice of the two arrays of points representing the interface planes of two phases. Appropriate transformations and calculations allow the O-points to be determined which are points where the match between the two interfacial structures are perfect. The boundary of the Wigner-Seitz cell centered around each O-point represents the region of worst fit. The cell walls can be considered dislocation lines. The O-points are not necessarily lattice points of either phase. The optimum incoherent boundary involves a maximum in the number of lattice sites being O-points. A burgers vector, b_i, is assigned to the dislocation formed by the O-lattice and the original crystal lattice for a direction,

i, in both lattices. The distance, d_i, is the lateral spacing between dislocation lines in the arrays. The two are related by:

$$P = \sum_i \frac{b_i^2}{d_i^2} \qquad [18]$$

where minima in the value of P represent best fit situations.

Ecob and Ralph[78] used a parameter, R, where:

$$R = \sum_{i,j} \left(\frac{b_i b_j}{d_i d_j}\right)^{\frac{1}{2}} \qquad [19]$$

This is similar to the P-parameter but takes into account dislocation interactions. The dependence on d changes from an inverse square to an inverse dependence making the parameter, R, a possible measure of relative energetic favorability of an interface. However, Knowles et al demonstrated that the use of this parameter or any geometrical parameter to predict minimum energy is subject to question.[79]

Based on the above interface models, a simplified approach was developed to attempt to rationalize some of the findings in the present study. The concepts of both nearest neighbor calculations (assuming the atomic potentials are inversely

proportional to the nearest neighbor distance) and geometrical fit have been combined to characterize an interface between the metal phase, β-NiAl, and any of the cubic spinel oxide phases. For simplicity of compositional nature, γ-Al_2O_3 was chosen. The model superimposes the parallel planes of oxide and metal found in the orientation relationships determined by electron diffraction. The parallel planes in both the metal and oxide phases are comprised of perfect arrays of atomic positions determined from the appropriate lattice parameters. Because the exact chemistry of the interface (unoccupied cation sites, Ni vs. Al positions) is not known, all points represent possible aluminum ion positions, all having the same valence state. Each position on the two lattices is occupied by an Al ion having an ionic radius of 0.42 Å.[80] The distance between every metal point and its nearest neighbor in the oxide lattice is calculated using iterative procedures on an Apple IIE computer. If the nearest neighbor distance is less than some assumed fraction of the ionic radii distance, the coordinates of both the oxide and metal positions are printed out along with the nearest neighbor distance. Assuming a hard sphere model for aluminum ions, the overlap area determined by the nearest neighbor ions is calculated. Figure 74 illustrates the model. The general programs used for calculating nearest neighbor distances, coordinates of nearest neighbors and overlap areas

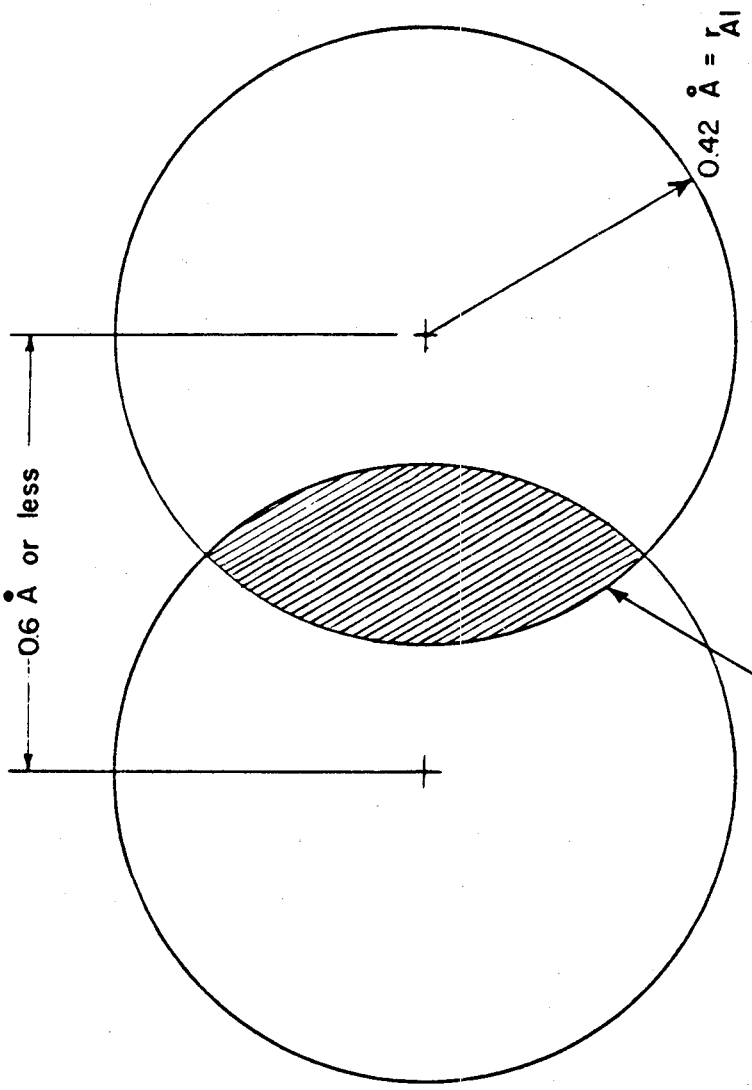

Figure 74

Representation of the overlap area criterion used for the computer model of interfaces in this study.

are listed in Appendix E. Actual calculations will be discussed as each orientation relationship is considered in the following section.

It is believed that the amount of overlap area is a relative measure of the strain energy in the interfacial plane of an oxide metal system. The more overlap area associated with an incoherent interface, the less would be the strain energy if that interface was fully coherent. This model only deals with incoherent interfaces and assumes only homogeneous strains at the interface. Contributions to bonding across the interface have been neglected.

3) Orientation relationships on oxidized, single crystal β-NiAl

The four metal orientations studied were (001), (012), (011), and (111). The experimental results for each metal orientation will be discussed separately. Computer modeling was performed for (001) and (011) metal orientations. The (012) metal orientation would require more complex alterations to the program. The (111) metal orientation requires a three dimensional model because of the complexity of the orientation relationships.

a) (001) metal orientation

The Bain relationship was found to occur for all conditions. This is given as:

$$(001)_{metal} \;||\; (001)_{oxide}$$
$$[110]_{metal} \;||\; [110]_{oxide}$$

The same orientation relationship is found for oxidized iron and its alloys[81-85] and oxidized chromium.[86] The metal, in all cases, has a body-centered cubic structures and the oxides all have spinel type structure for this orientation relationship. In the present study and for iron oxidation, the difference in lattice constants along the parallel directions is within 3%.

Figure 75 shows the results of the computer modeling techniques. The origin of the matrix is at 0,0. The points plotted in Figure 75 represent metal lattice positions where the center-to-center distance of the metal lattice position and the corresponding metal ion in a superimposed oxide lattice is 0.6 Å or less, i.e., the cut-off point equals 0.6 Å. The regions of best fit occupy blocks around a central point. This central point, determined by extrapolation of nearest neighbor distances, corresponds to Bollman's O-points of the O-lattice. In those terms, the O-lattice for a Bain relationship between

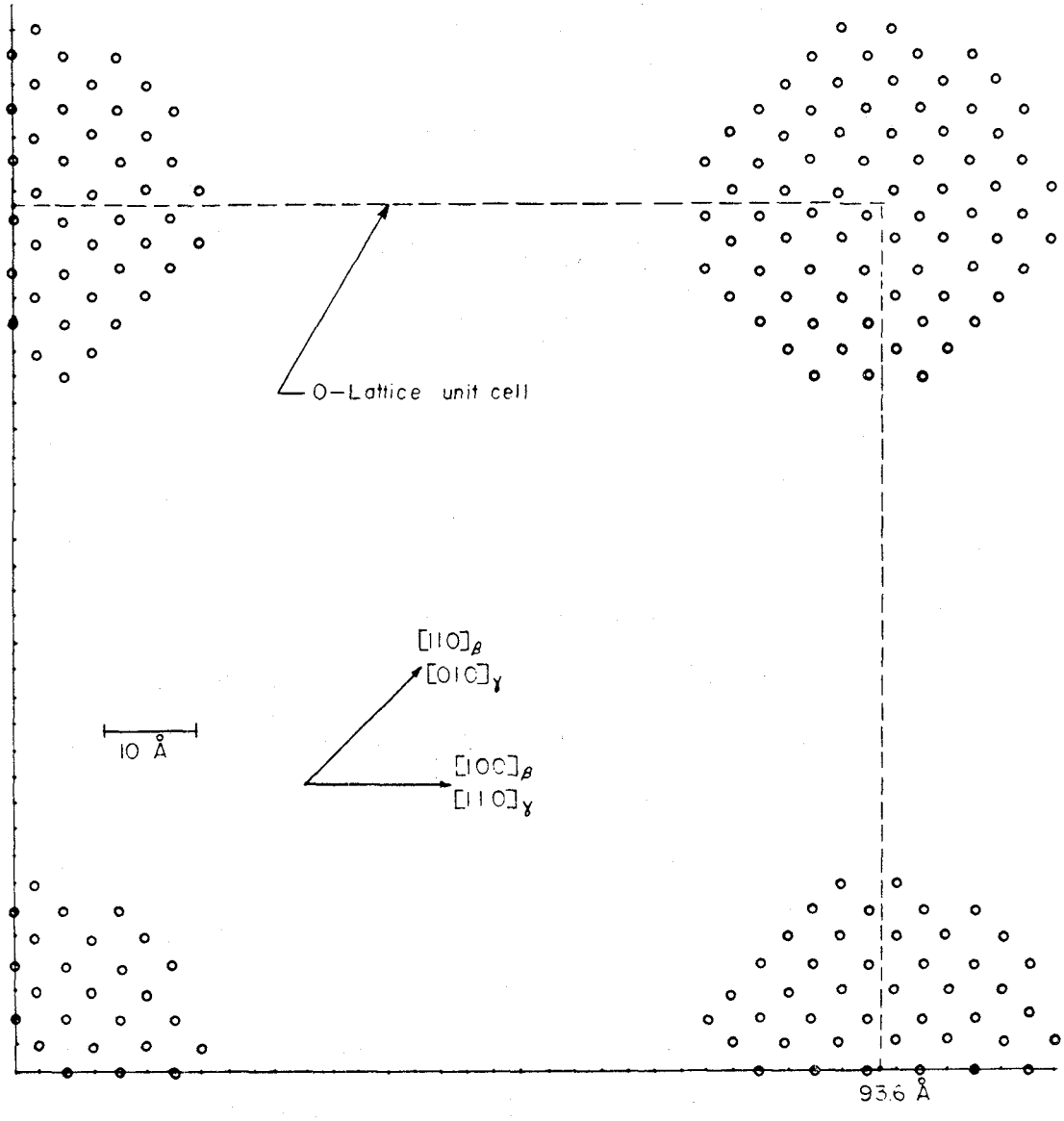

Figure 75

Computer model simulation of aluminum lattice site matching for a Bain relationship between β-NiAl and γ-Al_2O_3 for an (001) metal orientation.

β-NiAl and γ-Al_2O_3 was determined to be a square array with a dimension of 93.59 Å along the metal ⟨100⟩ directions. This implies misfit dislocations to be spaced 93.59 Å apart and have a line direction along ⟨100⟩ metal directions. The ⟨100⟩ line direction corresponds with the dislocations on an (001) oxidized metal in Figure 24, where the dislocations do lie along ⟨100⟩ metal directions.

Another aspect to consider in the computer model is the relative degree of mismatch. The parameter used to describe this is designated, σ, where:

$$\sigma = \frac{\text{overlap area } (\text{Å})^2}{\text{grid area } (\text{Å})^2} \qquad [20]$$

The overlap area is calculated by summing the individual overlaps for each nearest neighbor pair in a block of near coincident sites. For this particular system, the overlap area was calculated to be 17.45 $Å^2$. The grid area is just the area of a unit cell of the O-lattice. For this system, the grid area equals $(93.59\ Å)^2$ or $8.76 \times 10^3\ Å^2$. Therefore, for the Bain relationship between β-NiAl and γ-Al_2O_3, σ equals 1.99×10^{-3}.

Another parameter which appears to be more significant than is the parameter designated as ρ, where:

$$\rho=\sigma \cdot \frac{\text{\# of coincident sites/grid}}{\text{grid area } (\text{Å})^2}$$

This value, in units of Å^{-2}, takes into account the near coincident site density in each unit cell of the O-lattice. From Figure 75, the number of sites in one grid is 76. Therefore, ρ equals 1.73×10^{-5} Å^{-2} for this system. Both σ and ρ are dependent upon the limiting criterion of 0.6 Å as the maximum center-to-center distance for a nearest neighbor pair. The actual values of σ and ρ have little absolute significance but can be used to compare with values obtained from other orientation relationships.

There appears to be little difficulty in defining the orientation relationship when δ-Al_2O_3 is the primary oxide. Referring to the stereographic projections of Figure 65, two variants of δ-Al_2O_3 have their c-axes in the plane of oxidation and a third variant has the c-axes perpendicular to the oxidation plane. The overall orientation relationship for δ-Al_2O_3 and β-NiAl is given as:

$$(001)_{\beta\text{-NiAl}} \;||\; (0\bar{1}0)_{\delta\text{-}Al_2O_3}$$
$$[110]_{\beta\text{-NiAl}} \;||\; [001]_{\delta\text{-}Al_2O_3}\ *$$

and

$$(001)_{\beta\text{-NiAl}} \;||\; (001)_{\delta\text{-}Al_2O_3}$$
$$[110]_{\beta\text{-NiAl}} \;||\; [010]_{\delta\text{-}Al_2O_3}$$

*two variants

b) (012) metal orientation

One orientation relationship was found on this metal orientation for cubic oxides and one for δ-Al_2O_3. Each orientation relationship appeared to have only one variant. For cubic oxides the orientation relationship is given as:

$$(012)_{metal} \;||\; (112)_{oxide}$$
$$[100]_{metal} \;||\; [110]_{oxide}$$

Figure 76 shows the stereographic projection for this orientation relationship. The same close-packed direction as in the

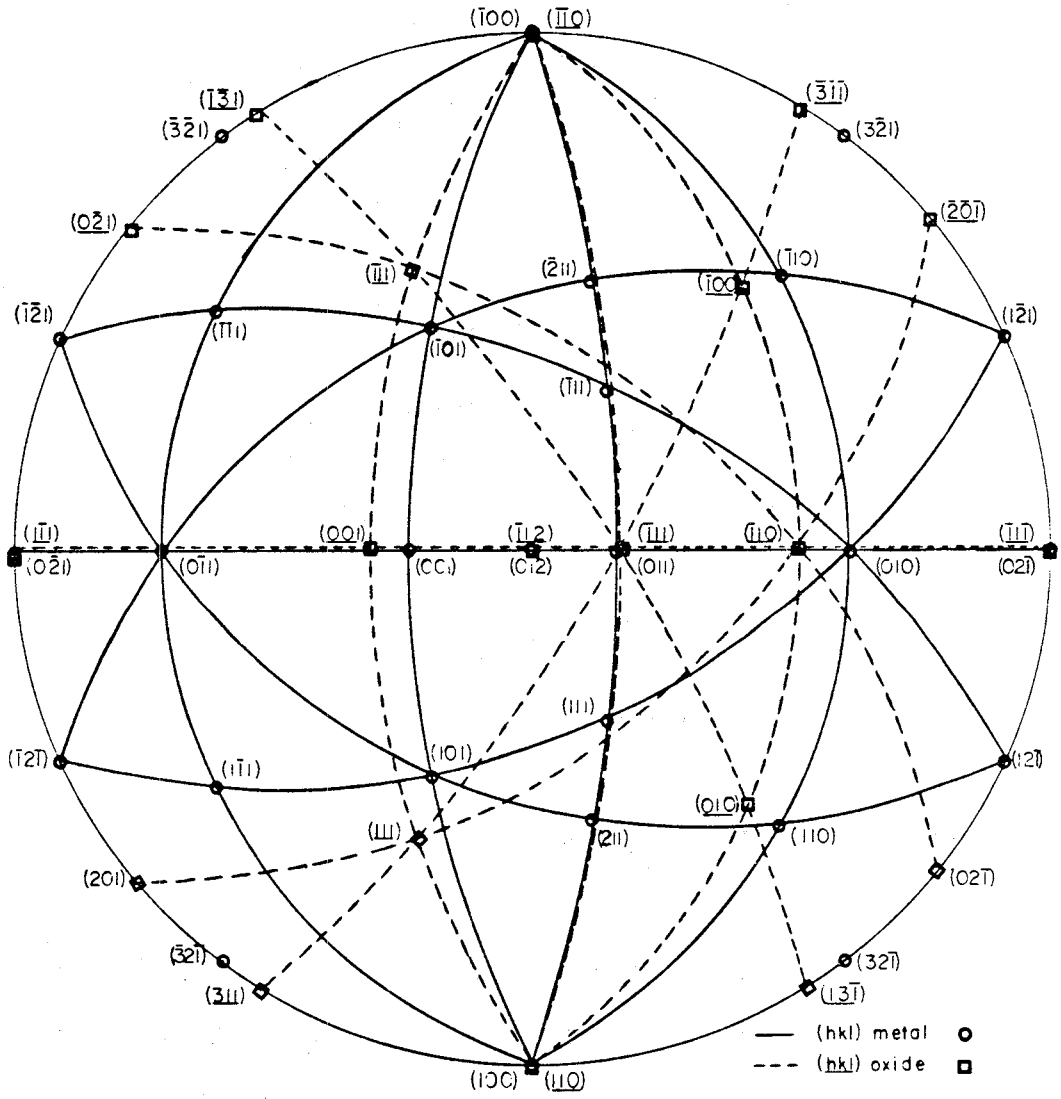

Figure 76

Orientation relationship on an (012) metal orientation with a cubic oxide represented by a stereographic projection.

Bain relationship is present. The (112) plane of spinel is not necessarily a close-packed plane. However, planes adjacent to any {112} plane appear to superimpose well over many metal lattice sites. Therefore, the orientation relationship might not be a function solely of the interface plane but of adjacent planes. In the spinel lattice, tetrahedral and octahedral sites are both incorporated into the {112} planes. Their degree of occupancy in the defective spinel structure is not necessarily ordered. Thus, at initial oxidation stages, higher occupancy of both sites could allow this strong orientation relationship to occur. In $NiAl_2O_4$, the local chemistry at the interface could change on the atomic scale to better mimic the metal nickel and aluminum sublattices.

When considering the orientation relationship between β-NiAl and δ -Al_2O_3, the tetragonal structure of δ-Al_2O_3 complicates an exact orientation relationship. Consider the stereographic projection of one of the three directions that the c-axes might be in δ-Al_2O_3. Because the c/a ratio is not exactly equal to three, the {103} reflections and {100} reflections are not at 45° from each other as the {101} and {100} reflections would be in a cubic system. This also means that the angle between $(0\bar{1}0)$ and $(1\bar{2}3)$ in the tetragonal projection of Figure 77 does not equal the angle between (001) and (112) in the cubic

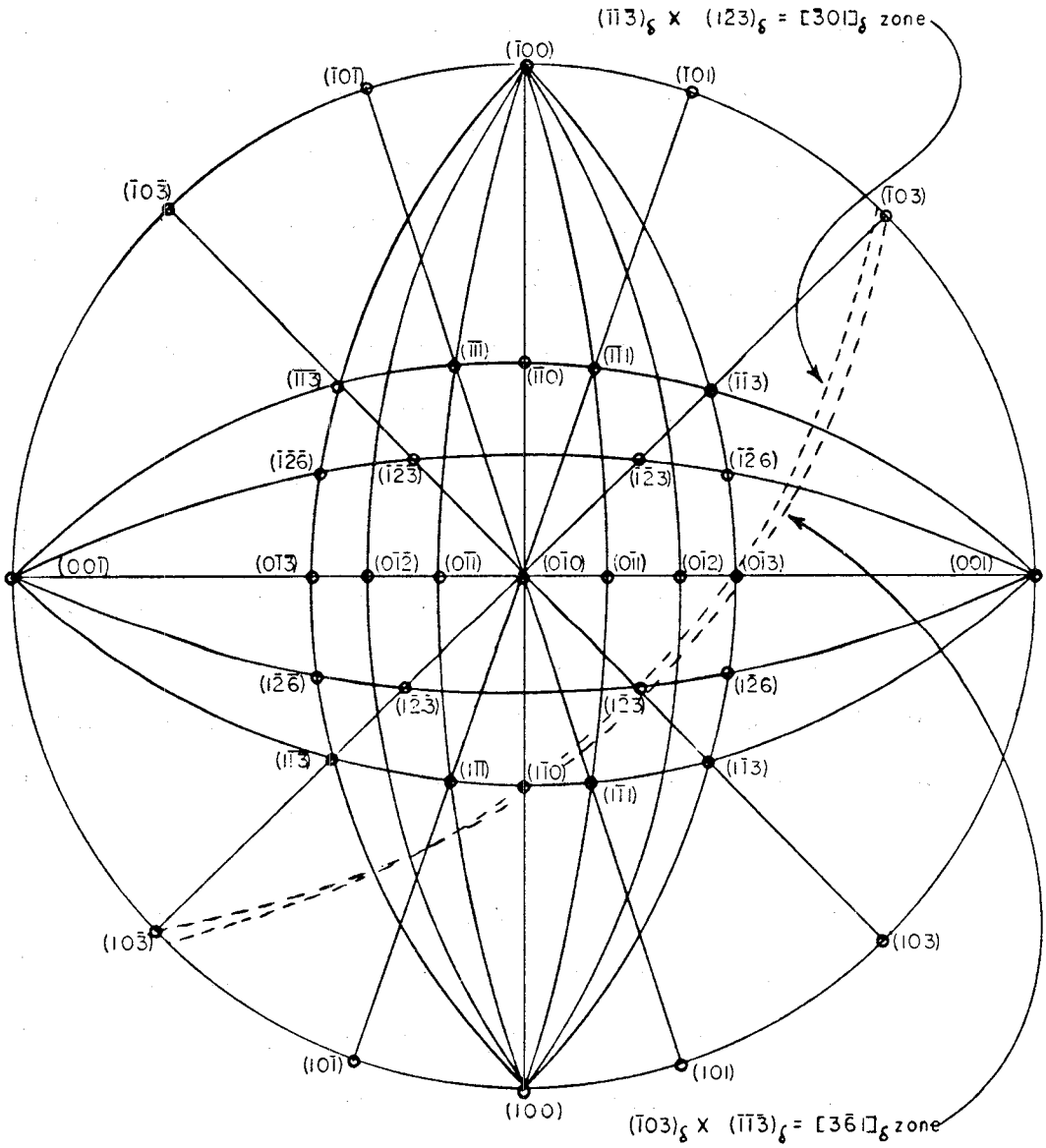

Figure 77

Stereographic projection of the tetragonal δ-Al_2O_3 phase.

system. In most cases, the angular difference between the cubic poles and corresponding tetragonal poles is less than 3°.

If the c/a ratio of δ-Al_2O_3 was equal to three, the same symmetry should exist in the [1$\bar{2}$3] tetragonal zone as in the [1$\bar{2}$1] cubic zone. Extra reflections from the tetragonal superlattice should also be in the tetragonal zone. However, as shown in Figure 78, the same symmetry is present between the tetragonal zone of δ-Al_2O_3 and the cubic zone of $NiAl_2O_4$. This should imply that the c/a ratio equals three. But the implication would be incorrect because the c/a ratio was, in all cases, measured to be less than three. Therefore, the reflections in the apparent zone axis patterns of δ-Al_2O_3 are assumed to be a combination of low index reflections from each orthogonal variant of δ-Al_2O_3. For two variants, the poles of the δ-Al_2O_3 diffraction pattern in Figure 78 would be near [1$\bar{2}$3] and a third would be near the [116] pole of the third orthogonal variant.

The orientation relationship between δ-Al_2O_3 scales formed on (012) oriented metal do not have a low index plane parallel to the metal plane. However, the same crystallographic directions as in the cubic oxide orientation relationship are aligned in the δ-Al_2O_3-metal orientation relationships. These directions are the $\langle 100 \rangle$ metal and the [110] or [103] δ-Al_2O_3 directions.

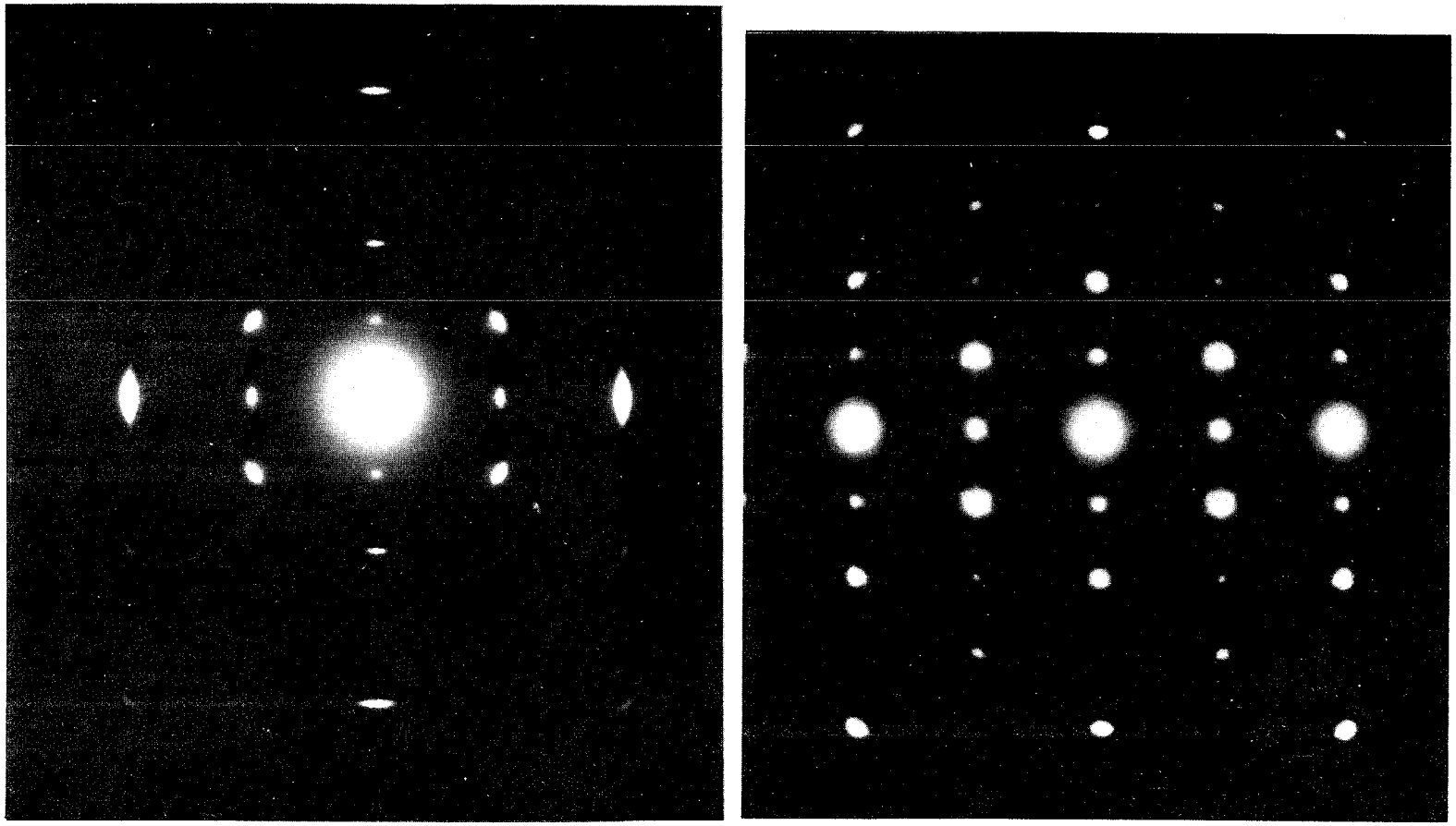

a) b)

Figure 78

Diffraction patterns of oxide formed on (012) metal to show the same symmetry between the a) $NiAl_2O_4$ found after 0.1 hours and b) δ-Al_2O_3 found after 10.0 hours.

This gives a strong indication that orientation relationships are more dependent upon alignment of close-packed directions than on the superposition of close-packed planes.

c) (011) metal orientation

More detailed research has been performed on this orientation for body-centered cubic metals because of the frequency of classical BCC-FCC orientation relationships occurring on this metal orientation. Both the Nishyama-Wassermann (N-W) and the Kurdjumov-Sachs (K-S) orientation relationships have been found to occur for many BCC-FCC systems. The N-W relationship, given as:

$$\begin{matrix}(011)_m & || & (\bar{1}11)_{ox} \\ [100]_m & || & [110]_{ox}\end{matrix}$$

is most prominent for the (011) metal orientation in this study and is found for all oxidizing conditions. The K-S relationship;

$$\begin{matrix}(011)_{metal} & || & (\bar{1}11)_{oxide} \\ [1\bar{1}1]_{metal} & || & [01\bar{1}]_{oxide}\end{matrix}$$

involves the same close-packed planes but is rotated by about 5.3° to align the two given directions. Many studies have indicated these two orientation relationships for

BCC-FCC systems.[82,84,87-91] However, no literature could be found which cited the third orientation relationship found on (011) metal in this study, namely:

$$(011)_{metal} \;||\; (\bar{1}11)_{oxide}$$
$$[21\bar{1}]_{metal} \;||\; [01\bar{1}]_{oxide}$$

This orientation relationship, as well as the K-S relationship, was only found at 0.1 hours oxidation time between spinel and the metal.

An obvious question arose as to why all three orientation relationships are present after 0.1 hours but only the N-W relationship is found after 1.0 hours oxidation time. Both the K-S and N-W relationship have been found previously in BCC-FCC systems. According to Knowles et al,[79] the predicted orientation relationship for a system having a lattice constant ratio of 1.39 ($0.5a_o$ γ-Al_2O_3/a_o β-NiAl) should be the same close-packed (111) oxide plane rotated approximately 1.4° away from the N-W relationship. A rotation of 5.3° would result in the K-S relationship.

A detailed examination of electron diffraction patterns provides some insight. Figure 45 shows that for a 0.1 hour oxidized specimen, the oxide orientations are centered around

either the N-W relationship or the third relationship mentioned. The intensity of the diffraction arcs decreases as the angle from the exact orientation relationships is increased. The majority of the oxide crystallites should then be found to have an orientation very near the exact orientation relationship. The changes in Moire fringe directions of oxide crystallites in Figure 79 are an indication of the amount of misorientation. The misorientation angles of Moire fringes were measured from a number of crystallites in Figure 79. The results are plotted in Figure 80 and are shown to follow a normal distribution with the mean to be near 0° away from the exact orientation relationship. The misorientation of islands away from the exact orientation relationship could result from strain changes developed upon misfit dislocation formation as mentioned by Matthews.[92]

The same degree of misorientation is found for the N-W relationship after 1.0 and 10.0 hours but not for the K-S relationship. Figure 48 shows that a complete range of orientation exists between the K-S and N-W relationships. Therefore, even though the K-S relationship is found in this one case, it is not the predominant orientation relationship. In fact, it appears to be less predominant than the third orientation relationship mentioned, both of which are secondary to the N-W relationship.

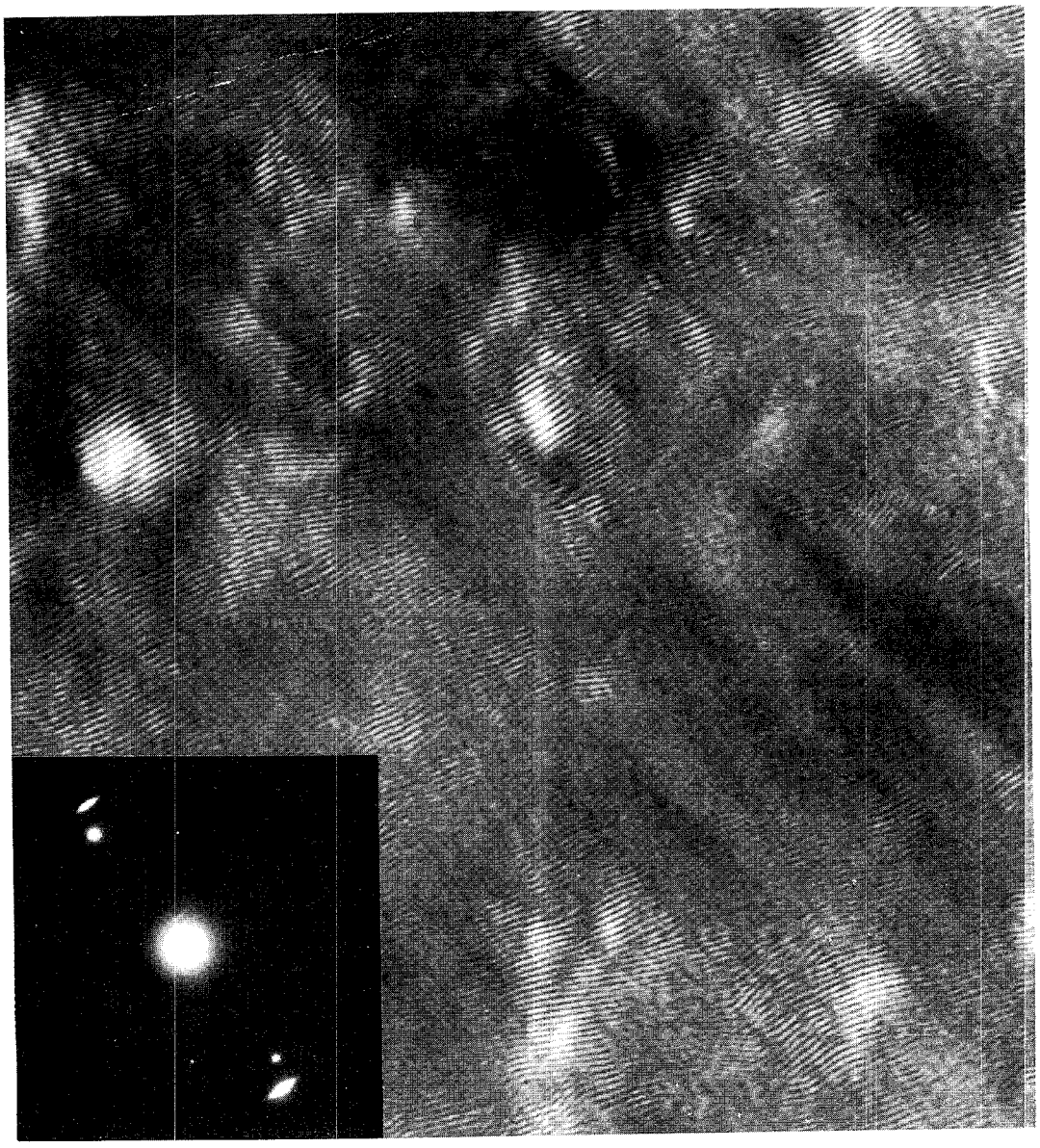

Figure 79

High resolution Moire fringe pattern between metal and oxide formed on an (011) metal orientation. The majority of fringes are aligned near the major orientation relationship.

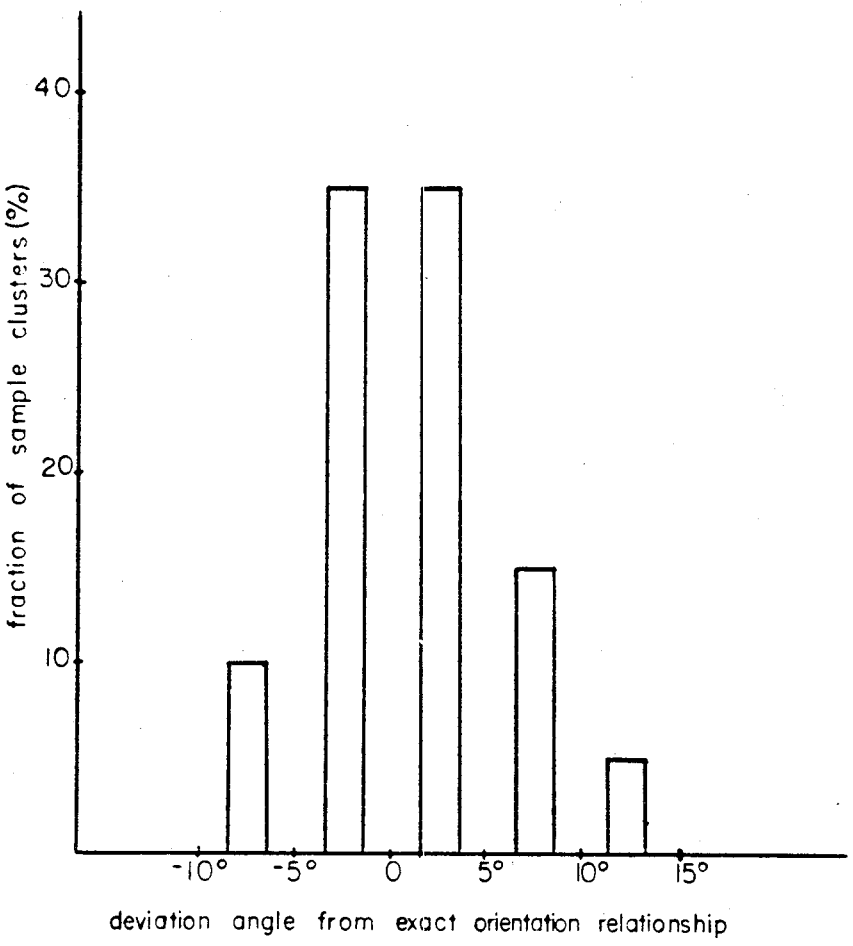

Figure 80

Plot of deviations in Moire fringe directions from the N-W orientation relationship taken from most of the fringe clusters in Figure 79.

All three orientation relationships were studied according to the computer model developed in this study. The plot of near coincident sites for the N-W relationship is shown in Figure 81. The repeat grid which represents a unit cell of the O-lattice is clearly indicated. These results agree with the geometry of those found for the N-W relationship in other interface studies.[78,91] As in the Bain relationship, the cell walls represent possible misfit dislocation arrays. From Figure 82 which shows interface dislocations on an (011) metal specimen, the dislocations are along ⟨111⟩ metal directions. The ⟨111⟩ metal directions are the close-packed directions of the B2 structure, but do not correspond with the misfit dislocation directions in the computer simulation. The interface dislocations may then be a result of a combination of misfit dislocations as in a stepped configuration mentioned by Hall et al.[91] The values for σ and ρ, the parameters used to measure the degree of overlap for each orientation relationship, are just mentioned now but will be discussed after the results of the other orientation relationships are presented. For the N-W relationship, $\sigma = 1.66 \times 10^{-3}$ and $\rho = 1.31 \times 10^{-5}$ Å^{-2}.

Both parameters are slightly less than that found for the Bain relationship.

C-3

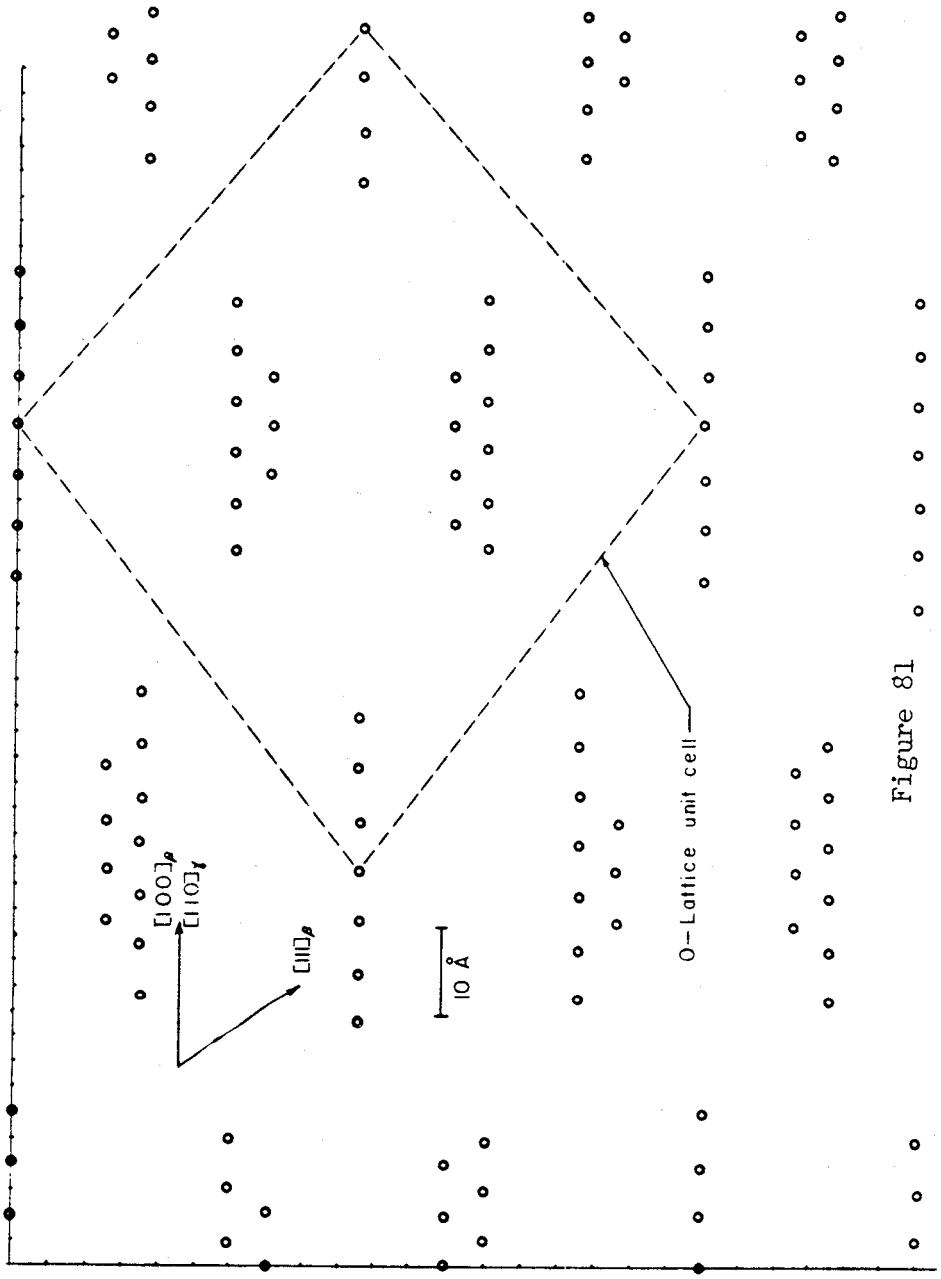

Figure 81

Computer model simulation of aluminum lattice site matching for a Nishyama-Wassermann relationship between β-NiAl and γ-Al_2O_3 on an (011) metal orientation.

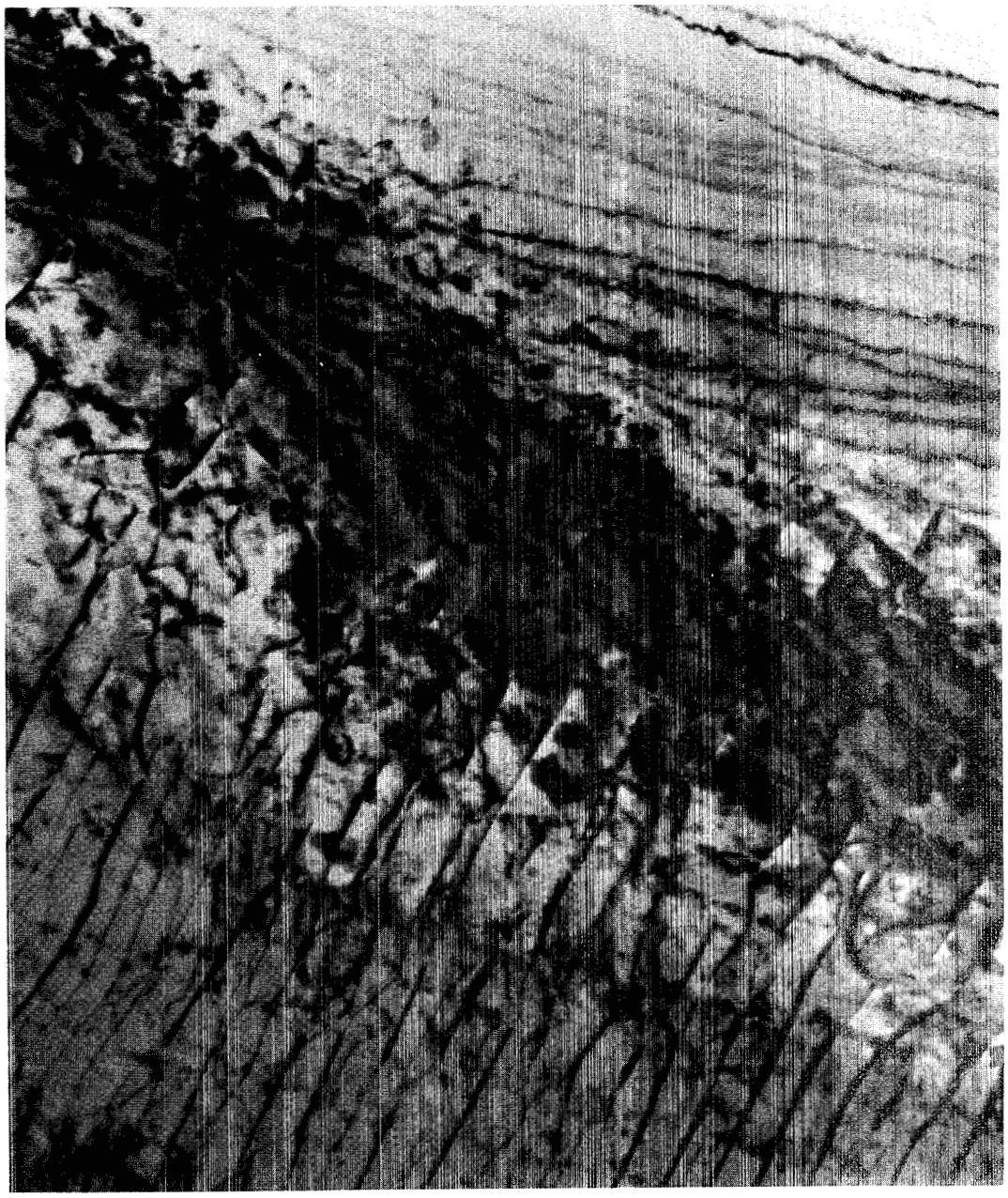

Figure 82 — 0.5 μm

Interface dislocations in an oxidized (011) metal specimen. The dislocation line directions are predominantly along ⟨111⟩ metal directions, with a spacing of about 0.2 μm.

For the K-S relationship, the results are shown in Figure 83. Wide bands of good fit regions are along the metal [111] direction. This agrees with both the close-packed metal direction of the orientation relationship, and also with interfacial dislocations which would run parallel to the wide bands. Each band consists of stepped regions of good fit, the general direction of each step being the [311] metal direction. The O-lattice was determined by extrapolation of nearest neighbor distances as in the Bain relationship. The outlined grid represents only 1/2 the unit cell of the O-lattice because the length dimension parallel to the [111] metal direction was out of the range of the calculations. The regions of best fit agree with the geometry of those found by Hall et al[91]. For the K-S relationship, $\sigma = 1.60 \times 10^{-3}$ and $\rho = 1.23 \times 10^{-5}$ Å.

The plot of the results for the third orientation relationship found on (011) metal is shown in Figure 84. Even though there is some feature to the distribution of near coincident sites, no repeat distance was found determinable for the dimensions of the computer simulation. There appears to be regions of worst fit where misfit dislocations would be expected. Again, the direction of misfit dislocations are along metal [111] directions. The values of σ and ρ were averaged by using the entire calculated area because no unit cell was evident. For

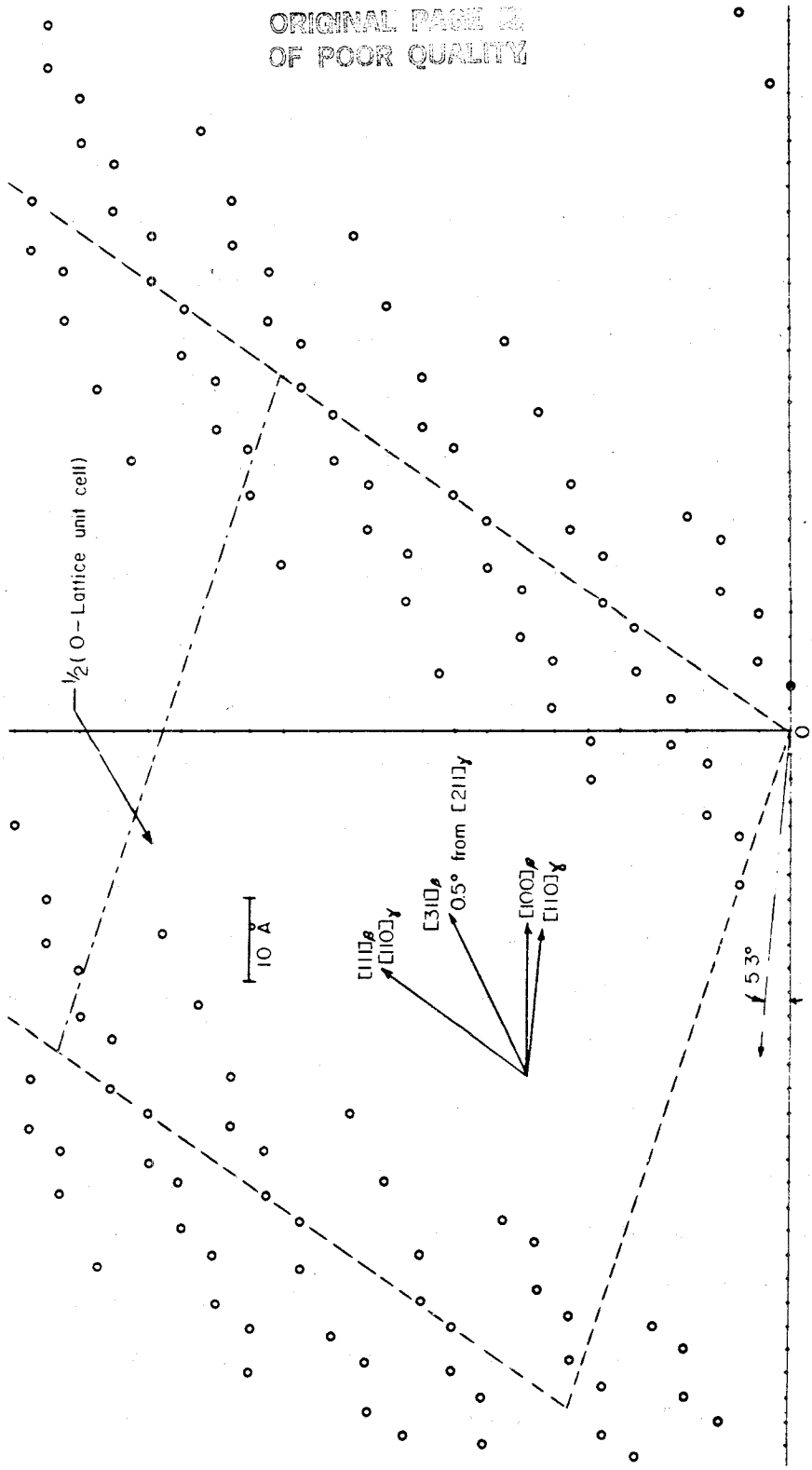

Figure 83

Computer model simulation of aluminum lattice site matching for a Kurdjumov-Sachs relationship between β-NiAl and γ-Al_2O_3 on an (011) metal orientation.

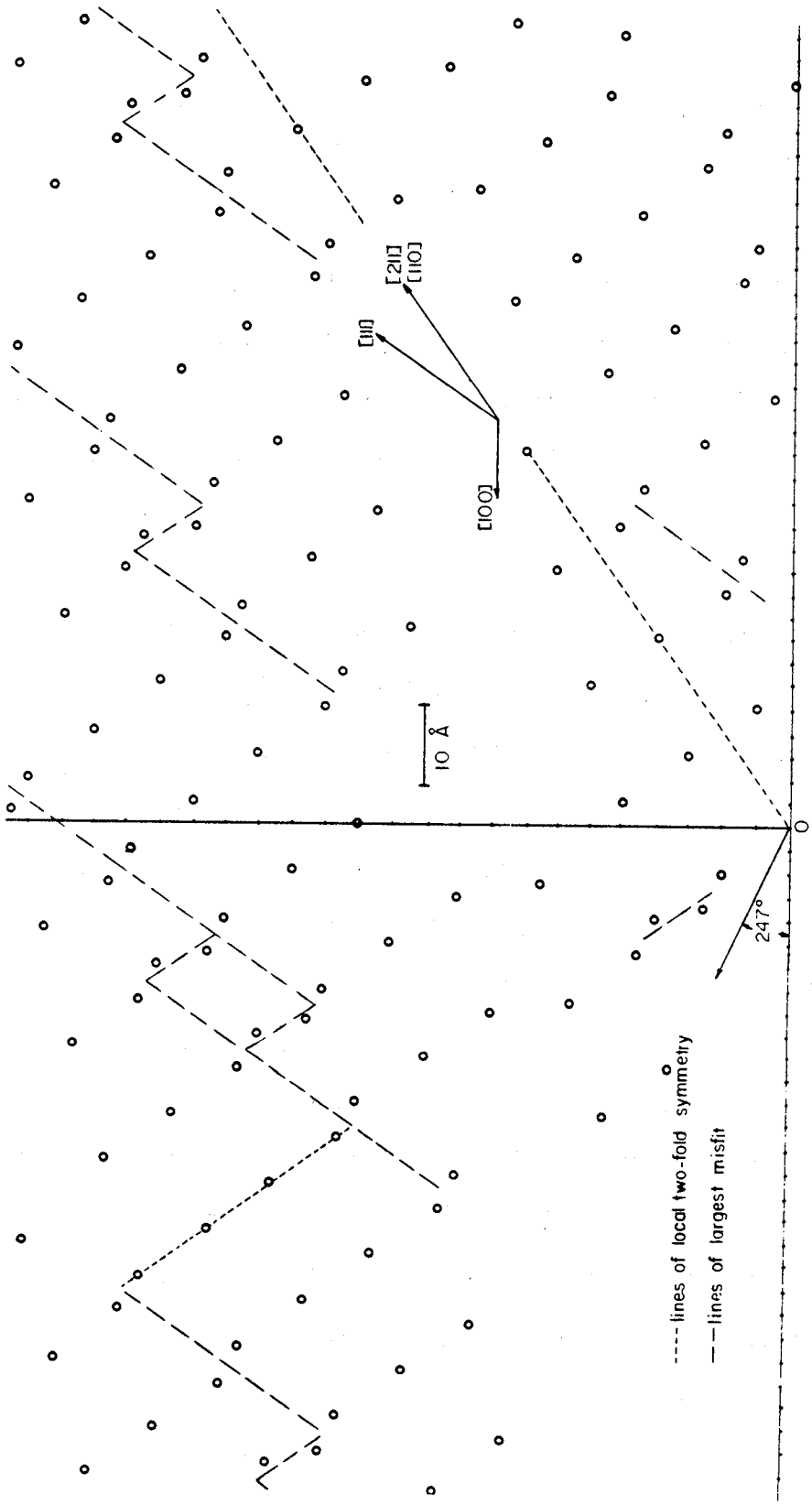

Figure 84

Computer model simulation of aluminum lattice site matching for the third orientation relationship between β-NiAl and γ-Al_2O_3 found on (011) metal orientations.

this orientation relationship, $\sigma = 1.76 \times 10^{-3}$ and $\rho = 1.45 \times 10^{-5}$ $\mathring{A}^{-2}$.

The differences among the plots of Figures 81, 83, and 84 are in the periodic distribution of near coincident sites. The values of σ and ρ, which were intended to be used as a comparison for the favorability of a particular orientation relationship, did not differ significantly from one orientation relationship to the other (see Table VIII). To test the validity of this comparison, a near coincident site lattice was generated for an orientation relationship 15° away from the N-W relationship. This puts the close-packed oxide direction exactly in between the K-S relationship and the third orientation relationship mentioned. This lattice is plotted in Figure 85. As can be seen, there appears to be no periodicity to the array of points in the calculated area. No regions of worst fit are noticed as in Figure 84, even though the overall distribution of near coincident points compares best with the third orientation relationship. The σ and ρ values of $\sigma = 1.77 \times 10^{-3}$ and $\rho = 1.35 \times 10^{-5}$ $\mathring{A}^{-2}$ respectively, are not significantly different than those values for the actual orientation relationships found in this study.

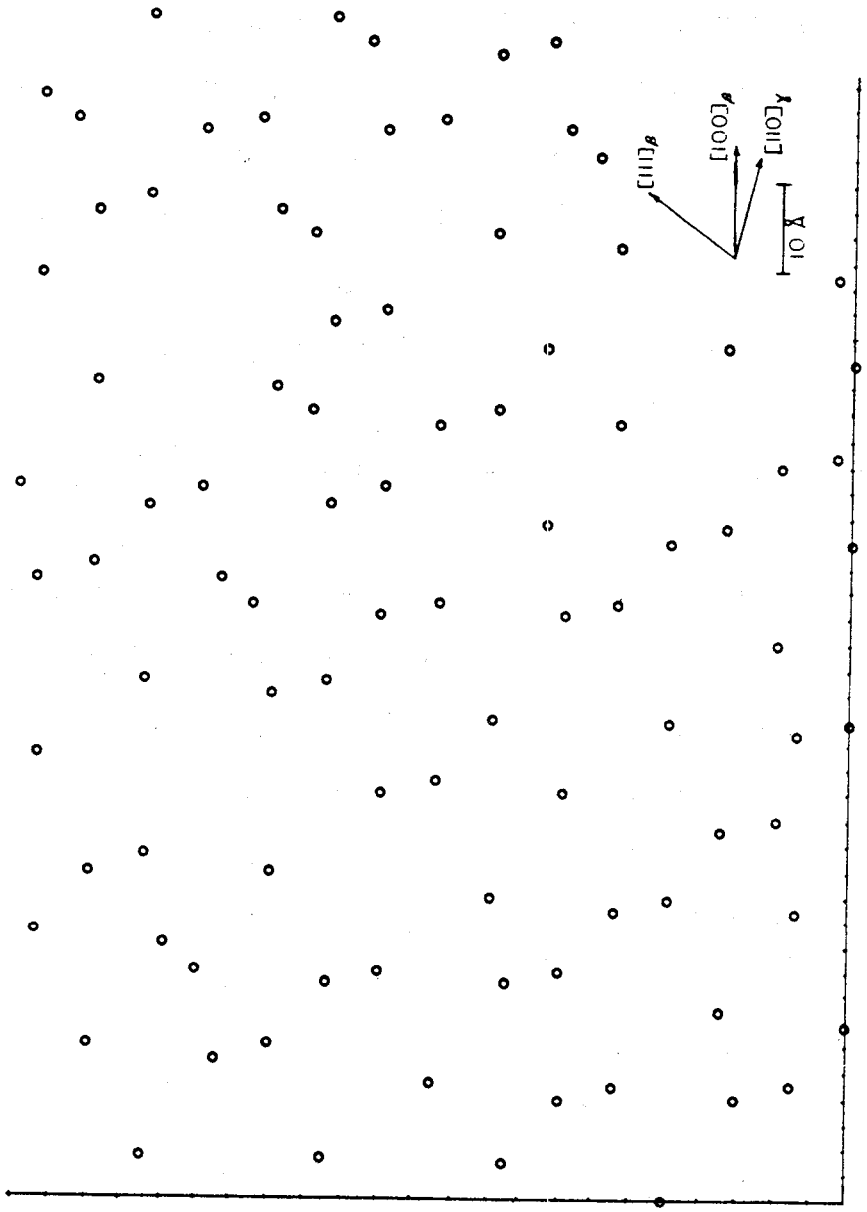

Figure 85

Computer model simulation of aluminum lattice site matching for an orientation relationship exactly in-between the Kurdjumov-Sachs and the third orientation relationship on (011) metal.

Table VIII lists values of σ and ρ found for all computer simulated orientation relationships. The values are also calculated for nearest neighbor cut-off distances of 0.42 Å and 0.21 Å. These values are included to determine if there is a tendency for certain orientation relationships to have a few near coincident sites of very good fit rather than many sites of poorer fit. As can be seen by comparing values for those orientation relationships that were found in this study and including the one not found, the parameters of σ and ρ exhibit no significance trend. However, changes may occur if the same calculations are carried out on arbitrary orientations not containing close-packed planes or directions. The merit of this computer model might lie simply in the determination of the periodic arrays of near coincident sites. There are definitely crystallographic features involving misfit dislocation regions for all orientation relationships, except for the 15° off-relationship used to test the model. Otherwise, this model was not able to predict the preference for one orientation relationship over another. However, the results might change if the calculations were carried out between β-NiAl and $NiAl_2O_4$, allowing for cation sublattices and a slightly larger lattice constant than γ-Al_2O_3.

TABLE VIII

Values of σ(overlap area/ grid area) and ρ(# of near coincident sites/ grid area) for the five computer models in this study.

	NNC(Å)^3	Overlap Area(Å)^2	Grid Area(Å)^2 x 10^3	σ x 10^{-3}	coincident sites / unit cell	ρ x 10^{-6}
Bain						
	0.6	17.45	8.76	1.99	76	17.29
	0.4	12.28	--	1.40	38	6.08
	0.2	3.57	--	0.41	8	0.37
NW						
	0.6	6.12	3.68	1.66	29	13.11
	0.4	4.27	--	1.16	13	4.09
	0.2	0.96	--	0.26	2	0.14
KS						
	0.6	10.17	6.36	1.60	49	12.34
	04	7.07	--	1.11	22	3.85
	0.2	2.51	--	0.39	6	0.37
SD[1]						
	0.6	43.25	24.59	1.76	203	14.53
	0.4	31.05	--	1.26	94	4.83
	0.2	11.78	--	0.48	27	0.53
WC[2]						
	0.6	26.04	14.68	1.77	112	13.53
	0.4	17.22	--	1.17	53	4.23
	0.2	6.48	--	0.44	15	0.45

1) third orientation relationship found on (011) metal

2) orientation relationship halfway between KS and SD

3) nearest neighbor cutoff

Given the three orientation relationships found on (011) metal, the differences in lattice constants along cation close-packed directions were calculated to determine their significance or favorability of the orientation relationships in this study. Table IX lists the percent difference for the two pairs of parallel directions found for each orientation relationship. Both the N-W and the third orientation relationship have values along one pair of parallel directions which are only 3% apart. The other set of parallel directions has a large misfit for the N-W relationship (26%) as compared to the third orientation relationship (19%). The K-S relationship has larger misfits of 37% and 19% and appears to be less favorable. This agrees with electron diffraction results in that the orientation relationship is quite diffuse. A range of oxide orientations between the K-S and N-W relationships are present in the diffraction pattern of Figure 48. The favorability of the third orientation relationship over the N-W over the K-S in terms of percent misfit along cation close-packed directions, is also portrayed in the σ and ρ values of Table VIII.

d) (111) metal orientation

Because of the threefold symmetry of the (111) plane of β-NiAl, three variants of oxide having the same orientation relationships grew on the metal surface.

TABLE IX

Percent misfit in cation close-packed directions for the orientation relationships in this study.

Parallel Directions $\frac{[hkl]_m}{[hkl]_{ox}}$	$\frac{[100]}{[1\bar{1}0]}$	$\frac{[\bar{1}10]}{[100]}$	$\frac{[\bar{1}10]}{[11\bar{2}]}$	$\frac{[02\bar{1}]}{[33\bar{3}]}$	$\frac{[2\bar{1}1]}{[10\bar{1}]}$	$\frac{[2\bar{1}\bar{1}]}{[2\bar{1}1]}$	$\frac{[\bar{1}11]}{[0\bar{1}1]}$	$\frac{[\bar{1}11]}{[\bar{1}2\bar{1}]}$	
(001) metal									
$(001)_m \parallel (001)_{ox}$	3%	3%							Bain
(012) metal									
$(012)_m \parallel (11\bar{2})_{ox}$	3%			13%					
(011) metal									
$(011)_m \parallel (1\bar{1}1)_{ox}$	3%		26%						NW
						37%	19%		KS
					19%			3%	SD
(111) metal									
$(\bar{1}11)_m \parallel$ near $(02\bar{1})_{ox}$		3%					19%		
$(\bar{1}11)_m \parallel (01\bar{1})_{ox}$		3%			19%				Ref. 86

This orientation relationship, with three variants, is given as:

$$(111)_{metal} \;||\; \text{near } (021)_{oxide}$$
$$[1\bar{1}0]_{metal} \;||\; [100]_{oxide}$$
$$[01\bar{1}]_{metal} \;||\; [100]_{oxide}$$
$$[\bar{1}01]_{metal} \;||\; [100]_{oxide}$$

A study by Wagner et al found this same orientation relationship to occur on a (111) face of oxidized iron.[82] The stereographic projection of the Bain relationship is shown in Figure 86 to demonstrate the rotation of the oxide projection which will give this orientation relationship. A rotation of 9.7° around the [110] metal direction will result in the orientation relationship. This translation leaves the [021] oxide pole about 1° away from the [111] metal pole. Two sets of parallel close-packed directions result from this rotation. They are:

$$[1\bar{1}0]_{metal} \;||\; [100]_{oxide}$$

and

$$[\bar{1}\bar{1}1]_{metal} \;||\; [0\bar{1}1]_{oxide}$$

The lattice constant differences in those directions are 3% and 19% respectively. When compared to the oxide (011) metal orientation, these values are the same for the third orientation relationship found on (011) metal.

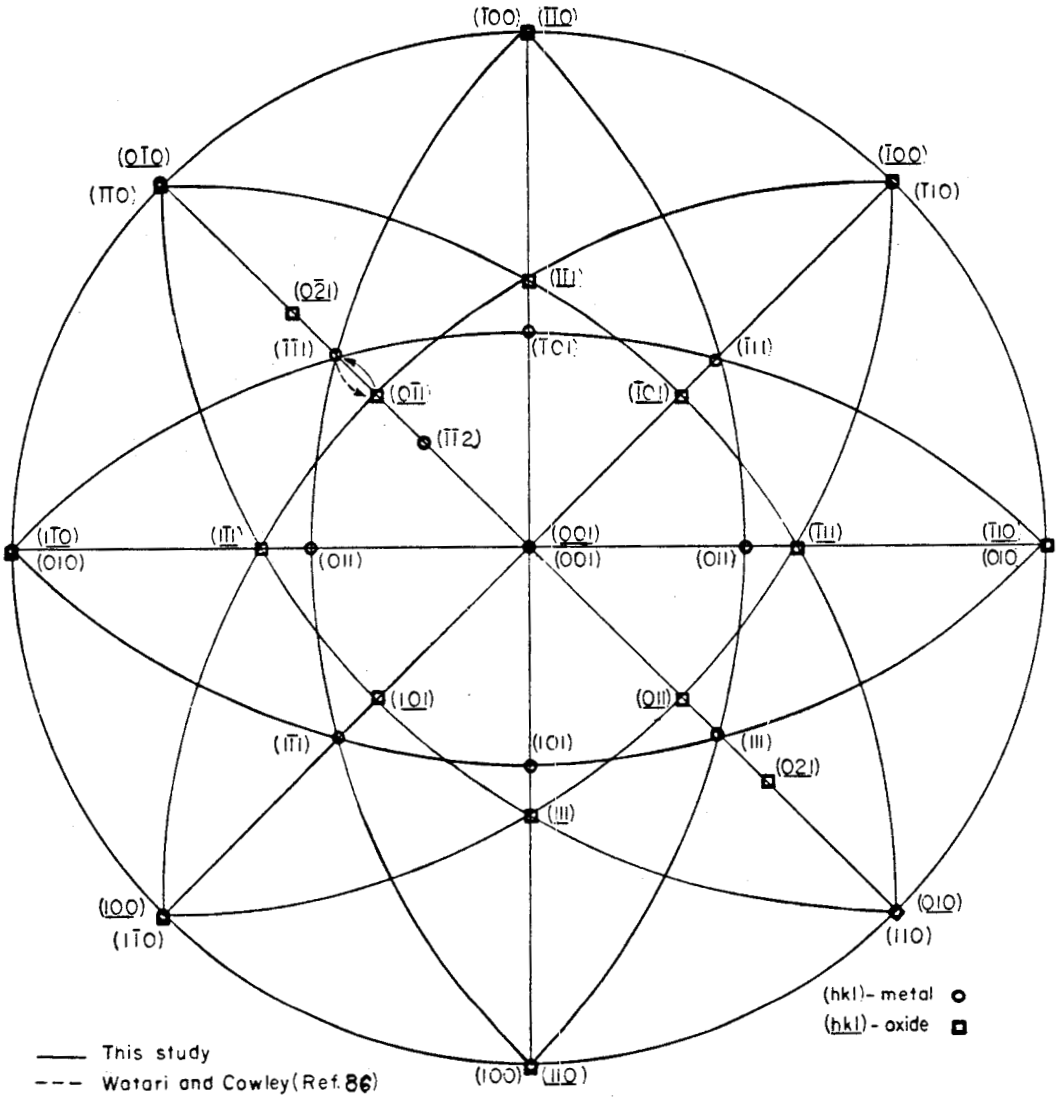

Figure 86

Stereographic projection of the Bain relationship to show the translations of the projections needed to result in the orientation relationships found on (111) metal orientations.

A similar orientation relationship to the one found in this study can be obtained by a rotation of the oxide stereographic projection the same 9.7°, but in the opposite direction to that mentioned beforehand. This places a [011] oxide pole on top of a [111] metal pole. When the [111] metal pole is made to be the projection normal, the same threefold symmetry can be realized and the oxide would have three variants. Watari and Cowley found this orientation relationship to occur on oxidized chromium where a Cr_2O_3 spinel like phase was formed.[88] This second orientation relationship is given as:

$$(111)_{metal} \;||\; (011)_{oxide}$$
$$[1\bar{1}0]_{metal} \;||\; [100]_{oxide}$$

One pair of close-packed directions remains the same as in the orientation relationships found in this study. However, the second pair is given as:

$$[\bar{1}\bar{1}2]_{metal} \;||\; [0\bar{1}1]_{oxide}$$

and also has a lattice constant difference of 19% in that direction.

Boggs et al found that on oxidized (111) iron, the first orientation relationship found in this study occurred when the single crystal was oriented 2° in the $[2\bar{1}\bar{1}]$ direction and 1° in

the [011] direction.[89] The orientation relationship seen by Watari and Cowley occurred when the single crystal was tilted less than 2° toward the $[2\bar{1}\bar{1}]$ direction away from the exact (111) orientation. This shows a high sensitivity to slight orientational differences in the initial substrate orientation. The specimen geometry in this study was not uniform enough to allow changes of 1° or so to be measured with accuracy.

4) Summary of orientation relationships

Figure 87 shows the stereographic triangle for a Bain relationship and indicates the rotations of the oxide projection needed to result in the orientation relationships found for each metal orientation. All rotations are seen to occur in major crystallographic directions. The interesting feature is that the same 9.7° rotation is needed to obtain the N-W relationship on (011) metal and the orientation relationship found on (111) metal. However, the direction of rotation is changed by 35.3°, the angle between the (111) and (011) planes.

Table IX lists the percent difference in lattice constants along parallel directions for all the orientation relationships. In all cases, except for the K-S relationship, at least one pair of directions has a difference of only 3%. This

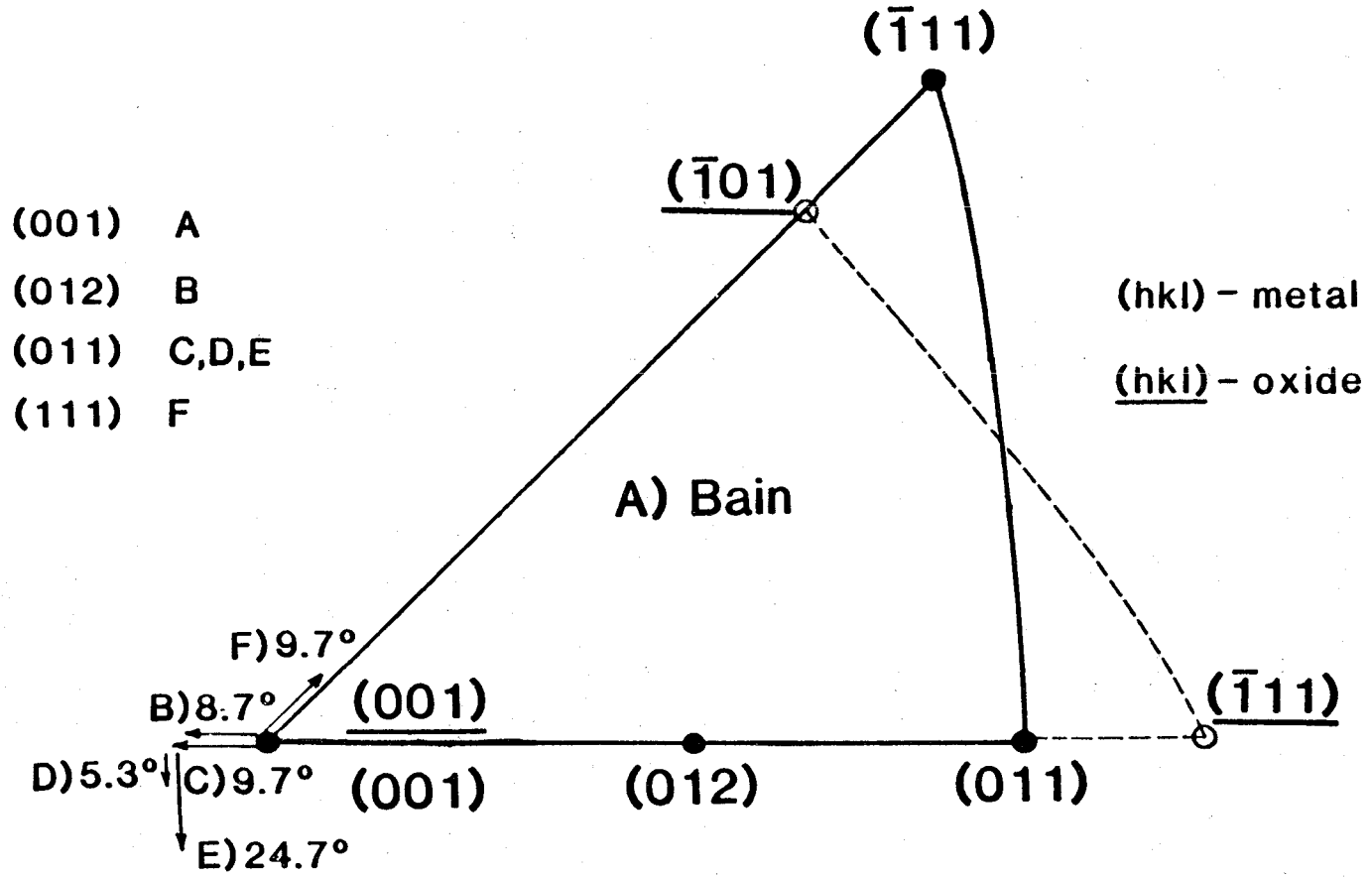

Figure 87

Stereographic triangles of the Bain relationship for metal and oxide. Arrows near (001) represent translations of the oxide projection needed to result in all of the orientation relationships found in this study between metal and cubic oxides.

difference is usually accommodated by the parallelism of the [100] or [110] directions of either phase. For the third orientation relationship on (011) metal, the 3% difference results from the [111] metal direction and the [112] oxide direction being parallel. The orientation relationships can be considered to be primarily dependent upon alignment of parallel directions where the misfit along those directions is a minimum.

Orientation relationships can explain why δ-Al_2O_3 is stable on (001) and (012) metal orientations but not stable on (011) and (111) orientations. The asymmetry of the δ-Al_2O_3 structure precludes more than one oxide close-packed direction from simultaneously aligning with other close-packed directions in the (011) or (111) metal planes. The inability of δ-Al_2O_3 to superimpose properly on the (011) and (111) metal planes along two close-packed metal directions results in a stabilization of the cation sublattice of the cubic spinel structure. Thus, γ-Al_2O_3 is the stable oxide phase on the (011) and (111) metal orientations.

C) Transient effects on the formation of α-Al_2O_3 on β-NiAl

This study has thus far dealt only with the transient stages of oxidation of alumina forming alloys. The major goal of this project, however, is to characterize the transient oxidation stages so that the formation of α-Al_2O_3 or the transformation to this stable phase can be controlled. Work by Felton and Pettit,[24] Hindam and Smeltzer[25] and Rybicki and Smialek[21] and Smialek and Gibala[93] has laid a foundation for the detailed study of α-Al_2O_3 formation from transient oxides on alumina forming alloys.

In the studies by these authors, oriented α-Al_2O_3 was predicted on β-NiAl and Pt-Al at temperatures greater than 1000°C. Regions of oriented α-Al_2O_3 corresponded to the oxide grain size and were surrounded by ridges of fine-grained random α-Al_2O_3. No results on the actual preferred orientation of the oxide grains were obtained, however.

Many studies have found epitaxially oriented α-Fe_2O_3 and α-Cr_2O_3 which are isostructural with α-Al_2O_3. However, the majority of the studies find that the α-phase is epitaxially related to the spinel phase and not necessarily to the metal.

The most prominent orientation relationship found has been:

$$\{111\}_{\text{spinel}} \;||\; (0001)_{\alpha\text{-}M_2O_3}$$
$$\langle 110\rangle_{\text{spinel}} \;||\; \langle 11\bar{2}0\rangle_{\alpha\text{-}M_2O_3}$$

The {111} planes of spinel have a hexagonal structure as does the (0001) basal plane of the α-M_2O_3 oxides. This relationship been found for oxidized iron[63,64,83,89] and for oxidized chromium.[88] Smialek found this orientation relationship for oxidized NiCrAl alloys.[18,22] This orientation relationship is said to occur because the anion lattices of the two structures in those orientations are similar. The final transformation to α-Al_2O_3 involves a restructuring of the cubic anion lattice to a near hexagonal anion lattice, therefore suggesting this orientation relationship.

Because of the strong orientation relationship between the {111} spinel plane and the (011) metal plane, epitaxially oriented α-Al_2O_3 would be expected on {011} planes of BCC metals. In the studies mentioned above, the {111} spinel orientations were obtained by oxidation of the (011) metal faces. In a study of CrPt growth on sapphire by Baglin and d'Heurle,[90] no cubic oxide phase was present yet the predicted orientation relationship occurred. This would indicate that there is a tendency for the hexagonal anion lattice of α-M_2O_3

to align itself with the metal much in the same way that the cation sublattice of the spinel phases are oriented upon nucleation.

Because of the high negative heat of formation and the relatively slow cation diffusion processes, α-Al_2O_3 nucleates and grows at the metal-oxide interface unlike α-Fe_2O_3 on oxidized iron. Therefore, both the metal and cubic oxides can play a role in the orientation of the α-Al_2O_3. Both should tend to cause a basal plane orientation of α-Al_2O_3 when an (011) metal interface is oxidized.

The nucleation of α-Al_2O_3 at the metal-oxide interface is not the same as the transformation from the transient Al_2O_3 phases to α-Al_2O_3. A restructuring of the anion lattice of the cubic oxide is involved when this occurs. This restructuring involves a 14% decrease in volume and thus induces tensile stresses in the pre-existing oxide layer. Even if the oxide is oriented, the tensile stresses would still develop. Therefore, it appears that the initial oxide layer could have little effect once the transformation to α-Al_2O_3 begins to occur.

Because the experiments were ended after ten hours of oxidation time, the transformation to α-Al_2O_3 had not yet begun. Even

so, there exist differences in oxide phases on different metal orientations. γ-Al_2O_3 exists on (011) and (111) metal orientations whereas δ-Al_2O_3 is present on (001) and (012) metal orientations. The γ- Al_2O_3 on (011) metal appears to be the best candidate to obtain oriented α-Al_2O_3. However, does γ-Al_2O_3 transform to α-Al_2O_3 or is γ-Al_2O_3 stabilized on (011) metal until the final transformation? If γ-Al_2O_3 transforms to δ-Al_2O_3, a different orientation of metal might form δ-Al_2O_3 having an orientation more suitable for oriented α-Al_2O_3 formation.

The transient oxidation of β-NiAl could therefore be an important factor in the final structure of the stable α-Al_2O_3 scale. The high degree of preferred orientation in the transient stages of oxidation might be carried over as α-Al_2O_3 begins to form. Single crystal or even highly textured α-Al_2O_3 scales should possess the optimium slow growth rate characteristics. The key to the attainment of these highly desirable α-Al_2O_3 scales might lie in optimizing the transient stages of oxidation on alumina forming alloys.

CONCLUSIONS

Results of this study indicate that the transient oxidation of NiAl+Zr is highly dependent on the metal substrate orientation. The difference in oxidation characteristics with metal orientation could be a major factor in obtaining slow growing, "single crystal" α-Al_2O_3 scales on these alloys.

At 800°C, for oxidizing times up to 10.0 hours, transient oxides based on the cubic spinel structure form on all metal orientations. The oxides are highly epitaxially related to the metal substrate. The strong epitaxy is a result of minimal amounts of mismatch along cation close-packed directions in both the metal lattice and the oxide cation sublattice.

The (001) and (012) metal orientations produce similar oxidation results. The oxide scales are initially $NiAl_2O_4$ which becomes a minor oxide phase as δ-Al_2O_3 forms and grows by outward cation diffusion. The orientation relationships between metal and oxide are based upon the close-packed [100] metal and [110] oxide directions where the lattice parameter mismatch is approximately 3% along these directions.

On (011) and (111) metal orientations, $NiAl_2O_4$ does not become a secondary oxide phase as quickly as on the other metal orientations. Also, γ-Al_2O_3, and not δ-Al_2O_3, becomes the predominant oxide phase. The orientation relationships on these metal orientations again follow the same principles of cation close-packed directions and appear to play a major role in the attainment of γ-Al_2O_3 versus δ-Al_2O_3.

δ-Al_2O_3 has a tetragonal spinel structure with an average c/a ration of 2.9. This appears to be the thermodynamically desirable phase at 800°C on β-NiAl. However, structural stability of γ-Al_2O_3 on (011) and (111) metal orientations overrides the thermodynamic favorability of δ-Al_2O_3.

The orientation relationships in this study are based on classical BCC-FCC orientation relationships. On (001) metal, the Bain relationship exists and is given as:

$$\begin{matrix} (001)_{metal} & || & (001)_{oxide} \\ [100]_{metal} & || & [110]_{oxide} \end{matrix}$$

On (012) metal, an orientation relationship occurs which is less than 1° away from the classical Nishyama-Wassermann relationship. The relationship is given as:

$$(012)_{metal} \;||\; (112)_{oxide}$$
$$[100]_{metal} \;||\; [110]_{oxide}$$

Three orientation relationships occur on (011) metal and include the Nishyama-Wassermann relationship, and the Kurdjumov-Sachs relationship and a third orientation relationship which appears to be more favorable than the Kurdjumov-Sachs but less favorable than the Nishyama-Wassermann relationship. These are given as:

(N-W)
$$(011)_{metal} \;||\; (\bar{1}11)_{oxide}$$
$$[100]_{metal} \;||\; [110]_{oxide}$$

(K-S)
$$(011)_{metal} \;||\; (\bar{1}11)_{oxide}$$
$$[11\bar{1}]_{metal} \;||\; [01\bar{1}]_{oxide}$$

(S-D)
$$(011)_{metal} \;||\; (\bar{1}11)_{oxide}$$
$$[21\bar{1}]_{metal} \;||\; [01\bar{1}]_{oxide}$$

On (111) metal, the orientation relationship that occurs is:

$$(111)_{metal} \;||\; \text{near } (021)_{oxide}$$
$$[1\bar{1}0]_{metal} \;||\; [100]_{oxide}$$

Computer modeling of these orientation relationships with a simplified geometrical approach, did not result in the ability to predict the energetically favorable orientation relationship.

Further work is needed to determine the extent of the metal orientation effect on the oxidation rates of alumina forming alloys. Optimium use of this effort could result in the formation of desirable α-Al_2O_3 scales with the superior property of growth of the oxide scale controlled more so by lattice diffusion.

REFERENCES

1 High-Temperature Oxidation-Resistant Coatings, NAS-NAE, Washington, D.C., 1970.

2. C. A. Barrett, C. E. Lowell: "Resistance of Ni-Cr-Al Alloys to Cyclic Oxidation at 1100°C and 1200°C," Oxid. Met., 11, p. 199 (1977).

3. L. J. Ebert, A. J. Kumnick: "Stress Generation in Thermally Grown Oxide Films," Final Report, NASA Grant No. NAG 3-49, 1981.

4. C. E. Lowell, R. G. Garlick, B. Henry: "Thermal Expansion in the Ni-Cr-Al and Co-Cr-Al Systems to 1200°C Determined by High-Temperature X-Ray Diffraction," Met. Trans. A, 7A, p. 655 (1976).

5. F. A. Golightly, F. H. Stott, F. C. Wood: "The Influence of Yttrium Additions on the Oxide-Scale Adhesion to an Iron-Chromium-Aluminum Alloy," Oxid. Met., 10, p. 163 (1976).

6. J. K. Tien, F. S. Pettit: "Mechanisms of Oxide Adherence on Fe-25Cr-4Al (Y or Sc) Alloys," Met. Trans., 3, p. 1587 (1972).

7. J. D. Kuenzly, D. L. Douglass: "The Oxidation Mechanisms of Ni_3Al Containing Yttrium," Oxid. Met., 8, p. 139 (1974).

8. I. M. Allam, D. P. Whittle, J. Stringer: "Improvements in Oxidation Resistance by Dispersed Oxide Addition: Al_2O_3 - Forming Alloys," Oxid. Met., 13, p. 381 (1978).

9. I. M. Allam, D. P. Whittle, J. Stringer: "The Oxidation Behavior of CoCrAl Systems Containing Active Element Additions," Oxid. Met., 12, p. 35 (1978).

10. C. A. Barrett, A. S. Khan, C. E. Lowell: "The Effect of Zirconium on the Cyclic Oxidation of NiCrAl Alloys," J. Electrochem. Soc., 128, P. 25 (1981).

11. C. Wagner: "Formation of Composite Scales Consisting of Oxides of Different Metals," J. Electrochem. Soc., 103, p. 627 (1956).

12. G. R. Wallwork: "The Oxidation of Alloys," Rep. Prog. Phys. 39, p. 401 (1976).

13. B. H. Kear, F. S. Pettit, D. E. Fornwalt, L. P. Lemaire: "On the Transient Oxidation of a Ni-15Cr-6Al Alloy," Oxid. Met., 3, p. 557 (1971).

14. F. S. Pettit: "Oxidation Mechanisms for Nickel-Aluminum Alloys at Temperatures Between 900° and 1300°C," Trans. Met. Soc. AIME, 239, p. 1296 (1967).

15. Y. Oishi, W. D. Kingery: "Self-Diffusion of Oxygen in Single Crystal and Polycrystalline Aluminum Oxide," J. Chem. Phys., 33, p. 480 (1960).

16. K. P. R. Reddy: "Oxygen Diffusion in Close Packed Oxide," Ph.D. Thesis, Case Western Reserve University, Cleveland, OH, 1979.

17. K. P. R. Reddy, J. L. Smialek, A. R. Cooper: "^{18}O Tracer Studies of Al_2O_3 Scale Formation on NiCrAl Alloys," Oxide. Met., 17, p. 429 (1982).

18. J. L. Smialek: "Microstructure of Al_2O_3 Scales Formed on NiCrAl Alloys," Ph.D. Thesis, Case Western Reserve University Cleveland, OH, 1981.

19. P. G. Shewmon: Diffusion of Solids, McGraw-Hill, New York, 1963, p. 172.

20. N. N. Khoi, W. W. Smeltzer, J. D. Embury: "Growth and Structure of Nickel Oxide on Nickel Crystal Faces," J. Electrochem. Soc., 122, p. 1495 (1975).

21. G. C. Rybicki, J. L. Smialek: NASA Lewis Research Center, unpublished research, 1982.

22. J. L. Smialek: "Some TEM Observations of Al_2O_3 Scales Formed on NiCrAl Alloys," NASA Technical Memorandum 79259.

23. E. F. Koch, G. Romeo: "Growth of Thin Oxide Scales for Electron Microscopy Studies," Metallography, 8, p. 509 (1975).

24. E. J. Felten, F. S. Pettit: "Development, Growth, and Adhesion of Al_2O_3 on Platinum-Aluminum Alloys," Oxide, Met., 10, p. 189 (1976).

25. H. M. Hindam, W. W. Smeltzer: "Growth and Microstructure of α-Al_2O_3 on β-NiAl," J. Electrochem. Soc., 127, p. 1639 (1980).

26. P. P. Budnikov, A. M. Ginstling, Principles of Solid State Chemistry, Translated from Russian, K. Shaw, Editor, p. 299, Gordon and Breach Sci. Pub., New York (1968).

27. W. H. Gitzen: Alumina as a Ceramic Material, American Ceramic Society, Columbus, Ohio, 1970.

28. E. J. W. Verwey: "The Structure of the Electrolytical Oxide Layer on Aluminum," Z. Kristallogr., 91, p. 317 (1935).

29. R. T. Phelps, E. A. Gulbransen, J. W. Hickman: "Electron Diffraction and Electron Microscope Study of Oxide Filems Formed on Metals and Alloys at Moderate Temperatures," Ind. Eng. Chem., 18, p. 391 (1946).

30. W. W. Smeltzer: "Oxidation of Aluminum in the Temperature Range 400°-600°C," J. Electrochem. Soc., 103, p. 209 (1956).

31. R. K. Hart, J. K. Maurin: "The Nucleation and Growth of Oxide Islands on Aluminum," Surf. Sci., 20, p. 285 (1970).

32. K. Thomas, M. W. Roberts: "Direct Observation in the Electron Microcope of Oxide Layers on Aluminum," J. Appl. Phys. 32, p. 70 (1961)

33. J. J. Randall, Jr., W. J. Bernard: "Some Observations on the Interfacial Topographies of Aluminum and Its Amorphous Oxide," J. Appl. Phys., 35, p. 1317 (1964).

34. G. M. Scamans, E. P. Butler: "In Situ Observations of Crystalline Oxide Formation During Aluminum and Aluminum Alloy Oxidation," Met. Trans. A, 6A, p. 2055 (1975).

35. A. J. Brock, M. J. Pryor: "The Kinetics of the Oxidation of Aluminum-Copper Alloys in Oxygen at High Temperature," Corr. Sci., 13, p. 199 (1973).

36. M. J. Dignam: "Oxide Films on Aluminum, I. Ionic Conduction and Structure," J. Electrochem. Soc., 190, p. 184 (1962).

37. G. C. Wood, B. Chattopadhyay: "Transient Oxidation of Ni-Base Alloys," Corros. Sci., 10, p. 471 (1970).

38. T. A. Ramanarayanan, M. Raghavan, R. Petkovic-Luton: "Al_2O_3 Scales on ODS Alloys," to be published in Proc. Symp. Corros. in Fossil Fuel Systems, 1983.

39. J. H. Westbrook: Intermetallic Compounds, John Wiley and Sons, Inc., New York, 1967.

40. H. Liu: "Radiation Damage in Ordered Alloys," Ph.D. Thesis, Case Western Reserve University, Cleveland, Ohio, 1981.

41. Powder Diffraction File, ASTM, Philladelphia, Penn., Card #'s 10-425, 10-339.

42. A. H. Heuer, T. E. Mitchell: "Further Discussion on the Space Group of Spinel," J. Phys. C.: Solid State Phys., 8, p. L541 (1975).

43. P. P. K. Smith: "Note on the Space Group of Spinel Minerals," Phil. Mag. B, 38, p. 99 (1978).

44. A. Parthasarathi: "Effects of Surface Oxidation on Vacancy Defects in Beta Nickel-Aluminum Alloys," Ph.D. Thesis, University of Illinois at Urbana-Champaign, Urbana, Illinois, 1980.

45. J. L. Smialek: "Oxide Morphology and Spalling Model for NiAl," Met. Trans. A, 9A, p. 309 (1978).

46. P. B. Hirsch, A. Howie, R. B. Nicholson, D. W. Pashley, M. J. Whelan: Electron Microscopy of Thin Crystals, Butterworth and Co., London, 1965.

47. W. L. Bell: "2½D Electron Microscopy: Through-Focus Dark-Field Image Shifts," J. Appl. Phys., 47, p. 1676 (1976).

48. W. H. Bragg: "The Structure of the Spinel Group of Crystals," Phil. Mag., 30, p. 305.

49. A. Navrotsky, O. J. Kleppa: "The Thermodynamics of Cation Distributions in Simple Spinels," J. Inorg. Nucl. Chem., 29, p. 2701 (1967).

50. W. D. Kingery, H. K. Bowen, D. R. Uhlmann: Introduction to Ceramics, John Wiley and Sons, New York, 1960, p. 64.

51. N. W. Grimes: "'Off-Centre' Ions in Compounds with Spinel Structure," Phil. Mag., 26, p. 1217 (1972).

52. L. Hwang, A. H. Heuer, T. E. Mitchell: "On the Space Group of $MgAl_2O_4$ Spinel," Phil. Mag., 28, p. 241 (1973).

53. E. J. W. Verwey: "Incomplete Atomic Arrangement in Crystals," J. Chem. Phys., 3, p. 592 (1935).

54. P. B. Braun: "A Superstructure in Spinels," Nature, 170, p. 1123 (1952).

55. G. W. van Oosterhout, C. J. M. Rooymans: "A New Superstructure in Gamma-Ferric Oxide," Nature, 181, p. 44 (1958).

56. P. P. K. Smith: "The Observation of Enantiomorphous Domains in a Natural Maghemite," Contr. Mineral. Petrol. 69, p. 249 (1979).

57. C. J. M. Rooymans, "A New Type of Cation-Vacancy Ordering in the Spinel Lattice of In_2S_3," J. Inorg. Nucl. Chem., 11, p. 78 (1959).

58. R. Tertian, D. Papee: "Thermal and Hydrothermal Transformations of Alumina," J. Chim. Phys., 55, p. 341 (1958).

59. Andrews, D. J. Dyson, S. R. Keown: Interpretation of Electron Diffraction Patterns, Plenum Press, New York, 1971.

60. B. C. Lippens, J. D. deBoer: "Study of Phase Transformations During Calcination of Aluminum Hydroxide by Selected Area Electron Diffraction," Acta Cryst., 17, p. 1312 (1964).

61. H. P. Rooksby: "The Preparation of Crystalline Delta Alumina," J. Appl. Chem. 8, p. 44 (1958).

62. G. Ervin, Jr.: "Structural Interpretation of the Diaspore-Corundum and Boehmite- γ-Al_2O_3 Transitions," Acta Cryst., 5, p. 103 (1952).

63. V. R. Howes: "The Early Growth of Oxide on a Fe-Cr Alloy," Corros. Sci., 7, p. 735 (1967).

64. G. O. Lloyd, S. R. J. Saunders, B. Kent, A. Fursey: "Breakaway Oxidation of Fe-10% Cr and Fe-20% Cr at Temperatures up to 1000°C," Corros. Sci., 17, p. 269 (1977).

65. M. G. C. Cox, B. McEnaney, V. D. Scott: "Phase Interactions in the Growth of Thin Oxide Films on Iron-Chromium Alloys," Phil. Mag., 29, p. 585 (1974).

66. W. J. Minford, V. S. Stubican: "Interdiffusion and Assocation Phenomena in the System NiO-Al_2O_3," J. Amer. Cer. Soc., 57, p. 363 (1974).

67. F. S. Pettit, E. H. Randklev, E. J. Felton: "Formation of $NiAl_2O_4$ by Solid State Reaction," J. Amer. Cer. Soc., 49, p. 199 (1966).

68. Y. Oishi, K. Ando: "Self-Diffusion of Oxygen in Polycrystalline $MgAl_2O_4$," J. Chem. Phys., 63, p. 376 (1975).

69. C. E. Birchenall: "The Role of Spinel Oxides in the Oxidation of Iron and Its Alloys," Z. Elektrochem., 63, p. 790 (1959).

70. K. Hauffe, K. Pschera: "The Mechanisms of the Formation of Spinels at Higher Temperatures," Z. Anorg. Chem., 262, p. 147 (1950).

71. J. W. Halloran, H. K. Bowen: "Iron Diffusion in Iron-Aluminate Spinels," J. Amer. Cer. Soc., 63, p. 58 (1980).

72. A. Dauger, D. Fargeot: "TEM Study of Al_2O_3 Metastable Phases," Proceedings of the Fourth Europhysical Topical Conference on "Lattice Defects in Ionic Crystals," Dublin, Ireland, (1982).

73. F. C. Frank, J. H. van der Merwe: "One-dimensional Dislocations, I. Statis Theory," Proc. Roy. Soc, 198, p. 205 (1949).

74. N. H. Fletcher, P. L. Adamson: "Structure and Energy of Crystal Interfaces, I. Formal Development," Phil. Mag., 14, p. 989 (1966).

75. W. Bollman: Crystal Defects and Crystalline Interfaces, Springer-Verlag, Berlin, 1970.

76. J. M. Rigsbee, H. I. Aaronson: "A Computer Modeling Study of Partially Coherent FCC:BCC Boundaries," Acta Met., 27, p. 351 (1979).

77. K. R. Kinsman, H. I. Aaronson: "Structure of Crystalline Interfaces," Metallography, 7, p. 361 (1974).

78. R. C. Ecob, B. Ralph: "A Model of the Equilibrium Structure of FCC/BCC Interfaces," Acta Met., 29, p. 1037 (1981).

79. K. M. Knowles, D. A. Smith, W. A. T. Clark: "On The Use of Geometric Parameters in the Theory of Interphase Bounaries," Scripta Met., 16, p. 413 (1982).

80. C. Kittel: Introduction to Solid State Physics, John Wiley and Sons, New York, 1976, p. 100.

81. R. F. Mehl, and E. L. McCandless: "Oxide Films on Iron," AIME Trans., 125, p. 531 (1937).

82. J. B. Wagner, Jr., K. R. Lawless, A. J. Gwathmey: "The Rates of Formation and Structure of Oxide Films Formed on a Single Crystal of Iron," Trans. Met. Soc. AIME, 221, p. 257 (1961).

83. P. B. Sewell, M. Cohen: "An Electron Diffraction Study of Thin Oxide Films on Iron Single Crystals," J. Electrochem. Soc., 111, p. 508 (1964).

84. K. Kuroda, B. D. Cahan, G. L. Nazri, E. Yeager, T. E. Mitchell: "Electron Diffraction Study of the Passive Film on Iron," J. Electrochem. Soc., 129, p. 2163 (1982).

85. C. L. Foley, J. Kruger, C. J. Bechtoldt: "Electron Diffraction Studies of Active, Passive and Transpassive Oxide Films Formed on Iron," J. Electrochem. Soc., 114, p. 994 (1967).

86. F. Watari, J. M. Cowley: "The Study of Oxide Formation on (001), (011), (111), and (113) Surfaces of Cr Thin Films Using STEM-Microdiffraction Methods," Surf. Sci., 105, p. 240 (1981).

87. W. E. Boggs, R. H. Kachik, G. E. Pellissier: "The Effects of Crystallographic Orientation and Oxygen Pressure on the Oxidation of Iron," J. Electrochem. Soc., 114, p. 32 (1967).

88. J. E. E. Baglin, F. M. D'Heurle: "Epitaxial Relations in Films of Cr, Pt, and CrPt on Saphire," J. Electrochem. Soc., 126, p. 277 (1979).

89. M. G. Hall, H. I. Aaronson, K. R. Kinsman: "The Structure of Nearly Coherent FCC:BCC Boundaries in Cu-Cr Alloy," Surf. Sci., 31, P. 257 (1972).

90. S. R. Keown, D. J. Dyson: "Observation and Orientation Relationship of an Epitaxial Oxide of R_3O_4 Type with Ferrite," JISI, 204, p. 832 (1966).

91. A. T. Davenport: "Occurence of 'Arced' Reflections in Diffraction Patterns from a Vanadium Steel," JISI, 206, p. 499 (1968).

92. J. W. Mathews: "Misfit Dislocations and the Alignment of Epitaxial Islands," Surf. Sci., 31, p. 241 (1972).

93. J. L. Smialek, R. Gibala: "Structure of Transient Oxides Formed on NiCrAl Alloys," Met. Trans A, 14A, p. 2143, (1983).

Appendix A

Published d-spacings for $NiAl_2O_4$ and γ-Al_2O_3.(Ref. 41) (Å)

γ-Al_2O_3	$NiAl_2O_4$
4.566(111)	4.650(111)
3.954(200)	4.024(200)
2.796(220)	2.942(220)
2.384(311)	2.427(311)
2.283(222)	2.322(222)
1.977(400)	2.013(400)
1.814(331)	1.846(331)
1.768(420)	1.800(420)
1.614(422)	1.641(422)
1.522(333)	1.549(333)
1.398(440)	1.423(440)

Appendix B

Relrod formation and positions in (001) and (111) oxide zones.

Relrod formation occurs because the intensity distribution of diffracted electrons is a function of the sample geometry. The intensity distribution is given as:

$$I = \left(\frac{F_g}{V_c} \right)^2 \frac{\sin^2(\pi t s_z)}{(\pi s_z)^2}$$

where I = intensity

F_g = structure factor

V_c = volume of a unit cell

t = foil thickness

s_z = distance from the reciprocal lattice point to the Ewald sphere in the z-direction.

A plot of this function is shown in Figure B1 and shows that the intensity is not a spot but actually in the shape of a rod in the z-direction with a length proportional to 1/t.

Figure B2 is a schematic of reciprocal space of an (001) $NiAl_2O_4$ zone and shows relrod intersections with the Ewald sphere. The projection of these intersections results in the two-dimensional diffraction pattern. Just the projection of a (111) $NiAl_2O_4$ zone is shown in Figure B3 to indicate from which Laue zone each reflection arises.

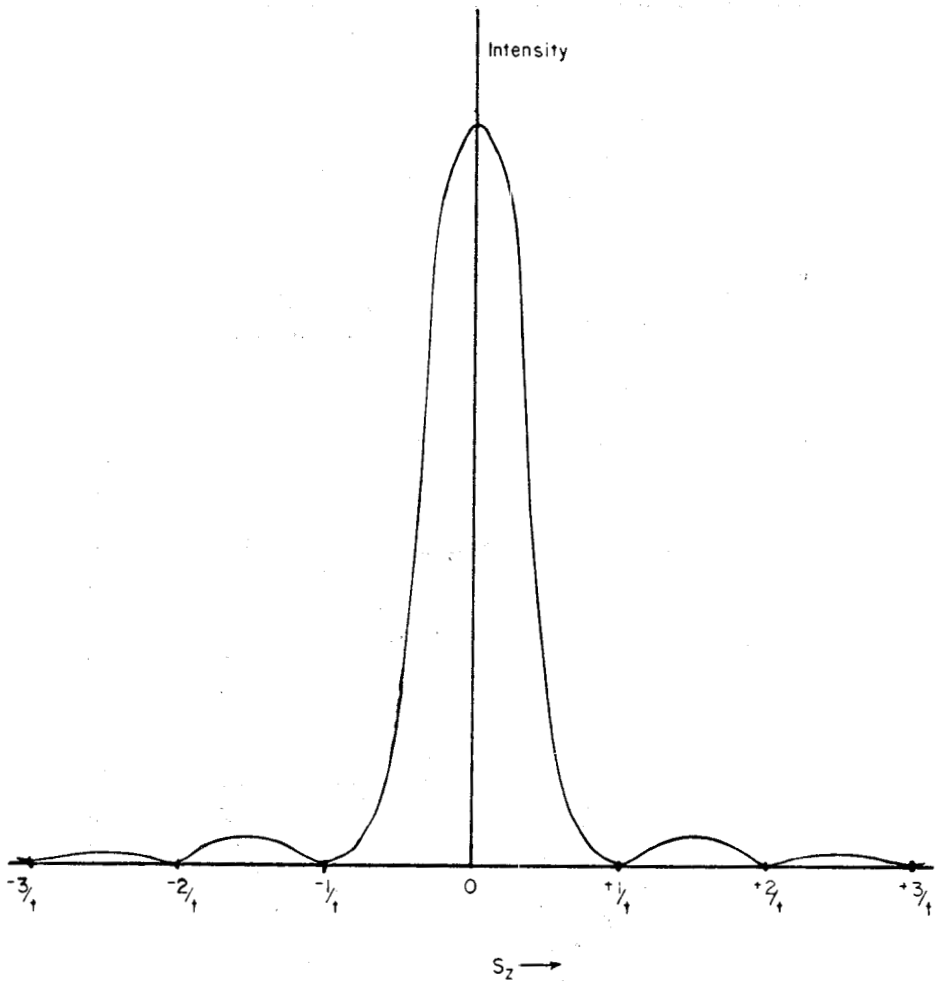

Figure B1

Plot of intensity versus distance from the reciprocal lattice point to the Ewald sphere in the z-direction.

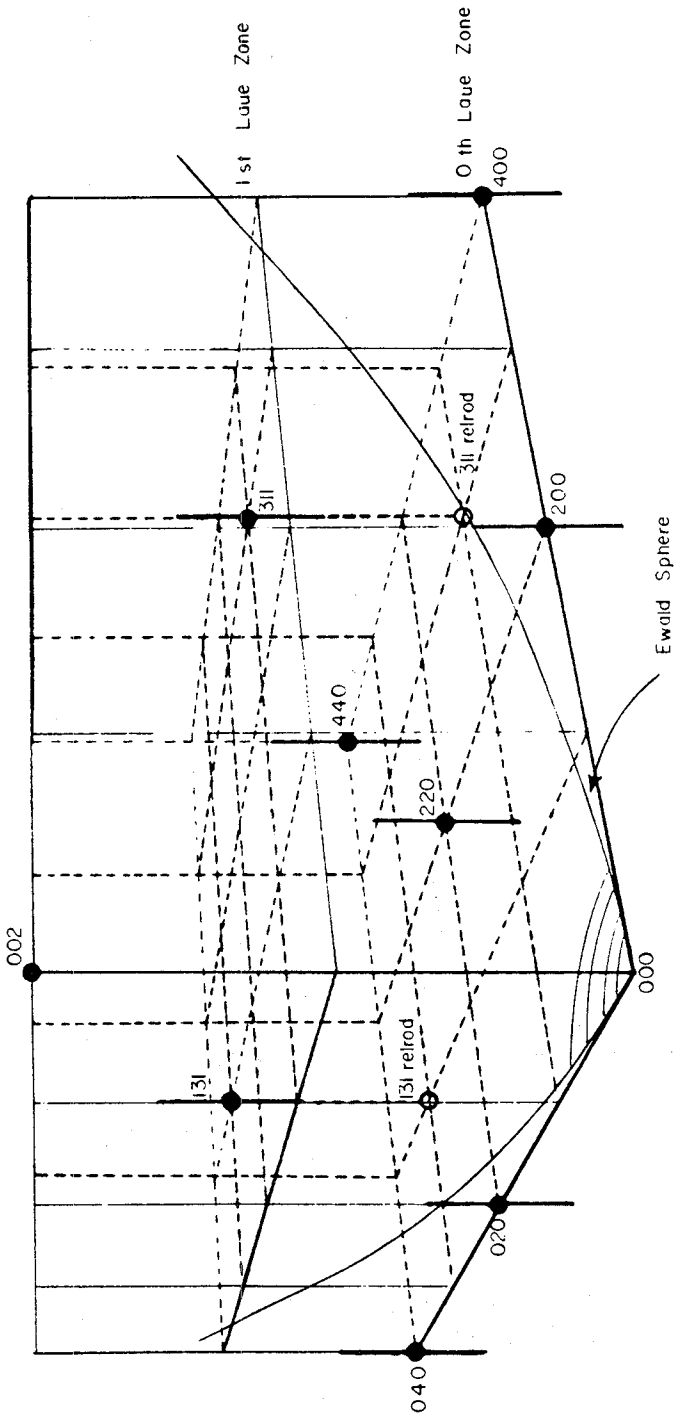

Figure B2

Schematic of a three-dimensional reciprocal lattice of an [001] oxide zone to show relrod reflections with the Ewald sphere. These higher order Laue zone relrod intersections account for the extra reflections in some diffraction patterns of [001] oxide zones.

Figure B3

Two-dimensional projection of higher order Laue zone relrod reflections from intersections with the Ewald sphere. In the case of a [$\bar{1}$11] oxide zone, the repeat unit in the reciprocal lattice is every third Laue zone.

Appendix C

Published d-spacings of δ-Al_2O_3 along with assigned indices to compare with the calculated values of d-spacings of δ-Al_2O_3 found in this study. The lattice constants of $a_o = 7.936$ Å $c_o = 23.356$ Å are the average values measured from diffraction patterns.

Published d-spacings(Å)	(hkl)	Calculated d-spacings(Å)
7.6	(101)	7.525
6.4	(102)	6.570
	(004)	5.835
5.53	(111)	5.465
5.10	(112)	5.065
4.57	(113)	4.557
4.07	(114)	4.048
	(105)	4.025
3.61	(115)	3.591
3.23	(116)	3.199
3.05	(107)	3.075
	(214)	3.036
2.881	(117)	2.868
2.728	(222)	2.733
2.601	(302)	2.590
	(118)	2.584
2.460	(312)	2.458
2.402	(313)	2.392
2.315	(314)	2.309
	(305)	2.305
2.279	(226)	2.278
2.160	(1·1·10)	2.156
1.986	(400)	1.988
1.953	(0·0·12)	1.945
1.914	(318)	1.904
1.827	(333)	1.822
1.810	(319)	1.805
	(2·2·10)	1.796
1.628	(3·1·11)	1.621
	(426)	1.617
1.604	(1·1·14)	1.598
1.538	(513)	1.529
1.517	(1·1·15)	1.500
1.456	(523)	1.450
	(516)	1.447
1.407	(440)	1.405
1.396	(4·0·12)	1.390

Appendix D

δ-Al_2O_3 zone axis diffraction patterns from(001) and (012) metal oxidized for 10.0 hours at 800°C. The indices of the zones correspond to a cubic stereographic projection and not to the tetragonal projection of δ-Al_2O_3.

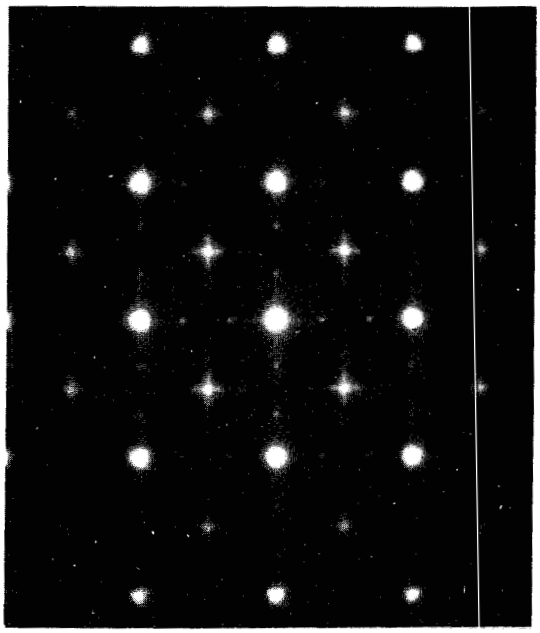

$[001]_{ox}$

$(001)_m$

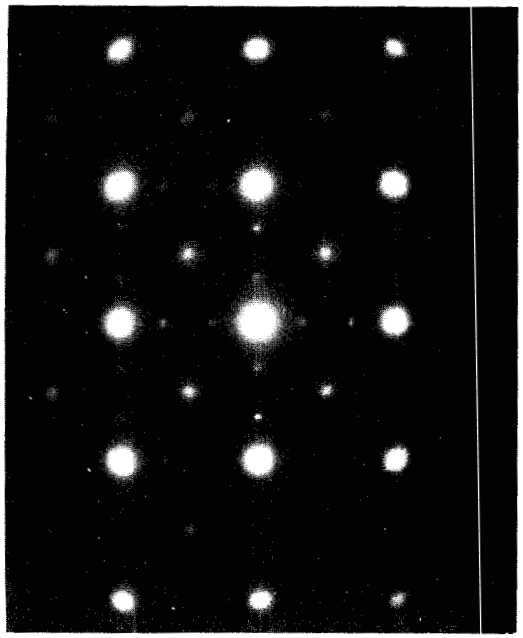

$(012)_m$

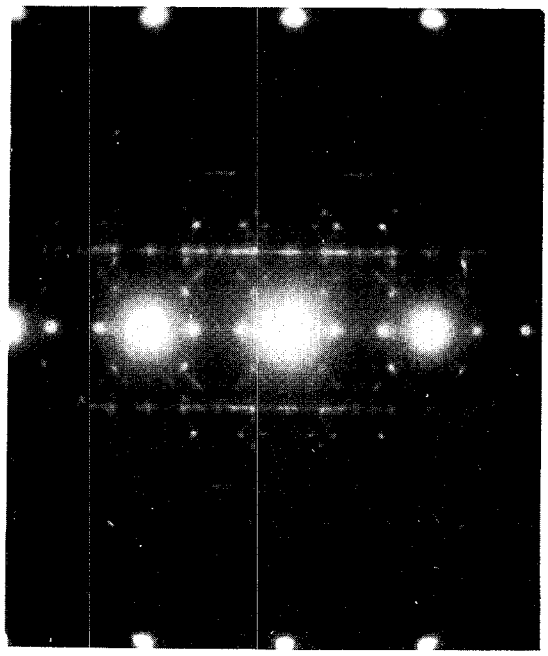

$(001)_m$

$[012]_{ox}$

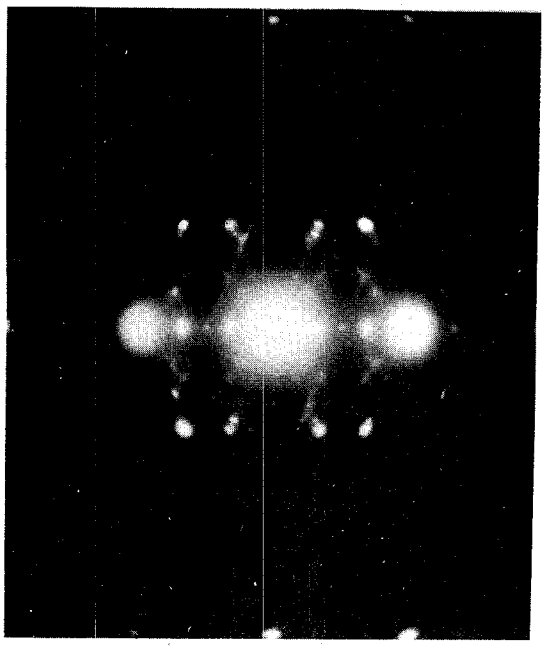

$(012)_m$

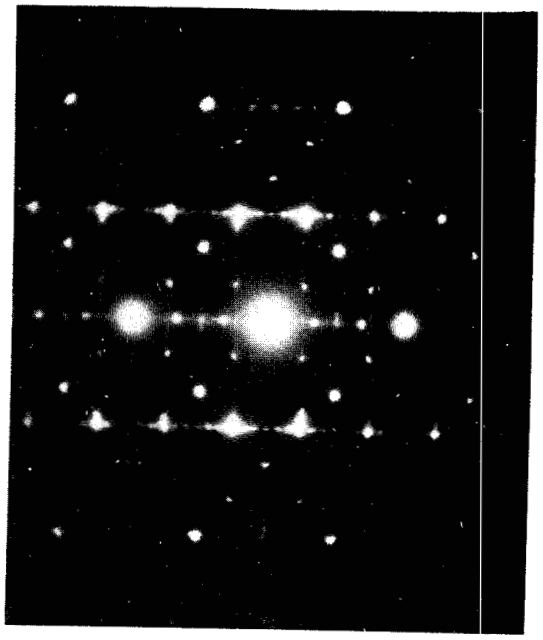

$(001)_m$

$[013]_{ox}$

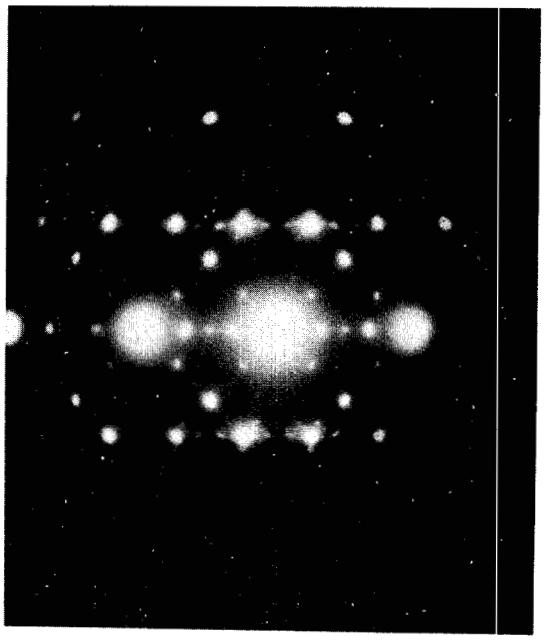

$(012)_m$

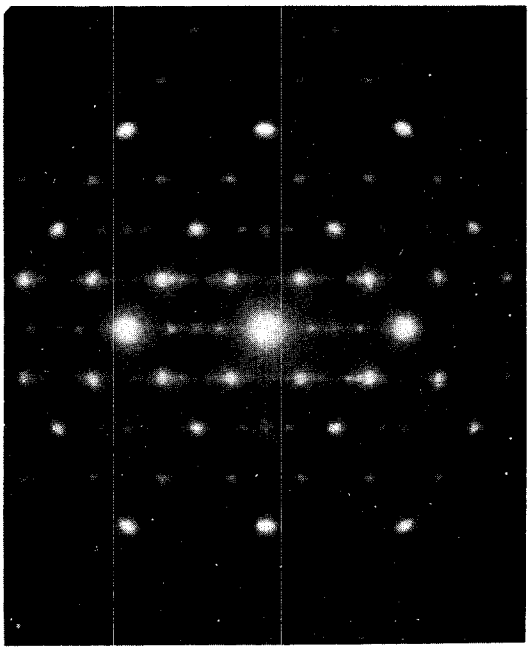

$(001)_m$

$[011]_{ox}$

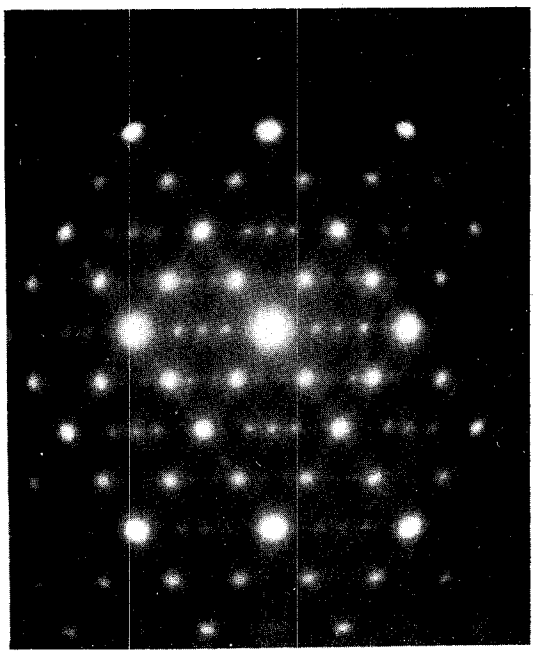

$(012)_m$

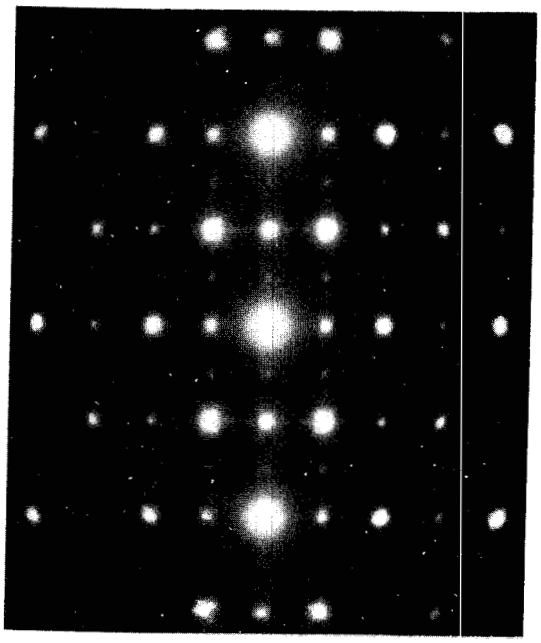

$(001)_m$

$[112]_{ox}$

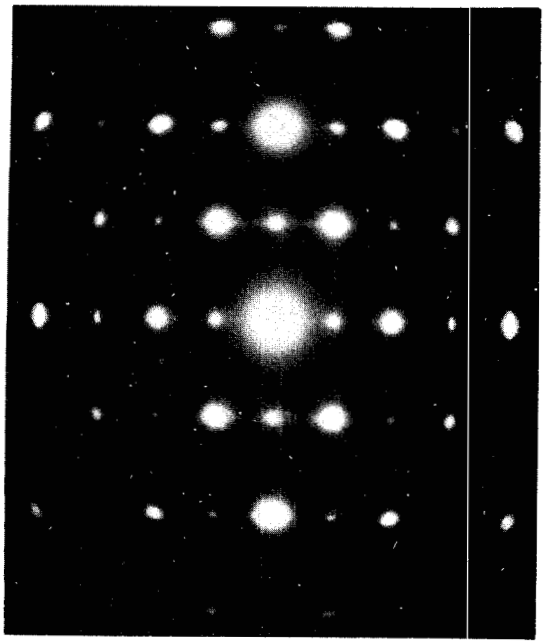

$(012)_m$

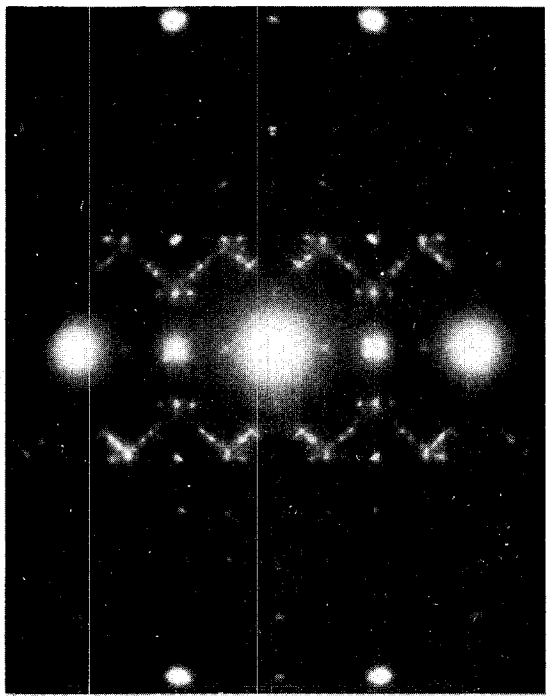

$(001)_m$

$[113]_{ox}$

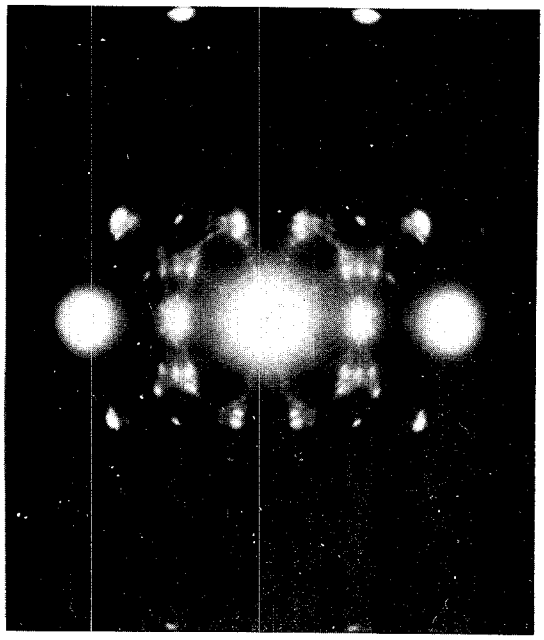

$(012)_m$

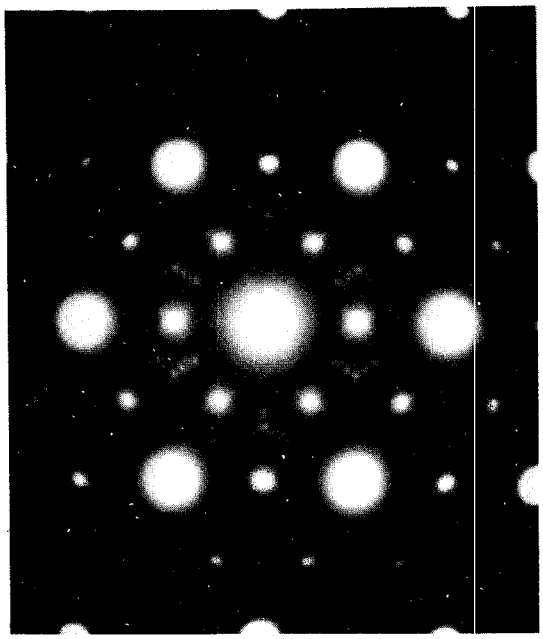

$[111]_{ox}$

$(012)_m$

Appendix E

Computer programs used to determine nearest neighbor distances in the computer models for the five orientation relationships mentioned in this study. The basic programs listed below are adjusted to allow for different rotations and spacings of the two-dimensional interface lattices.

```
5  DIM AL001(100,60)
20 Q = 0
25  TRACE
26  NOTRACE
30 RA1 = 2.862
31 BA2 = 2 ^ 0.5 / 2 * RA1
35 AA1 = (7.908 / 2)
36 AA2 = 2 ^ 0.5 * AA1
37 SS2 = 3 ^ 0.5 / 2 * AA2
38 C =  - 28
42  FOR X =  - 50 TO 50
43  PRINT "X=";X
44  FOR Y = 0 TO 50
62 I = 0
63 J = 0
64 NN = 0
65 LET = 0
69  PRINT "Y=";Y
70 ALP = 0
80 GAM = 0
100 H = RA1 * (X *  COS (ALP) - Y
     *  SIN (ALP))
110 K = BA2 * (X *  SIN (ALP) + Y
     *  COS (ALP))
111  IF Y / 2 =  INT (Y / 2) THEN
     GOTO 120
112 H = H + 0.5 * RA1 *  COS (ALP
    )
120 R = (H ^ 2 + K ^ 2) ^ 0.5
127 Z = X
128  IF X < 0 THEN Z =  ABS (X)
130 AL001(Z,Y) = R
140  IF H = 0 THEN GAM = 3.141592
    65 / 2
150  IF H <  > 0 THEN GAM =  ATN
    (K / H)
151  IF H < 0 THEN GAM = 3.141592
    65 +  ATN (K / H)
160  FOR M = C TO 50
170 NN1 = 0
180 NN2 = 0
190 T0 = 0
200 T1 = 0
210 T2 = 0
220  FOR N = 0 TO 50
230 BET = 0
240 RHO = 0
250 U = AA2 * M
252 V = SS2 * N
254  IF N / 2 =  INT (N / 2) THEN
     GOTO 256
256 U = U + 0.5 * AA2
258  IF U = 0 THEN RHO = 3.141592
    65 / 2
260  IF U > 0 THEN RHO =  ATN (V /
    U)
262  IF U < 0 THEN RHO = 3.141592
    65 +  ATN (V / U)
264 RHO = RHO + BET
266 W = (U ^ 2 + V ^ 2) ^ 0.5
268 U = W *  COS (RHO)
270 V = W *  SIN (RHO)
272  IF V = 0 THEN W = U
294  IF GAM < RHO THEN THETA = RH
    O - GAM
295  IF GAM > RHO THEN THETA = GA
    M - RHO
296  IF GAM = RHO THEN THETA = 0
297  IF THETA = 3.14159265 THEN  GOTO
    299
298  GOTO 305
```

```
299  IF  SGN (W) <  > SGN (R) THEN
     THETA = 0
300  GOTO 305
305  IF GAM = 3.14159265 THEN  GOTO
     307
306  GOTO 310
307  IF THETA = 0 THEN R = U
310 T1 = (R ^ 2 + W ^ 2 - 2 * R *
     W *  COS (THETA)) ^ 0.5
320  IF T1 = 0 THEN  GOTO 460
330  IF T1 < NN1 THEN  GOTO 390
340  IF NN2 < NN1 THEN  GOTO 420
350 NN2 = NN1
360  IF N = 0 THEN  GOTO 380
370  GOTO 420
380  IF T1 > T0 THEN T0 = T1
390 NN1 = T1
400 NN2 = T1
405 S = U
406 L = V
410  NEXT
420  IF LE3 = 0 THEN LE3 = NN2
430  IF LE3 < NN2 THEN  GOTO 480
440 LE3 = NN2
445 I = S
446 J = L
450  NEXT M
460 NN = T1
470  GOTO 490
480 NN = LE3
490  IF NN < 0.60 THEN  GOTO 510
500  GOTO 580
510  PR# 1
511  PRINT "NN=";NN
520  PRINT "H=";H
530  PRINT "K=";K
540  PRINT "U=";I
550  PRINT "V=";J
560  PRINT "Q=";Q
561  PR# 0
570 Q = Q + 1
580  NEXT Y
585  IF X / 2 =  INT (X / 2) THEN
     C = C + 1
590  NEXT X
600  END
```

```
5 R = 0.42
10  PRINT "NN="
15  INPUT NN
16 N = NN / 2
20 A = 3.14159265 / 2 -  ATN (N /
     R / (1 - (N / R) ^ 2) ^ 0.5)

21 B = N * ((R - N) * (R + N)) ^
     0.5
22 C = 2 * (R ^ 2 * A - B)
25 TA = TA + C
30  PR# 1
31  PRINT "A=";C
32  PRINT "SUMMED AREA=";TA
33  PR# 0
35  GOTO 10
36  END
```

☆USGPO: 1984 — 559-109/10413

1. Report No.	2. Government Accession No.	3. Recipient's Catalog No.
NASA CR-174756		

4. Title and Subtitle	5. Report Date
The Transient Oxidation of Single Crystal NiAl+Zr	September 1984
	6. Performing Organization Code

7. Author(s)	8. Performing Organization Report No.
Joseph K. Doychak	None
	10. Work Unit No.

9. Performing Organization Name and Address	11. Contract or Grant No.
Case Western Reserve University Dept. of Metallurgy and Materials Science Cleveland, Ohio 44106	NAG 3-58
	13. Type of Report and Period Covered
12. Sponsoring Agency Name and Address	Contractor Report
National Aeronautics and Space Administration Washington, D.C. 20546	14. Sponsoring Agency Code
	505-36-12

15. Supplementary Notes

Final report. Project Manager, James L. Smialek, Materials Division, NASA Lewis Research Center, Cleveland, Ohio 44135. This report was submitted as a thesis in partial fulfillment of the requirements for the Degree of Master of Science to Case Western Reserve University in May 1984.

16. Abstract

The 800° C oxidation of oriented single crystals of Zr doped β-NiAl was studied using transmission electron microscopy. The oxide phases and metal-oxide orientation relationships were determined to characterize the transient stages of oxidation prior to the transformation to or formation of α-Al_2O_3. On (001) and (012) metal orientations, $NiAl_2O_4$ was the first oxide to form followed by δ-Al_2O_3 which becomes the predominant oxide phase. All oxides were highly epitaxially related to the metal; the orientation relationships being a function of parallel cation close-packed directions in the metal and oxide. On (011) and (111) metal orientations, γ-Al_2O_3 became the predominant oxide phase rather than δ-Al_2O_3, indicating a structural stability resulting from the highly epitaxial oxides. The relative concentration of aluminum in the oxide scales increased with time indicating preferential γ-or δ-Al_2O_3 growth. The major oxide-metal orientations relationships were:

on (001) metal	$(001)_m \parallel (001)_{ox}$; $[100]_m \parallel [110]_{ox}$
on (012) metal	$(012)_m \parallel (\bar{1}12)_{ox}$; $[100]_m \parallel [110]_{ox}$
on (011) metal	$(011)_m \parallel (\bar{1}11)_{ox}$; $[100]_m \parallel [110]_{ox}$
on (111) metal	$(111)_m \parallel (021)_{ox}$; $[1\bar{1}0]_m \parallel [100]_{ox}$
	(three variants)

The striking feature common to these orientation relationships is the alignment of $[100]_m$ and $[110]_{ox}$ directions, believed to result from the minimal 3 percent mismatch between the corresponding $(100)_m$ and $(110)_{ox}$ planes.

17. Key Words (Suggested by Author(s))	18. Distribution Statement
Al_2O_3 scales Oxidation TEM NiAl Epitaxy	Unclassified - unlimited STAR Category 26

19. Security Classif. (of this report)	20. Security Classif. (of this page)	21. No. of pages	22. Price*
Unclassified	Unclassified	242	A11

*For sale by the National Technical Information Service, Springfield, Virginia 22161

National Aeronautics and
Space Administration

Washington, D.C.
20546

Official Business
Penalty for Private Use, $300

SPECIAL FOURTH CLASS MAIL
BOOK

Postage and Fees Paid
National Aeronautics ar
Space Administration
NASA-451

NASA

POSTMASTER: If Undeliverable (Section 158
Postal Manual) Do Not Return